KAON IDENTIFICATION AND SEARCH FOR LEPTON NUMBER VIOLATION IN $K^\pm$ DECAY-IN-FLIGHT EXPERIMENTS AT CERN

Karim Massri

Thesis submitted for the degree of
Doctor of Philosophy

Particle Physics Group,
School of Physics and Astronomy,
University of Birmingham.

August 11, 2014

Abstract

A search for the Lepton Number Violating decay $K^{\pm} \to \pi^{\mp} \mu^{\pm} \mu^{\pm}$ has been performed using the data collected by the NA48/2 experiment in 2003 and 2004. The signal event selection, the background rejection, the evaluation of the muon identification efficiency and the statistical methods used for the data interpretation are presented. Based on 1.8×10^{11} kaon decays in the fiducial volume and using several models for the signal, upper limits for the branching fraction $\mathcal{B}(K^{\pm} \to \pi^{\mp} \mu^{\pm} \mu^{\pm})$ of the order of 10^{-10} have been obtained for 90%, 95% and 99% confidence levels, improving the previous best limit by one order of magnitude.

The Cherenkov differential counter used for kaon identification in the NA62 experiment, equipped with approximately 30% of the photo-detectors, was installed and tested during a Technical Run in 2012. The counter's ability of distinguishing between kaons and pions has been validated via pressure scan procedure. The data collected have been used for evaluating the kaon identification efficiency and time resolution. The extrapolation to the full-sized detector has been also estimated.

Declaration of author's contribution

The search of the $K^\pm \to \pi^\mp \mu^\pm \mu^\pm$ decay presented in Chapter 3 is the result of my own work. The data sample analysed was collected by the NA48/2 experiment in 2003 and 2004. I was not involved in the design, construction and operation of the NA48/2 experiment and the description provided in Chapter 2 is only included to support the $K^\pm \to \pi^\mp \mu^\pm \mu^\pm$ analysis.

Over the course of my Ph.D. I conducted a number of technical studies on the CEDAR/KTAG detector, which is employed for kaon identification in the NA62 experiment. Some of the design and construction choices described in Chapter 5 are the consequence of my own work. During the NA62 Technical Run in 2012 I was responsible for the installation and operation of the CEDAR/KTAG detector and I developed the KTAG online data quality monitor and related software. The Technical Run procedures and findings presented in Chapter 6 are the result of my own work, except where explicitly stated. An overview of the NA62 experiment and the other subdetectors is presented in Chapter 4 to give the context for the description of the CEDAR/KTAG detector and of the performed measurements.

No other qualifications have been achieved with the work reported in this thesis.

Acknowledgements

I would like to thank all the people who have helped me, in one way or another, during the preparation of this thesis. First, a sincere thanks to my supervisors Cristina Lazzeroni and Evgueni Goudzovski for all the help and valuable comments, suggestions and advices they have provided since my arrival in Birmingham. I would also like to thank Tonino Sergi and Angela Romano for the friendly discussions and for all the tips they gave me (and Tonino especially for urging me to switch to *vim*!). Thanks to Francis, Nicolas, Jimmy and Nathaniel, the inhabitants of W313, also known as "the flavour office", for the enjoyable working environment; to Max and Pallavi for giving me shelter (I owe you a big one!) and to the "Bhamhood": Claudio, il sig. Carlo, Walter, Giacomino and Giacomone, for the uncountable laughs during all these years. I would also like to thank my parents for even starting to use Skype despite their retro style and the rest of my family which, as the Universe, is in expansion! *Dulcis in fundus*, I thank Rossella for her love and support, because the last four years would have been a disaster without her!

Contents

List of Figures

List of Tables

Acronyms

AGS Alternating Gradient Synchrotron. 32

BNL Brookhaven National Laboratory. 32

BSM Beyond the Standard Model. 3, 169

CAN Control Area Network. 140, 148

CCPC Credit-Card PC. 142

CDA Closest Distance of Approach. 47, 59, 64

CEDAR ChErenkov Differential counter with Achromatic Ring focus. 127, 145, 148

CKM Cabibbo-Kobayashi-Maskawa. 19–21

CL Confidence Level. 16, 17, 50, 51, 97–99, 101, 103–105, 156, 170

CR Control Region. 88, 89

DCH Drift CHamber. 39, 40, 47, 55, 56, 65

DCS Detector Control System. 146, 148

DSS Detector Safety System. 146, 148

ELMB Embedded Local Monitoring Board. 140

FCNC Flavour Changing Neutral Current. 18, 19

FWHM Full Width at Half Maximum. 32

GIM Glashow-Iliopoulos-Maiani. 19

GTK GigaTracKer. 114

GUTs Grand Unified Theories. 8

HAC HAdronic Calorimeter. 44

Introduction

Since their discovery in late '40s, kaons have been instrumental in understanding the fundamental interactions of nature. The tremendous impact of kaon physics in the development of the Standard Model includes the observation of kaon decay modes with different parity (the so-called "$\vartheta - \tau$ paradox"), which led to the discovery of the parity symmetry violation in weak interactions, and the evidence for a second generation of quarks. In fact, the quantum number "strangeness" was introduced to explain the anomalously large lifetime of kaons, which successively led to the postulation of the "strange" quark and the quark model, while the existence of the "charm" quark was hypothesised to explain the observed suppression of the $K_L \to \mu^+\mu^-$ with respect to the charged analogous $K^\pm \to \mu^\pm \nu$ (GIM mechanism). Another milestone of the kaon physics was to provide the first evidence of indirect and direct CP violation, by the precision measurement of neutral kaon decay rates.

Nowadays, kaon physics is still a unique probe of the flavour sector of the Standard Model. In particular, there are special kaon decays with high experimental sensitivity to new physics, due to their very precise theoretical predictions. The work reported in this thesis has been carried out using data collected by the NA48/2 and NA62 experiments, the two most recent in a long tradition of fixed-target kaon experiments in the CERN North Area (NA).

The presented thesis is organised in two parts: the first part is dedicated to the search for $K^\pm \to \pi^\mp \mu^\pm \mu^\pm$ decays performed with the data collected by the NA48/2 experiment, the second part is devoted to the work on the kaon identification detector

in the NA62 experiment. The first chapter reviews the theoretical framework behind the $K^\pm \to \pi^\mp \mu^\pm \mu^\pm$ decay, which is forbidden in the Standard Model, and the $K^+ \to \pi^+ \nu \bar{\nu}$ decay, the study of which is the main goal of the NA62 experiment. The NA48/2 beam line, the detector and the data acquisition system are briefly introduced in Chapter 2, focussing in particular on the sub-systems involved in the $K^\pm \to \pi^\mp \mu^\pm \mu^\pm$ analysis. The signal event selection, the background rejection, the evaluation of the muon identification efficiency and the statistical methods used for the data interpretation are presented in Chapter 3. Chapter 4 provides an overview of the NA62 experimental strategy, the experimental apparatus and the data acquisition system, while Chapter 5 is dedicated to the description of the CEDAR/KTAG detector. Finally, the work performed for the operation of the CEDAR/KTAG detector during the NA62 Technical Run in 2012 is reported in Chapter 6, together with the evaluation of the kaon identification efficiency, the time resolution and the ability to distinguish between kaons and pions, which have been obtained from a dedicated analysis of the collected data.

Chapter 1

Theoretical framework

1.1 The $K^\pm \to \pi^\mp \mu^\pm \mu^\pm$ decay

Lepton Flavour (LF) and Lepton Number (LN) are accidentally conserved quantities within the Standard Model (SM). Unlike other quantum numbers, e.g. the electric charge, their conservation is not imposed by the theory as a consequence of a local gauge symmetry (Noether's theorem).

While Lepton Flavour Violation (LFV) has been observed in neutrino mixing experiments [1], leading to the first evidence of physics Beyond the Standard Model (BSM), Lepton Number Violation (LNV) has never been observed. In this scenario, the search for LNV processes plays a crucial role. In particular, processes violating LN by two units ($\Delta L = 2$) are a unique tool to address pressing open questions, as the Dirac or Majorana nature of the neutrino and the origin of its mass, and to probe the leptonic sector of the Standard Model.

The search for the $K^\pm \to \pi^\mp \mu^\pm \mu^\pm$ decay, which is one of the LNV processes, is discussed in Chapter 3. A theoretical model involving heavy Majorana neutrinos, which could describe the mechanism behind $\Delta L = 2$ processes, will be presented in this section, together with the relevant framework. The experimental status of the

$K^\pm \to \pi^\mp \mu^\pm \mu^\pm$ search will also be discussed.

1.1.1 Massive neutrinos

Neutrinos are strictly massless within the SM. A neutrino mass term is not allowed in the SM lagrangian $\mathcal{L}$, due to the absence of right-handed neutrino states. However, since the observation of neutrino oscillations [1] has unambiguously demonstrated the massive nature of neutrinos[1], right-handed neutrino states must be included. From a theoretical point of view, such extension leads to the problem of the neutrino nature. In fact, neutrinos can be either Dirac or Majorana particles, and the description of the right-handed neutrino states, as well as the neutrino mass term, depends on this.

1.1.1.1 Dirac and Majorana particles

Dirac particles are fermions described by fields ψ which satisfy the Dirac equation

$$(i\partial_\mu \gamma^\mu - m)\psi = 0, \tag{1.1}$$

and, in general, are described by 4-component complex fields (Dirac spinors). A Majorana particle is a fermion described by a field χ which satisfies the condition

$$C\bar{\chi}^{\mathrm{T}} = e^{i\xi}\chi, \quad |e^{i\xi}|^2 = 1, \tag{1.2}$$

where C is the charge conjugation operator and $e^{i\xi}$ is an arbitrary phase. Unlike Dirac fermions, Majorana particles cannot carry any $U(1)$ charge (electric charge, lepton number, etc). Therefore, neutrinos are the only known particles which are possible Majorana candidates.

From eq. 1.2 it follows that a Majorana fermion is an eigenstate of the C operator, i.e. it is its own antiparticle. Such property is crucial: it means that unlike Dirac fields ψ, for which the only non-zero propagator is $\langle 0|T(\psi_\alpha(x)\bar{\psi}_\beta(y))|0\rangle$, Majorana fields have

---

[1]In particular, the observed oscillations can occur only if the three neutrino mass eigenstates have different eigenvalues, implying that at least two must have non-zero mass.

also non-zero propagators such as $\langle 0|T(\psi_\alpha(x)\psi_\beta(y))|0\rangle$ and $\langle 0|T(\bar{\psi}_\alpha(x)\bar{\psi}_\beta(y))|0\rangle$, where T is the time-ordering operator. In fact, the condition in eq. 1.2 implies that

$$\langle 0|T(\psi_\alpha(x)\psi_\beta(y))|0\rangle = -e^{-i\xi}\langle 0|T(\psi_\alpha(x)\bar{\psi}_\beta(y))|0\rangle C \neq 0, \qquad (1.3)$$

$$\langle 0|T(\bar{\psi}_\alpha(x)\bar{\psi}_\beta(y))|0\rangle = e^{i\xi}C^{-1}\langle 0|T(\psi_\alpha(x)\bar{\psi}_\beta(y))|0\rangle \neq 0. \qquad (1.4)$$

If neutrinos were Majorana particles, neutrino propagators of such form would violate the LN by 2 units. Therefore, $\Delta L = 2$ processes such as neutrinoless double beta ($0\nu\beta\beta$) decays or $K^\pm \to \pi^\mp \ell^\pm \ell^\pm$ ($\ell = e, \mu$) decays could be mediated by the exchange of neutrinos. In general, as it will be discussed, any massive[2] Majorana particle interacting with the $W^\pm$ and Z^0 bosons would contribute to such processes.

1.1.1.2 Dirac and Majorana mass terms

Mass terms for Dirac and Majorana particles do not have the same form, due to the different assumptions on the right-handed fields. The neutrino mass terms in the two scenarios are discussed below.

If neutrinos are Dirac particles, they can be treated as all the other massive fermions. In a minimally extended SM, three neutrino right-handed singlets $\nu_{\ell R}$ ($\ell = e, \mu, \tau$) are introduced in the SM lagrangian and the Dirac mass terms

$$\mathcal{L}_D^\nu(x) = -\overline{\nu_{\ell L}}(x) m_{D\ell\ell'} \nu_{\ell' R}(x) + h.c., \qquad (1.5)$$

arise from the Yukawa couplings Y^ν of the lepton doublets $\psi_L = (\nu_\ell, \ell)_L$ ($\ell = e, \mu, \tau$), the Higgs doublet H and the right-handed neutrinos $\nu_{\ell R}$ [2]

$$\mathcal{L}_Y = -Y^\nu_{\ell\ell'}\overline{\psi_{\ell L}}(x)H(x)\nu_{\ell' R}(x) + h.c., \qquad (1.6)$$

after the spontaneous symmetry breaking. Analogously to charged leptons and quarks, $m_D \stackrel{def}{=} vY^\nu$ is in general a complex 3×3 matrix, where $v = 247\,\text{GeV}$ is the vacuum expectation value of the Higgs doublet and Y^ν is the neutrino Yukawa

---

[2]As it will be shown, massless Majorana particles do not contribute to $\Delta L = 2$ processes.

coupling matrix. However, the current limits on the neutrino masses ($m_\nu \lesssim 0.1\,\text{eV}$ [1]) would require neutrino Yukawa couplings much smaller than their analogous Y^ℓ for charged fermions:

$$Y^\nu \lesssim 10^{-10} Y^\ell, \tag{1.7}$$

and such a difference is widely considered unlikely [3–5].

On the other hand, if neutrinos are Majorana particles, it is in principle possible to build a so-called Majorana mass term without introducing neutrino right-handed singlets, since $\nu^c_{\ell' R} \equiv C(\overline{\nu_{\ell' L}}(x))^{\text{T}}$ is already a right-handed state:

$$\mathcal{L}^\nu_M(x) = -\frac{1}{2}\overline{\nu_{\ell L}}(x) m_{M\ell\ell'} \nu^c_{\ell' R}(x) + h.c.. \tag{1.8}$$

However, such a mass term cannot be obtained from the spontaneous symmetry breaking as for the Dirac mass term, because all the possible Yukawa coupling terms involving $\overline{\nu_{\ell L}}$, $\nu^c_{\ell' R}$ and a Higgs doublet are not gauge-invariant. In fact, it is not possible to build a $SU(2)_L$-scalar quantity using an odd number of $SU(2)_L$ doublets. Therefore, as in the case of Dirac neutrinos, a minimally extended SM foresees the introduction of sterile ($SU(2)_L$ singlets) neutrinos to generate the neutrino mass terms.

1.1.1.3 See-saw mechanism

A variety of different mechanisms have been proposed to generate neutrino mass terms. A detailed description of the most widely accepted ones can be found in Ref. [3]. Here, as an example, the so-called "type I see-saw mechanism" [6] will be discussed. In this particular model, n_s sterile ($SU(2)_L$ singlet) Majorana neutrinos N_m ($m = 4, \ldots, n_s + 3$) are introduced, which interact with the SM lepton doublets $\psi_{\ell L}$ ($\ell = e, \mu, \tau$) and the Higgs doublet H via Yukawa coupling Y^N and also

possess a Majorana mass term M_R:

$$
\begin{aligned}
\mathcal{L}_{Y,M}(x) &\equiv \mathcal{L}_Y(x) + \mathcal{L}_M^N(x) \\
&= -Y_{\ell m}^{\text{N}}\overline{\psi_{\ell L}}(x)H(x)N_{mR}(x) - \frac{1}{2}M_{Rm'm}\overline{N_{m'L}^c}(x)N_{mR}(x) + h.c..
\end{aligned} \tag{1.9}
$$

Analogously to eqs. 1.5–1.6, a Dirac[3] mass term is generated after spontaneous symmetry breaking:

$$
\mathcal{L}_D^\nu(x) = -\overline{\nu_{\ell L}}(x)m_{D\ell m}N_{mR}(x) + h.c., \tag{1.10}
$$

hence the total mass term $\mathcal{L}_{D,M} \equiv \mathcal{L}_D^\nu + \mathcal{L}_M^N$ is

$$
\begin{aligned}
\mathcal{L}_{D,M}(x) &= -\overline{\nu_{\ell L}}(x)m_{D\ell m}N_{mR}(x) - \frac{1}{2}M_{Rm'm}\overline{N_{m'L}^c}(x)N_{mR}(x) + h.c., \\
&\overset{def}{=} -\frac{1}{2}(\bar{\nu}_L, \overline{N^c}_L)\begin{pmatrix} 0 & M_D \\ (M_D)^{\text{T}} & M_R \end{pmatrix}\begin{pmatrix} \nu_R^c \\ N_R \end{pmatrix} + h.c.,
\end{aligned} \tag{1.11}
$$

where $\nu_L = (\nu_e, \nu_\mu, \nu_\tau)_L$ is a 3-component vector formed of the SM neutrinos and $N_R = (N_4, \ldots, N_{n_s+3})$ is a n_s-component vector formed of the right-handed singlets N_m. $M_D \overset{def}{=} vY^{\text{N}}$ is a $3 \times n_s$ matrix, while M_R is a $n_s \times n_s$ matrix. By choosing a suitable basis, the $(n_s + 3) \times (n_s + 3)$ matrix in eq. 1.11 can be transformed in to the block-diagonal matrix $\mathcal{M}$

$$
\mathcal{M} = \begin{pmatrix} M_\nu & 0 \\ 0 & M_N \end{pmatrix}, \qquad \begin{aligned} M_\nu &\simeq m_D^{\text{T}}M_R^{-1}m_D, \\ M_N &\simeq M_R. \end{aligned} \tag{1.12}
$$

The mass eigenvalues and eigenstates m_{ν_i}, ν_i^{M} $(i = 1, 2, 3)$ and m_{N_m}, N_m^{M} $(m = 4, \ldots, n_s+3)$ respectively of the SM and sterile neutrinos are obtained by diagonalising the 3×3 matrix M_ν and the $n_s \times n_s$ matrix M_N.

The theoretical interest behind this mechanism is due to the fact that if the sterile

---

[3]Indeed, the generated mass term is actually a Dirac mass term, rather than a Majorana, because the two fields ν_L and N_R are not related from the Majorana condition, as it would be required in eq. 1.8. However, the fields themselves are assumed to be of Majorana type, since no right-handed fields ν_R are included in the model.

Majorana neutrino masses $m_{N_m} \sim M_R$ were much heavier than the typical value of $m_D = vY^\text{N}$, the SM neutrino masses $m_{\nu_i} \sim M_\nu \sim m_D^2/M_R$ would be naturally much smaller than the ones of charged leptons and quarks, even with Yukawa couplings Y^N and Y^ℓ of the same order. Indicatively, a sterile Majorana neutrino with mass $m_{N_4} \sim 10^{14}\,\text{GeV}$ would generate SM neutrino masses $m_{\nu_i} \sim 0.1\,\text{eV}$, considering $m_D \sim 100\,\text{GeV}$. Such a mass scale is close to the scale $M_\text{GUT} \cong 2 \times 10^{16}\,\text{GeV}$ of unification of the electroweak and strong interactions, foreseen by Grand Unified Theories (GUTs) [7]. However, models implementing the see-saw mechanism with neutrino masses below the TeV scale have been recently considered [8, 9]: in this case, the generated neutrino masses are accidentally of the order of the charged lepton ones. As will be discussed in the next section, such a scenario predicts an enhancement in the $K^\pm \to \pi^\mp \ell^\pm \ell^\pm$ ($\ell = e, \mu$) decay rate which can be probed with the current experimental sensitivity[4].

1.1.2 Majorana neutrinos as $K^\pm \to \pi^\mp \ell^\pm \ell^\pm$ mediator

As discussed in Sec. 1.1.1, a minimally extended SM foresees the introduction of right-handed singlets to generate the neutrino mass terms. In the following, n_s sterile (right-handed SM singlets) Majorana neutrinos N_m ($m = 4, \ldots, n_s + 3$) will be considered, which interact with the SM lepton doublets $\psi_L = (\nu_i, \ell_i)_L$ ($i = 1, 2, 3$) and the Higgs doublet H via Yukawa coupling Y^N and possess a Majorana mass term $M_R \gg m_D \overset{def}{=} vY^\text{N}$. After the spontaneous symmetry breaking, SM neutrino masses are generated with the type I see-saw mechanism (Sec. 1.1.1) and the total neutrino mass term can be expressed as

$$-\mathcal{L}_m^\nu = \frac{1}{2} \left(\sum_{i=1}^{3} \sum_{k=1}^{n_s} \left(\overline{\nu_{iL}} m_{Dik} N_{kR} + \overline{N_{kL}^c} m_{Dki}^\text{T} \nu_{iR}^c \right) + \sum_{k,k'=1}^{n_s} \overline{N_{kL}^c} M_{Rkk'} N_{k'R} \right) + h.c.,$$

$$= \frac{1}{2} \left(\sum_{i=1}^{3} m_{\nu_i} \overline{\nu_{iL}^\text{M}} \nu_{mR}^\text{M c} + \sum_{m=4}^{n_s+3} m_{N_m} \overline{N_{mL}^\text{M c}} N_{mR}^\text{M} \right) + h.c., \tag{1.13}$$

---

[4]In the following, the NA48/2 experimental sensitivity $\mathcal{O}(10^{-10})$ will be considered.

respectively for the electroweak and mass eigenstates. The mass eigenvalues of SM and sterile ($SU(2)_L$-singlet) neutrinos are $m_{\nu_i} \sim m_D^2/M_R$ ($i = 1, 2, 3$) and $m_{N_m} \sim M_R$ ($m = 4, \ldots, n_s + 3$) respectively (Sec. 1.1.1). The mixing between the electroweak and mass eigenstates is described by the relation

$$\nu_{\ell L} = \sum_{i=1}^{3} U_{\ell i} \nu_{iL}^{\text{м}} + \sum_{m=4}^{n_s+3} \mathcal{U}_{\ell m} N_{mL}^{\text{м}c}, \quad UU^\dagger + \mathcal{U}\mathcal{U}^\dagger = \mathbb{1}, \tag{1.14}$$

where U is a 3×3 matrix determining the SM neutrino mixing and $\mathcal{U}$ is a $3 \times n_s$ matrix describing the mixing between sterile and SM neutrinos. In particular, the see-saw mechanism imposes a suppression in the magnitude of the latter term: $\mathcal{U}\mathcal{U}^\dagger \sim m_D^2/M_R^2 \ll 1$, therefore $UU^\dagger \sim 1$.

A crucial aspect of the type I see-saw mechanism described above is that a non-zero $\mathcal{U}$ matrix implies the existence of interaction terms between sterile neutrinos and $W^\pm$, Z^0 bosons, which can be obtained by writing the gauge interaction Lagrangian in terms of the mass eigenstates:

$$-\mathcal{L} = \frac{g}{\sqrt{2}} W_\mu^+ \left(\sum_\ell \sum_{i=1}^{3} U_{\ell i}^* \overline{\nu_{iL}^{\text{м}}} \gamma^\mu P_L \ell + \sum_\ell \sum_{m=4}^{n_s+3} \mathcal{U}_{\ell m}^* \overline{N_{mL}^c} \gamma^\mu P_L \ell \right) + h.c. \tag{1.15}$$

$$+ \frac{g}{2\cos\theta_W} Z_\mu \left(\sum_\ell \sum_{i=1}^{3} U_{\ell i}^* \overline{\nu_{iL}^{\text{м}}} \gamma^\mu P_L \nu_\ell + \sum_\ell \sum_{m=4}^{n_s+3} \mathcal{U}_{\ell m}^* \overline{N_{mL}^c} \gamma^\mu P_L \nu_\ell \right) + h.c.,$$

where g is the weak interaction coupling constant, θ_W is the weak mixing angle, γ^μ are the Dirac matrices and $P_L = (1 - \gamma_5)/2$ is the left-handed chiral projection operator.

In the considered scenario, the lowest-order contributions to the amplitude $\mathcal{A}_{\pi\ell\ell} \equiv \mathcal{A}(K^\pm \to \pi^\mp \ell^\pm \ell^\pm)$ are described by the Feynman diagrams in Fig. 1.1. In literature, the first diagram is called the s-channel diagram, the second the t-channel diagram. While the s-channel diagram can be expressed in a model independent way as a function of the measured decay constants f_K and f_π, the t-channel depends on non-perturbative effects of the hadron dynamics. However, in the case of an on-shell Majorana neutrino mediating the decay [4], which is of particular interest from the

experimental point of view, only the s-channel contributes. For the cases in which the Majorana neutrino is virtual, considering the s-channel only, it is possible to estimate the expected order of magnitude of the branching fraction $\mathcal{B}(K^\pm \to \pi^\mp \ell^\pm \ell^\pm)$ as a function of the Majorana neutrino masses m_{N_m} $(m = 4, \ldots, n_s + 3)$, since it is either dominant or of the same order as the t-channel [10,11]. Its contribution to the decay amplitude $\mathcal{A}_{\pi\ell\ell}$ can be written as [4,10]

$$\mathcal{A}_{\pi\ell\ell} = 2G_F^2 f_K f_\pi V_{ud}^* V_{us} \sum_{m=4}^{n_s+3} \mathcal{U}_{\ell m}^* \mathcal{U}_{\ell m} p_{K,\alpha} p_{\pi,\beta} \left[L_m^{\alpha\beta}(p_\ell) - L_m^{\alpha\beta}(p_{\ell'}) \right], \qquad (1.16)$$

where G_F is the Fermi constant; V_{us} and V_{ud} are elements of the Cabibbo-Kobayashi-Maskawa matrix (Sec. 1.2.1); p_K, p_π, p_ℓ and $p_{\ell'}$ are the kaon, pion and the two leptons 4-momenta respectively; and $L_m^{\alpha\beta}(p)$ is defined as

$$L_m^{\alpha\beta}(p) = \frac{m_{N_m} \bar{u}(p_\ell) \gamma^\alpha \gamma^\beta P_R v(p_{\ell'})}{(p_K - p)^2 - m_{N_m}^2 + i\Gamma_{N_m} m_{N_m}}, \qquad (1.17)$$

where $P_R = (1 + \gamma_5)/2$ is the right-handed chiral projection operator; u and v are the spinors of the charged leptons; and m_{N_m} and Γ_{N_m} are the mass and the decay width of the Majorana neutrino N_m.

In the following, the two limits of light and heavy sterile neutrinos are discussed, as well as the case in which sterile neutrinos are resonant.
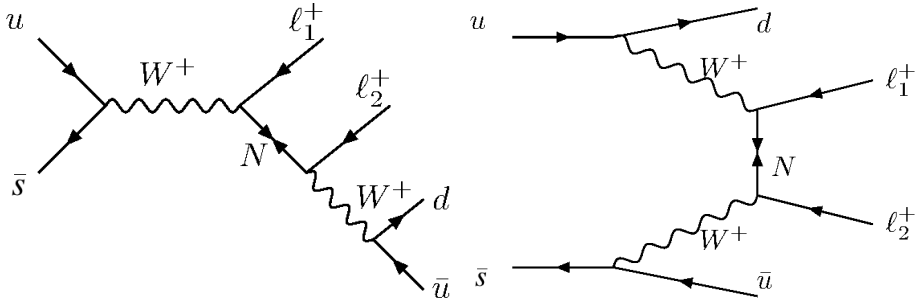
Figure 1.1: Feynman diagrams describing the massive Majorana neutrinos contributions to the $\Delta L = 2$ process $K^\pm \to \pi^\mp \ell_1^\pm \ell_2^\pm$.

1.1.2.1 $\mathcal{B}(K^\pm \to \pi^\mp \ell^\pm \ell^\pm)$ in the limit $m_N \ll m_K$

In the limit of light sterile neutrinos ($m_{N_m} \ll m_K$) the leptonic tensor $L_m^{\alpha\beta}$ defined in eq. 1.17 can be approximated as

$$L_m^{\alpha\beta}(p) \approx m_{N_m} \frac{\bar{u}(p_\ell)\gamma^\alpha \gamma^\beta P_R v(p_{\ell'})}{(p_K - p)^2}. \tag{1.18}$$

In such limit, the branching fraction $\mathcal{B}(K^\pm \to \pi^\mp \ell^\pm \ell^\pm)$ has been calculated by Ali et al. [11] to be

$$\begin{aligned} \mathcal{B}(K^\pm \to \pi^\mp \ell^\pm \ell^\pm) &\approx \tau_K \frac{G_F^4 m_K^3}{16\pi^3} f_K^2 f_\pi^2 |V_{us} V_{ud}|^2 \phi_{\ell\ell}^L \langle m_{\ell\ell} \rangle^2, \\ &\approx 1.7 \times 10^{-18}\, \mathrm{MeV}^{-2} \phi_{\ell\ell}^L \langle m_{\ell\ell} \rangle^2, \end{aligned} \tag{1.19}$$

where τ_K is the kaon lifetime, $\phi_{\ell\ell}^L$ is the obtained value for the integral on the reduced phase space, defined as the adimensional phase space obtained by factorising out the the kaon mass dependence:

$$\phi_{\mu\mu}^L \approx 0.008, \quad \phi_{ee}^L \approx 0.03, \tag{1.20}$$

and $\langle m_{\ell\ell} \rangle$ is the effective Majorana mass

$$\langle m_{\ell\ell} \rangle \overset{def}{=} \left| \sum_{m=4}^{n_s+3} \mathcal{U}_{\ell m}^* \mathcal{U}_{\ell m} m_{N_m} \right|. \tag{1.21}$$

From eq. 1.19 it is evident that the current experimental sensitivity $\mathcal{O}(10^{-10})$ would not be sufficient to probe the theoretical expectation for the branching fraction $\mathcal{B}(K^\pm \to \pi^\mp \ell^\pm \ell^\pm)$: even considering a maximal mixing $\mathcal{U}_{\ell m}^* \mathcal{U}_{\ell m} \sim 1$ and $m_{N_m} \sim m_K$, which does not meet the condition $m_N \ll m_K$, the expected branching fraction would be $\mathcal{B}(K^\pm \to \pi^\mp \ell^\pm \ell^\pm) \lesssim 10^{-14}$.

Another finding from eq. 1.19 is that massless sterile Majorana neutrinos do not contribute to the process. This is due to the required chirality change, which is forbidden for massless particles.

1.1.2.2 $\mathcal{B}(K^\pm \to \pi^\mp \ell^\pm \ell^\pm)$ in the limit $m_N \gg m_K$

In the limit of heavy sterile neutrinos ($m_{N_m} \gg m_K$) the leptonic tensor $L_m^{\alpha\beta}$ defined in eq. 1.17 can be approximated as

$$L_m^{\alpha\beta}(p) \approx -\frac{1}{m_{N_m}} \bar{u}(p_\ell)\gamma^\alpha\gamma^\beta P_R v(p_{\ell'}). \tag{1.22}$$

Analogously as for the case $m_{N_m} \ll m_K$, Ali *et al.* [11] have estimated the branching fraction $\mathcal{B}(K^\pm \to \pi^\mp \ell^\pm \ell^\pm)$ to be

$$\begin{aligned}
\mathcal{B}(K^\pm \to \pi^\mp \ell^\pm \ell^\pm) &\approx \tau_K \frac{G_F^4 m_K^7}{128\pi^3} f_K^2 f_\pi^2 |V_{us}V_{ud}|^2 \phi_{\ell\ell}^H \langle m_{\ell\ell}^{-1}\rangle^2, \\
&\approx 2.3 \times 10^{-8}\,\mathrm{MeV}^2 \phi_{\ell\ell}^H \langle m_{\ell\ell}^{-1}\rangle^2,
\end{aligned} \tag{1.23}$$

where τ_K is the kaon lifetime, $\phi_{\ell\ell}^H$ is the obtained value for the integral on the reduced phase space:

$$\phi_{\mu\mu}^H \approx 0.011, \quad \phi_{ee}^H \approx 0.038, \tag{1.24}$$

and $\langle m_{\ell\ell}^{-1}\rangle$ is the effective inverse Majorana mass

$$\langle m_{\ell\ell}^{-1}\rangle \stackrel{def}{=} \left| \sum_{m=4}^{n_s+3} \mathcal{U}_{\ell m}^* \mathcal{U}_{\ell m} \frac{1}{m_{N_m}} \right|. \tag{1.25}$$

From eq. 1.23 it can be seen that, as for the limit $m_N \ll m_K$, the theoretical expectation for the branching fraction $\mathcal{B}(K^\pm \to \pi^\mp \ell^\pm \ell^\pm)$ cannot be probed by the current experimental sensitivity $\mathcal{O}(10^{-10})$: even considering a maximal mixing $\mathcal{U}_{\ell m}^* \mathcal{U}_{\ell m} \sim 1$ and $m_{N_m} \sim m_K$, which does not meet the condition $m_N \gg m_K$, a branching fraction $\mathcal{B}(K^\pm \to \pi^\mp \ell^\pm \ell^\pm) \lesssim 10^{-14}$ is expected.

1.1.2.3 $\mathcal{B}(K^\pm \to \pi^\mp \ell^\pm \ell^\pm)$ for resonant sterile neutrinos

If at least one sterile Majorana neutrino has a mass m_{N_m} in the range

$$m_\pi + m_\ell \leq m_{N_m} \leq m_K - m_\ell, \tag{1.26}$$

the $K^\pm \to \pi^\mp \ell^\pm \ell^\pm$ decay may occur via resonant production of the heavy neutrino. In this case, the decay rate is enhanced and the expected branching fraction may be above the current experimental sensitivity. The upper limit of the range in eq. 1.26 is dictated by the threshold of the production process $K^\pm \to \ell^\pm N_m$, the lower limit by the threshold of the decay $N_m \to \pi^\mp \ell^\pm$. For simplicity, the case of only one sterile resonant Majorana neutrino is considered, which will be indicated as N_4.

The branching fraction $\mathcal{B}(K^\pm \to \pi^\mp \ell^\pm \ell^\pm)$ of the $K^\pm \to \pi^\mp \ell^\pm \ell^\pm$ decay via resonant sterile neutrino N_4 has been calculated by Atre *et al.* [4] to be

$$\mathcal{B}(K^\pm \to \pi^\mp \ell^\pm \ell^\pm) = \tau_K \frac{G_F^4 m_K}{128\pi^2} f_K^2 f_\pi^2 |V_{us}V_{ud}|^2 \frac{m_{N_4}^5}{\Gamma_{N_4}} |\mathcal{U}_{\ell 4}|^4 \phi_{\ell\ell}^R, \qquad (1.27)$$

in which $\phi_{\ell\ell}^R$ is the obtained value for the integral of the reduced phase space [4, 12]:

$$\phi_{\ell\ell}^R = \chi(r_\ell, r_{N_4}, \rho_\ell, \rho_\pi) \lambda^{\frac{1}{2}} \left(1, r_\ell^2, r_{N_4}^2\right) \lambda^{\frac{1}{2}} \left(1, \rho_\pi^2, \rho_\ell^2\right), \qquad (1.28)$$

$$\chi \stackrel{def}{=} [(1 + \rho_\ell^2) - (r_{N_4}^2 - r_\ell^2)(1 - \rho_\ell^2)][(1 - \rho_\ell^2)^2 - (1 + \rho_\ell^2)\rho_\pi^2], \quad (1.29)$$

$$\lambda(a, b, c) \stackrel{def}{=} a^2 + b^2 + c^2 - 2ab - 2ac - 2bc, \qquad (1.30)$$

where $r_i \stackrel{def}{=} m_i/m_K$, $\rho_i \stackrel{def}{=} m_i/m_{N_4}$ ($i = \ell, \pi, N_4$). The dependence of $\phi_{\ell\ell}^R$ on the neutrino mass in the kinematically allowed mass region is shown in Fig. 1.2.

For $m_{N_4} = 300 \,\mathrm{MeV}/c^2$, $\phi_{ee}^R \approx 0.24$ and $\phi_{\mu\mu}^R \approx 0.13$, and the branching fraction is estimated to be

$$\begin{aligned}
\mathcal{B}(K^\pm \to \pi^\mp \ell^\pm \ell^\pm) &\sim& 10^{-19} \,\mathrm{GeV} \times \frac{1}{\Gamma_{N_4}} |\mathcal{U}_{\ell 4}|^4, \\
&\sim& 10^{-7} \,\mathrm{ps}^{-1} \times \tau_{N_4} |\mathcal{U}_{\ell 4}|^4. \qquad (1.31)
\end{aligned}$$

Therefore, if $\Gamma_{N_4} \lesssim 10^{-9} \,\mathrm{GeV}$ (corresponding to a neutrino lifetime $\tau_{N_4} \gtrsim 10^{-3} \,\mathrm{ps}$), the branching fraction may be probed with the current experimental sensitivity $\mathcal{O}(10^{-10})$, possibly constraining the magnitude of the mixing matrix element $\mathcal{U}_{\ell 4}$.

The decay width Γ_{N_4} of the resonant sterile neutrino N_4 can be evaluated by summing all the partial decay widths $\Gamma(N_4 \to f_i)$ of the kinematically allowed decay channels
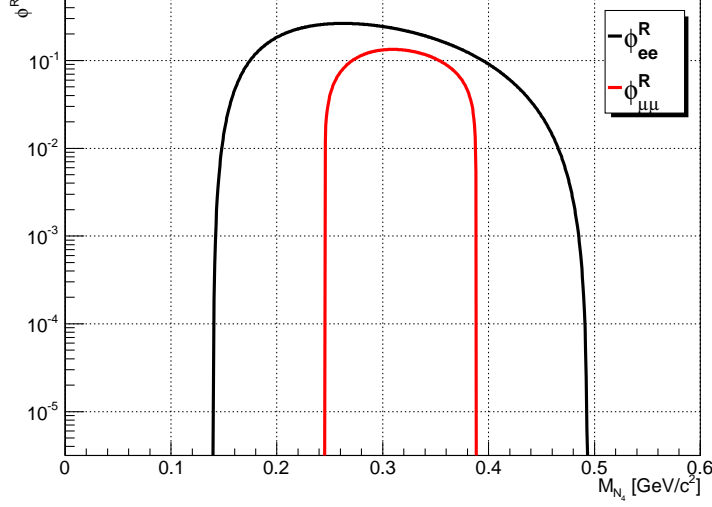
Figure 1.2: Dependence of the reduced phase space integral $\phi_{\ell\ell}^{R}$ on the neutrino mass M_{N_4}.

$N_4 \to f_i$, which have been estimated by Atre *et al.* [4]:

$$
\begin{aligned}
\Gamma_{N_4} &= 2 \sum_{\ell_1 = e,\mu} \Gamma(N_4 \to \pi^{\mp}\ell_1^{\pm}) + 2 \sum_{\ell_1,\ell_2 = e,\mu} \sum_{\ell_1 \neq \ell_2} \Gamma(N_4 \to \ell_1^{\mp}\ell_2^{\pm}\nu_{\ell_2}) \\
&\quad + \sum_{\ell_1 = e,\mu,\tau} \Gamma(N_4 \to \pi^0 \nu_{\ell_1}) + \sum_{\ell_1 = e,\mu,\tau} \sum_{\ell_2 = e,\mu} \Gamma(N_4 \to \nu_{\ell_1}\ell_2^{+}\ell_2^{-}) \\
&\quad + \sum_{\ell_1 = e,\mu,\tau} \sum_{\ell_2 = e,\mu,\tau} \Gamma(N_4 \to \nu_{\ell_1}\nu_{\ell_2}\bar{\nu}_{\ell_2}) \\
&\sim (3\alpha m_{N_4}^3 + 7\beta m_{N_4}^5) \sum_{\ell = e,\mu} |\mathcal{U}_{\ell 4}|^2 + (\alpha m_{N_4}^3 + 5\beta m_{N_4}^5)|\mathcal{U}_{\tau 4}|^2, \quad (1.32)
\end{aligned}
$$

where for the 2-body decays $\Gamma_{2body} \sim \alpha m_{N_4}^3 |\mathcal{U}_{\ell_1 4}|^2$, with $\alpha \sim 10^{-13}\,\mathrm{GeV}^{-2}$, and for the 3-body decays $\Gamma_{3body} \sim \beta m_{N_4}^5 |\mathcal{U}_{\ell_1 4}|^2$, with $\beta \sim 10^{-13}\,\mathrm{GeV}^{-4}$.

As an example, for $m_{N_4} = 300\,\mathrm{MeV}/c^2$, $\Gamma_{N_4} \sim 10^{-14}\,\mathrm{GeV} \times (\sum_{\ell = e,\mu} |\mathcal{U}_{\ell 4}|^2 + 0.3|\mathcal{U}_{\tau 4}|^2)$, which corresponds to a branching fraction

$$
\mathcal{B}(K^{\pm} \to \pi^{\mp}\ell^{\pm}\ell^{\pm}) \sim 10^{-5} \times \frac{|\mathcal{U}_{\ell 4}|^4}{|\mathcal{U}_{e4}|^2 + |\mathcal{U}_{\mu 4}|^2 + 0.3|\mathcal{U}_{\tau 4}|^2}. \quad (1.33)
$$

However, the theoretical expectation value of Γ_{N_4} is strongly dependent on the model considered. For instance, if a coupling of the type $gN\nu\phi$ with a scalar

particle ϕ is introduced, the decay width Γ_{N_4} may increase significantly [13, 14]. Therefore, from the experimental point of view, a valid approach is to consider m_{N_4} and Γ_{N_4} as free parameters and evaluate the Upper Limits (ULs) on the branching fraction $\mathcal{B}(K^\pm \to \pi^\mp \ell^\pm \ell^\pm)$ as a function of m_{N_4} and Γ_{N_4}.

1.1.3 Experimental status

The most stringent limit on the branching fraction $\mathcal{B}(K^\pm \to \pi^\mp \mu^\pm \mu^\pm)$ comes from the NA48/2 experiment at CERN [15], which is extensively described in Chapter 2. The $K^\pm \to \pi^\mp \mu^\pm \mu^\pm$ findings from NA48/2, obtained as a by-product of the precise measurement of the $K^\pm \to \pi^\pm \mu^+ \mu^-$ decay [16], are briefly reported in this section. A dedicated $K^\pm \to \pi^\mp \mu^\pm \mu^\pm$ analysis, optimised to improve the sensitivity by an order of magnitude, based on the same data sample is presented in Chapter 3 of this thesis.

The collected data sample the $K^\pm \to \pi^\pm \mu^+ \mu^-$ analysis was based on corresponds to 1.9×10^{11} kaon decays in the NA48/2 fiducial volume. The $K^\pm \to \pi^\pm \mu^+ \mu^-$ events were required to have two muon-candidates of opposite sign and a pion-candidate, all compatible with originating from the same vertex, and corresponding to a total momentum consistent with the nominal kaon one. The event kinematics were studied by reconstructing the squared invariant mass variable $m^2_{\pi\mu\mu}$, defined as the square of the total 4-momentum of the three candidates, obtained from the measured 3-momenta and assuming the muon and the pion masses, according to the candidate type. All the events within a Signal Region defined by the condition $|m_{\pi\mu\mu} - m_K| < 8\,\mathrm{MeV/c^2}$ were selected. The primary source of the residual background was due to $K^\pm \to \pi^\pm \pi^+ \pi^-$ events with two subsequent $\pi^\pm \to \mu^\pm \nu$ decays in flight.

The $K^\pm \to \pi^\mp \mu^\pm \mu^\pm$ candidates were selected applying the $K^\pm \to \pi^\pm \mu^+ \mu^-$ requirements with minimal changes accounting for the different signs of the pion-candidate and one of the muon-candidates, and were used to estimate the $K^\pm \to \pi^\pm \pi^+ \pi^-$ background contribution to the $K^\pm \to \pi^\pm \mu^+ \mu^-$ events. Fig. 1.3 shows the reconstructed $m_{\pi\mu\mu}$ spectra for $K^\pm \to \pi^\pm \mu^+ \mu^-$ and $K^\pm \to \pi^\mp \mu^\pm \mu^\pm$ candidates [16].
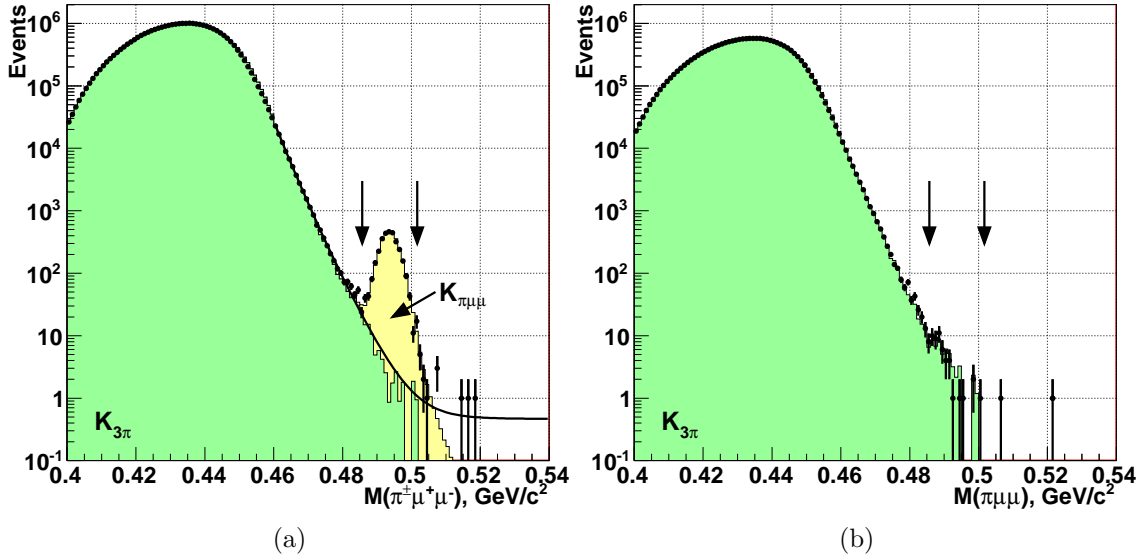
Figure 1.3: Reconstructed $m_{\pi\mu\mu}$ spectra of (a) $K^{\pm} \rightarrow \pi^{\pm}\mu^{+}\mu^{-}$ and (b) $K^{\pm} \rightarrow \pi^{\mp}\mu^{\pm}\mu^{\pm}$ candidates for data (dots) and MC simulations (filled areas). The boundaries of the Signal Regions are indicated by arrows.

A total of 52 events were observed in the $K^{\pm} \rightarrow \pi^{\mp}\mu^{\pm}\mu^{\pm}$ Signal Region. Comparing this result with the number of expected events $N_{exp} = 52.6 \pm 19.8$, obtained from a $K^{\pm} \rightarrow \pi^{\pm}\pi^{+}\pi^{-}$ MC simulation, an UL at 90% Confidence Level (CL) on the branching fraction $\mathcal{B}(K^{\pm} \rightarrow \pi^{\mp}\mu^{\pm}\mu^{\pm})$ was established [16]:

$$\mathcal{B}(K^{\pm} \rightarrow \pi^{\mp}\mu^{\pm}\mu^{\pm}) < 1.1 \times 10^{-9} \quad @ \; 90\% \; \text{CL}. \tag{1.34}$$

The main limitation of this measurement is the number of $K^{\pm} \rightarrow \pi^{\pm}\pi^{+}\pi^{-}$ background events in the Signal Region. This can be noticed calculating the expected Single-Event Sensitivity (SES), which is defined as the branching fraction corresponding to the observation of 1 signal event with no background. Given the number of kaon decays $N_K = 1.9 \times 10^{11}$ collected and the typical $K^{\pm} \rightarrow \pi^{\mp}\mu^{\pm}\mu^{\pm}$ acceptance $\varepsilon_{\pi\mu\mu} \sim 10\%$, one finds

$$\text{SES} \stackrel{def}{=} \frac{1}{N_K \varepsilon_{\pi\mu\mu}} \sim 5 \times 10^{-11}, \tag{1.35}$$

which is ~ 20 times lower than the obtained UL (a factor of ~ 2 is due to the conversion between SES and 90% CL). This evaluation demonstrated the possibility

16

of a major improvement of the UL on the branching fraction $\mathcal{B}(K^{\pm} \to \pi^{\mp}\mu^{\pm}\mu^{\pm})$, motivating the dedicated $K^{\pm} \to \pi^{\mp}\mu^{\pm}\mu^{\pm}$ analysis, which is presented and discussed in Chapter 3.

1.1.4 Related searches in heavy meson decays

Analogous searches of LNV meson decays with two same sign muons in the final state have been performed. The LHCb collaboration has published limits on the branching fractions $\mathcal{B}(B^{\pm} \to h^{\mp}\mu^{\pm}\mu^{\pm})$ ($h = \pi, K, D_{(s)}$) [17–19] and $\mathcal{B}(D_{(s)}^{\pm} \to \pi^{\mp}\mu^{\pm}\mu^{\pm})$ [20] at 95% CL:

$$\mathcal{B}(B^{\pm} \to \pi^{\mp}\mu^{\pm}\mu^{\pm}) \quad < \quad 4.0 \times 10^{-9}, \tag{1.36}$$

$$\mathcal{B}(B^{\pm} \to K^{\mp}\mu^{\pm}\mu^{\pm}) \quad < \quad 5.4 \times 10^{-8}, \tag{1.37}$$

$$\mathcal{B}(B^{\pm} \to D^{\mp}\mu^{\pm}\mu^{\pm}) \quad < \quad 6.9 \times 10^{-7}, \tag{1.38}$$

$$\mathcal{B}(B^{\pm} \to D_s^{\mp}\mu^{\pm}\mu^{\pm}) \quad < \quad 5.8 \times 10^{-7}, \tag{1.39}$$

$$\mathcal{B}(D^{\pm} \to \pi^{\mp}\mu^{\pm}\mu^{\pm}) \quad < \quad 2.5 \times 10^{-8}, \tag{1.40}$$

$$\mathcal{B}(D_s^{\pm} \to \pi^{\mp}\mu^{\pm}\mu^{\pm}) \quad < \quad 1.4 \times 10^{-7}. \tag{1.41}$$

Although all those measurements provide limits on different decays, they can be compared to the $K^{\pm} \to \pi^{\mp}\mu^{\pm}\mu^{\pm}$ results in a model-dependent approach. In particular, considering the heavy resonant Majorana neutrino model proposed by Atre *et al.* [4] described in Sec. 1.1.2, all the quoted limits determine a constraint on the magnitude of the matrix element $\mathcal{U}_{\mu 4}$ in the allowed N_4 mass range. The B and $D_{(s)}$ meson decays are sensitive to a broader range of N_4 masses than kaon ones: rewriting eq. 1.26 for a generic $h_1^{\pm} \to h_2^{\mp}\ell^{\pm}\ell^{\pm}$ decay one finds $m_{h_2} + m_{\ell} \le m_{N_4} \le m_{h_1} - m_{\ell}$. Therefore, B and $D_{(s)}$ decays provide an additional coverage on the N_4 mass region forbidden in kaon decays. On the other hand, the sensitivity to $|\mathcal{U}_{\ell 4}|$ of each decay channel can be compared in the mass region $m_{\pi} + m_{\ell} \le m_{N_4} \le m_K - m_{\ell}$, rewriting

eq. 1.27 for a generic $h_1^\pm \to h_2^\mp \ell^\pm \ell^\pm$ decay:

$$\mathcal{B}(h_1^\pm \to h_2^\mp \ell^\pm \ell^\pm) = \tau_{h_1} \frac{G_F^4 m_{h_1}}{128\pi^2} f_{h_1}^2 f_{h_2}^2 |V_{h_1} V_{h_2}|^2 \frac{m_{N_4}^5}{\Gamma_{N_4}} |\mathcal{U}_{\ell 4}|^4 \phi_{\ell\ell}^{R\,h_1,h_2} \qquad (1.42)$$

and evaluating $\mathcal{B}(h_1^\pm \to h_2^\mp \ell^\pm \ell^\pm)$ for a fixed value of $|\mathcal{U}_{\ell 4}|$. For instance, considering $\mathcal{B}(B^\pm \to \pi^\mp \ell^\pm \ell^\pm)$ and $\mathcal{B}(K^\pm \to \pi^\mp \ell^\pm \ell^\pm)$, the relation

$$\frac{\mathcal{B}(B^\pm \to \pi^\mp \ell^\pm \ell^\pm)}{\mathcal{B}(K^\pm \to \pi^\mp \ell^\pm \ell^\pm)} = \frac{\tau_B}{\tau_K} \left(\frac{m_B}{m_K}\right) \left(\frac{f_B}{f_K}\right)^2 \frac{|V_{ub} V_{ud}|^2}{|V_{us} V_{ud}|^2} \frac{\phi_{\ell\ell}^{RB}}{\phi_{\ell\ell}^{RK}} \sim 10^{-6} \qquad (1.43)$$

indicates that to achieve the same sensitivity of a $K^\pm \to \pi^\mp \ell^\pm \ell^\pm$ search, a $B^\pm \to \pi^\mp \ell^\pm \ell^\pm$ search is required to reach a branching fraction $\sim 10^6$ times smaller. Analogously, for $D^\pm \to \pi^\mp \ell^\pm \ell^\pm$ searches one finds that a branching fraction $\sim 10^3$ times smaller than the $K^\pm \to \pi^\mp \ell^\pm \ell^\pm$ one is required, while for $D_s^\pm \to \pi^\mp \ell^\pm \ell^\pm$ it is sufficient to reach a branching fraction $\sim 10^2$ times smaller. Given these results, it follows from eqs. 1.36–1.41 that the current $\mathcal{B}(K^\pm \to \pi^\mp \mu^\pm \mu^\pm)$ limit [16] in eq. 1.34 already provides the most stringent constraint on the magnitude of the matrix element $\mathcal{U}_{\mu 4}$, in the mass region $m_\pi + m_\mu \leq m_{N_4} \leq m_K - m_\mu$.

1.2 The $K^+ \to \pi^+ \nu\bar{\nu}$ decay

Flavour Changing Neutral Current (FCNC) processes are a very useful tool to probe the SM and search for new physics. In the SM all the neutral current vertices (involving γ, Z, gluons) are diagonal in the flavour space (GIM mechanism [21]), therefore all the FCNC processes are forbidden at the tree level. However, they are allowed at 1-loop level: combining the $W^\pm$ vertices, it is possible to build effective flavour changing vertices with positive-negative current exchanges, in such a way that they are overall neutral. The fact that FCNC processes cannot occur at tree level makes them rare, but also suitable to study the quantum structure of the theory, arising from the loop-level contribution, and to search for new physics in a clean environment. In particular, among the FCNC processes, there are a few special cases, such as the $K \to \pi\nu\bar{\nu}$ and the $B \to X_{d,s}\nu\bar{\nu}$ decays, in which the hadronic matrix

element, which is the main source of theoretical uncertainty in the study of meson decays, can be extracted from empirical quantities (such as the branching fraction) of other well known decay channels. In this way, the theoretical uncertainty is reduced and the remaining contribution is mostly due to the input parameters and to higher orders perturbative corrections.

In this section, the theoretical description of the $K \to \pi \nu \bar{\nu}$ decays will be discussed, together with the relevant framework. Finally, a review of the experimental results regarding the $K^+ \to \pi^+ \nu \bar{\nu}$ decay will be presented.

1.2.1 The CKM framework

The Cabibbo-Kobayashi-Maskawa (CKM) matrix [22, 23] is the matrix $\hat{V}$ that relates the quark mass (and flavour) eigenstates d, s, b to the weak interaction ones $d\,'$, $s\,'$, $b\,'$, which interact with the u, c, t quarks (mass and flavour eigenstates) respectively:

$$
\begin{pmatrix} d\,' \\ s\,' \\ b\,' \end{pmatrix} = \hat{V} \begin{pmatrix} d \\ s \\ b \end{pmatrix} = \begin{pmatrix} V_{ud} & V_{us} & V_{ub} \\ V_{cd} & V_{cs} & V_{cb} \\ V_{td} & V_{ts} & V_{tb} \end{pmatrix} \begin{pmatrix} d \\ s \\ b \end{pmatrix} .
\tag{1.44}
$$

The choice of introducing a quark mixing between negatively charged quarks, instead of the positively charged ones, is completely arbitrary and it is due to historical reasons, since only the u, d and s quarks had been discovered by 1963, the year when Cabibbo suggested this mechanism.

In the SM, FCNC processes are suppressed via the so-called Glashow-Iliopoulos-Maiani (GIM) mechanism [21], that requires the matrix $\hat{V}^\dagger \hat{V}$ to be diagonal: in order to maintain the orthogonality of the flavour eigenstates $D = (d, s, b)$, the neutral currents $J_{0i}^\mu \propto \bar{D}_i\,' \gamma^\mu D_i\,'$ ($i = 1, 2, 3$) must be proportional to the flavour currents

$\propto \bar{D}_i \gamma^\mu D_i$, that is

$$\bar{D}_i{}' \gamma^\mu D_j{}' = \bar{D}_i \gamma^\mu (\hat{V}^\dagger \hat{V})_{ij} D_j = \lambda_i \delta_{ij} \bar{D}_i \gamma^\mu D_j \ \Rightarrow \ \hat{V}^\dagger \hat{V} = \begin{pmatrix} \lambda_1 & 0 & 0 \\ 0 & \lambda_2 & 0 \\ 0 & 0 & \lambda_3 \end{pmatrix}. \qquad (1.45)$$

Besides, adding the three constraints $\lambda_i = 1$ ($i = 1, 2, 3$) due to the weak interaction universality hypothesis to the condition on the $\hat{V}^\dagger V$ matrix in eq. 1.45, the $\hat{V}^\dagger V$ matrix must be unitary:

$$\hat{V}^\dagger \hat{V} = \mathbb{1}. \qquad (1.46)$$

In general, considering n quark families, the CKM matrix would be a $n \times n$ unitary matrix, i.e. it would belong to the $U(n)$ group. The most general matrix $M \in U(n)$ has n^2 free parameters, $2n - 1$ of which, in the CKM case, can be absorbed by the arbitrary (and unobservable) phases of each eigenstate (n for the mass eigenstates, n for the weak eigenstates, minus a residual global phase). Therefore, the number N of residual parameters for the CKM matrix is

$$N = n^2 - (2n - 1) = (n - 1)^2. \qquad (1.47)$$

In particular, the number N can be expressed as a sum of the number N_R of real parameters, defined as the number of parameters of a $n \times n$ orthogonal matrix, and of the number N_ϕ of complex phases:

$$N_R = \frac{1}{2} n(n - 1); \qquad (1.48)$$
$$N_\phi = \frac{1}{2} (n - 1)(n - 2). \qquad (1.49)$$

In the SM ($n = 3$), the CKM matrix has $N_R = 3$ real parameters and $N_\phi = 1$ complex phase: this complex phase is responsible for the CP violation [23].

The current estimates[5] of the magnitudes $|V_{ij}|$, $i = (u, c, t)$, $j = (d, s, b)$ of the nine

---

[5]without assuming CKM matrix unitarity or three quarks generations.

CKM elements obtained from experimental measurements are [1]

$$|\hat{V}_{\text{CKM}}| = \begin{pmatrix} 0.97425 \pm 0.00022 & 0.2252 \pm 0.0009 & (4.15 \pm 0.49) \times 10^{-3} \\ 0.230 \pm 0.011 & 1.006 \pm 0.023 & (4.09 \pm 0.11) \times 10^{-2} \\ (8.4 \pm 0.6) \times 10^{-3} & (4.29 \pm 0.26) \times 10^{-2} & 0.89 \pm 0.07 \end{pmatrix} \quad (1.50)$$

The reported values are obtained by combining the results of different measurements: the six values $|V_{uq}|$ and $|V_{cq}|$ ($q = d, s, b$) are obtained from the leptonic ($q_1 \bar{q}_2 \rightarrow \ell \nu$) and semileptonic ($q_1 \rightarrow q_2 \ell \nu$) decay rates of the π, K, D and B mesons, and from their mass and lifetime measurements. The top-quark related parameters $|V_{tq}|$ ($q = d, s, b$) cannot be extracted with an analogous method, since the top quark mass is above the Wb threshold and the process $t \rightarrow Wb$ occurs before the top hadronisation. However, the single-top production cross-sections $\sigma(p\bar{p} \rightarrow t\bar{b})$ and $\sigma(pp \rightarrow tb)$ are proportional to $|V_{tb}|^2$, and the measurement of the magnitude $|V_{tb}|$ reported in eq. 1.50 is obtained from these quantities. Unfortunately, this approach is not suitable for the measurement of $|V_{td}|$ and $|V_{ts}|$, because the processes $p\bar{p} \rightarrow t\bar{q}$ ($pp \rightarrow tq$) with $q = d, s$ are suppressed by at least a factor 10^3 with respect to the process $p\bar{p} \rightarrow t\bar{b}$ ($pp \rightarrow tb$), which is measured with $\sim 1\%$ accuracy and would overwhelm the signal. In summary, no tree-level processes are suitable for such measurements, therefore the determination of $|V_{td}|$ and $|V_{ts}|$ requires the study of loop-mediated processes, such as $B - \bar{B}$ oscillations or rare K and B decays. In particular, the values reported in eq. 1.50 are obtained from the $B - \bar{B}$ and $B_s - \bar{B}_s$ oscillation measurements. The magnitude $|V_{td}V_{ts}^*|$ can be determined independently in a theoretically clean way from the branching fraction of the $K^+ \rightarrow \pi^+ \nu \bar{\nu}$ decay (Sec. 1.2.3), which is the main goal of the NA62 experiment (Chapter 4).

Many CKM matrix parametrisations exist in literature. However, the two most widely used are the so-called *standard* parametrisation (recommended by the Particle Data Group [1]) and the Wolfenstein one [24].

1.2.1.1 Standard parametrisation

Defining ϑ_{ij} as the mixing angle between the mass eigenstate D_i and the weak eigenstate D'_j, and δ as the unique complex phase, the CKM matrix can be expressed, in the standard parametrisation [1], as

$$\hat{V}_{\text{CKM}} = \begin{pmatrix} c_{12}c_{13} & s_{12}c_{13} & s_{13}e^{-i\delta} \\ -s_{12}c_{23} - c_{12}s_{23}s_{13}e^{i\delta} & c_{12}c_{23} - s_{12}s_{23}s_{13}e^{i\delta} & s_{23}c_{13} \\ s_{12}s_{23} - c_{12}c_{23}s_{13}e^{i\delta} & -s_{23}c_{12} - s_{12}c_{23}s_{13}e^{i\delta} & c_{23}c_{13} \end{pmatrix} \quad (1.51)$$

where $c_{ij} = \cos\vartheta_{ij}$ and $s_{ij} = \sin\vartheta_{ij}$ $(i, j = 1, 2, 3)$. Choosing ϑ_{ij} adequately, all the values of c_{ij} and s_{ij} can be positive, while δ can be chosen in the interval $0 \leq \delta < 2\pi$. Besides, as eq. 1.50 shows, $s_{13} \sim \mathcal{O}(10^{-3})$ and $s_{23} \sim \mathcal{O}(10^{-2})$. Therefore, given that $c_{13} = 1 + \mathcal{O}(10^{-6})$, the following relations are satisfied with an accuracy of 10^{-6}:

$$s_{12} = |V_{us}|, \quad s_{13} = |V_{ub}|, \quad s_{23} = |V_{cb}|. \quad (1.52)$$

So, in this approximation, the four parameters

$$|V_{us}|, \quad |V_{ub}|, \quad |V_{cb}|, \quad \delta \quad (1.53)$$

are independent and can be used to parametrise the CKM matrix. As discussed above, the first three can be measured from the tree-level decays $s \to u$, $b \to u$ and $b \to c$ respectively. The phase δ can be measured from CP-violating decays or from the measurement of $|V_{td}|$: since experimentally $0 \leq \delta < \pi$ [1], the relation

$$|V_{td}| = \sqrt{a^2 + b^2 - 2ab\cos\delta}, \quad a = |V_{cd}V_{cb}|, \quad b = |V_{ud}V_{ub}|, \quad (1.54)$$

obtained from eq. 1.51 provides a one-to-one correspondence between δ and $|V_{td}|$. The advantages of using the standard parametrisation, with respect to the others, are the following:

- The three parameters s_{12}, s_{13} and s_{23} are essentially equal to $|V_{us}|$, $|V_{ub}|$ and

$|V_{cb}|$ respectively, which can be measured independently in three different decay channels.

- The CP-violating phase δ is multiplied by $s_{13} \sim \mathcal{O}(10^{-3})$. This manifestly shows the suppression of CP-violation, regardless the value of δ.

For numerical evaluations, the standard parametrisation is recommended. However, the orders of magnitude of the CKM matrix elements are not immediately evident in the standard parametrisation: this is the main reason behind the Wolfenstein parametrisation.

1.2.1.2 Wolfenstein parametrisation

Wolfenstein parametrisation [24] is obtained expanding each CKM matrix element in power series of the parameter $\lambda = |V_{us}| \simeq 0.22$, imposing

$$s_{12} = \lambda, \qquad s_{23} = A\lambda^2, \qquad s_{13}e^{-i\delta} = A\lambda^3(\rho - i\eta). \qquad (1.55)$$

The three relations are chosen to include into the λ-dependence the difference observed experimentally in the magnitudes of the parameters s_{12}, s_{23} and s_{13}, with A, ρ and $\eta \sim 1$. The advantage of this parametrisation is that, by construction, the order of magnitude of each CKM matrix element is determined by the power of λ. With an accuracy of $\mathcal{O}(\lambda^4) \simeq \mathcal{O}(10^{-3})$, the CKM matrix in eq. 1.51 can be rewritten as

$$\hat{V}_{\text{CKM}} = \begin{pmatrix} 1 - \frac{\lambda^2}{2} & \lambda & A\lambda^3(\rho - i\eta) \\ -\lambda & 1 - \frac{\lambda^2}{2} & A\lambda^2 \\ A\lambda^3(1 - \rho - i\eta) & -A\lambda^2 & 1 \end{pmatrix} + \mathcal{O}(\lambda^4), \qquad (1.56)$$

having substituted the parameters in eq. 1.53 with

$$\lambda, \quad A, \quad \rho, \quad \eta. \qquad (1.57)$$

In this parametrisation, CP violation is described by η, which is the imaginary part of the complex phase δ. In case an accuracy greater than $\mathcal{O}(\lambda^4) \simeq \mathcal{O}(10^{-3})$ is required, further terms of the λ power series can be added in eq. 1.56: including the corrections $\sim \mathcal{O}(\lambda^4)$, the CKM matrix elements become

$$V_{ud} = 1 - \frac{1}{2}\lambda^2 - \frac{1}{8}\lambda^4 + \mathcal{O}(\lambda^6), \tag{1.58}$$

$$V_{us} = \lambda + \mathcal{O}(\lambda^7), \tag{1.59}$$

$$V_{ub} = A\lambda^3(\rho - i\eta), \tag{1.60}$$

$$V_{cd} = -\lambda + \frac{1}{2}A^2\lambda^5[1 - 2(\rho + i\eta)] + \mathcal{O}(\lambda^7), \tag{1.61}$$

$$V_{cs} = 1 - \frac{1}{2}\lambda^2 - \frac{1}{8}\lambda^4(1 + 4A^2) + \mathcal{O}(\lambda^6), \tag{1.62}$$

$$V_{cb} = A\lambda^2 + \mathcal{O}(\lambda^8), \tag{1.63}$$

$$V_{td} = A\lambda^3[1 - (\rho + i\eta)(1 - \frac{1}{2}\lambda^2)] + \mathcal{O}(\lambda^7), \tag{1.64}$$

$$V_{ts} = -A\lambda^2 + \frac{1}{2}A(1 - 2\rho)\lambda^4 - i\eta A\lambda^4 + \mathcal{O}(\lambda^6), \tag{1.65}$$

$$V_{tb} = 1 - \frac{1}{2}A^2\lambda^4 + \mathcal{O}(\lambda^6). \tag{1.66}$$

Afterwards, the variables $\bar{\rho}$ and $\bar{\eta}$, defined as

$$\bar{\rho} \overset{def}{=} \rho\,(1 - \frac{1}{2}\lambda^2), \quad \bar{\eta} \overset{def}{=} \eta\,(1 - \frac{1}{2}\lambda^2) \tag{1.67}$$

will be used, in order to simplify the notation for V_{td}:

$$V_{td} = A\lambda^3[1 - (\bar{\rho} + i\bar{\eta})] + \mathcal{O}(\lambda^7). \tag{1.68}$$

1.2.2 The unitary triangles

The CKM matrix unitarity [1] leads to eighteen relations, one for each element of the $V^{\dagger}V$ and $VV^{\dagger}$ matrices. The six relations obtained from the two diagonals are

$$|V_{uq}|^2 + |V_{cq}|^2 + |V_{tq}|^2 = 1 \quad (q = d, s, b) \tag{1.69}$$

$$|V_{qd}|^2 + |V_{qs}|^2 + |V_{qb}|^2 = 1 \quad (q = u, c, t) \tag{1.70}$$

while only six relations can be obtained from the elements outside the diagonals, given that $(V^\dagger V)_{ij} = (V^\dagger V)^*_{ji}$ and $(VV^\dagger)_{ij} = (VV^\dagger)^*_{ji}$:

$$V^*_{ud}V_{us} + V^*_{cd}V_{cs} + V^*_{td}V_{ts} = 0 \tag{1.71}$$

$$V^*_{us}V_{ub} + V^*_{cs}V_{cb} + V^*_{ts}V_{tb} = 0 \tag{1.72}$$

$$V^*_{ub}V_{ud} + V^*_{cb}V_{cd} + V^*_{tb}V_{td} = 0 \tag{1.73}$$

$$V_{ud}V^*_{cd} + V_{us}V^*_{cs} + V_{ub}V^*_{cb} = 0 \tag{1.74}$$

$$V_{cd}V^*_{td} + V_{cs}V^*_{ts} + V_{cb}V^*_{tb} = 0 \tag{1.75}$$

$$V_{td}V^*_{ud} + V_{ts}V^*_{us} + V_{tb}V^*_{ub} = 0. \tag{1.76}$$

All the terms in eqs. 1.69 and 1.70 are real, while the ones in eqs. 1.71-1.76 are complex, in general. This makes the latter suitable for CP-violation studies.

Each of the eqs. 1.71-1.76 can be represented graphically in the complex plane ($\mathrm{Re}\, z$, $\mathrm{Im}\, z$), $z \in \mathbb{C}$ by a triangle made of three vectors, each one corresponding to a term in each relation, the vectorial sum of which is 0.

The side lengths and the angles sizes of each triangle are physical observables. Hence, the constraints in eqs. 1.71-1.76 can be tested experimentally, verifying the CKM matrix unitarity and, as a consequence, the SM.

However, using eqs. 1.58-1.66 to determine the λ-dependence of the terms in eqs. 1.71-1.76, one notices that the triangles related to eqs. 1.71, 1.72, 1.74 and 1.75 are degenerate:

$$V^*_{ud}V_{us} + V^*_{cd}V_{cs} + V^*_{td}V_{ts} = \mathcal{O}(\lambda) + \mathcal{O}(\lambda) + \mathcal{O}(\lambda^5), \tag{1.77}$$

$$V^*_{us}V_{ub} + V^*_{cs}V_{cb} + V^*_{ts}V_{tb} = \mathcal{O}(\lambda^4) + \mathcal{O}(\lambda^2) + \mathcal{O}(\lambda^2), \tag{1.78}$$

$$V^*_{ub}V_{ud} + V^*_{cb}V_{cd} + V^*_{tb}V_{td} = \mathcal{O}(\lambda^3) + \mathcal{O}(\lambda^3) + \mathcal{O}(\lambda^3) \tag{1.79}$$

$$V_{ud}V^*_{cd} + V_{us}V^*_{cs} + V_{ub}V^*_{cb} = \mathcal{O}(\lambda) + \mathcal{O}(\lambda) + \mathcal{O}(\lambda^5), \tag{1.80}$$

$$V_{cd}V^*_{td} + V_{cs}V^*_{ts} + V_{cb}V^*_{tb} = \mathcal{O}(\lambda^4) + \mathcal{O}(\lambda^2) + \mathcal{O}(\lambda^2), \tag{1.81}$$

$$V_{td}V^*_{ud} + V_{ts}V^*_{us} + V_{tb}V^*_{ub} = \mathcal{O}(\lambda^3) + \mathcal{O}(\lambda^3) + \mathcal{O}(\lambda^3). \tag{1.82}$$

The triangles related to the eqs. 1.73 and 1.76, instead, have all the sides of the same order of magnitude $\mathcal{O}(\lambda^3)$, which makes them more attractive for experimental purposes, since the measurements of all the sides and all the angles are equally feasible. For historical reasons, the most frequently-quoted triangle is the one related to eq. 1.73.

1.2.2.1   The unitary triangle $V_{ud}V_{ub}^* + V_{cd}V_{cb}^* + V_{td}V_{tb}^* = 0$

The expression for each side of the triangle related to eq. 1.73 can be derived from eqs. 1.58-1.66:

$$V_{ud}V_{ub}^* = A\lambda^3(\bar{\rho} + i\bar{\eta}) + \mathcal{O}(\lambda^7), \tag{1.83}$$

$$V_{cd}V_{cb}^* = -A\lambda^3 + \mathcal{O}(\lambda^7), \tag{1.84}$$

$$V_{td}V_{tb}^* = A\lambda^3[1 - (\bar{\rho} + i\bar{\eta})] + \mathcal{O}(\lambda^7). \tag{1.85}$$

With an accuracy $\sim \mathcal{O}(\lambda^7) \simeq \mathcal{O}(10^{-5})$ the term $V_{cd}V_{cb}^*$ can be considered as real. Fig. 1.4 shows the graphical representation of the unitary triangle in the complex plane. By convention, all the terms are divided by $|V_{cd}V_{cb}^*| = A\lambda^3$. The vector $\overline{CA}$ points to 0 because of the minus sign in eq. 1.84. The relation between the unitary
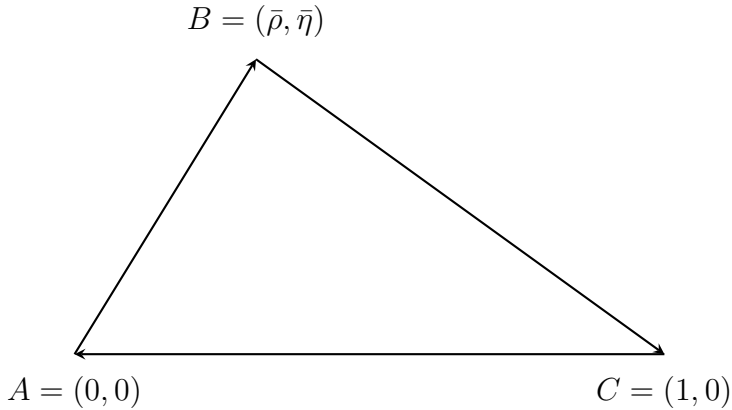
Figure 1.4: The unitary triangle related to the eq. 1.73.

triangle and the branching fractions $\mathcal{B}(K \to \pi\nu\bar{\nu})$ will be discussed in the next section.

1.2.3 The branching fractions $\mathcal{B}(K \to \pi\nu\bar{\nu})$

For the theoretical calculation of the branching fraction $\mathcal{B}(X \to Y)$, it is useful to introduce the decay width $\Gamma(X \to Y)$, defined as [1]

$$\Gamma(X \to Y) \stackrel{def}{=} \frac{1}{2m_X} \int |\mathcal{A}(X \to Y)|^2 d\Phi(Y) \tag{1.86}$$

where $\mathcal{A}(X \to Y)$, called amplitude, is a matrix element containing all the dynamics of the process $X \to Y$, while $\Phi(Y)$ is the phase space of the final state Y and depends on kinematics only.

The branching fraction $\mathcal{B}(X \to Y)$ can be expressed as the ratio between the decay width $\Gamma(X \to Y)$ of the decay channel Y and the sum of all the decay widths of the N possible decays Y_n $(n = 1, \dots, N)$ of the particle X:

$$\mathcal{B}(X \to Y) \stackrel{def}{=} \frac{\Gamma(X \to Y)}{\sum_n \Gamma(X \to Y_n)}. \tag{1.87}$$

If k different final states Y_i $(i = 1, \dots, k)$ are experimentally indistinguishable, the expected value for the measured branching fraction is given by the sum of the branching fractions $\mathcal{B}(X \to Y_i)$:

$$\mathcal{B}(X \to Y_1 \vee \cdots \vee Y_k) = \frac{\sum_i \Gamma(X \to Y_i)}{\sum_n \Gamma(X \to Y_n)}. \tag{1.88}$$

Since the three neutrino flavours are indistinguishable in the experimental detection of the $K \to \pi\nu\bar{\nu}$ decays, from eqs. 1.86 and 1.88 it follows that the branching fractions $\mathcal{B}(K \to \pi\nu\bar{\nu})$ are given by

$$\mathcal{B}(K \to \pi\nu\bar{\nu}) = \sum_{\ell = e, \mu, \tau} \frac{1}{2m_K \Gamma_{tot}} \int |\mathcal{A}_\ell|^2 d\Phi(\pi\nu_\ell\bar{\nu}_\ell), \tag{1.89}$$

where $\mathcal{A}_\ell \equiv \mathcal{A}(K \to \pi\nu_\ell\bar{\nu}_\ell)$ and $\Gamma_{tot} \equiv \sum_n \Gamma(K \to Y_n)$. In the SM, the main contributions to the amplitude $\mathcal{A}_\ell$ are described by the Feynman diagrams in Fig. 1.5. In the literature, the first of them is called the *box* diagram, the others the *penguin*

diagrams. The quarks u, c and t contribute as internal lines to each of these diagrams,
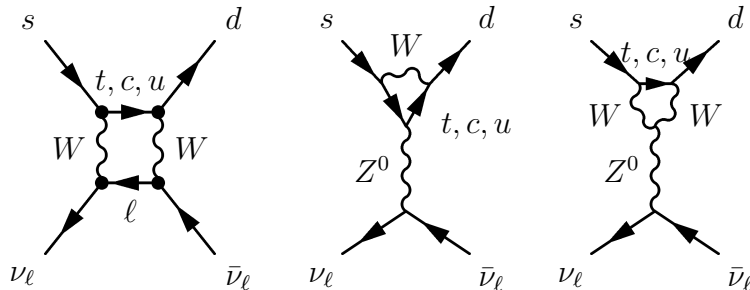
Figure 1.5: Feynman diagrams describing the SM contributions to the FCNC process $s \to d\nu_\ell\bar{\nu}_\ell$ ($\ell = e$, μ, τ).

while the leptons e, μ and τ contribute to the box diagram only.

From the theoretical point of view, one of the aspects that make the $K \to \pi\nu\bar{\nu}$ decays particularly interesting is that long-distance contributions, which are non-perturbative QCD effects, are negligible [25–27]. Therefore they can be precisely described by Fermi-like effective vertices, whose Hamiltonian $\mathcal{H}_{\text{eff}}^{\text{SM}}$ can be written as [28, 29]

$$\mathcal{H}_{\text{eff}}^{\text{SM}} = \frac{G_{\text{F}}}{\sqrt{2}} \frac{\alpha}{2\pi \sin^2 \vartheta_W} \sum_{\ell = e,\mu,\tau} \sum_{q = u,c,t} V_{qs}^* V_{qd} X_q^\ell (\bar{s}d)_{V-A} (\bar{\nu}_\ell \nu_\ell)_{V-A} + h.c. \qquad (1.90)$$

where G_{F} is the Fermi constant, α is the electromagnetic coupling constant and ϑ_W is the weak mixing angle, while X_q^ℓ are functions describing the contribution of the quark q to the amplitude $\mathcal{A}_\ell$ ($\ell = e, \mu, \tau$).

In particular, in the limit $m_q \ll M_W$, the function X_q^ℓ depends linearly on $x_q \overset{def}{=} \frac{m_q^2}{M_W^2}$. Thus, the function X_u^ℓ can be considered as independent of the quark flavour and the sum $\sum_q V_{qs}^* V_{qd} X_u^\ell$ ($q = u, c, t$) vanishes because of the GIM mechanism. Redefining the functions X_q^ℓ as $\tilde{X}_q^\ell = X_q^\ell - X_u^\ell$, the effective Hamiltonian $\mathcal{H}_{\text{eff}}^{\text{SM}}$ in eq. 1.90 becomes [28, 29]

$$\mathcal{H}_{\text{eff}}^{\text{SM}} = \frac{G_{\text{F}}}{\sqrt{2}} \frac{\alpha}{2\pi \sin^2 \vartheta_W} \sum_{\ell = e,\mu,\tau} \left[V_{ts}^* V_{td} \tilde{X}_t^\ell + V_{cs}^* V_{cd} \tilde{X}_c^\ell \right] (\bar{s}d)_{V-A} (\bar{\nu}_\ell \nu_\ell)_{V-A} + h.c. \quad (1.91)$$

By definition of effective Hamiltonian, the amplitude is $\mathcal{A} = -i\mathcal{H}_{\text{eff}}$ at all perturbative

orders, and from eq. 1.89 follows that the branching fractions $\mathcal{B}(K \to \pi\nu\bar{\nu})$ can be written as

$$\mathcal{B}(K^+ \to \pi^+\nu\bar{\nu}) = \sum_{\ell=e,\mu,\tau} \frac{|G_\ell|^2}{4m_K\Gamma_{tot}} \int |(\bar{s}d)_{V-A}(\bar{\nu}_\ell\nu_\ell)_{V-A}|^2 d\Phi(\pi^+\nu_\ell\bar{\nu}_\ell), \qquad (1.92)$$

$$\mathcal{B}(K_L \to \pi^0\nu\bar{\nu}) = \sum_{\ell=e,\mu,\tau} \frac{|\mathrm{Im}G_\ell|^2}{4m_K\Gamma_{tot}} \int |(\bar{s}d)_{V-A}(\bar{\nu}_\ell\nu_\ell)_{V-A}|^2 d\Phi(\pi^0\nu_\ell\bar{\nu}_\ell), \qquad (1.93)$$

where

$$G_\ell \overset{def}{=} \frac{G_{\mathrm{F}}\alpha}{2\pi\sin^2\vartheta_W} \left[V_{ts}^*V_{td}\tilde{X}_t^\ell + V_{cs}^*V_{cd}\tilde{X}_c^\ell \right]. \qquad (1.94)$$

The dependence on $\mathrm{Im}G_\ell$ of $\mathcal{B}(K_L \to \pi^0\nu\bar{\nu})$ is due to the K_L being a superposition of the $\bar{s}d$ and $s\bar{d}$ states:

$$|K_L\rangle = \frac{|\bar{s}d\rangle + |s\bar{d}\rangle}{\sqrt{2}}. \qquad (1.95)$$

Another important quality of the $K \to \pi\nu\bar{\nu}$ decays is that the hadronic matrix element, which usually limits the precision of the measurement because of non-perturbative effects, can be extracted from the branching fractions of the $K \to \pi e\nu$ decays

$$\mathcal{B}(K \to \pi e\nu) = \frac{G_F^2|V_{us}|^2}{4m_K\Gamma_{tot}} \int |(\bar{s}u)_{V-A}(\bar{\nu}_e e)_{V-A}|^2 d\Phi(\pi e\nu), \qquad (1.96)$$

which are large and well-measured. By using the eq. 1.96, eqs. 1.92-1.93 can be rewritten as

$$\mathcal{B}(K^+ \to \pi^+\nu\bar{\nu}) = \sum_{\ell=e,\mu,\tau} \frac{|G_\ell|^2}{G_F^2|V_{us}|^2} 2r_{K^+}\mathcal{B}(K^+ \to \pi^0 e^+\nu), \qquad (1.97)$$

$$\mathcal{B}(K_L \to \pi^0\nu\bar{\nu}) = \sum_{\ell=e,\mu,\tau} \frac{|\mathrm{Im}G_\ell|^2}{G_F^2|V_{us}|^2} 2r_{K_L}\mathcal{B}(K_L \to \pi^\pm e^\mp\nu), \qquad (1.98)$$

where $r_{K^+} = 0.901 \pm 0.027$ and $r_{K_L} = 0.944 \pm 0.028$ are the isospin breaking

corrections [30, 31]. The notation

$$\kappa_+ \overset{def}{=} r_{K^+} \frac{3\alpha^2 \mathcal{B}(K^+ \to \pi^0 e^+ \nu)}{2\pi^2 \sin^4 \vartheta_W} \lambda^8, \tag{1.99}$$

$$\kappa_L \overset{def}{=} r_{K_L} \frac{3\alpha^2 \mathcal{B}(K_L \to \pi^\pm e^\mp \nu)}{2\pi^2 \sin^4 \vartheta_W} \lambda^8, \tag{1.100}$$

$$P_c(X) \overset{def}{=} \frac{1}{\lambda^4} \left(\frac{2}{3} \tilde{X}_c^e + \frac{1}{3} \tilde{X}_c^\tau \right), \tag{1.101}$$

is often used in literature in order to rewrite the eqs. 1.97 and 1.98 as

$$\mathcal{B}(K^+ \to \pi^+ \nu \bar{\nu}(\gamma)) = \kappa_+(1 + \Delta_{\text{EM}}) \left[\left(\frac{\text{Im}[V_{ts}^* V_{td}]}{\lambda^5} \tilde{X}_t \right)^2 \right.$$
$$\left. + \left(\frac{\text{Re}[V_{ts}^* V_{td}]}{\lambda^5} \tilde{X}_t + \frac{\text{Re}[V_{cs}^* V_{cd}]}{\lambda} (P_c + \delta P_{c,u}) \right)^2 \right], \tag{1.102}$$

$$\mathcal{B}(K_L \to \pi^0 \nu \bar{\nu}) = \kappa_L \left(\frac{\text{Im}[V_{ts}^* V_{td}]}{\lambda^5} \tilde{X}_t \right)^2, \tag{1.103}$$

where $\delta P_{c,u} = 0.04 \pm 0.02$ and $\Delta_{\text{EM}} = -0.003$ are corrections due to the QCD and QED long distance contributions [32, 33] respectively. The function $\tilde{X}_t^\ell$ in eqs. 1.102 and 1.103 has been evaluated including the QCD Next-to-Leading Order (NLO) corrections [28] and the two-loop electroweak corrections [34], while P_c in eq. 1.102 has been calculated including the QCD Next-to-Next-to-Leading Order (NNLO) corrections [35–37] and the one-loop electroweak corrections [38]. The most updated estimates of the $K \to \pi \nu \bar{\nu}$ branching fractions are [34]

$$\mathcal{B}(K^+ \to \pi^+ \nu \bar{\nu}) = (7.81^{+0.80}_{-0.71} \pm 0.29) \times 10^{-11}, \tag{1.104}$$

$$\mathcal{B}(K_L \to \pi^0 \nu \bar{\nu}) = (2.43^{+0.40}_{-0.37} \pm 0.06) \times 10^{-11}. \tag{1.105}$$

The first error in eqs. 1.104 and 1.105 refers to the uncertainties of the input parameters: for the $K^+ \to \pi^+ \nu \bar{\nu}$ decay, 81% of this uncertainty is related to the CKM matrix parameters (56% V_{cb}, 21% $\bar{\rho}$ and 4% $\bar{\eta}$) and the remaining is mostly due to the charm and top quark masses, while for the $K_L \to \pi^0 \nu \bar{\nu}$ decay the CKM matrix accounts for 93% of this uncertainty (54% V_{cb} and 39% $\bar{\eta}$) and the remaining

7% is due to the top quark mass.

The second error in eqs. 1.104 and 1.105 is related to the remaining theoretical uncertainty: for the $K^+ \to \pi^+ \nu \bar{\nu}$ decay, it is dominated by the charm contribution ($46\%\ \delta P_{c,u}$, $20\%\ P_c$) and by the QCD corrections beyond the NLO for $\tilde{X}_t$ (24%), while for the $K_L \to \pi^0 \nu \bar{\nu}$ decay the latter accounts for 73% of the remaining theoretical uncertainty.

1.2.3.1 Relation between $\mathcal{B}(K \to \pi \nu \bar{\nu})$ and the unitary triangle

From eqs. 1.102 and 1.103 the dependence of the branching fractions on the CKM matrix elements is evident. In particular, $V_{ts}^* V_{td}$ and $V_{cs}^* V_{cd}$ can be expressed in the Wolfenstein parametrisation (Sec. 1.2.1):

$$
\begin{aligned}
\mathrm{Re}[V_{ts}^* V_{td}] &= -A^2 \lambda^5 (1 - \bar{\rho}) + \mathcal{O}(\lambda^7), & (1.106) \\
\mathrm{Im}[V_{ts}^* V_{td}] &= -A^2 \lambda^5 \bar{\eta} + \mathcal{O}(\lambda^7), & (1.107) \\
\mathrm{Re}[V_{cs}^* V_{cd}] &= -\lambda + \frac{\lambda^3}{2} + \frac{\lambda^5}{8} + A^2 \lambda^5 (1 - \bar{\rho}) + \mathcal{O}(\lambda^7), & (1.108) \\
\mathrm{Im}[V_{cs}^* V_{cd}] &= -A^2 \lambda^5 \bar{\eta} + \mathcal{O}(\lambda^7), & (1.109)
\end{aligned}
$$

in order to write the eqs. 1.102 and 1.103 as

$$
\mathcal{B}(K^+ \to \pi^+ \nu \bar{\nu}(\gamma)) = \kappa_+ (1 + \Delta_{\mathrm{EM}}) \tilde{X}_t^2 A^4 \left[\bar{\eta}^2 + (\rho_0 - \bar{\rho})^2 \right], \tag{1.110}
$$

$$
\mathcal{B}(K_L \to \pi^0 \nu \bar{\nu}) = \kappa_L \tilde{X}_t^2 A^4 \bar{\eta}^2, \tag{1.111}
$$

where ρ_0 has been defined as

$$
\rho_0 \stackrel{def}{=} 1 + \frac{P_c + \delta P_{c,u}}{A^2 \tilde{X}_t}. \tag{1.112}
$$

Therefore, the branching fraction $\mathcal{B}(K^+ \to \pi^+ \nu \bar{\nu})$ is proportional to the square of the hypotenuse of the right-angled triangle having as catheti the height $\bar{\eta}$ of the unitary triangle (Fig. 1.4) and one side of length $\rho_0 - \bar{\rho}$, while the branching fraction $\mathcal{B}(K_L \to \pi^0 \nu \bar{\nu})$ is proportional to the square of the height $\bar{\eta}$ of the unitary

triangle. Fig. 1.6 shows the graphical representation of such relations.
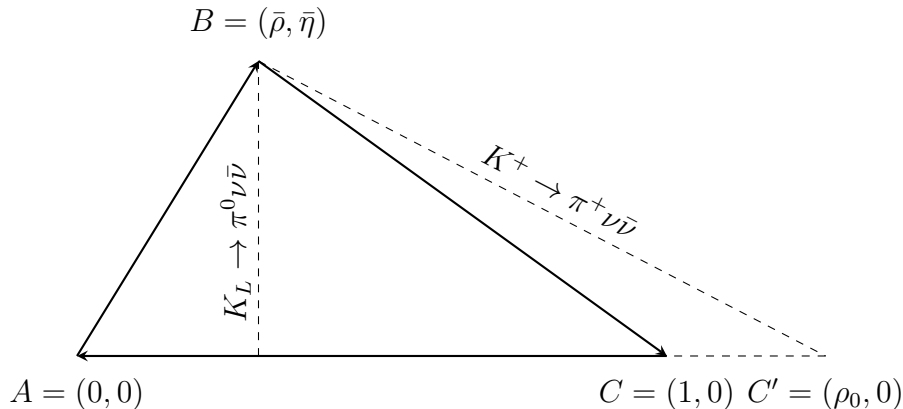
Figure 1.6: Relation between the unitary triangle related to the eq. 1.73 and the branching fractions $\mathcal{B}(K \to \pi\nu\bar{\nu})$.

1.2.4 Experimental status

The E787 and E949 experiments [39, 40] at the Brookhaven National Laboratory (BNL) are the only ones so far to have observed the process $K^+ \to \pi^+\nu\bar{\nu}$. These measurements were performed using K^+ decaying at rest inside an active target made of scintillator fibres, placed in the centre of a cylindrical experimental apparatus, immersed in a $1\,\mathrm{T}$ magnetic field. Figure 1.7 shows the layout of the E787/E949 detector [41].

Both experiments employed $24\,\mathrm{GeV}/c$ primary protons from the Alternating Gradient Synchrotron (AGS) to produce a secondary beam with K/π ratio ~ 3, after selection by the beam optics in a momentum range centred at $710\,\mathrm{MeV}/c$ and Full Width at Half Maximum (FWHM) of 4.5%.

Kaons in the secondary beam were identified by a Cherenkov counter and reached the scintillating fibre target after passing through two charged particle trackers, a $11.1\,\mathrm{cm}$ thick BeO absorber and a $17\,\mathrm{cm}$ thick active absorber. The typical instantaneous rate of kaons entering the target was of $1\text{-}2\,\mathrm{MHz}$, corresponding to $3\text{-}6\,\mathrm{MHz}$ at the Cherenkov counter. The target was made of 413 scintillating fibres of $310\,\mathrm{cm}$ length
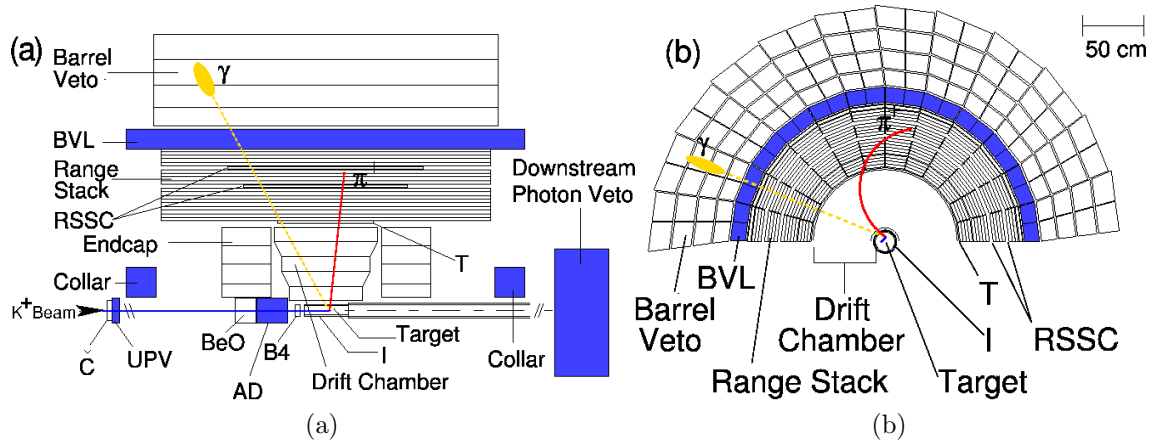
Figure 1.7: Schematic layout of the E787/E949 experimental apparatus: (a) side view, (b) front view.

and $5 \times 5\,\text{mm}^2$ cross-section, assembled into a cylinder of 6 cm radius and arranged along the beam direction. In order to record the activity in the target, each fibre was connected to a PMT. The upstream part (24 cm long) of the target was surrounded radially by two 6.4 mm thick layers of plastic scintillators and was used as fiducial volume.

Decay products exiting from the fiducial volume and traversing the plastic scintillators entered a cylindrical drift chamber with inner and outer radii of 7.85 cm and 43.31 cm, respectively, which was employed to measure the 3-momenta of charged particles. Outside the drift chamber, 19 layers of segmented plastic scintillators formed the Range Stack, a detector with inner and outer radii of 45 cm and 84 cm respectively, used to measure energy and range of charged particles and as photon veto. The outermost detector, a shashlyk electromagnetic calorimeter (Barrel Veto) with inner and outer radii of 94.5 cm and 145 cm respectively, consisted of 75 lead-scintillator layers of thickness 1 mm+5 mm, corresponding to a total thickness of 14.3 radiation lengths (X_0), and was used as photon veto, covering 2/3 of the 4π solid angle. The remaining 1/3 was covered by several calorimeters with a total thickness from $7X_0$ to $15X_0$, among which two upstream and downstream end caps, each formed of four rings of segmented Cesium Iodide (CsI) crystals.

The combined E787+E949 data sample consisted of $(5.9 + 1.8) \times 10^{12}$ kaon decays in the target. The $K^+ \to \pi^+ \nu \bar{\nu}$ events were selected requiring a π^+ candidate and the simultaneous absence of any other activities in the detector. Charged tracks were identified as a π^+ by reconstructing the $\pi^+ \to \mu^+ \to e^+$ decay sequence and combining momentum, range and energy measurements. In particular, the π^+ momentum p_π was required to be either $(140 < p_\pi < 195)\,\mathrm{MeV}/c$ or $(211 < p_\pi < 229)\,\mathrm{MeV}/c$, in order to avoid the $K^+ \to \pi^+ \pi^0$ peak at $205\,\mathrm{MeV}/c$. Moreover, two Signal Regions were defined in the (energy, range) plane, as shown in Fig. 1.8. The primary sources of the residual background were $K^+ \to \pi^+ \pi^0$ and $K^+ \to \mu^+ \nu$ decays in which the outgoing charged track scattered in the target, as well as $K^+ \to \pi^+ \pi^- \ell^+ \nu$ ($\ell = e, \mu$) decays and charge exchange processes $K^+ n \to K^0 p$ with subsequent $K_L \to \pi^+ \mu^- \bar{\nu}$ decays.

A total of 5+2 events (E787+E949) were observed in the Signal Regions, corresponding to the measured branching fraction $\mathcal{B}(K^+ \to \pi^+ \nu \bar{\nu})$ [42]

$$\mathcal{B}(K^+ \to \pi^+ \nu \bar{\nu}) = 1.73^{+1.15}_{-1.05} \times 10^{-10}, \tag{1.113}$$

obtained with the likelihood method, assuming the SM $K^+ \to \pi^+ \nu \bar{\nu}$ decay spectrum and taking into account the uncertainties due to the evaluation of background and acceptance. The probability that all the 7 observed events were due to background has been estimated to be 10^{-3}. The E787+E949 result is within one standard deviation from the SM prediction (eq. 1.104).
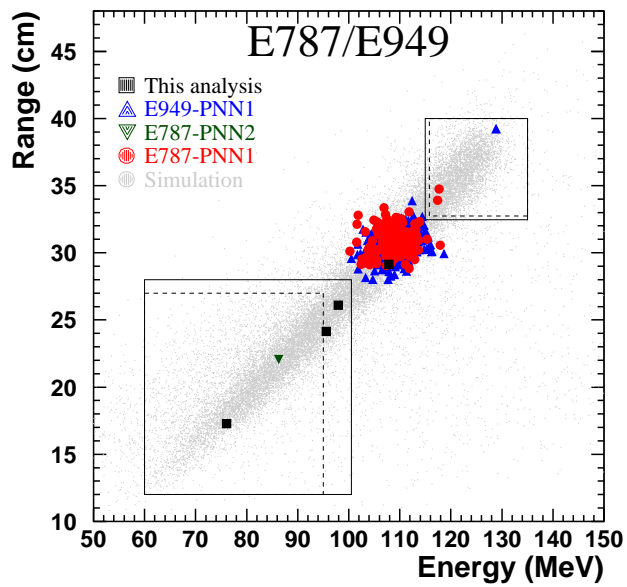
Figure 1.8: The 2+5 $K^+ \rightarrow \pi^+ \nu \bar{\nu}$ candidates observed in the E787+E949 experiments. The kinetic energy and the range of the π^+ candidates are shown. Signal Regions are delimited by the solid lines. Dashed lines show the Signal Regions of earlier analyses. Grey points are obtained from a MC simulation of the signal. The cluster of events between the two Signal Regions is due to $K^+ \rightarrow \pi^+ \pi^0$ events with an undetected π^0.

Chapter 2

The NA48/2 experiment

The NA48/2 experiment at CERN Super-Proton-Synchrotron (SPS) [15] was a multi-purpose $K^\pm$ experiment, whose main goal was to search for direct CP violation in the $K^\pm \to \pi^\pm\pi^+\pi^-$ and $K^\pm \to \pi^\pm\pi^0\pi^0$ decays.

The matrix element of the $K^\pm \to \pi^\pm\pi\pi$ decays can be parametrised in the form [1]

$$|M(u,v)|^2 \propto 1 + gu + hu^2 + kv^2, \tag{2.1}$$

where $u = (s_3 - s_0)/m_\pi^2$, $v = (s_1 - s_2)/m_\pi^2$, $s_0 = \frac{1}{3}(s_1 + s_2 + s_3)$, $s_i = (P_K - P_i)^2$, P_K and P_i are the 4-momenta of the kaon and of the pions respectively ($i = 1, 2$ for the two identical pions), and m_π is the pion mass. In case of CP conservation, the coefficients g, h and k must be the same for K^+ and K^- decays. Thus, an evidence of direct CP violation would be the non-zero measurement of A_g or A_g^0, defined as

$$A_g = \frac{g^+ - g^-}{g^+ + g^-}, \tag{2.2}$$

$$A_g^0 = \frac{g_0^+ - g_0^-}{g_0^+ + g_0^-}, \tag{2.3}$$

where $g^\pm$ and $g_0^\pm$ are the coefficients g obtained from eq. 2.1 for the $K^\pm \to \pi^\pm\pi^+\pi^-$ and $K^\pm \to \pi^\pm\pi^0\pi^0$ decays respectively.

The measurement of the charge asymmetries A_g and A_g^0 is preferred to the one of asymmetries in the integrated decay rates because it is expected to be more sensitive to direct CP violation [43].

Results on the charge asymmetries A_g and A_g^0 based on 3.11×10^9 $K^\pm \to \pi^\pm \pi^+ \pi^-$ and 9.13×10^7 $K^\pm \to \pi^\pm \pi^0 \pi^0$ decays have been published by the NA48/2 collaboration [44]:

$$A_g = (1.5 \pm 2.2) \times 10^{-4}, \qquad (2.4)$$
$$A_g^0 = (1.8 \pm 1.8) \times 10^{-4}. \qquad (2.5)$$

The precision of the A_g and A_g^0 results is limited mainly by the size of the $K^\pm \to \pi^\pm \pi \pi$ samples, collected during two runs in 2003 and 2004, in ~ 50 days of effective data taking.

The detector used in the NA48/2 experiment is shown in Fig. 2.1 and will be described in this chapter, focussing in particular on the detectors used for the $K^\pm \to \pi^\mp \mu^\pm \mu^\pm$ analysis, which is the topic of this thesis. A detailed description of the NA48/2 detector can be found in Ref. [45]. The Cartesian coordinate system chosen in the laboratory reference frame is the following: the origin is 120 m downstream of the point where the secondary beam is produced, the z-axis is collinear with the detector axis and points downstream, the y-axis points up and the x-axis is defined to form a right-handed system.

2.1 K^+ and K^- beam line

In order to minimise the systematic bias in the comparison between K^+ and K^- decays, simultaneous and collinear K^+ and K^- beams of the same momentum were steered into the decay region. To produce the $K^\pm$ beam, the 400 GeV/c primary proton beam from the SPS was steered to a cylindrical Beryllium target (T10) with diameter of 2 mm and length of 400 mm. The intensity of the proton beam was 7×10^{11} protons per cycle, with a 4.8 s flat top (called "burst") and 16.8 s
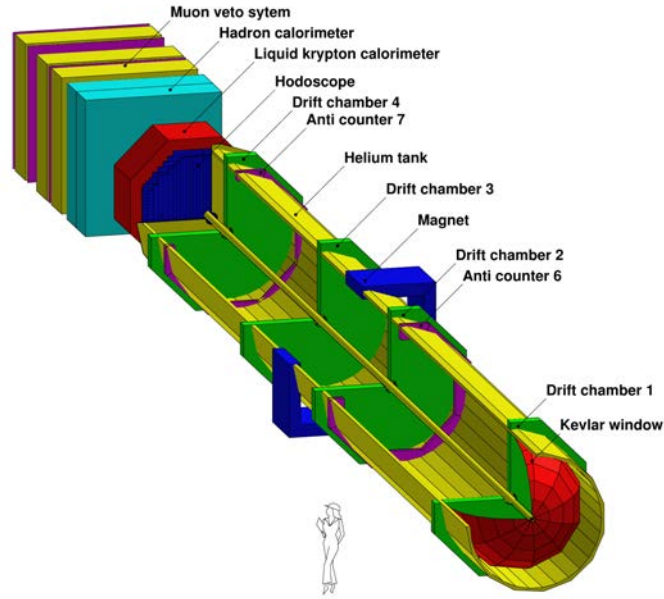
Figure 2.1: The NA48/2 detector.

duty cycle. Positively and negatively charged particles in a narrow momentum band centred at 60 GeV/c and with a Root Mean Square (RMS) of 3.7 GeV/c were selected from the secondary beam using a set of collimators and bending magnets. Fig. 2.2 shows the NA48/2 beam line [44].
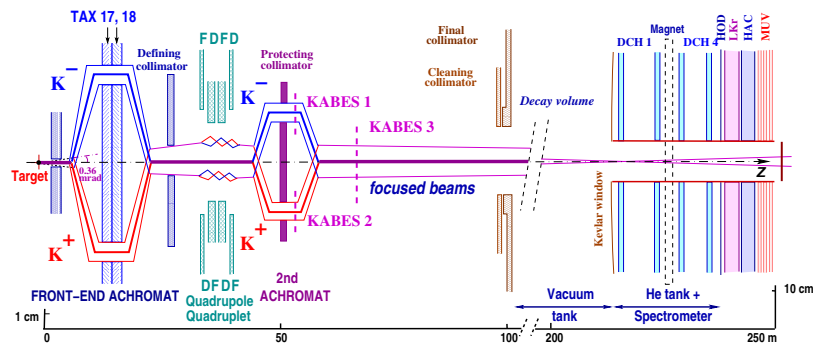
Figure 2.2: The NA48/2 beam line and detector.

At the entrance of the decay volume, the positive (negative) beam consisted of 3.8×10^7 (2.5×10^7) particles per pulse, mostly charged pions. This corresponded to 2.2×10^6 K^+ (1.2×10^6 K^-), with a K^+/K^- flux ratio of 1.8. The two beams had a transverse size $\delta x = \delta y = 10$ mm (RMS) and their axes coincided to 1 mm.

The fraction of kaons decaying in the decay region at nominal momentum was 22%, corresponding to $\sim 4.8 \times 10^5\ K^+$ and $\sim 2.7 \times 10^5\ K^-$ decays per pulse [44].

2.2 Decay region

The decay region started 102 m downstream of the Beryllium target and was contained in a vacuum (at $< 10^{-4}$ mbar) cylindrical tank, to avoid interactions of kaon decay products before detection. The cylindrical tank was 114 m long and its diameter varied from 1.92 m in the first 65 m to 2.4 m in its last 49 m. The downstream part of the vacuum tank was sealed by a convex Kevlar window, that separated the vacuum from the helium at atmospheric pressure in the Spectrometer (described in Sec. 2.3). The thickness of the window was 0.9 mm, corresponding to $3 \times 10^{-3}X_0$. Downstream of the Kevlar window, the undecayed beam particles were kept in the vacuum, contained in an aluminium pipe of 152 mm inner diameter and 1.2 mm thickness.

2.3 Magnetic spectrometer

The magnetic spectrometer was formed of 4 Drift CHambers (DCHs) and a dipole magnet, placed after the first pair of drift chambers, and provided a horizontal momentum kick $p_t = 120$ MeV/c (corresponding to an integrated magnetic field of ~ 0.5 Tm). Each pair of chambers was needed to track respectively the trajectories of the particles before and after the momentum kick provided by the magnet and to measure their momenta from the induced deflection. The magnet polarity was inverted on a daily basis (every 3 hours for the 2004 run), in order to minimise the systematic bias due to different acceptances for the K^+ and K^- decay products. The entire spectrometer was contained in a tank filled with helium at atmospheric pressure, in order to reduce the effect of the multiple Coulomb scattering.

Every chamber had an octagonal shape with radius of 1.45 m and a central hole with diameter of 16 cm for the beam pipe, and was formed of 8 planes of 256 sense

wires, arranged on 4 different orientations (called views), orthogonally to the beam axis: X(0°), Y(90°), U(−45°) and V(+45°). Fig. 2.3a shows a sketch illustrating the view orientations of a single drift chamber. Each view consisted of two planes of sense wires surrounded by potential wires, in a gas mixture of Argon (50%) + Ethane (50%). The potential wires were staggered by 5 mm, which was half of the distance between two sense wires. Such a layout, shown in Fig. 2.3b, was required for resolving reconstruction ambiguities. The maximum drift time corresponding to the chosen half wire pitch ($\sim$ 5 mm) was 100 ns. The fast rise time of the pulses and the high performance of the Time to Digital Converters allowed to obtain a time resolution of 700 ps.
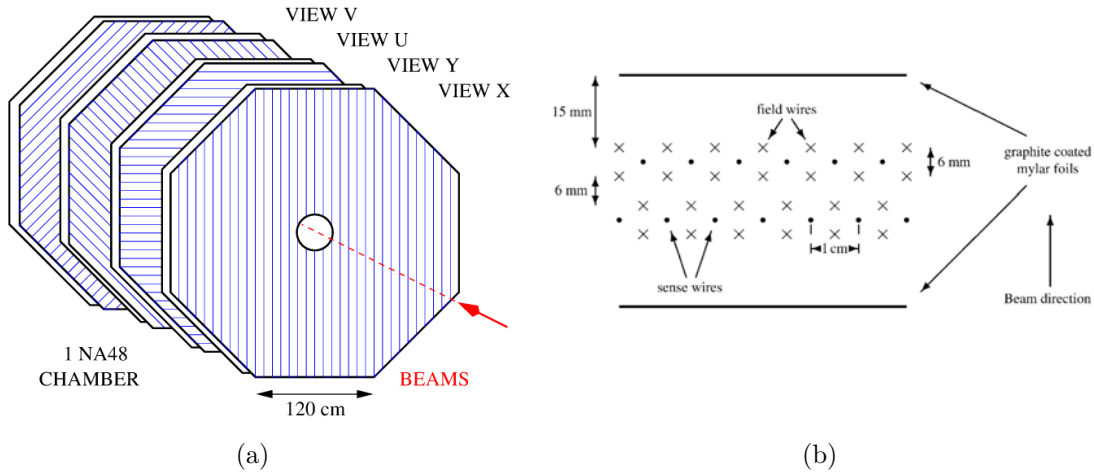
Figure 2.3: Wires arrangement (a) in a drift chamber and (b) in a view.

The spatial resolution of each DCH was $\sigma_x = \sigma_y = 90$ μm, while the momentum resolution of the spectrometer was [44]

$$\frac{\sigma(p)}{p} = (1.02 \oplus 0.044 \cdot p)\%, \tag{2.6}$$

where the momentum p is measured in GeV/c. The first term is due to the effect of the multiple scattering, while the second one is a consequence of the spatial resolution on the reconstructed track points. As a consequence, the resolution on

the reconstructed kaon mass $m(\pi^\pm\pi^+\pi^-)$ obtained from the $K^\pm \to \pi^\pm\pi^+\pi^-$ decays, which is a quantity entirely determined from the spectrometer information, was $\approx 1.7\,\mathrm{MeV}/c^2$.

2.4 Hodoscope

The HODoscope (HOD) [45] was a system of scintillator counters aimed to provide a fast signal for trigger purposes. It consisted of two octagonal-shaped planes, separated by 74 cm, formed of 64 scintillator counters each, arranged vertically and horizontally respectively. Each plane was divided in four quadrants of 16 counters, with the radius of the inscribed circle being 121 cm and with a central hole radius of 12.8 cm for the beam pipe. The dimension of each scintillator strip varied from 60 cm to 121 cm length and from 6.5 cm to 9.9 cm in width, depending on the position, while the thickness was 2 cm. Fig. 2.4 shows the HOD layout [45]. Such a layout was
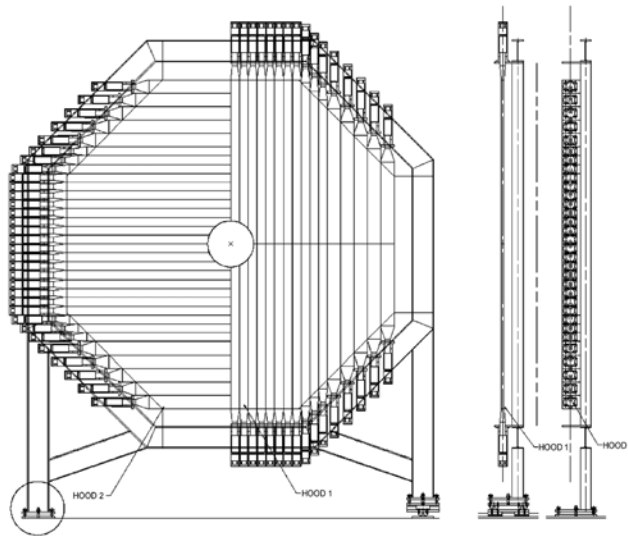
Figure 2.4: The HOD layout (front view).

suitable for defining a set of logical conditions, used by the trigger. In particular, the Q_1 signal was defined as a coincidence in the same quadrant in the two HOD planes and it was used as minimum bias 1-track trigger. For multiple-track events, it was convenient to define also the subquadrant as one quarter of the HOD quadrant

and the Q_2 as the coincidence of at least two Q_1 signals in at least two different subquadrants.

The HOD time resolution, after adding the impact point corrections which used the track information from the spectrometer, was ~ 300 ps.

2.5   Liquid Krypton calorimeter

The NA48 electromagnetic calorimeter [45] was a quasi-homogeneous ionisation chamber, built for the earlier NA48 experiment, which used ~ 7 m^3 of Liquid Krypton (LKr) as active material. The front plane had an octagonal shape, designed to contain a circle of 128 cm radius and with a central hole with radius of 10 cm for the beam pipe. The calorimeter depth was 127 cm, corresponding to 27 radiation lengths.

Thin (40 μm thickness) Cu-Be ribbons of 18 mm width and 127 cm length, corresponding to the whole calorimeter depth, were regularly placed within the LKr volume, orthogonally to the calorimeter front plane, in such a way that they defined 13248 cells with size 2×2 cm^2. This choice corresponded to a high calorimeter granularity, considering that the LKr Molière radius is 4.7 cm. Fig. 2.5 shows the LKr calorimeter and the schematic view of the LKr cell structure. The LKr temperature was kept constant at 121 K within $\pm 0.1\%$ by a cryogenic system. The whole cryostat corresponded to $\sim 0.65 X_0$ of passive material upstream the LKr, that lead to an average $50\,\mathrm{MeV}$ loss in the recostructed photon energy. Another source of energy mis-reconstruction was given by the so called *dead cells*, a small fraction (~ 100 out of 13248) of the LKr cells with inadequate response, mostly due to faults in the electronics chain; however, they were accurately mapped and they are taken into account during the data analysis.

Dedicated data, taken using electrons with a momentum spread of 0.1% and an adjustable average momentum, were collected in order to measure the LKr energy

<div align="center">(a)   (b)</div>
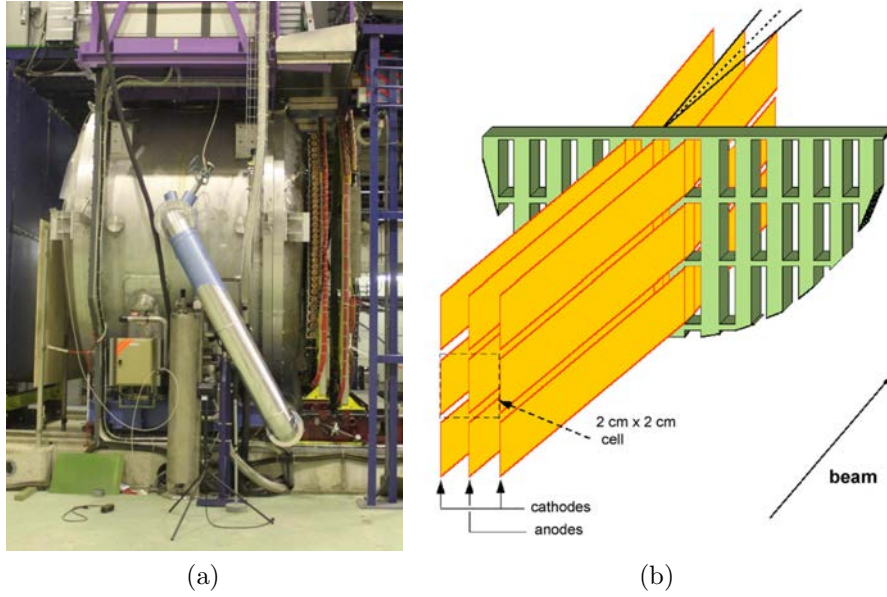
Figure 2.5: (a) The NA48 LKr calorimeter and (b) the schematic view of the LKr cell structure.

resolution σ_E. The result is parametrized by

$$\frac{\sigma_E}{E} = \frac{0.032}{\sqrt{E}} \oplus \frac{0.09}{E} \oplus 0.0042, \qquad (2.7)$$

where E is the energy expressed in GeV. The first term is characteristic of the Poisson statistics affecting the fluctuations in the shower development; the second one arises from the electronic noise and the natural LKr radioactivity; the last one is due to the non perfect cell calibration. The space resolution $\sigma_{x,y}$ of the LKr was:

$$\sigma_{x,y} = \left(\frac{4.2}{\sqrt{E}} \oplus 0.6 \right) \text{ mm}. \qquad (2.8)$$

The first term is due to the Poisson statistics; the second one is related to the non perfect cell calibration. The time resolution on the single shower was

$$\sigma_t = \frac{2.5 \text{ ns}}{\sqrt{E}}. \qquad (2.9)$$

For trigger purposes, a plane of scintillating fibres oriented vertically was installed inside the LKr, at a depth of $9.5X_0$, where the electromagnetic shower development

<div align="center">43</div>

has its maximum. Such a plane of scintillating fibres was called a Neutral HODoscope (NHOD), in analogy of the HOD, used for charged particles triggers. The scintillating fibres had a diameter of 1 mm and were contained in fibreglass tubes with inner and outer diameter of 7 and 8 mm respectively. The NHOD was read-out by 32 channels; its time resolution was of the order of 260 ps and its efficiency was 95% for photon energies above 25 GeV and 99% for photon energies above 35 GeV [45].

2.6   Hadronic Calorimeter

The HAdronic Calorimeter (HAC) [45] was an iron-scintillator sandwich of 1.2 m total iron thickness, placed immediately downstream of the LKr calorimeter. Fig. 2.6 shows the HAC layout [45]. The HAC consisted of two modules, each one made
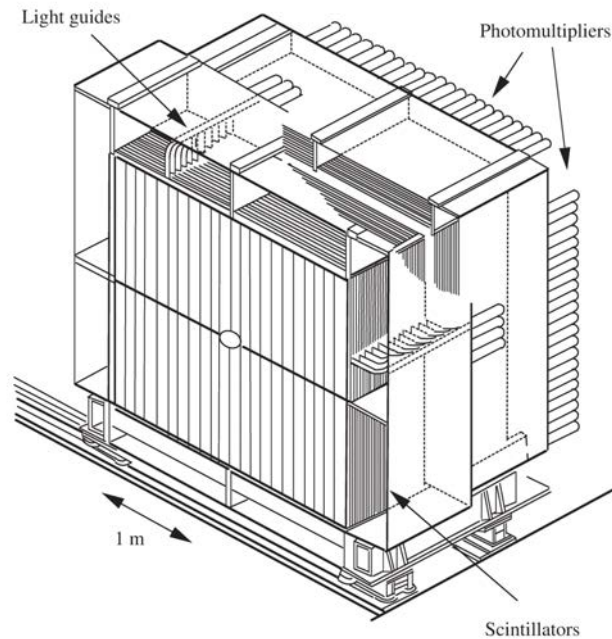
Figure 2.6: Structure of the NA48/2 hadronic calorimeter.

of 24 iron plates with dimensions $2600 \times 2600 \times 25$ mm^3 and a central hole of 212 mm diameter, alternated to scintillator planes made of 44 strips, 1300 mm long and 119 mm wide, with a thickness of 4.5 mm. In both modules, the scintillator strips were alternately oriented in the horizontal and vertical directions. The HAC energy

resolution was $\sigma_E/E = 0.69/\sqrt{E}$ for hadronic showers, where E is expressed in GeV.

2.7 Muon Veto system

The MUon Veto (MUV) [45] consisted of three 2.7×2.7 m^2 scintillator planes orthogonal to the beam axis, each one preceded by a 80 cm thick iron wall. The first two counters (MUV1 and MUV2) were formed of 11 overlapping (as detailed below) scintillator strips with a width of 25 cm, length of 2.7 m and thickness of 2 cm, oriented horizontally and vertically respectively. The third one (MUV3) was formed of 6 scintillator strips with width of 45 cm, length of 2.7 m and thickness 2 cm, arranged horizontally, and was used for monitoring and operational studies only. Fig. 2.7 shows the MUV layout. Each scintillator strip was read out from both sides
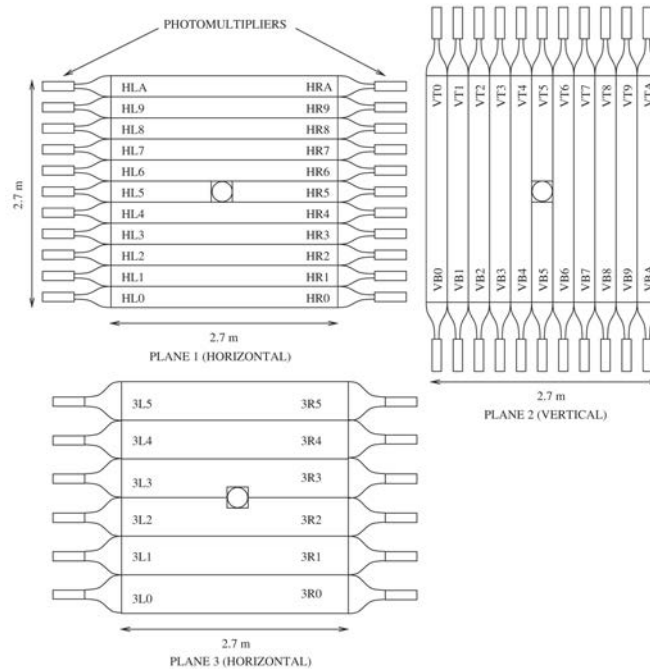
Figure 2.7: Schematic layout of the NA48/2 Muon Veto counters.

by two PhotoMultiplier Tubes (PMTs), in order to cancel the delay depending to the hit position by averaging the two PMT times. In case of one detected signal only, the time had to be corrected using the hit point from the track extrapolation. For MUV1 and MUV2, the central strip was divided in two halves, leaving a 22×22 cm^2

45

central hole to accommodate the beam pipe. Therefore, for such a strip, the signals from the two PMTs were unrelated. For single muon events ($p > 10\,\mathrm{GeV}/c$), the MUV efficiency was $> 99\%$ and the typical time resolution was 350 ps [45]. The strip overlap in MUV1 and MUV2 is a design feature intended to avoid inefficiencies in the muon detection due to gaps in the MUV geometry. The overlap was more pronounced in the region surrounding the beam pipe, to cope with the higher muon rate. The map of the overlapping regions is shown in Fig. 2.8 [46].

Figure 2.8: Map of the overlapping region (a) for MUV1 and (b) for MUV2. The overlap between each strip has been measured in six positions (marked by the dashed lines) along the strip length. For those six positions, the transverse size of each MUV has been measured and is reported at one end of the dashed lines. The numbers in the centre refer to the size of the central hole. All the measurements are expressed in mm.

2.8   Trigger Logic

In principle, the most flexible and unbiased way to read out sub-detector data would be using a "triggerless" acquisition system, in which all the data are unconditionally transferred to PCs. However, in the NA48/2 experiment, this choice was unfeasible: the NA48/2 detector was exposed to a particle rate of $\sim 450\,\mathrm{kHz}$ [15, 44], most of

which was due to the decay of the pions ($\sim 380\,\mathrm{kHz}$) and kaons ($\sim 170\,\mathrm{kHz}$) from the beam (Sec. 2.1), while the maximum sustainable rate was ~ 10 kHz, limited by the LKr calorimeter and the DCH readout [45, 47]. In order to reduce the overall rate to ~ 10 kHz by rejecting uninteresting events while selecting the $K^\pm \to \pi^\pm \pi \pi$ decays with an efficiency $> 99\%$, a two-level trigger system was deployed. In particular, two different trigger subsystems, called "charged" and "neutral" triggers, were used to select respectively $K^\pm \to \pi^\pm \pi^+ \pi^-$ and $K^\pm \to \pi^\pm \pi^0 \pi^0$ decays. The charged trigger was used to collect the data sample on which the $K^\pm \to \pi^\mp \mu^\pm \mu^\pm$ analysis presented in this thesis is based, and is described in detail below.

The charged trigger was composed of a fast first level trigger (L1C) and a second level trigger (L2C). The L1C trigger was hardware-based and consisted in a logical OR of the following requirements:

- Q_2 condition (Sec. 2.4) and simultaneous absence of signal in the monitoring anti counters surrounding the decay region;

- Q_1 condition (Sec. 2.4) downscaled by a factor of 100.

Requiring the L1C condition, the initial beam intensity rate ($\sim 450\,\mathrm{kHz}$) was reduced to $\sim 100\,\mathrm{kHz}$, which was affordable as input rate to the L2C trigger. The L2C consisted of a software-based trigger, with a maximum latency of $100\,\mu$s, which used information from the DCH1, DCH2 and DCH4 to estimate coordinates and tracks, in order to study the kinematics of the events satisfying the L1C condition. Due to its capability of calculating invariant masses, the L2C trigger software was called the Mass-BoX (MBX).

After reconstructing the tracks, the MBX algorithm looked for compatible two-track vertices in the fiducial region. A vertex was considered found if the Closest Distance of Approach (CDA) between the tracks was below 5 cm. The condition MB-2VTX corresponded to finding at least two vertices, possibly sharing a track. If MB-2VTX was not satisfied, the MBX algorithm looked for at least one vertex with reconstructed

invariant mass $m_{\pi\pi} < 390 \, \mathrm{MeV}/c^2$ (MB-1VTX condition), where $m_{\pi\pi}^2$ is defined as

$$m_{\pi\pi}^2 \overset{def}{=} (P_{\pi_1} + P_{\pi_2})^2 = 2m_\pi^2 + 2E_{\pi_1}E_{\pi_2} - 2\vec{p}_{\pi_1}\vec{p}_{\pi_2}. \qquad (2.10)$$

In eq 2.10, $P_{\pi_{1,2}}$, $\vec{p}_{\pi_{1,2}}$ and $E_{\pi_{1,2}}$ are the two tracks 4-momenta, 3-momenta and energies assuming the pion masses. If the MB-1VTX requirement was not satisfied, the variable m_{fake}, defined as

$$m_{fake}^2 \overset{def}{=} 2P_K P_\pi = 2E_K E_\pi - 2\vec{p}_K \vec{p}_\pi, \qquad (2.11)$$

was calculated for each track, assuming the pion mass (P_π, $\vec{p}_\pi$ and E_π are the track 4-momentum, 3-momentum and energy; P_K, $\vec{p}_K$ and E_K are the nominal kaon 4-momentum, 3-momentum and energy). Such a variable was used to reject $K^\pm \to \pi^\pm \pi^0$ decays, for which $m_{fake} = \sqrt{m_K^2 + m_\pi^2 - m_{\pi^0}^2} \simeq 495 \, \mathrm{MeV}/c^2$, with a resolution of about $7.5 \, \mathrm{MeV}/c^2$. The condition MB-1TRK-P required at least one track returning $m_{fake} < 475 \, \mathrm{MeV}/c^2$. Fig. 2.9 shows the MBX trigger algorithm. A more detailed description of the NA48/2 charged trigger can be found in Ref. [48].

The trigger requirement adopted for the $K^\pm \to \pi^\mp \mu^\pm \mu^\pm$ analysis consists of the logical OR of the MB-2VTX, MB-1VTX and MB-1TRK-P conditions. For a 3-track decay, the trigger efficiency of the MB-2VTX condition alone was about 96%, while the efficiency of the MB-1VTX condition alone was about 99% [47].
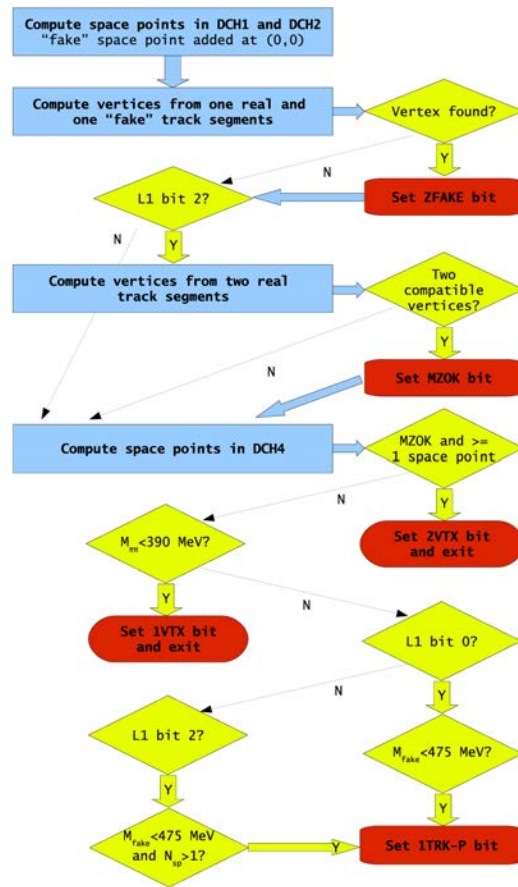
Figure 2.9: MBX trigger algorithm used for the L2C trigger. $m_{\pi\pi}$ is defined in eq. 2.10 and is computed for the two tracks corresponding to the reconstructed vertex. The variable m_{fake} is defined in eq. 2.11. The condition $N_{sp} > 1$ requires at least two DCHs with at least two reconstructed points.

Chapter 3

The $K^\pm \to \pi^\mp \mu^\pm \mu^\pm$ analysis

The presented search for the $K^\pm \to \pi^\mp \mu^\pm \mu^\pm$ decay is based on the full NA48/2 data sample collected in 2003 and 2004. An UL for the branching fraction $\mathcal{B}(K^\pm \to \pi^\mp \mu^\pm \mu^\pm)$ is set for 90%, 95% and 99% CLs.

3.1 Method

A blind analysis has been performed in order to avoid any bias during the finalisation of the event selection criteria. The event selection has been finalised by studying the MC simulations of the signal and of the main source of background, which is due to $K^\pm \to \pi^\pm \pi^+ \pi^-$ decays. Two $K^\pm \to \pi^\pm \pi^+ \pi^-$ MC samples of the same statistical significance have been produced: one has been used exclusively to tune the $K^\pm \to \pi^\mp \mu^\pm \mu^\pm$ event selection, while the other has been employed to estimate the number of expected background events, after the final selection was established. Other background sources have been considered and included in the expected background.

The selection strategy is based on the reconstruction of a three-track vertex: since the vertex z-coordinate resolution is $\sigma_z \sim 1\,\mathrm{m}$, the analysis is sensitive to resonant heavy Majorana neutrinos with lifetime $\tau \lesssim 10\,\mathrm{ps}$ (cf. eq. 1.31).

The UL for the number $N(K^\pm \to \pi^\mp \mu^\pm \mu^\pm)$ of signal candidates in the analysed

data sample has been obtained using the Rolke-Lopez statistical method described in Sec. 3.8.1, for 90%, 95% and 99% CLs.

As will be reported in Sec. 3.4, the number N_K of kaon decays in the fiducial volume has been measured using reconstructed $K^\pm \to \pi^\pm\pi^+\pi^-$ decays, collected using the same trigger (Sec. 2.8) of the data sample employed for the $K^\pm \to \pi^\mp\mu^\pm\mu^\pm$ analysis. The similarity of $\mu^\pm$ and $\pi^\pm$ masses ($m_\mu/m_\pi = 0.76$) leads to similar topologies for $K^\pm \to \pi^\pm\pi^+\pi^-$ and $K^\pm \to \pi^\mp\mu^\pm\mu^\pm$ decays, resulting in a first order cancellation of the systematic effects due to local detector and trigger inefficiencies. Residual effects are dominated by the muon identification efficiency, which has been studied.

The UL for the branching fraction $\mathcal{B}(K^\pm \to \pi^\mp\mu^\pm\mu^\pm)$ has been estimated using the relation

$$\mathcal{B}(K^\pm \to \pi^\mp\mu^\pm\mu^\pm) = \frac{N(K^\pm \to \pi^\mp\mu^\pm\mu^\pm)}{N_K\varepsilon_{\pi\mu\mu}}, \tag{3.1}$$

where $\varepsilon_{\pi\mu\mu}$ is the $K^\pm \to \pi^\mp\mu^\pm\mu^\pm$ acceptance, defined as the probability of selecting a $K^\pm \to \pi^\mp\mu^\pm\mu^\pm$ decay occurring in the fiducial volume. The acceptance $\varepsilon_{\pi\mu\mu}$ has been evaluated for different MC models of the signal, described in Sec. 3.2.2.

3.2   Data and MC samples

3.2.1   Data samples

The data samples considered during the presented analysis are summarised below.

FULL: the full NA48/2 data sample. Due to the physics programme of the NA48/2 experiment (Chapter 2), the triggers were mostly aimed to select $K^\pm \to \pi^\pm\pi^+\pi^-$ and $K^\pm \to \pi^\pm\pi^0\pi^0$ decays;

DIMUON: the full NA48/2 data sample filtered by requiring the conditions [49]:

- at least one three-track vertex;

- at least three tracks with momentum above $3\,\mathrm{GeV}/c$;

- at least two reconstructed muons (Sec. 3.5.2).

D100: the full NA48/2 data sample downscaled by a factor $D = 100$, obtained by selecting the data events with timestamp ending in "00";

MB2004: an additional data sample, collected at the end of 2004 with minimum bias trigger (Q_1 condition (Sec. 2.4) downscaled by a factor 100).

The search for $K^\pm \to \pi^\mp \mu^\pm \mu^\pm$ decays has been performed using the DIMUON data sample, since the event selection requirements (Sec. 3.3) always satisfy the filtering conditions.

The integrated kaon flux (Sec. 3.4) has been evaluated using the D100 data sample. The choice of using a downscaled data sample does not affect the precision of the flux measurement, limited by the error on the $K^\pm \to \pi^\pm \pi^+ \pi^-$ branching fraction, and is aimed to reduce the data volume, given the large amount of $K^\pm \to \pi^\pm \pi^+ \pi^-$ events available in the NA48/2 data [44].

The muon identification efficiency (Sec. 3.5) has been monitored in the FULL data sample on a burst-by-burst basis, by reconstructing $K^\pm \to \mu^\pm \nu$ decays collected with the L1C trigger condition (Sec. 2.8) downscaled by 100. Bursts with a low value of the measured efficiency have been identified and removed from all the data samples. However, the momentum-dependence of the muon identification efficiency has been studied on the MB2004 data sample, because the trigger condition available in the FULL samples accepts a higher level of $K^\pm \to \pi^\pm \pi^0$ contamination, which affects the $K^\pm \to \mu^\pm \nu$ selection for high track momenta ($p > 40\,\text{GeV}/c$).

3.2.2 $K^\pm \to \pi^\mp \mu^\pm \mu^\pm$ MC models

Dedicated MC simulations of the $K^\pm \to \pi^\mp \mu^\pm \mu^\pm$ signal have been produced with the official NA48/2 software [50], based on the Geant3 package [51], which reproduces

- the beam line optics;

52

- the detector geometry and material;

- the main physical processes of interaction with matter, as well as secondary decays.

The output of the simulation has the same format of the NA48/2 data (COm-PACT [52]), therefore the same analysis framework is used for both data and MC.

Three models have been considered for the MC simulation of the $K^\pm \to \pi^\mp \mu^\pm \mu^\pm$ decay and are described below.

Resonance with $m_{N_4} = 300\,\mathrm{MeV/c^2}$ and $\Gamma_{N_4} = 1\,\mathrm{MeV}$: the first model describes $K^\pm \to \pi^\mp \mu^\pm \mu^\pm$ decays occurring via resonant Majorana neutrinos N_4 (Sec. 1.1.2.3), i.e. $K^\pm \to \mu^\pm N_4$ decays followed by $N_4 \to \pi^\mp \mu^\pm$ decays. The mass $m_{N_4} = 300\,\mathrm{MeV/c^2}$ and the decay width $\Gamma_{N_4} = 1\,\mathrm{MeV}$ of the Majorana neutrino N_4 have been considered, corresponding to $\tau \simeq 6.6 \times 10^{-10}\,\mathrm{ps}$. The matrix element $\mathcal{A}_{\pi\mu\mu}$ implemented in the generator has the form

$$|\mathcal{A}_{\pi\mu\mu}|^2 \propto \frac{m_{N_4}}{(q^2 - m_{N_4}^2)^2 - \Gamma_{N_4}^2 m_{N_4}^2} f(p_K, p_\pi, p_{\mu_1} p_{\mu_2}, m_{N_4}, \Gamma_{N_4}), \qquad (3.2)$$

where p_K, p_π, p_{μ_1} and p_{μ_2} are the kaon, pion and muons 4-momenta, $q \overset{def}{=} p_K - p_{\mu_1}$ and the function $f(p_K, p_\pi, p_{\mu_1} p_{\mu_2}, m_{N_4}, \Gamma_{N_4})$ is taken from Ref. [4]. The evaluation of the $K^\pm \to \pi^\mp \mu^\pm \mu^\pm$ acceptance as a function of m_{N_4} and Γ_{N_4} is foreseen as a future development of the presented analysis.

In addition, in order to evaluate how sensitive the acceptance is to various models, two simple matrix elements have been considered:

Phase Space: $|\mathcal{A}_{\pi\mu\mu}|^2 = 1$.

$\pi\mu^+\mu^-$-like: $|\mathcal{A}_{\pi\mu\mu}|^2$ based on the matrix element of the $K^\pm \to \pi^\pm \mu^+ \mu^-$ decay [16]:

$$|\mathcal{A}_{\pi\mu\mu}|^2 \propto 4\left[(x - r_\mu^2)(1 - z - x + r_\mu^2) + r_\pi^2(r_\mu^2 + x - 1)\right]|W(z)|^2, \qquad (3.3)$$

where $z = m_{\mu\mu}/m_K$, $x = m_{\pi\mu}/m_K$, $r_\mu = m_\mu/m_K$, $r_\pi = m_\pi/m_K$ and $W(z) = G_F m_K^2 f_0(1 + \delta z)$ is the form factor in the linear expansion. In the model considered, $f_0 = 1$ and $\delta = 0$.

In the following, for historical reasons, the latter two models will be referred to as "scalar" and "vector" models respectively.

For each of the three MC models, 10M events have been produced, covering the full NA48/2 data sample and taking into account the different integrated kaon flux of each run and the appropriate beam conditions, as recorded on the NA48/2 database.

3.3 $K^\pm \to \pi^\mp \mu^\pm \mu^\pm$ event selection

The $K^\pm \to \pi^\mp \mu^\pm \mu^\pm$ decay is characterised by two reconstructed muons of the same sign and one reconstructed pion of opposite sign, originating from the same three-track vertex.

A baseline event selection, based on the previous NA48/2 $K^\pm \to \pi^\pm \mu^+ \mu^-$ analysis [16], was implemented and is described in Sec. 3.3.1. The final event selection, after optimising the particle identification criteria and further rejecting the $K^\pm \to \pi^\pm \pi^+ \pi^-$ background, is described in Sec. 3.3.2.

3.3.1 Baseline selection

The considered requirements can be divided in three groups:

1. three-track vertex and reconstructed momenta requirements;

2. particle identification requirements;

3. $m_{\pi\mu\mu}$ mass cut and definition of the signal region.

Each group will be discussed in detail in the following sections.

3.3.1.1 Three-track vertex and reconstructed momenta

Three-track vertices are reconstructed, for those events having more than 2 and less than 10 reconstructed tracks, by extrapolating the track trajectories to the decay volume. A Kalman filter fit [53] is used to take into account the effects of stray fields due to the magnetisation of the vacuum tank and multiple scattering. No vertex is returned if the fit procedure does not converge or if the three-track vertex χ^2, defined as the sum of the three reduced χ^2 from each track fit, is greater than 100.

Each event is required to have at least one vertex formed of three tracks satisfying the following conditions:

- the total charge of the tracks must be $Q = \pm 1$;

- all the vertex tracks must have a momentum p within $3\,\mathrm{GeV}/c$ and $60\,\mathrm{GeV}/c$;

- the z-coordinate of the vertex must be within $-20\,\mathrm{m}$ and $90\,\mathrm{m}$;

- the total reconstructed momentum $\vec{p}_{3trk}$, defined as the sum of the three track momenta, must be within the nominal beam momentum range: $54\,\mathrm{GeV}/c < |\vec{p}_{3trk}| < 66\,\mathrm{GeV}/c$;

- the total reconstructed transverse momentum $\vec{p}_{\perp 3trk}$, defined as the $\vec{p}_{3trk}$ component orthogonal to the kaon direction (assumed to be along the z axis), must be consistent with zero: $|\vec{p}_{\perp 3trk}| < 22\,\mathrm{MeV}/c$.

If more than one three-track vertex satisfies the described requirements, the one with the smallest χ^2 is considered. The reconstructed three-track vertex is required to have a χ^2 smaller than 40 and to be within the fiducial decay region ($-18\,\mathrm{m} < z < 80\,\mathrm{m}$), defined by the start of the vacuum tank ($z = -18\,\mathrm{m}$) and by the geometric acceptance of the first DCH, placed at $z_{\mathrm{DCH1}} = 97\,\mathrm{m}$.

The trajectories of the vertex tracks are required to be within the DCH, LKr and MUV geometrical acceptances. Furthermore, each track must be away from any

other vertex track by at least $2\,\mathrm{cm}$ at the DCH1 plane, to reject e^+e^- pairs from photon conversions, and by at least $20\,\mathrm{cm}$ at the LKr, the MUV1 and MUV2 planes, to reduce the wrong particle identification assignment to the tracks. In addition, the vertex tracks are required to have a minimum momentum of $10\,\mathrm{GeV}/c$ (and consequently a maximum of $46\,\mathrm{GeV}/c$), to ensure high MUV efficiency (see Sec. 3.5).

Extra tracks not belonging to the three-track vertex are allowed, in order to decrease the sensitivity to accidental activity, and are ignored for the rest of the event selection.

3.3.1.2 Particle identification

The muon and pion identification is mostly based on the MUV system: the muon reconstruction algorithm will be described in detail in Sec. 3.5, together with the measurement of the related identification efficiency.

A further constraint is given by the track energy deposition in the LKr: the ratio E/p of the energy E of the cluster associated to a track[1] to its momentum p is sensitive to the particle type, and can be used to reduce the particle mis-identification. For example, electron interactions will produce bremsstrahlung radiation and the subsequent electromagnetic shower will be almost entirely absorbed by the calorimeter, leading to a ratio $E/p \approx 1$. Muons, due to their higher mass, behave as Minimum Ionising Particles (MIPs) and release a small fraction of energy via atomic excitation and ionisation processes, while pions can also lose energy via strong interaction processes. Therefore, a pion has a higher probability than a muon of the same momentum p of releasing energy in the LKr, i.e. of having a greater E/p ratio. Fig. 3.1 shows the E/p distribution for electrons, muons and pions, as measured from the data. A detailed description of the applied selection is reported in Appendix A.

Muon identification The two tracks with same sign are the μ-candidates. Those tracks are required to satisfy the conditions listed below.

---

[1] A cluster is associated to a track if its reconstructed position is within 5 cm from the track impact point at the LKr front plane and if it is the closest cluster to the track.
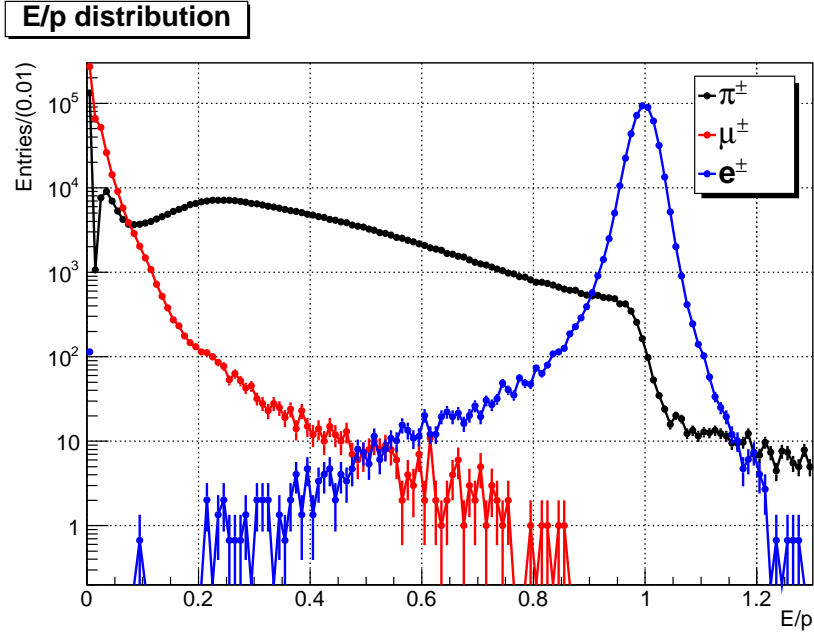
Figure 3.1: E/p distribution for electrons, muons and pions, as obtained from data. Details on the applied selections are reported in Appendix A.

- Be associated to at least one hit in the MUV1 and at least one in the MUV2, both consistent with the time and the expected impact point of the track, taking into account the deflection due to multiple scattering and the spectrometer spatial resolution (see Sec. 3.5).

- The ratio E/p between the energy E of the cluster associated to the track and the track momentum p must be smaller than 0.2.

Pion identification   The track with the opposite sign is the pion candidate. This track must satisfy the conditions listed below.

- The track must not be associated to any pair of hits which are from different MUV planes and both consistent with the time and the expected impact point of the track, taking into account the possible deflection due to multiple scattering and the spectrometer spatial resolution.

- The ratio E/p between the energy E of the cluster associated to the track and its momentum p must be smaller than 0.95, in order to reject electrons.

57

The probability of satisfying the requirements $E/p < 0.2$ and $E/p < 0.95$ has been measured for $e^\pm$, $\mu^\pm$ and $\pi^\pm$ in the momentum range $[5, 50]\,\mathrm{GeV}/c$ and is reported in Tab. 3.1.

Table 3.1: Probability of satisfying $E/p < 0.2$ and $E/p < 0.95$ for $e^\pm$, $\mu^\pm$ and $\pi^\pm$ in the momentum range $[5, 50]\,\mathrm{GeV}/c$, as obtained from data. The quoted limit for $P_\mu(E/p < 0.95)$ is at 95% CL.

Criterion	$P(E/p < 0.2)$	$P(E/p < 0.95)$
$e^\pm$	$(0.025 \pm 0.002)\%$	$(2.82 \pm 0.02)\%$
$\mu^\pm$	$(99.74 \pm 0.01)\%$	$> 99.9993\%$
$\pi^\pm$	$(49.62 \pm 0.04)\%$	$(99.55 \pm 0.01)\%$

3.3.1.3 $m_{\pi\mu\mu}$ mass cut and definition of the signal region

The kinematics of the selected events is analysed by using the reconstructed invariant mass variable $m_{\pi\mu\mu}$, defined as

$$m^2_{\pi\mu\mu} \stackrel{def}{=} (P_\pi + P_{\mu_1} + P_{\mu_2})^2 \tag{3.4}$$
$$= m^2_\pi + 2m^2_\mu + 2\left(\sum_{i=1}^{2}(E_\pi E_{\mu_i} - \vec{p}_\pi \cdot \vec{p}_{\mu_i}) + E_{\mu_1} E_{\mu_2} - \vec{p}_{\mu_1} \cdot \vec{p}_{\mu_2}\right),$$

which results in a peak at $m^2_{\pi\mu\mu} = m^2_K$ for the $K^\pm \to \pi^\mp \mu^\pm \mu^\pm$ decay. The variables m_π, E_π, $\vec{p}_\pi$ and P_π represent mass, energy, 3-momentum and 4-momentum of the pion, while m_μ, E_{μ_i}, $\vec{p}_{\mu_i}$ and P_{μ_i} ($i = 1, 2$) indicate mass, energy, 3-momentum and 4-momentum of the two identical muons respectively. The resolution on the reconstructed mass $m_{\pi\mu\mu}$ is $\sigma_m \approx 2.5\,\mathrm{MeV}/c^2$, in agreement with the NA48/2 $K^\pm \to \pi^\pm \mu^+ \mu^-$ data [16]. A Signal Region (SR) has been defined as the mass region

$$|m_{\pi\mu\mu} - m_K| \leq 8\,\mathrm{MeV}/c^2. \tag{3.5}$$

With the described selection, the estimated $K^{\pm} \to \pi^{\mp}\mu^{\pm}\mu^{\pm}$ acceptances $\varepsilon_{\pi\mu\mu}^{(r)}$, $\varepsilon_{\pi\mu\mu}^{(s)}$ and $\varepsilon_{\pi\mu\mu}^{(v)}$, respectively for the resonant neutrino, scalar and vector models, are

$$\varepsilon_{\pi\mu\mu}^{(r)} = (13.28 \pm 0.01)\%, \tag{3.6}$$

$$\varepsilon_{\pi\mu\mu}^{(s)} = (14.73 \pm 0.01)\%, \tag{3.7}$$

$$\varepsilon_{\pi\mu\mu}^{(v)} = (17.25 \pm 0.01)\%. \tag{3.8}$$

The uncertainties quoted in eqs. 3.6-3.8 are statistical, due to the limited size (10^7 events) of the considered signal samples.

This selection is substantially similar to the one described in Ref. [16]. Applying minimal changes to account for the different signs of the pion-candidate and of one of the muon-candidates, 3109 $K^{\pm} \to \pi^{\pm}\mu^{+}\mu^{-}$ candidates are selected from the DIMUON data sample, which are only 11 candidates ($\simeq 0.4\%$ relative) less than the 3120 quoted in Ref. [16].

3.3.2 Final $K^{\pm} \to \pi^{\mp}\mu^{\pm}\mu^{\pm}$ event selection

After studying the muon reconstruction (Sec. 3.5) and the background sources (Sec. 3.6) in detail, modifications to the baseline selection (Sec. 3.3.1) have been identified. The changes are summarised and discussed below.

3.3.2.1 Three-track vertex and reconstructed momenta

In order to strengthen the three-track vertex reconstruction, all the three possible two-track vertices formed by the three tracks have been reconstructed as well[2]. The CDA of each two-track vertex, defined as the minimum distance between the two extrapolated track trajectories, and the distances d^{2trk} between pairs of reconstructed two-track vertices have been evaluated. The maximum CDA of the three two-track vertices is required to be smaller than $3\,\mathrm{cm}$, and the maximum distance d_{max}^{2trk} between

---

[2]For each pair of tracks, a modified version ($n_{trk} = 2$) of the Kalman filter fit procedure employed for the three-track vertex computation has been used.

two-track vertices must be smaller than $5\,\mathrm{m}$. Furthermore, the χ^2 of the three-track vertex is required to be smaller than 20 (instead of 40). As it will be discussed in Sec. 3.6, these further requirements on the vertex contribute to reject significantly the $K^\pm \to \pi^\pm \pi^+ \pi^-$ background, while decreasing the $K^\pm \to \pi^\mp \mu^\pm \mu^\pm$ acceptance of $\sim 1.5\%$ (absolute) or $\sim 7\%$ (relative).

The momentum requirements have been tightened: the total momentum $|\vec{p}_{3trk}|$ must be in the range [55,65] GeV/c, and the total transverse momentum $|\vec{p}_{\perp 3trk}|$ is required to be smaller than $10\,\mathrm{MeV}/c$. The chosen values are the result of a compromise between reducing the $K^\pm \to \pi^\pm \pi^+ \pi^-$ background and not losing too much signal acceptance. The loss of signal acceptance is of $\sim 2.5\%$ (absolute) or $\sim 10\%$ (relative).

The track momenta requirements have been refined by distinguishing between pion and muon candidates: the muon identification efficiency (Sec. 3.5.3) should be as high as possible for the pion-candidate, in order to veto mis-reconstructed $K^\pm \to \pi^\pm \pi^+ \pi^-$ events (Sec. 3.6). This results in requiring a pion-candidate momentum p_π greater than $15\,\mathrm{GeV}/c$. On the other hand, since the muon-candidates are positively identified by the MUV system, the requirement on the muon identification efficiency can be relaxed, leading to a looser momentum requirement $p_\mu > 5\,\mathrm{GeV}/c$. While the pion-candidate momentum requirement decreases the acceptance of about 1.8% (absolute) or 17% (relative), the looser condition on the muon-candidate momenta leads to an increase of $\sim 6\%$ (absolute) or $\sim 42\%$ (relative), for an overall increase of $\sim 2\%$ (absolute) or $\sim 10\%$ (relative).

3.3.2.2 Particle identification

Muon identification has been extensively studied and will be discussed in Sec. 3.5. In particular, muon reconstruction has been optimised for a di-muon search, and the pion-identification requirements have been modified, in order to reduce the interference of non-related muon activities (Sec. 3.5.4). The MUV geometrical acceptance has been also changed, after a MUV misalignment of $\sim 2\,\mathrm{cm}$ was observed (Appendix B), in order to be consistent with the real position of MUV planes.

Muon identification Additional requirements have been applied in order to reduce the contribution of $K^\pm \to \pi^\pm \pi^+ \pi^-$ events with less than two pion decays (Sec. 3.6):

- non-zero distance between the two reconstructed muons, which reduces the signal acceptance of 0.4% (absolute) or 2% (relative);

- muon-candidates tracks within a maximum distance of 35 cm from the associated reconstructed muons, decreasing the signal acceptance of 0.3% (absolute) or 1.5% (relative).

Pion identification The pion identification requirements have been relaxed: all the pairs of hits which are not formed of one signal from MUV1 and one from MUV2 (i.e. pairs with at least one signal from the MUV3) are now allowed to be associated to the pion-candidate track. Pairs formed of one signal from MUV1 and one from MUV2 may be associated to the pion-candidate track only if either of the hits is not consistent with the time and the expected impact point of the track, as for the baseline selection.

With this choice, explained in detail in Sec. 3.5, the signal acceptance increases of about 7% (absolute) or 45% (relative). In fact, the interference of the MUV activities associated to the muon-candidate tracks, which prevents from a correct pion identification, is dominated by the MUV3 contribution because of the larger size of its strips (Sec. 2.7).

3.3.2.3 $m_{\pi\mu\mu}$ mass cut and definition of the signal region

Due to the presence of the $K^\pm \to \pi^\pm \pi^+ \pi^-$ background, a smaller SR is proposed:

$$|m_{\pi\mu\mu} - m_K| \leq 5 \,\mathrm{MeV}/c^2, \tag{3.9}$$

where the limits correspond to a distance of $2\sigma_m$ from the kaon mass m_K.

The estimated $K^\pm \to \pi^\mp \mu^\pm \mu^\pm$ acceptances $\varepsilon_{\pi\mu\mu}^{(r)}$, $\varepsilon_{\pi\mu\mu}^{(s)}$ and $\varepsilon_{\pi\mu\mu}^{(v)}$ obtained with the

61

final selection are

$$\varepsilon_{\pi\mu\mu}^{(r)} \;=\; (19.44 \pm 0.01)\%, \tag{3.10}$$

$$\varepsilon_{\pi\mu\mu}^{(s)} \;=\; (20.62 \pm 0.01)\%, \tag{3.11}$$

$$\varepsilon_{\pi\mu\mu}^{(v)} \;=\; (22.75 \pm 0.01)\%. \tag{3.12}$$

The uncertainty quoted in eqs. 3.10–3.12 is statistical, due to the limited size (10^7 events) of the considered signal samples. The signal acceptances have been increased by $\sim 6\%$ (absolute) or $\sim 40\%$ (relative). This increase is mostly due to the different pion identification criteria adopted (Sec. 3.5.4.2) and to the optimised track momentum requirements.

Furthermore, as it will be shown in Sec. 3.6, the background rejection has been improved by a factor ~ 50. The main selections responsible of such an improvement are the requirements on $|\vec{p}_{\perp 3trk}|$, p_π and on the reconstructed vertex.

3.4 Measurement of the integrated kaon flux

In order to minimise the systematic uncertainties due to the differences between $K^\pm \to \pi^\pm\pi^+\pi^-$ and $K^\pm \to \pi^\mp\mu^\pm\mu^\pm$ selections, the $K^\pm \to \pi^\pm\pi^+\pi^-$ sample has been selected applying the same requirements described in Sec. 3.3.2, with two unavoidable changes:

- no particle identification for the two tracks with same sign;

- requirement on the $m_{\pi\mu\mu}$ variable replaced by one on $m_{\pi\pi\pi}$, defined as

$$m_{\pi\pi\pi}^2 \overset{def}{=} \left(P_{\pi_1} + P_{\pi_2} + P_{\pi_3} \right)^2 \tag{3.13}$$

$$= 3m_\pi^2 + \sum_{i \neq j} (E_{\pi_i} E_{\pi_j} - \vec{p}_{\pi_i} \cdot \vec{p}_{\pi_j}), \tag{3.14}$$

which results in a peak at $m_{\pi\pi\pi}^2 = m_K^2$ for the $K^\pm \to \pi^\pm\pi^+\pi^-$ decay.

Fig. 3.2 shows the $m_{\pi\pi\pi}$ distribution for the selected $K^\pm \to \pi^\pm\pi^+\pi^-$ decays from the D100 data sample (Sec. 3.2.1), compared with the MC simulation. The resolution on the reconstructed mass $m_{\pi\pi\pi}$ is $\sigma_m \approx 1.7 \, \text{MeV}/c^2$, consistent with previous NA48/2 results [44]. The events within $3\sigma_m$ from the kaon mass m_K have been

(a)   (b)
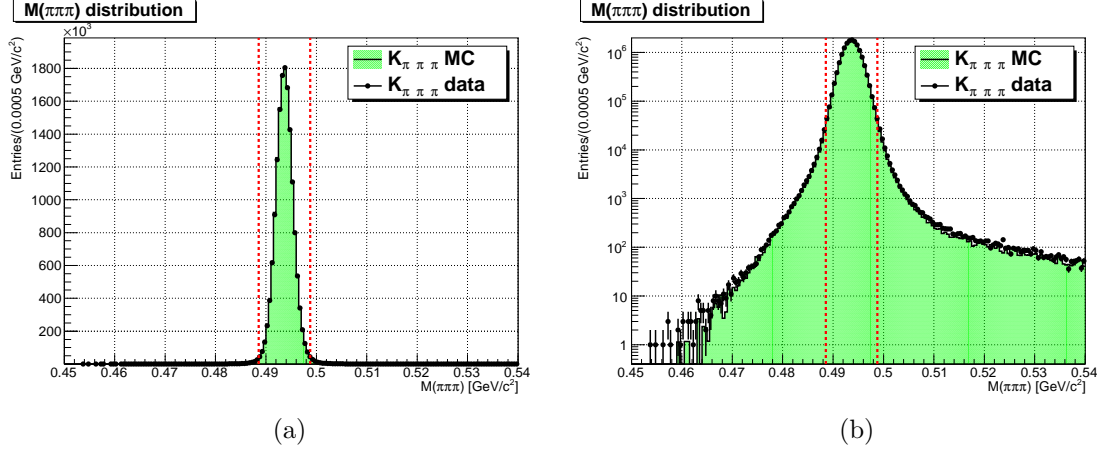
Figure 3.2: Reconstructed invariant mass $m_{\pi\pi\pi}$ distribution for the selected $K^\pm \to \pi^\pm\pi^+\pi^-$ decays, compared with the MC simulation: (a) linear scale, (b) logarithmic scale. The boundaries of the signal region are shown by the dashed lines.

selected as $K^\pm \to \pi^\pm\pi^+\pi^-$ candidates. With the described selection, the estimated $K^\pm \to \pi^\pm\pi^+\pi^-$ acceptance $\varepsilon_{\pi\pi\pi}$ is

$$\varepsilon_{\pi\pi\pi} = (14.721 \pm 0.004)\%. \tag{3.15}$$

The numbers $N_{\pi\pi\pi}^{tot}$ and $N_{\pi\pi\pi}$ of reconstructed $K^\pm \to \pi^\pm\pi^+\pi^-$ events in the D100 data sample before and after inefficient bursts have been removed (Sec. 3.5.3) are

$$N_{\pi\pi\pi}^{tot} = 1.57 \times 10^7, \quad N_{\pi\pi\pi} = 1.51 \times 10^7. \tag{3.16}$$

Taking into account the downscaling factor $D = 100$, the $K^\pm \to \pi^\pm\pi^+\pi^-$ acceptance $\varepsilon_{\pi\pi\pi}$ and the $\mathcal{B}(K^\pm \to \pi^\pm\pi^+\pi^-)$ [1], the estimated "effective"[3] numbers N_K^{tot} and N_K of kaon decays in the fiducial volume for the data sample considered,

---

[3]The estimated values of N_K^{tot} and N_K are inclusive of the $K^\pm \to \pi^\pm\pi^+\pi^-$ trigger inefficiency: as discussed in Sec. 3.1, due to the similarity of pion and muon masses, trigger inefficiency is assumed to be the same for both $K^\pm \to \pi^\pm\pi^+\pi^-$ and $K^\pm \to \pi^\mp\mu^\pm\mu^\pm$ decays.

respectively before and after inefficient bursts have been removed, are

$$N_K^{tot} = \frac{N_{\pi\pi\pi}^{tot}}{\mathcal{B}(K^\pm \to \pi^\pm\pi^+\pi^-)\varepsilon_{\pi\pi\pi}}\frac{1}{D} = (1.901 \pm 0.014) \times 10^{11}, \qquad (3.17)$$

$$N_K = \frac{N_{\pi\pi\pi}}{\mathcal{B}(K^\pm \to \pi^\pm\pi^+\pi^-)\varepsilon_{\pi\pi\pi}}\frac{1}{D} = (1.832 \pm 0.014) \times 10^{11}. \qquad (3.18)$$

The $K^\pm \to \pi^\pm\pi^+\pi^-$ branching fraction [1] is taken as external parameter and its limited precision accounts for 99.8% of the quoted uncertainties.

The number N_K^{tot} of kaon decays in the fiducial volume for the whole NA48/2 data sample has been compared to previous NA48/2 results as a cross-check and is consistent with the value of 1.9×10^{11} obtained from previous analyses [16, 44].

The reduction in the data volume caused by the removal of the bursts affected by high MUV inefficiency is about 4%.

3.5 Muon identification study

The muon identification efficiency of the MUV system has been studied by selecting a $K^\pm \to \mu^\pm\nu$ decay sample, using kinematic constraints only, and measuring the number of inefficient events after applying the particle identification requirements.

In addition, the muon reconstruction and the identification requirements have been optimised for a di-muon analysis, as reported in Sec. 3.5.4.

3.5.1 $K^\pm \to \mu^\pm\nu$ event selection

The $K^\pm \to \mu^\pm\nu$ sample has been selected by requiring every event to have exactly one track geometrically consistent with being produced by a kaon decay. Such consistency has been checked for each track, requiring the decay vertex, defined as the point of closest approach of the track and the kaon beam, to be within the fiducial decay region ($-18\,\mathrm{m} < z < 80\,\mathrm{m}$) and the CDA to be smaller than 3.5 cm. The kaon beam has been assumed to be centred on the z-axis and the track trajectory has been

extrapolated to the decay volume, taking into account the effects of Earth's magnetic field and of the stray fields due to the magnetisation of the vacuum tank. Extra tracks with momentum smaller than $3\,\mathrm{GeV}/c$ or greater than $60\,\mathrm{GeV}/c$, with z-vertex coordinate outside the region $(-20\,\mathrm{m}, 90\,\mathrm{m})$ or with CDA greater than $10\,\mathrm{cm}$, are allowed and are ignored for the rest of the event selection. The extrapolated track trajectory must be within the geometrical acceptances of the DCHs, LKr and MUV detectors, taking in account the detectors edges and the LKr dead cells. No LKr clusters with energy greater than 2 GeV and within 12 ns from the track time are allowed, unless they are consistent with being due to the track energy deposition. Finally, the kinematics of the selected events are analysed by using the squared missing mass variable $m_{miss}^{2\,(\mu)}$, defined as the square of the difference between the nominal kaon 4-momentum P_K and the track 4-momentum P_μ, assuming the μ mass:

$$
\begin{aligned}
m_{miss}^{2\,(\mu)} &\overset{def}{=} (P_K - P_\mu)^2 \\
&= m_K^2 + m_\mu^2 - 2E_K E_\mu + 2|\vec{p}_K||\vec{p}_\mu|\cos\theta_{\mu K}.
\end{aligned}
\tag{3.19}
$$

Here $\vec{p}_K = (0, 0, 60\,\mathrm{GeV}/c)$, $\vec{p}_\mu$ is the track momentum, $E_K = \sqrt{|\vec{p}_K|^2 + m_K^2}$, $E_\mu = \sqrt{|\vec{p}_\mu|^2 + m_\mu^2}$ and $\theta_{\mu K}$ is the angle between $\vec{p}_K$ and $\vec{p}_\mu$. Fig. 3.3 shows the $m_{miss}^{2\,(\mu)}$ distribution of the $K^\pm \to \mu^\pm \nu$ candidates selected using the MB2004 data sample. The $K^\pm \to \mu^\pm \nu$ background is dominated by the muon halo, which does not affect the purity of the muon sample. The enhancement at $m_{miss}^{2\,(\mu)} \sim 0.025\,\mathrm{GeV^2/c^4}$ is caused by $K^\pm \to \pi^\pm \pi^0$ decays with an undetected π^0, which are rejected with a cut on the $m_{miss}^{2\,(\mu)}$ variable: the events with $|m_{miss}^{2\,(\mu)}| < 0.01\,\mathrm{GeV^2/c^4}$ fulfilling all the requirements listed above have been selected, corresponding to a total of 22.7×10^6 and 6.7×10^6 for the FULL and the MB2004 data samples respectively.

3.5.2 Muon reconstruction

The reconstruction of a muon track is performed offline by the NA48/2 COmPACT software, processing the information of the MUV channel response.

The algorithm is track-based: the trajectory of each track reconstructed by the
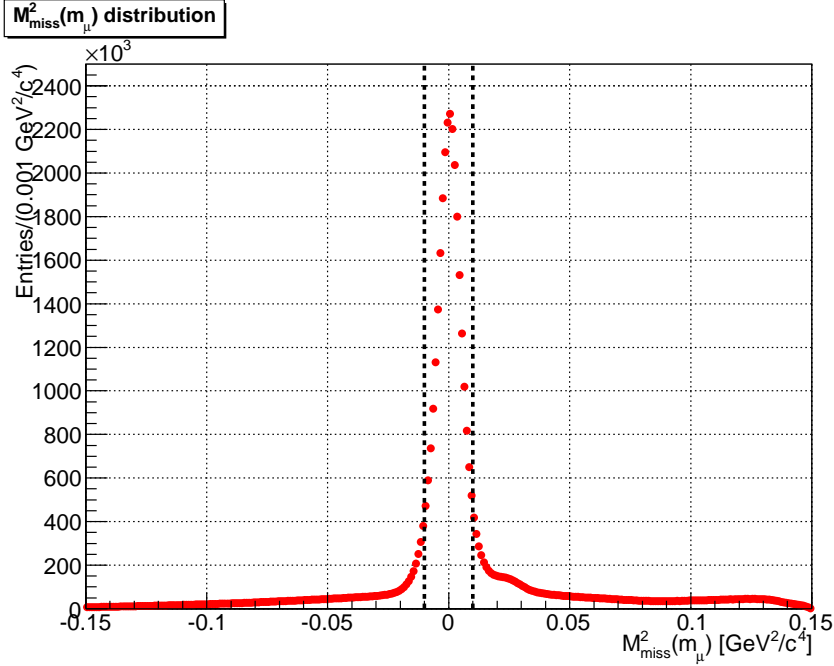
Figure 3.3: $m_{miss}^{2\,(\mu)}$ distribution for the $K^{\pm} \to \mu^{\pm}\nu$ candidates selected using the MB2004 data sample. The requirement $m_{miss}^{2\,(\mu)} < 0.01\,\mathrm{GeV}^2/c^4$ is shown by the dashed lines. The $K^{\pm} \to \mu^{\pm}\nu$ background is dominated by the muon halo, which does not affect the purity of the muon sample. The enhancement at $m_{miss}^{2\,(\mu)} \sim 0.025\,\mathrm{GeV}^2/c^4$ is caused by $K^{\pm} \to \pi^{\pm}\pi^0$ decays with an undetected π^0.

magnetic spectrometer is extrapolated to the MUV1, MUV2 and MUV3 planes and only the channels located within a momentum-dependent search radius from the expected track impact point are considered. The choice of the search radius will be discussed in detail in Sec. 3.5.4, together with the performed di-muon reconstruction optimisation.

If a hit from one of the selected channels is within 10 ns from the track time after considering the time of light propagation along the strip, the hit is associated to the track. Each hit can be shared by multiple tracks. If a track is associated to at least 2 hits from different MUV stations, a muon is reconstructed and associated to a track. To distinguish different combination of MUV planes, a status is associated to each reconstructed muon. The definition of each status is reported in Tab. 3.2.

As described in Sec. 2.7, the MUV1 and MUV3 strips are oriented horizontally, the

Table 3.2: Muon status definition depending on the combination of the MUV planes. The requirement on the MUV hits associated to the μ-candidates in both baseline (Sec. 3.3.1) and final (Sec. 3.3.2) selections corresponds to requiring the μ-candidate status to be either 1 or 2.

Muon status	MUV1	MUV2	MUV3
1	✓	✓	✓
2	✓	✓	
3		✓	✓
4	✓		✓

MUV2 ones vertically. The x and y coordinates of the reconstructed muons are determined averaging the x and the y coordinates of the strip centres of all the associated channel hits from the MUV2 and from the MUV1 planes respectively. If the status is equal to 3, i.e. no MUV1 hits are found, the MUV3 strips are used to reconstruct the y coordinate. If the status is equal to 4, i.e. no MUV2 hits are found, the x coordinate is taken from the extrapolated track hit point, since neither the MUV1 or the MUV3 can resolve the horizontal ambiguity.

The time of the reconstructed muons is evaluated averaging all the associated hit times from the MUV1 and the MUV2 planes. The MUV3 hits are included in the average only in case of missing hits in MUV1 or MUV2 (i.e. status equal to 3 or 4).

3.5.3 Muon identification efficiency

As discussed in Sec. 3.2.1, two different data samples have been used for the measurement of muon identification efficiency. The selected $K^{\pm} \to \mu^{\pm}\nu$ events from the FULL data sample have been studied in order to monitor the stability of the muon identification efficiency in 2003 and 2004, while the momentum-dependence of the muon identification efficiency has been studied on the MB2004 sample, because the trigger condition available in the FULL samples accepts a higher level of $K^{\pm} \to \pi^{\pm}\pi^0$ contamination, which affects the applied $K^{\pm} \to \mu^{\pm}\nu$ selection for high track momenta ($p > 40\,\mathrm{GeV}/c$).

Several muon identification criteria have been considered:

1. requiring the ratio E/p between the energy E of the LKr cluster associated to the track and its momentum p to be smaller than 0.2;

2. requiring the track to be associated to at least one MUV1 hit and at least one MUV2 hit, i.e. to a reconstructed muon with status equal to 1 or 2, within a maximum distance $d_{max}^{\mu} = 35\,\mathrm{cm}$ from the track;

3. both the requirements 1 and 2.

The criterion 3 corresponds to the requirement adopted for the muon identification in the presented analysis (Sec. 3.3.1.2). Fig. 3.4 shows the measured muon identification efficiency of the considered criteria as a function of the run number, obtained from the $K^{\pm} \to \mu^{\pm}\nu$ candidates selected using the FULL data sample (Sec. 3.2.1). It can be seen that there are some runs with lower muon identification efficiency; bursts with a measured identification efficiency according to criterion 3 more than 5σ below 0.98 have been identified and removed. As discussed in Sec. 3.4, this choice leads to a reduction of about 4% in the kaon flux.

Fig. 3.5 shows the measured muon identification efficiency as a function of the track momentum, obtained from the $K^{\pm} \to \mu^{\pm}\nu$ candidates selected using the MB2004 data sample (Sec. 3.2.1). The inefficiency for low momenta is mostly due to the multiple Coulomb scattering of the muons in the material upstream the MUV system, and is simulated to within 10% relative accuracy. In particular, the MC underestimates the efficiency, resulting in an underestimation of the signal acceptance. Momentum-dependent corrections have been applied to the MC, to compensate this effect. The related increase in the $K^{\pm} \to \pi^{\mp}\mu^{\pm}\mu^{\pm}$ acceptance is of about 0.4% (absolute) or 2% (relative). The average muon identification efficiency requiring $p > 5\,\mathrm{GeV}/c$, $p > 10\,\mathrm{GeV}/c$ and $p > 15\,\mathrm{GeV}/c$ has been measured. The results are reported in Tab. 3.3, for the three different criteria considered.
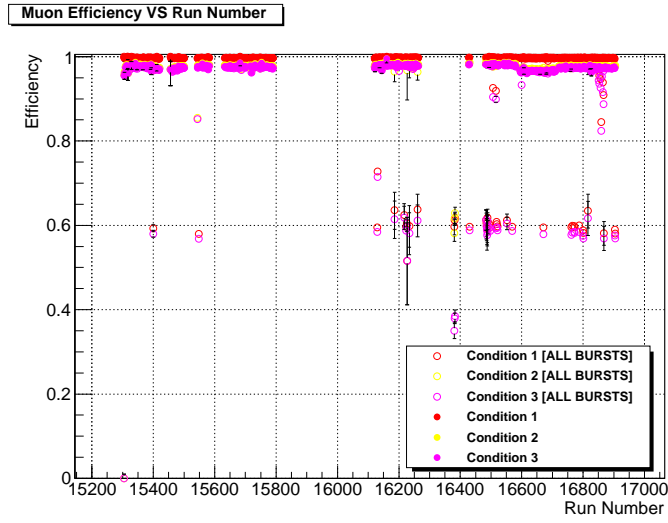
Figure 3.4: Muon identification efficiency of the considered criteria (Sec. 3.5.3) as a function of the Run Number, for the $K^\pm \to \mu^\pm \nu$ candidates selected using the FULL data sample, before (empty circles) and after (full circles) removing the inefficient bursts.
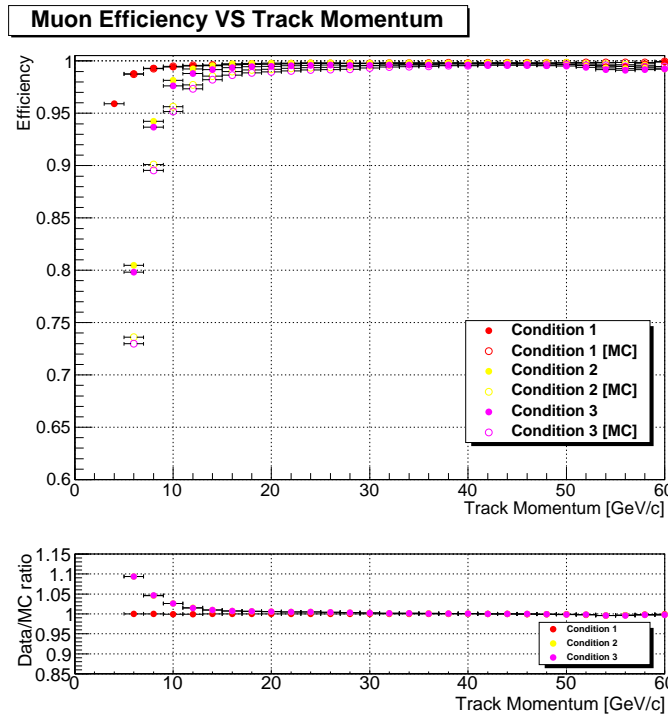
Figure 3.5: Muon identification efficiency of the considered criteria (Sec. 3.5.3) as a function of the Track Momentum for the $K^\pm \to \mu^\pm \nu$ candidates selected using the MB2004 data sample, compared with the MC simulation. The respective data-MC ratio is shown.

69

Table 3.3: Average muon identification efficiency requiring $p > 5\,\mathrm{GeV}/c$, $p > 10\,\mathrm{GeV}/c$ and $p > 15\,\mathrm{GeV}/c$ over the MB2004 data sample, for the different criteria considered. The criterion 3 has been chosen for the presented analysis. The errors are statistical, due to the limited size of the $K^{\pm} \to \mu^{\pm}\nu$ sample (6.7×10^6 events).

Criterion	$\varepsilon(p > 5\,\mathrm{GeV}/c)$	$\varepsilon(p > 10\,\mathrm{GeV}/c)$	$\varepsilon(p > 15\,\mathrm{GeV}/c)$
1	$(99.707 \pm 0.002)\%$	$(99.731 \pm 0.002)\%$	$(99.745 \pm 0.002)\%$
2	$(99.354 \pm 0.003)\%$	$(99.732 \pm 0.002)\%$	$(99.770 \pm 0.002)\%$
3	$(99.110 \pm 0.004)\%$	$(99.502 \pm 0.003)\%$	$(99.554 \pm 0.003)\%$

3.5.4   Di-muon optimisation

To associate a muon to a reconstructed track, the muon reconstruction algorithm implemented in the COmPACT software accepts only the hits from those channels whose strip centres are located within a certain search radius r_{search} from the expected track impact point. The search radius is intended to take into account the effect of the multiple Coulomb scattering of the muon with the material before the MUV planes, while rejecting any other activity (e.g. noise from the electronics or a hit related to another track) not consistent with the considered track. However, the balance between identification inefficiency and interference of non-related activities depends on the particular task the MUV system is required to perform. For example, if the MUV is employed as a veto system, a greater search radius might be preferable in order to achieve lower inefficiencies, despite the higher level of pion mis-tagging. On the other hand, if the MUV system is used to detect di-muon pairs, a smaller search radius might be considered to reduce the pion mis-identification as muon.

Therefore, the search radius r_{search} should be tuned accordingly to the MUV system functionality in the considered analysis. In this section, the search radius is optimised for a di-muon analysis by analysing the produced $K^{\pm} \to \pi^{\mp}\mu^{\pm}\mu^{\pm}$ MC samples, after the muon interference on non-related tracks is assessed.

3.5.4.1 Search radius definition

For each track, the search radius r_{search} is evaluated as

$$r_{search}(p) \overset{def}{=} r_0 + m\psi_0(p)(z_{\text{MUV}} - z_{\text{LKr}}), \qquad (3.20)$$

where

- r_0 is the half strip width: $r_0 = 12.5\,\text{cm}$ for MUV1 and MUV2, $r_0 = 22.5\,\text{cm}$ for MUV3;

- z_{LKr} and z_{MUV} are the z-coordinates of the LKr and MUV front planes: $z_{\text{MUV1}} - z_{\text{LKr}} = 6.70\,\text{m}$, $z_{\text{MUV2}} - z_{\text{LKr}} = 7.95\,\text{m}$, $z_{\text{MUV3}} - z_{\text{LKr}} = 9.04\,\text{m}$;

- $\psi_0(p)$ is the angular deflection (RMS) of the track particle, travelling in x/X_0 radiation lengths of matter[4], from the trajectory it would have followed in vacuum, and is described by the formula [1]

$$\psi_0(p) = \frac{1}{\sqrt{3}} \frac{13.6\,\text{MeV}}{\beta cp} z \sqrt{\frac{x}{X_0}} \left[1 + 0.038 \ln\left(\frac{x}{X_0}\right) \right] \overset{def}{=} \frac{\alpha}{p}, \qquad (3.21)$$

  in which z, p and βc are respectively the charge, the momentum and the velocity of the particle; $\alpha_{\text{MUV1}} = 110.3\,\text{MeV/c}$, $\alpha_{\text{MUV2}} = 128.1\,\text{MeV/c}$, $\alpha_{\text{MUV3}} = 143.9\,\text{MeV/c}$; the multiple Coulomb scattering is described through the small angles approximation;

- m, called *multiplier*, is an empirical proportionality constant, introduced to ensure a MUV identification inefficiency smaller than 10^{-3}. The smallest m satisfying this requirement was determined to be $m = 4$ [54], which was set as default value in the COmPACT muon reconstruction. In the following, the optimal value of m for a di-muon analysis will be evaluated.

---

[4]This evaluation is valid also for different materials, if air gaps between scattering materials are small compared to the lengths of scatterers. Starting from the LKr front plane, the value x/X_0 estimated for the total amount of the material upstream the MUV1, MUV2 and MUV3 planes is 139.8, 185.2 and 230.7 respectively.

In the considered momentum range $5\,\text{GeV}/c < p < 60\,\text{GeV}/c$, for $m = 4$, the search radius spans between 115.1 cm (for $p = 5\,\text{GeV}/c$, at the MUV3 plane) and 13.5 cm (for $p = 60\,\text{GeV}/c$, at the MUV1 plane). The contribution of the uncertainty due to the spectrometer spatial resolution is negligible with respect to the one due to the multiple Coulomb scattering, being at least 50 times smaller.

3.5.4.2 Muon interference on non-related tracks

The interference of muon activities on non-related tracks has been studied by considering the different-sign track, which is the pion-candidate. Figure 3.6 shows the signal acceptance for the final selection as a function of the status of the reconstructed muon associated to the pion-candidate track. If no muons are associated, the status is set to 0.
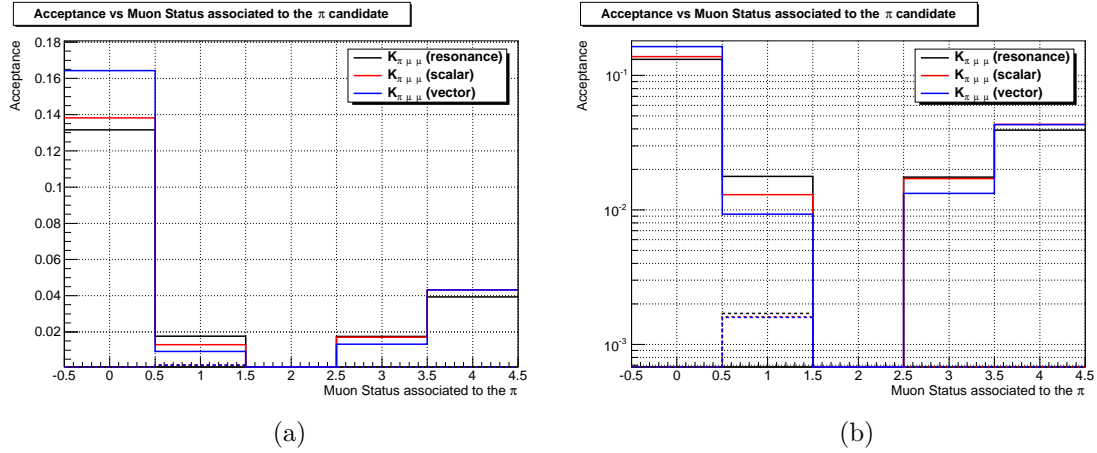
Figure 3.6: $K^{\pm} \rightarrow \pi^{\mp}\mu^{\pm}\mu^{\pm}$ acceptance as a function of the status of the reconstructed muon associated to the pion-candidate track: (a) linear scale, (b) logarithmic scale. If no muons are associated, the status is set to 0. The dashed lines indicate the fraction of events in which the pion decays into a muon.

Pions decaying in flight into muons after the last drift chamber lead to muon activities associated to the pion track. However, this source of irreducible pion mis-identification (dashed lines in Fig. 3.6) accounts for only a 2% of events having a reconstructed muon associated to the pion track. Furthermore, reconstructed muons with status 3 or 4 are unrelated with the track activities. Therefore, they have been

considered as valid status for the pion identification. The final pion identification criterion in Sec. 3.3.2 in terms of muon status associated to the pion track reads as "no reconstructed muons with status equal to 1 or 2 associated to the pion track".

As can be seen from Fig. 3.6, after changing the pion identification criterion the gain in signal acceptance is of 6% (absolute) or 40% (relative). The reason behind the high level of interference involving the MUV3 is due to the larger size of its strips (45 cm against 25 cm, Sec. 2.7). Furthermore, MUV1 and MUV3 strips are both horizontal, therefore the inability of reconstructing a vertical coordinate induces an additional source of interference: for instance, two synchronous tracks whose trajectories are within the same MUV1 and MUV3 strip are associated to a reconstructed muon (with status 4), even if their impact points were 2 m away from each other and only one of them was actually generated by a muon.

3.5.4.3 Multiplier scan

For multi-track analyses where at least a reconstructed muon is required, the activities in the MUV system due to muon tracks may cause other non-muonic tracks with trajectories accidentally within the search radius from the muon hits to be mis-identified as muons. This may result in background enhancement as well as a loss of signal acceptance.

In particular, the $K^\pm \to \pi^\mp \mu^\pm \mu^\pm$ signal acceptance as a function of the multiplier m is expected to have a local maximum: the acceptance should decrease for both $m \to 0$ and $m \to \infty$ (for the latter it approaches zero), due to the decrease in the muon identification efficiency caused by muons scattering outside the search radius and to the increase in the probability of a pion being mis-identified as a muon.

Therefore, in order to find the optimal value of the multiplier m for the $K^\pm \to \pi^\mp \mu^\pm \mu^\pm$ analysis, the $K^\pm \to \pi^\mp \mu^\pm \mu^\pm$ acceptance has been evaluated for different values of m using the MC signal samples. Fig. 3.7 shows the acceptance for final and baseline selections as a function of the multiplier m. The optimal value of the
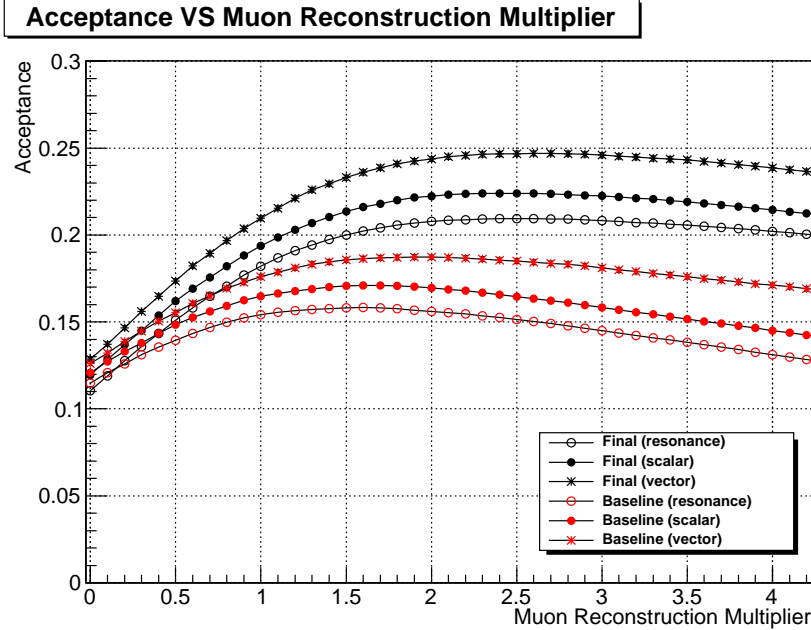
Figure 3.7: $K^{\pm} \to \pi^{\mp}\mu^{\pm}\mu^{\pm}$ acceptance as a function of the multiplier m, obtained from the produced MC samples.

multiplier m obtained from the multiplier scan performed is $m = 2.5$, which will be used in the rest of the analysis. Fig. 3.8 shows the comparison of the search radii for $m = 4$ and $m = 2.5$.

It is worth noting that the different pion identification criterion adopted (Sec. 3.5.4.2) reduces the loss of acceptance for larger search radii. The optimisation of the multiplier value results to an increase in the final signal acceptance of 1% (absolute) or 5% (relative) only, to be compared with the 3% (absolute) or 20% (relative) for the baseline selection.

3.6 Background sources

Due to the particular signature of the $K^{\pm} \to \pi^{\mp}\mu^{\pm}\mu^{\pm}$ decay, only three-track kaon decays with a muon pair in the final state contribute to the background. Tab. 3.4 shows the subset of kaon decays with such characteristics, along with the measured (or expected) branching fractions [1, 55].
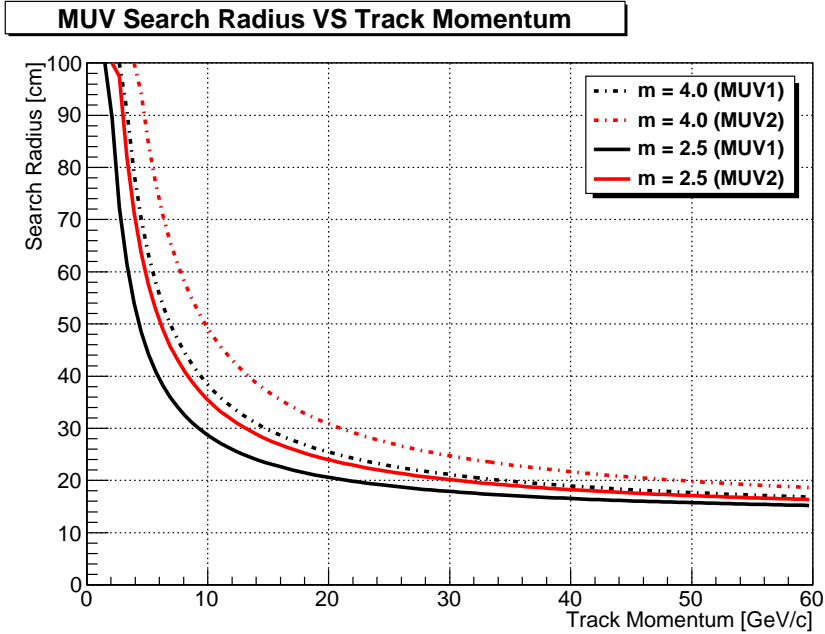
Figure 3.8: Search radius r_{search} as a function of the track momentum p, for $m = 4$ and $m = 2.5$.

Dedicated MC simulations of the decays in Tab. 3.4 have been produced and they have been used for the background estimation. The MC events have been generated in the z-coordinate range $(-22\,\text{m}, 90\,\text{m})$, which is broader than the fiducial volume, defined as $-18\,\text{m} < z < 80\,\text{m}$, in order to avoid border effects. For each background channel $K^{\pm} \to f_i$ considered, the minimum number N_{min}^{MC} of events required to be simulated in order to have the same statistical significance of data has been evaluated as $N_{min}^{\text{MC}} = N_K \mathcal{B}(K^{\pm} \to f_i)/\alpha_{\text{FV}}$, where N_K is the number of kaon decays in the fiducial volume (Sec. 3.4) and $\alpha_{\text{FV}} = 0.8803$ takes into account the 11.97% of events not generated in the fiducial volume.

3.6.1 $K^{\pm} \to \pi^{\pm}\pi^{+}\pi^{-}$ background

3.6.1.1 Simulation

Given the integrated kaon flux for the considered data sample (Sec. 3.4), about 1.06×10^{10} $K^{\pm} \to \pi^{\pm}\pi^{+}\pi^{-}$ decays are expected in the fiducial volume. To reach

Table 3.4: $K^{\pm}$ decay channels presenting three-track and a muon pair in the final state. For the $K^{\pm} \to \mu^+\mu^-\mu^{\pm}\nu$ decay the ChPT expectation branching fraction is reported.

Decay channel		Branching fraction [1]
$K^{\pm} \to \pi^{\pm}\pi^+\pi^-$	$2 \times (\pi^{\pm} \to \mu^{\pm}\nu)$	$(5.59 \pm 0.04) \times 10^{-2}$
$K^{\pm} \to \pi^+\pi^-e^{\pm}\nu$	$2 \times (\pi^{\pm} \to \mu^{\pm}\nu)$	$(4.09 \pm 0.10) \times 10^{-5}$
$K^{\pm} \to \pi^+\pi^-\mu^{\pm}\nu$	$1 \times (\pi^{\pm} \to \mu^{\pm}\nu)$	$(1.4 \ \pm 0.9 \ ) \times 10^{-5}$
$K^{\pm} \to \pi^{\pm}\mu^+\mu^-$		$(9.4 \ \pm 0.6 \ ) \times 10^{-8}$
$K^{\pm} \to \mu^+\mu^-e^{\pm}\nu$		$(1.7 \ \pm 0.5 \ ) \times 10^{-8}$
$K^{\pm} \to \mu^+\mu^-\mu^{\pm}\nu$		1.35×10^{-8} (expected [55])

a $K^{\pm} \to \pi^{\pm}\pi^+\pi^-$ background contribution of $\lesssim \mathcal{O}(1)$ events, a $K^{\pm} \to \pi^{\pm}\pi^+\pi^-$ suppression of $\mathcal{O}(10^{10})$ is required. To tune the event selection and to check the $K^{\pm} \to \pi^{\pm}\pi^+\pi^-$ rejection at that level, a MC production simulating $\mathcal{O}(10^{10})$ events is needed. The full simulation of such amount of events is unfeasible given the computing power it would require: it has been estimated that such simulation, due to the pion shower development in the LKr, would take more than 6×10^6 KSI2K hours of CPU time, corresponding to a time of ~ 4 years, assuming a set of 100 continuously running parallel jobs. LKr shower libraries were developed by the NA48 collaboration and can be enabled, but due to a feature of the software in fast mode, the multiple Coulomb scattering of muons, which plays a crucial role in the muon mis-reconstruction, is not properly simulated. Therefore, an optimised method has been implemented, in order to pre-filter and fully simulate only the events with at least a three-track vertex with reconstructed mass $m_{\pi\mu\mu} > 0.455$ GeV/c^2, $50 \, \text{GeV}/c < |\vec{p}_{3trk}| < 70 \, \text{GeV}/c$ and $|\vec{p}_{\perp 3trk}| < 31.6 \, \text{MeV}/c$. The procedure is described in Appendix C. Using this technique, two $K^{\pm} \to \pi^{\pm}\pi^+\pi^-$ MC samples equivalent to 1.2×10^{10} events each have been produced: one sample has been used exclusively to finalise the $K^{\pm} \to \pi^{\mp}\mu^{\pm}\mu^{\pm}$ event selection, while the other has been employed to estimate the number of expected background events, after the selection was finalised.

The $K^{\pm} \to \pi^{\pm}\pi^+\pi^-$ MC sample dedicated to the finalisation of the $K^{\pm} \to \pi^{\mp}\mu^{\pm}\mu^{\pm}$ event selection has been analysed applying the baseline requirements described in Sec. 3.3.1. Fig. 3.9 shows the obtained $m_{\pi\mu\mu}$ distribution. 49.6 events are observed

in the SR, which is consistent with the value of 52.6 ± 19.8 reported in Ref. [16]. The error quoted in Ref. [16] is systematic and the background estimate was obtained with a MC simulation in fast mode, while in the presented analysis the full simulation is used. Therefore, the two values should not necessarily be consistent. In the

Figure 3.9: $m_{\pi\mu\mu}$ distribution obtained for the $K^{\pm} \to \pi^{\pm}\pi^{+}\pi^{-}$ MC sample, after applying the baseline selection described in Sec. 3.3.1.

following, the mechanisms behind the $K^{\pm} \to \pi^{\pm}\pi^{+}\pi^{-}$ background are studied and the requirements to reject the different topologies are identified.

3.6.1.2 Event migration to the Signal Region

Even without considering the particle identification criteria, only a specific subset of $K^{\pm} \to \pi^{\pm}\pi^{+}\pi^{-}$ decays can enter the SR. For instance, $K^{\pm} \to \pi^{\pm}\pi^{+}\pi^{-}$ events, in which pions do not decay or decay downstream of the spectrometer, have a reconstructed $m_{\pi\mu\mu}$ variable significantly smaller than the kaon mass, because the 4-momenta of the same-sign tracks are evaluated assuming the muon mass, instead of the pion mass. Same-sign pion decays upstream of the spectrometer allow a correct mass assignment, but also in this case the reconstructed $m_{\pi\mu\mu}$ is smaller than the kaon mass, because of the missing momentum due to the presence of the undetected

neutrinos. Three mechanisms have been identified as being mainly responsible for the migration to the SR:

- the decay of any pion between the first and the last drift chamber;

- the strong interaction of any pion with the material constituting the first three drift chambers or with the helium within the first and the last drift chamber;

- the decay of the different-sign pion before reaching the first drift chamber, with consequent wrong mass assignment due to pion mis-identification.

In the first two cases, the momentum kick due to the pion decay or interaction may be misinterpreted as the effect of the magnetic field, leading to a biased measurement of the track momentum. In the third case, events may be reconstructed in the SR because the 4-momentum of the different-sign track is evaluated assuming the pion mass, instead of the muon mass. Fig. 3.10 shows the $m_{\pi\mu\mu}$ distribution obtained from a $K^{\pm} \to \pi^{\pm}\pi^{+}\pi^{-}$ MC sample of 10^8 events after applying baseline and final selections with no identification requirements, and distinguishing the contributions of the different pion decays topologies.

The most common mechanism accounting for the migration of $K^{\pm} \to \pi^{\pm}\pi^{+}\pi^{-}$ events to the SR is the decay of a different-sign pion, occurring in about 96% of the $K^{\pm} \to \pi^{\pm}\pi^{+}\pi^{-}$ events in the SR for the baseline selection (113.3 events out of 117.3). This contribution is strongly reduced in the final selection: as will be discussed in the next section, its suppression is mostly due to the stricter pion-candidate momentum requirement ($p_{\pi} > 15\,\mathrm{GeV}/c$ instead of $p_{\pi} > 10\,\mathrm{GeV}/c$). However, such a mechanism can contribute only if particle mis-identification occurs. In the extreme case of an ideal MUV system, the most relevant contribution would be due to two same-sign pion decays, with at least one of them occurring in the spectrometer.

Figure 3.10: $m_{\pi\mu\mu}$ distribution obtained for a $K^{\pm} \to \pi^{\pm}\pi^{+}\pi^{-}$ MC sample of 10^{8} events, after applying (a) the baseline selection, (b) the final selection, with no particle identification requirements. The contributions of the different pion decays topologies are shown. Decaying pions are labelled as "same sign" (s) if their charge is the same as the kaon and as "different sign" (d) otherwise.

3.6.1.3 Particle mis-identification

In the following, the baseline selection is updated according to the findings of Sec. 3.5.4: the search radius multiplier m is set to 2.5 and the final pion identification criteria are adopted. In addition, events with minimum track momenta above $5\,\mathrm{GeV}/c$ are included, in order to enhance the background and evaluate the optimal momentum requirements for pion and muon candidates. Fig. 3.11 shows the $m_{\pi\mu\mu}$ distribution obtained, distinguishing the contributions of the different pion decay topologies.

The updated requirements lead to 288.9 $K^{\pm} \to \pi^{\pm}\pi^{+}\pi^{-}$ events in the SR. This increase of background with respect to the baseline selection is dominated by the (temporarily) looser pion-candidate momentum requirement.

Most of the events (220.2 out of 288.9) in the SR are due to two same-sign $\pi^{\pm} \to \mu^{\pm}\nu$ decays. However, there is a non-negligible contribution of other topologies, which indicates the presence of muon mis-reconstruction (in case of less than 2 pion decays), track–muon mismatching (in case of different-sign pion decays) or is due to the muon
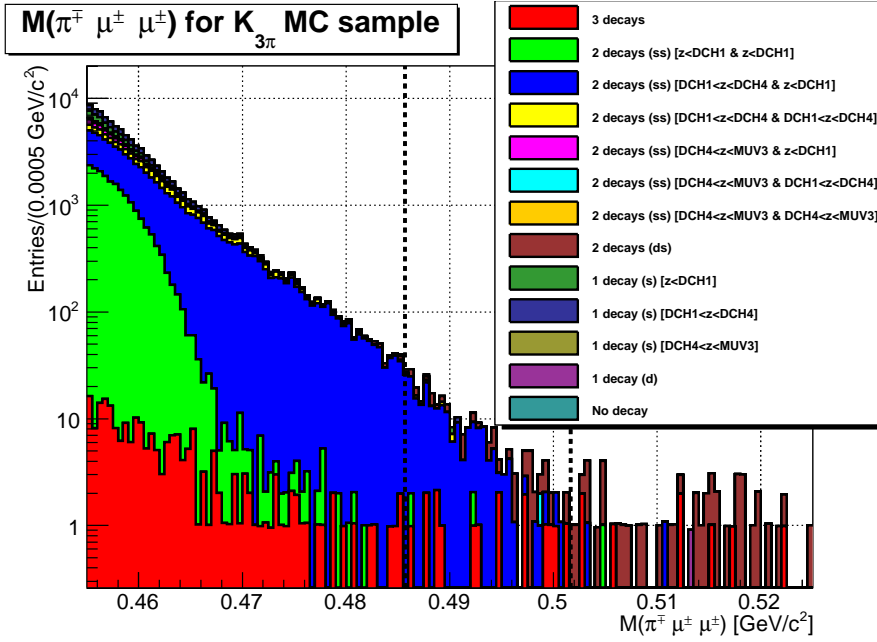
Figure 3.11: $m_{\pi\mu\mu}$ distribution obtained for the $K^\pm \to \pi^\pm\pi^+\pi^-$ MC sample, after applying the updated baseline selection, with search radius multiplier $m = 2.5$ and the final pion identification criteria. The minimum pion candidate momentum is temporarily set to $5\,\mathrm{GeV}/c$.

identification inefficiency (in case of 3 pion decays). After investigation, two simple mis-identification mechanisms have been identified:

Muon Duplication: This mechanism is responsible for the accepted $K^\pm \to \pi^\pm\pi^+\pi^-$ events with 1 pion decay only. The same set or a subset of MUV strips may be associated to more than one track, if the regions defined by the tracks search radii overlap (Sec. 3.5.2). If the set of MUV strips is the same, the reconstructed muons are the exact duplicates: status, reconstructed time and coordinates (x, y) are identical. The requirement of a non-zero distance between reconstructed muons in the final selection (Sec. 3.3.2.2) aims to reduce the contribution of this mechanism. If only a subset of strips is common to two or more search regions, the reconstructed muons may have different status, reconstructed time or coordinates (x, y); therefore, such events cannot be efficiently distinguished from genuine di-muons events.

Muon Swap: This mechanism contributes to the accepted $K^\pm \to \pi^\pm\pi^+\pi^-$ events

with 2 decays, of which one is a different sign decay (ds). The scattering of the different-sign muon in the material upstream the MUV planes can deflect it towards another track trajectory. In this case, the muon may be associated to the other (same-sign) track and not to the different-sign track that was actually produced by the muon, which may be identified as a pion. If the E/p ratio of the other track is $E/p < 0.2$, as it happens to about 50% of pions (Sec. 3.3.1.2), the other track is identified as a muon.

In order to verify precisely such hypothesis, a MC event display was created: the events of interest were reproduced and the track positions at each step of the simulation were saved in an external file; then, all the points saved were drawn, taking into account the particle type. Fig. 3.12 shows the (x, z) and (y, z) projections for a different-sign (ds) decay populating the SR: the presence of a muon scattering is evident.

(a)   (b)
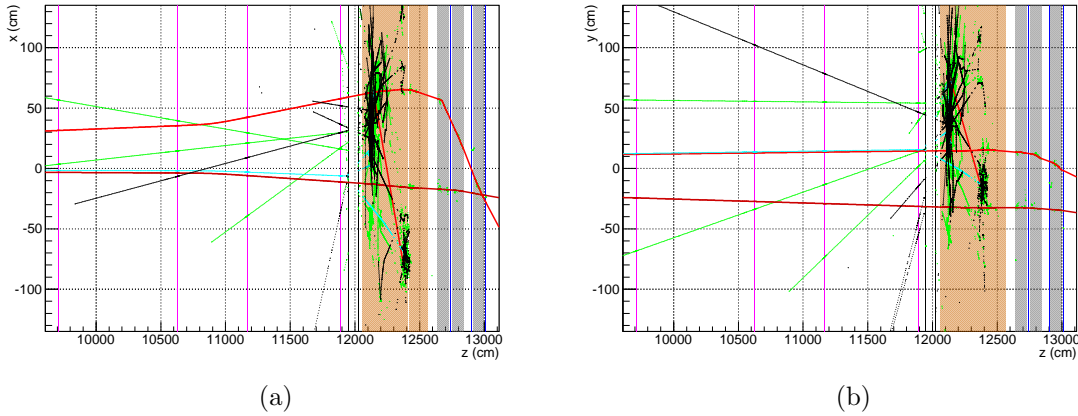
Figure 3.12: (a) (x, z) and (b) (y, z) projections of a different-sign (ds) decay populating the Signal Region. Muon points are shown in red, pion ones in cyan. Green points refer to electrons or photons, black to protons or neutrons. The volume of the LKr and of the HAC calorimeters are indicated with an orange shaded area, the iron walls preceding the MUV planes with a grey shaded area. The three MUV planes are pictured with blue lines and the drift chambers with magenta lines.

3.6.1.4 Requirements to reduce the $K^\pm \to \pi^\pm\pi^+\pi^-$ background

In order to reduce the contribution of the muon duplication, a non-zero distance between the coordinates (x, y) of the two reconstructed muons is required. The contribution of the different-sign pion decays ("muon swap") is reduced by:

- requiring the muon-candidate tracks to be within a maximum distance $d^\mu_{max} = 35\,\mathrm{cm}$ from the associated reconstructed muons;

- increasing to $p^\pi_{min} = 15\,\mathrm{GeV}/c$ the minimum momentum for the pion-candidates.

The first condition reduces the accidental association between another track and the reconstructed muon, while the second increases the muon veto efficiency for the pion-candidate track, by redefining an accepted momentum range with lower probability of multiple Coulomb scattering outside the muon search radius. Hence, the latter contributes to reject the events with 3 pion decays as well.

In addition, the kinematics of the $K^\pm \to \pi^\pm\pi^+\pi^-$ events with a different-sign decay is such that the highest $m_{\pi\mu\mu}$ values are obtained for the lowest pion-candidate momenta p_π. Fig. 3.13 shows the distribution of the $m_{\pi\mu\mu}$ variable as a function of the pion-candidate momentum p_π, obtained for $K^\pm \to \pi^\pm\pi^+\pi^-$ MC events without imposing any particle identification criteria. Therefore, strengthening the requirement on the minimum pion-candidate momentum p^π_{min} is convenient for both particle identification and kinematic rejection.

With these chosen values of d^μ_{max} and p^π_{min}, all the 94.7 remaining events are due to two same-sign $\pi^\pm \to \mu^\pm\nu$ decays. Unlike the others, the contribution due to two same-sign $\pi^\pm \to \mu^\pm\nu$ decays cannot be reduced with additional particle identification requirements, being due to two genuine same-sign $\mu^\pm$. All the events constituting the remaining background have two pion decays before reaching the last drift chamber, with at least one of them occurring into the spectrometer, causing momentum mis-reconstruction. Therefore, the requirements on such variables might be reconsidered and tightened: a possible compromise between reducing the
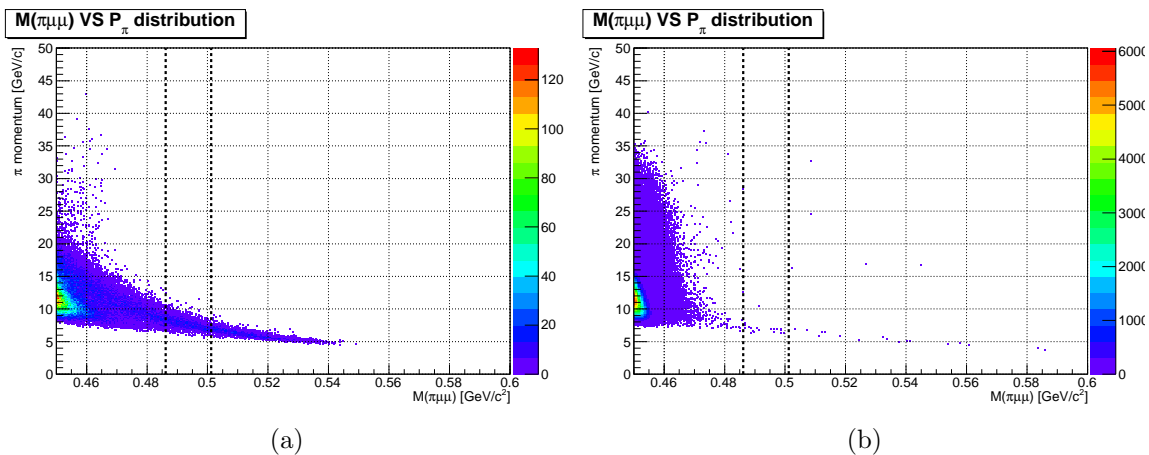
Figure 3.13: Distribution of $m_{\pi\mu\mu}$ as a function of the pion-candidate momentum p_π obtained without imposing any particle identification criteria, for $K^\pm \to \pi^\pm\pi^+\pi^-$ MC events with (a) at least a different-sign decay and (b) with no different-sign decays.

$K^\pm \to \pi^\pm\pi^+\pi^-$ background and not losing too much signal acceptance is requiring the total momentum $|\vec{p}_{3trk}|$ to be in the range [55,65] GeV/c, and the total transverse momentum $|\vec{p}_{\perp 3trk}|$ to be smaller than $10\,\mathrm{MeV}/c$. With this choice, more than 80% of the residual events are rejected; 15.8 events remain in the SR.

For most (14.7 out of 15.8) of those events, the reconstructed three-track vertices consist of a two-track vertex accidentally compatible with the muon coming from the pion decay. Such compatibility is an artefact of the Kalman filter fit induced by the pion decay and may have led to a wrong estimation of the original kaon decay vertex. In order to strengthen the three-track vertex reconstruction, the maximum allowed vertex χ^2 is decreased to 20 (from 40) and all the three two-track vertices formed by the three tracks are reconstructed as well[5]. For each two-track vertex, the closest distance of approach (CDA), defined as the minimum distance between the two extrapolated track trajectories, has been evaluated. Then, the maximum CDA of the three two-track vertices and the maximum distance d_{max}^{2trk} between two reconstructed two-track vertices have been considered for further requirements. These variables are sensitive to the vertex nature: if the three-track vertex is genuine, as for a

---

[5]For each pair of tracks, a modified version ($n_{trk} = 2$) of the same Kalman filter fit procedure employed for the three-track vertex computation has been used.

$K^{\pm} \to \pi^{\mp}\mu^{\pm}\mu^{\pm}$ event, the three CDAs obtained should be all consistent with zero, taking into account the spectrometer resolution; all the two-track vertices should be reconstructed in the proximity of the original kaon decay vertex, resulting in a maximum distance d_{max}^{2trk} between two reconstructed two-track vertices comparable with resolution effects. On the other hand, if one of the tracks composing the reconstructed three-track vertex is not produced by a kaon decay product, there is at least one two-track vertex independent of such track, which may provide a more accurate vertex estimation. In this case, the maximum distance between two reconstructed two-track vertices may be significantly larger, and so the maximum CDA, if coming from one of the two mis-reconstructed two-track vertices.

A suitable choice of the additional constraints is to require the maximum distance d_{max}^{2trk} between two reconstructed two-track vertices to be smaller than $5\,\mathrm{m}$, and the maximum CDA of the two-track vertices to be smaller than $3\,\mathrm{cm}$ (see Sec. 3.7.2 for signal–background comparisons).

After implementing all the proposed requirements, all the 1.2×10^{10} $K^{\pm} \to \pi^{\pm}\pi^{+}\pi^{-}$ events of the considered MC sample are rejected. Fig. 3.14 shows the distribution of the residual $K^{\pm} \to \pi^{\pm}\pi^{+}\pi^{-}$ events after applying the described cuts. Due to the proximity of the $K^{\pm} \to \pi^{\pm}\pi^{+}\pi^{-}$ background to the signal region, a smaller signal region is proposed:

$$|m_{\pi\mu\mu} - m_K| \leq 5\,\mathrm{MeV}/c^2, \tag{3.22}$$

where the limits correspond to a distance of $2\sigma_m = 5\,\mathrm{MeV}/c^2$ from the kaon mass m_K.

3.6.2 $K^{\pm} \to \pi^{+}\pi^{-}\mu^{\pm}\nu$ background

Given the integrated kaon flux for the considered data sample (Sec. 3.4), about 3×10^6 $K^{\pm} \to \pi^{+}\pi^{-}\mu^{\pm}\nu$ decays are expected. A $K^{\pm} \to \pi^{+}\pi^{-}\mu^{\pm}\nu$ MC sample of 10^8 events has been produced to study the impact of such decay on the $K^{\pm} \to \pi^{\mp}\mu^{\pm}\mu^{\pm}$ background.

Because of the similarities with the subset of $K^{\pm} \to \pi^{\pm}\pi^{+}\pi^{-}$ decays with an
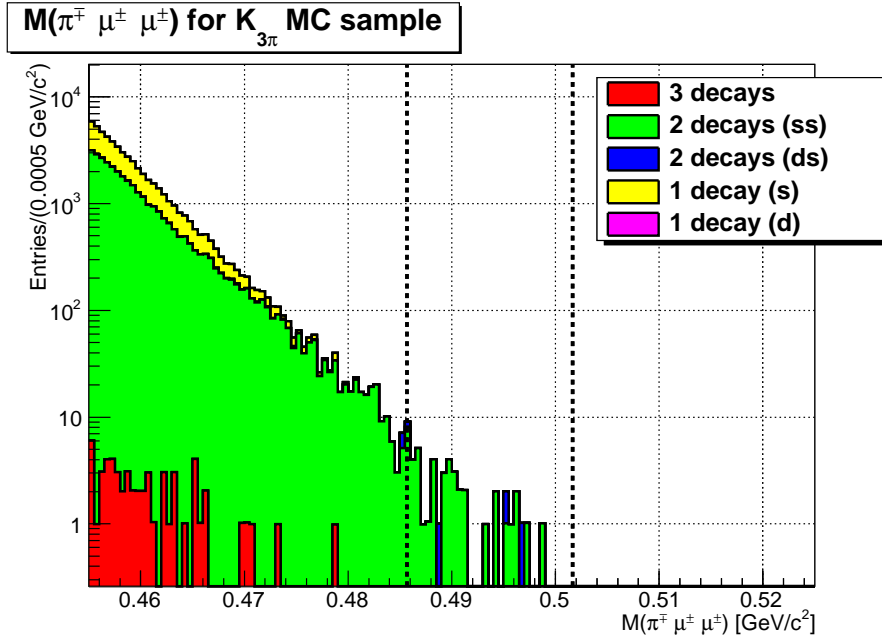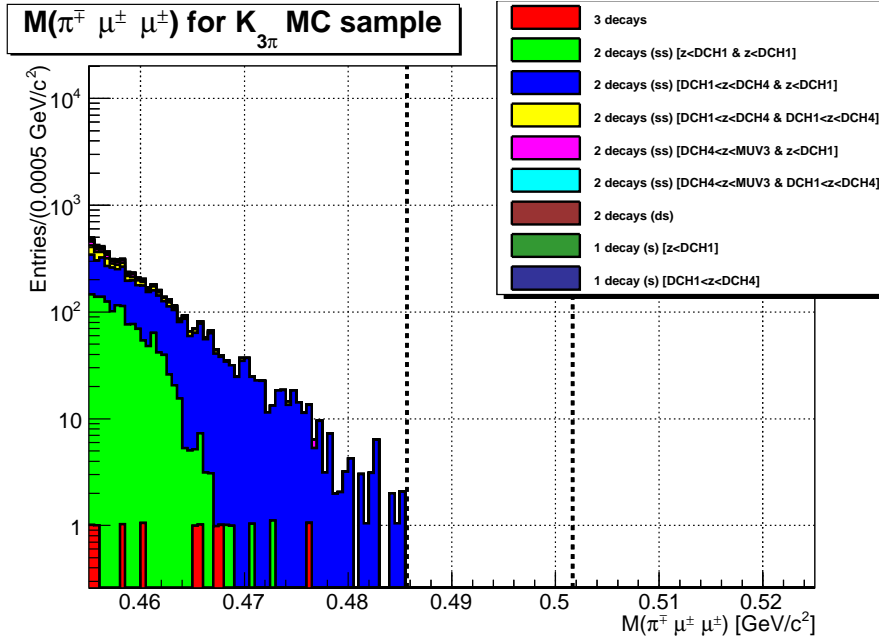
Figure 3.14: $m_{\pi\mu\mu}$ distribution obtained for the $K^\pm \to \pi^\pm\pi^+\pi^-$ MC sample, after applying the final selection described in Sec. 3.3.2. The contributions of the different pion decays topologies are shown. The dashed lines indicate the SR of the baseline selection.

immediately subsequent same-sign pion decay, the requirements proposed in Sec. 3.6.1 to reduce the $K^\pm \to \pi^\pm\pi^+\pi^-$ background are effective for the $K^\pm \to \pi^+\pi^-\mu^\pm\nu$ contribution as well. Fig. 3.15 shows the $m_{\pi\mu\mu}$ distribution obtained for the $K^\pm \to \pi^+\pi^-\mu^\pm\nu$ MC sample, after applying the baseline and final selections.

After applying the final selection in Sec. 3.3.2, 3.22 events remain out of the 10^8 $K^\pm \to \pi^+\pi^-\mu^\pm\nu$ in the considered MC sample, corresponding to $0.09 \pm 0.05_{stat} \pm 0.06_{syst}$ expected background events in the $K^\pm \to \pi^\mp\mu^\pm\mu^\pm$ sample (Sec. 3.7.3).

3.6.3 $K^\pm \to \pi^\pm\mu^+\mu^-$ background

Given the integrated kaon flux for the considered data sample (Sec. 3.4), about 2×10^4 $K^\pm \to \pi^\pm\mu^+\mu^-$ decays are expected. Despite its branching fraction being six orders of magnitude smaller than the $K^\pm \to \pi^\pm\pi^+\pi^-$ one, the $K^\pm \to \pi^\pm\mu^+\mu^-$ decay might contribute to the background at the same level. For this decay it is not possible
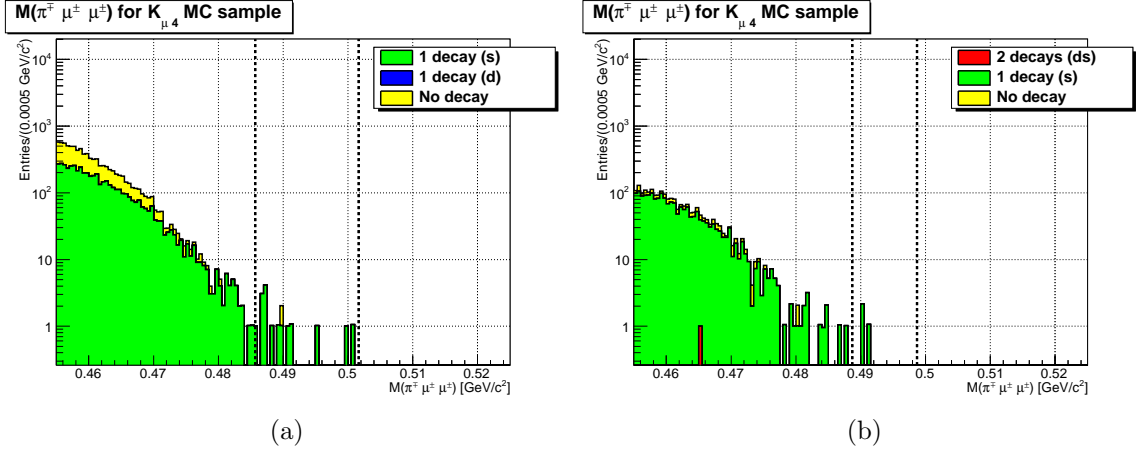
Figure 3.15: $m_{\pi\mu\mu}$ distribution obtained for a $K^\pm \to \pi^+\pi^-\mu^\pm\nu$ MC sample of 10^8 events, after applying (a) the baseline selection, (b) the final selection. The contributions of the different pion decays topologies are shown.

to benefit from the background reduction deriving from $\vec{p}_{3trk}$, $\vec{p}_{\perp 3trk}$ nor vertex-related requirements, since, as far as those variables are concerned, the $K^\pm \to \pi^\pm\mu^+\mu^-$ decay is not different from the signal. A $K^\pm \to \pi^\pm\mu^+\mu^-$ MC sample of 10^7 events has been produced to study the impact of such decay on the $K^\pm \to \pi^\mp\mu^\pm\mu^\pm$ background.

Fig. 3.16 shows the $m_{\pi\mu\mu}$ distribution obtained for the $K^\pm \to \pi^\pm\mu^+\mu^-$ MC sample, after applying baseline and final selections. After applying the final selection in
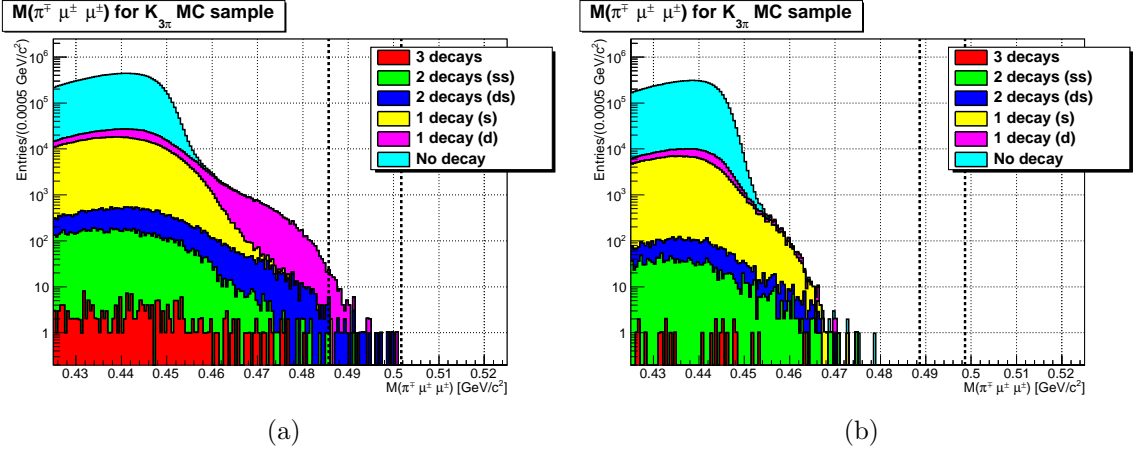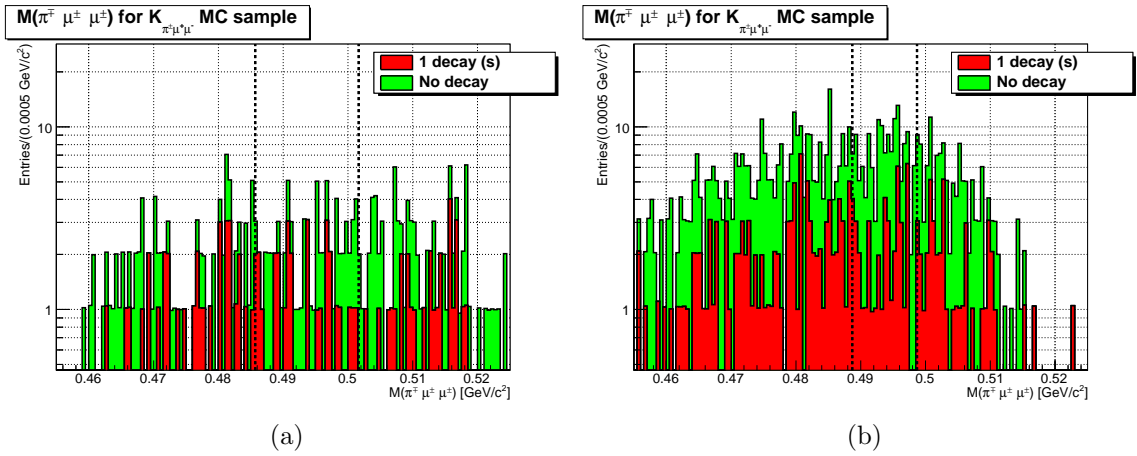

Figure 3.16: $m_{\pi\mu\mu}$ distribution obtained for a $K^\pm \to \pi^\pm\mu^+\mu^-$ MC sample of 10^7 events, after applying (a) the baseline selection, (b) the final selection. The contributions of the different pion decays topologies are shown.

Sec. 3.3.2, 147.1 events remain out of the 10^7 $K^\pm \to \pi^\pm \mu^+ \mu^-$ in the considered MC sample, corresponding to $0.28 \pm 0.02_{stat} \pm 0.02_{syst}$ expected background events in the $K^\pm \to \pi^\mp \mu^\pm \mu^\pm$ sample. The enhancement of $K^\pm \to \pi^\pm \mu^+ \mu^-$ background events for the final selection with respect to the baseline selection, for which 75.3 events are in the SR, is a consequence of the optimised muon reconstruction for a di-muon search (Sec. 3.5.4). However, since the $K^\pm \to \pi^\pm \mu^+ \mu^-$ decay is not the dominant background, the performed optimisation increases the signal acceptance of $\sim 40\%$ (relative), without increasing significantly the expected background.

3.6.4 $K^\pm \to \mu^+ \mu^- \mu^\pm \nu$ background

Given the integrated kaon flux for the considered data sample (Sec. 3.4), about 3×10^3 $K^\pm \to \mu^+ \mu^- \mu^\pm \nu$ decays are expected. A $K^\pm \to \mu^+ \mu^- \mu^\pm \nu$ MC sample of 10^7 events has been produced to study the contribution of such decay on the $K^\pm \to \pi^\mp \mu^\pm \mu^\pm$ background. Due to a branching fraction 7 times smaller than the one of the $K^\pm \to \pi^\pm \mu^+ \mu^-$ decay and to the presence of an undetected neutrino, the background contribution to the $K^\pm \to \pi^\mp \mu^\pm \mu^\pm$ background is likely to be negligible.

Fig. 3.17 shows the $m_{\pi\mu\mu}$ distribution obtained for the $K^\pm \to \mu^+ \mu^- \mu^\pm \nu$ MC sample, after applying the baseline and final selections. After implementing the requirements of the final selection (Sec. 3.3.2), 47.8 events are observed in the SR, out of the 10^7 $K^\pm \to \mu^+ \mu^- \mu^\pm \nu$ in the considered MC sample, corresponding to $0.01 \pm 0.002_{stat} \pm 0.01_{syst}$ expected background events in the $K^\pm \to \pi^\mp \mu^\pm \mu^\pm$ sample[6].

3.6.5 $K^\pm \to \pi^+ \pi^- e^\pm \nu$ and $K^\pm \to \mu^+ \mu^- e^\pm \nu$ backgrounds

Given the integrated kaon flux for the considered data sample (Sec. 3.4), about 7.7×10^6 $K^\pm \to \pi^+ \pi^- e^\pm \nu$ and 3.2×10^3 $K^\pm \to \mu^+ \mu^- e^\pm \nu$ decays are expected. However, they can contribute to the $K^\pm \to \pi^\mp \mu^\pm \mu^\pm$ background only if the $e^\pm$ is mis-identified as a $\mu^\pm$. Although the probability of associating a reconstructed

---

[6]Due to the absence of a proper theoretical uncertainty, an error of 10^{-8} has been assumed for the branching fraction $\mathcal{B}(K^\pm \to \mu^+ \mu^- \mu^\pm \nu)$.
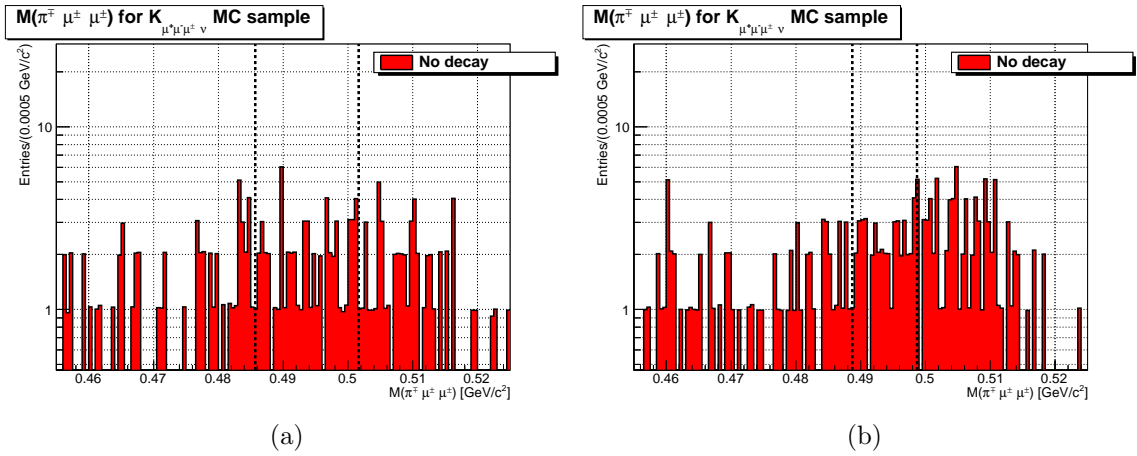
Figure 3.17: $m_{\pi\mu\mu}$ distribution obtained for a $K^{\pm} \to \mu^{+}\mu^{-}\mu^{\pm}\nu$ MC sample of 10^7 events, after applying (a) the baseline selection (b) the final selection. The contributions of the different pion decays topologies are shown.

muon to the $e^{\pm}$ track due to other tracks activity is not negligible (see for instance Sec. 3.5.4.2), the probability for a $e^{\pm}$ of having an E/p ratio below 0.2 is of the order of 10^{-4} (Sec. 3.3.1.2). As a consequence, the "muon swap" with electrons, which is the only possible mechanism to accept such decays, is suppressed by four orders of magnitude with respect to the one with pions, described in Sec. 3.6.1. All the 10^8 $K^{\pm} \to \pi^{+}\pi^{-}e^{\pm}\nu$ and the 10^7 $K^{\pm} \to \mu^{+}\mu^{-}e^{\pm}\nu$ MC events have been rejected applying the particle identification requirements only. Therefore, the contribution of these decays to the $K^{\pm} \to \pi^{\mp}\mu^{\pm}\mu^{\pm}$ background can be neglected.

3.7 Background expectation study

The number of expected background events with the final selection is reported in this section. In order to confirm the quality of the MC simulation, the data–MC ratios for the most relevant variables of the analysis are presented. Then, signal and background distributions are compared to confirm the convenient choice of the applied cuts.

3.7.1 Data-MC comparison in the Control Region

The quality of the MC simulation has been checked by studying the data–MC ratios within the $K^{\pm} \to \pi^{\mp} \mu^{\pm} \mu^{\pm}$ event selection for the most relevant variables of the analysis. The reconstructed mass range $0.456 \,\mathrm{GeV}/c^2 \leq m_{\pi\mu\mu} \leq 0.480 \,\mathrm{GeV}/c^2$ is used as Control Region (CR) for the data–MC comparison. The choice of the lower limit is determined by the pre-filter conditions applied during the $K^{\pm} \to \pi^{\pm} \pi^{+} \pi^{-}$ MC production (Appendix C), while the upper limit is chosen in order to be at least 3σ from the lower edge of the SR. The MC samples have been normalised according to their branching fractions and using the estimate of the number N_K of kaon decays in the fiducial volume, obtained in Sec. 3.4. The number of data events selected in the CR is $N_{data}^{\mathrm{CR}} = 5402$, while the expected number of background events is $N_{bkg}^{\mathrm{CR}} = 5250 \pm 73_{stat} \pm 55_{syst}$. The obtained data–MC comparisons are shown in Figs. 3.18–3.22. For each variable considered, the final selection is applied except for any requirement on the considered variable and for the condition on the $m_{\pi\mu\mu}$ variable, which must be within the Control Region. The values of the applied cuts are indicated by the arrows.

Given that the studied data–MC ratios do not show disagreement in any of the distributions, the final event selection described in Sec. 3.3.2 has been validated.

3.7.2 Signal-Background distributions

The comparisons between signal and background MC distributions of the most relevant variables are shown in Figs. 3.23–3.27. For each variable, the final selection is applied except for any requirement on the considered variable itself and, in order to increase the background statistics, on the $m_{\pi\mu\mu}$ variable. The values of the final cuts are indicated by the arrows.

3.7.3 Expected number of background events

For each background channel $K^\pm \to f_i$ considered, the number N^i_{exp} of expected events in the SR has been determined as

$$N^i_{exp} = \frac{N^i_{SR}}{\tau_i}, \qquad (3.23)$$

where N^i_{SR} is the number of MC events observed in the SR, while τ_i is the size of the generated MC sample in units of the data volume:

$$\tau_i \stackrel{def}{=} \frac{\alpha_{fv} N^i_{gen}}{N_K \mathcal{B}(K^\pm \to f_i)}. \qquad (3.24)$$

In eq. 3.24, N^i_{gen} is the total number of generated events (in the z-range $-22\,\mathrm{m} < z < 90\,\mathrm{m}$), N_K is the number of kaon decays in the fiducial volume, measured in Sec. 3.4 and $\mathcal{B}(K^\pm \to f_i)$ is the branching fraction of the channel $K^\pm \to i$; the value $\alpha_{fv} = 0.8803$ is the fraction of events generated in the fiducial volume $(-18\,\mathrm{m}, 80\,\mathrm{m})$ and is fixed for all the produced MC samples.

For the $K^\pm \to \pi^\pm \pi^+ \pi^-$ background, N_{exp} has been evaluated from an independent MC sample of the same size as that used to optimise the signal selection. This method prevents any bias induced by the choice of the event selection, purposely tuned in order to reject as many $K^\pm \to \pi^\pm \pi^+ \pi^-$ events as possible of that particular sample.

Tab. 3.5 shows the expected number of background events, obtained with the final $K^\pm \to \pi^\mp \mu^\pm \mu^\pm$ selection and using the branching fractions in Tab. 3.4. The error quoted for τ is systematic and is dominated by the branching fraction of its own decay channel. Considering all the examined background sources, a total of $1.36 \pm 0.97_{stat} \pm 0.06_{syst}$ events are expected. The total systematic error is dominated by the error of the $K^\pm \to \pi^+ \pi^- \mu^\pm \nu$ branching fraction.

Table 3.5: Numbers of expected events N_{exp} in the Signal Region for the MC samples considered, obtained with the final $K^{\pm} \to \pi^{\mp}\mu^{\pm}\mu^{\pm}$ selection.

Decay channel	N_{gen}	N_{SR}	τ	N_{exp}
$K^{\pm} \to \pi^{\pm}\pi^+\pi^-$	1.2×10^{10}	1	1.03 ± 0.01	$0.97 \pm 0.97 \pm 0.01$
$K^{\pm} \to \pi^+\pi^-\mu^{\pm}\nu$	10^8	3.2	34.32 ± 22.1	$0.09 \pm 0.05 \pm 0.06$
$K^{\pm} \to \pi^{\pm}\mu^+\mu^-$	10^7	147.1	511.2 ± 32.9	$0.29 \pm 0.02 \pm 0.02$
$K^{\pm} \to \mu^+\mu^-\mu^{\pm}\nu$	10^7	47.8	3559 ± 2636	$0.013 \pm 0.001 \pm 0.01$
Total	–	–	–	$1.36 \pm 0.97 \pm 0.06$

(a)   (b)
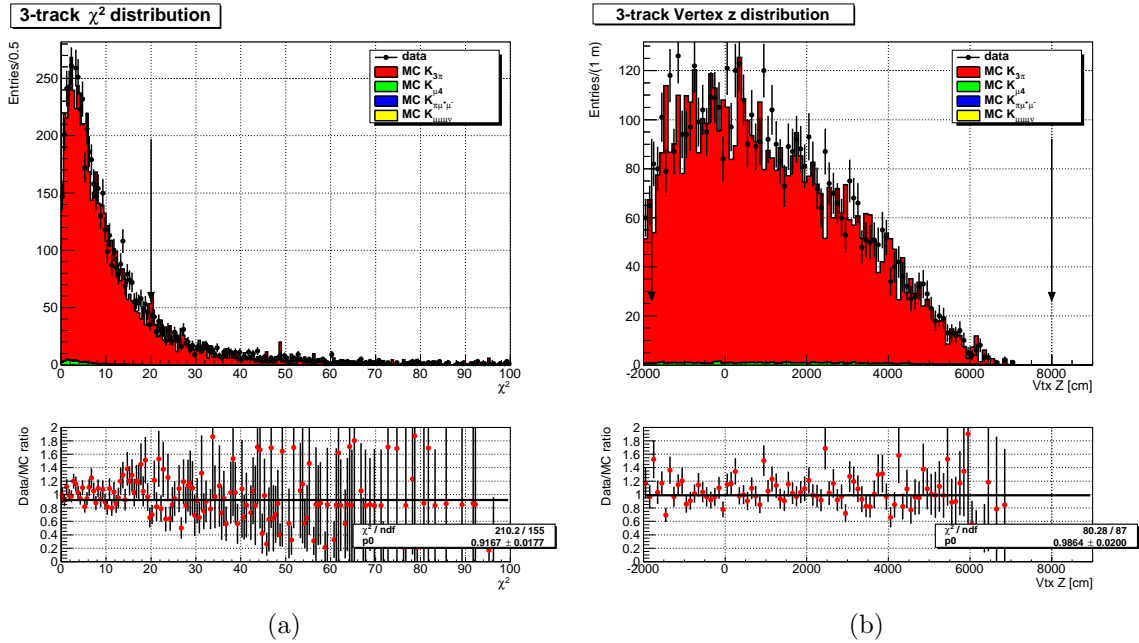
Figure 3.18: Distributions of (a) the χ^2 and (b) the z-coordinate of the reconstructed three-track vertex, for data and MC simulation of the considered backgrounds. The respective data-MC ratios are shown. The values of the applied cuts are indicated by the arrows.
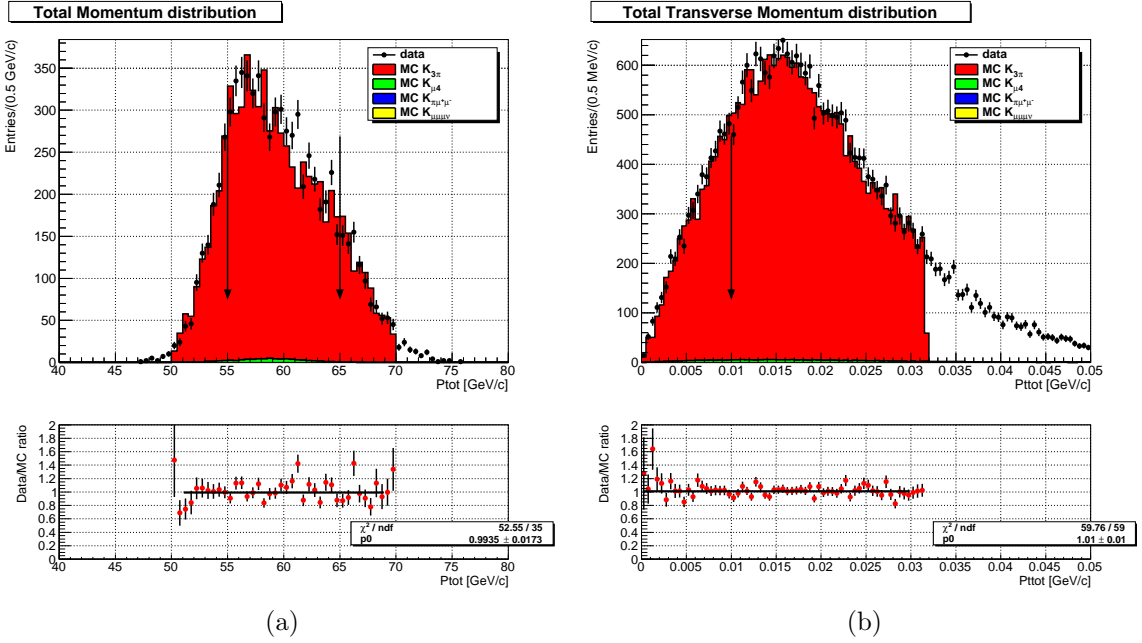
Figure 3.19: Distributions of (a) the reconstructed total momentum $|\vec{p}_{3trk}|$ and (b) the total transverse momentum $|\vec{p}_{\perp 3trk}|$ for data and MC simulation of the considered backgrounds. The respective data-MC ratios are shown. The values of the applied cuts are indicated by the arrows.
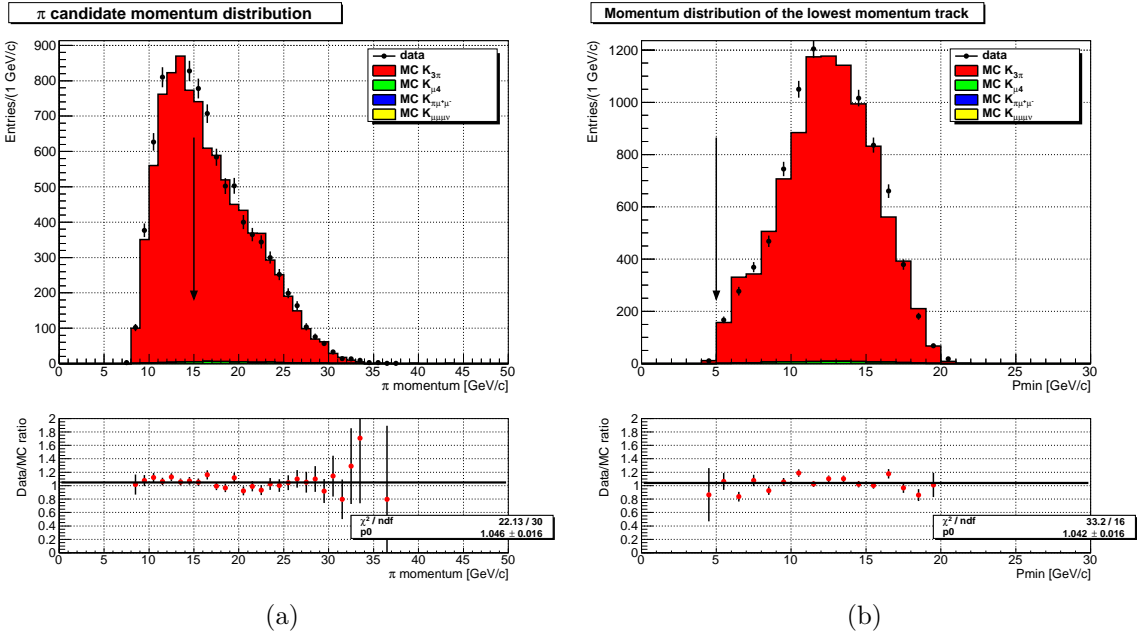
Figure 3.20: Distributions of (a) the π-candidate momentum and (b) the lowest track momentum for data and MC simulation of the considered backgrounds. The respective data-MC ratios are shown. The values of the applied cuts are indicated by the arrows.
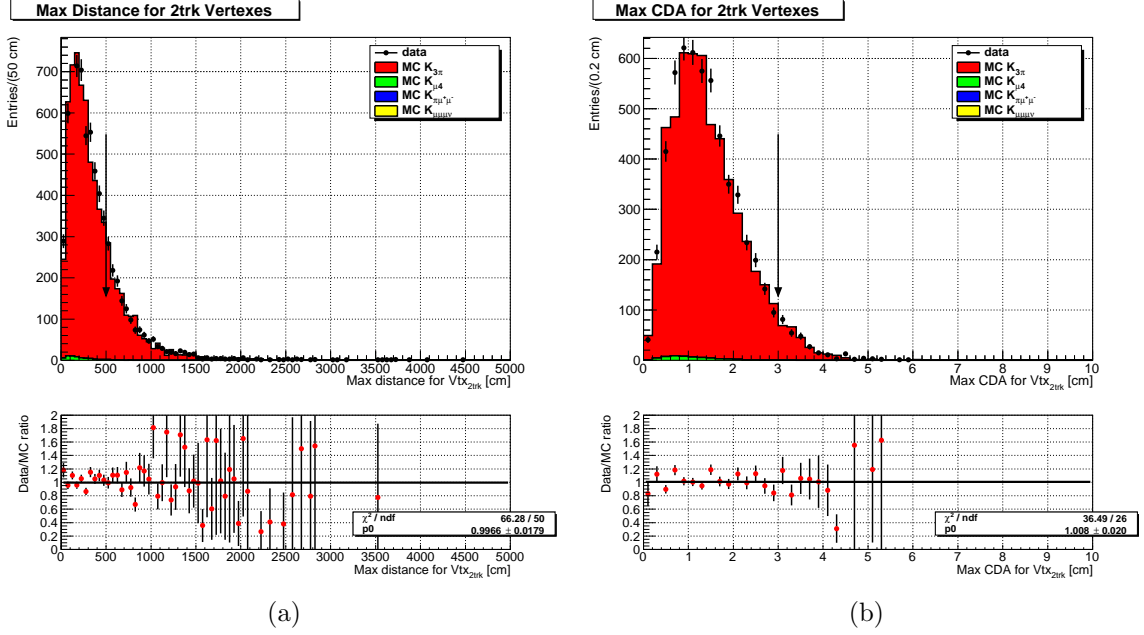
Figure 3.21: Distributions of (a) the maximum distance d_{max}^{2trk} between two reconstructed two-track vertices and (b) the maximum CDA of the three two-track vertices for data and MC simulation of the considered backgrounds. The respective data-MC ratios are shown. The values of the applied cuts are indicated by the arrows.
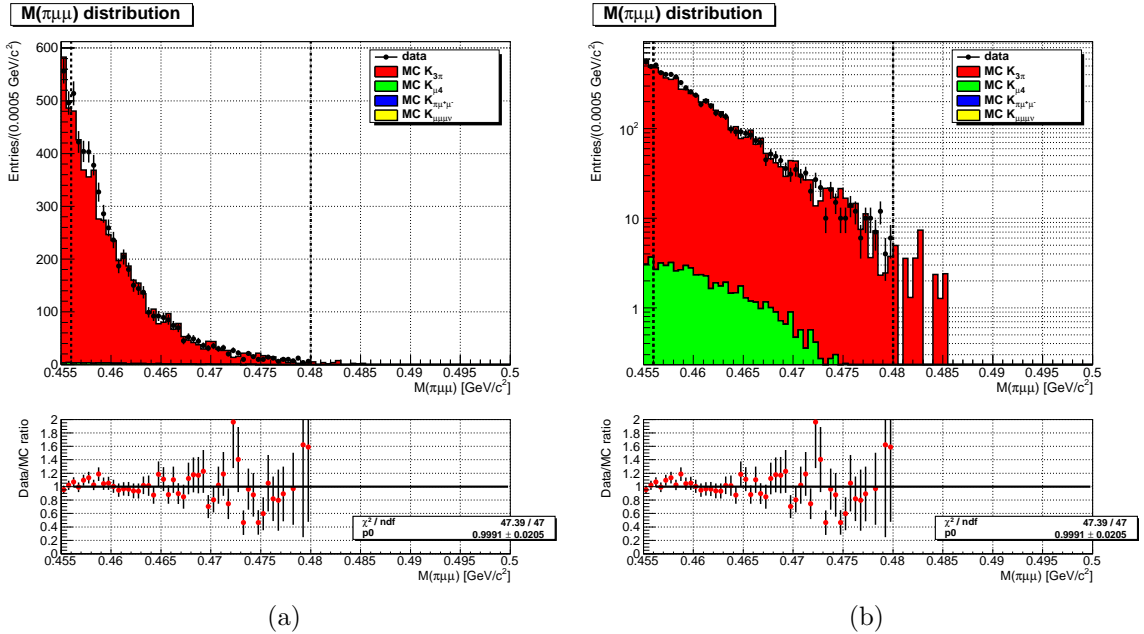
Figure 3.22: Reconstructed invariant mass $m_{\pi\mu\mu}$ distribution for data and MC simulation of the considered backgrounds: (a) linear scale, (b) logarithmic scale. The respective data-MC ratios are shown. The boundaries of the Control Region are shown by the dashed lines.
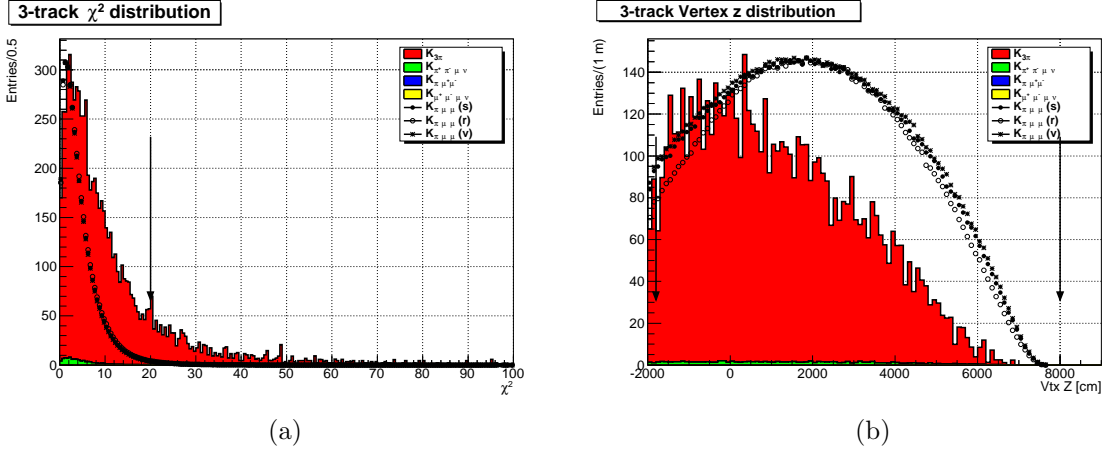
Figure 3.23: Distributions of (a) the χ^2 and (b) the z-coordinate of the reconstructed three-track vertex, for signal and backgrounds, obtained from the produced MC samples. The values of the applied cuts are indicated by the arrows. No requirement on the $m_{\pi\mu\mu}$ variable is applied, in order to increase the background statistics.
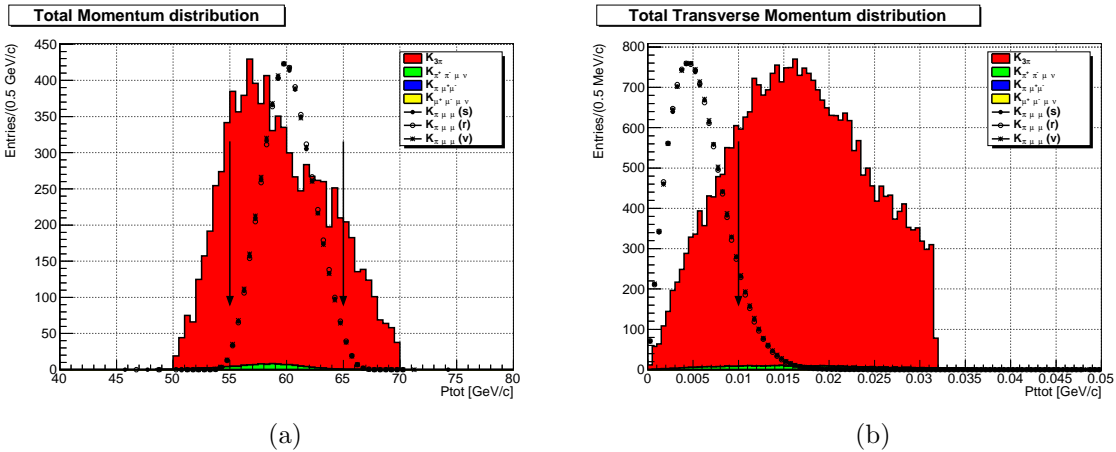
Figure 3.24: Distributions of (a) the reconstructed total momentum $|\vec{p}_{3trk}|$ and (b) the total transverse momentum $|\vec{p}_{\perp 3trk}|$ for signal and backgrounds, obtained from the produced MC samples. The values of the applied cuts are indicated by the arrows. No requirement on the $m_{\pi\mu\mu}$ variable is applied, in order to increase the background statistics.

94

(a)

(b)
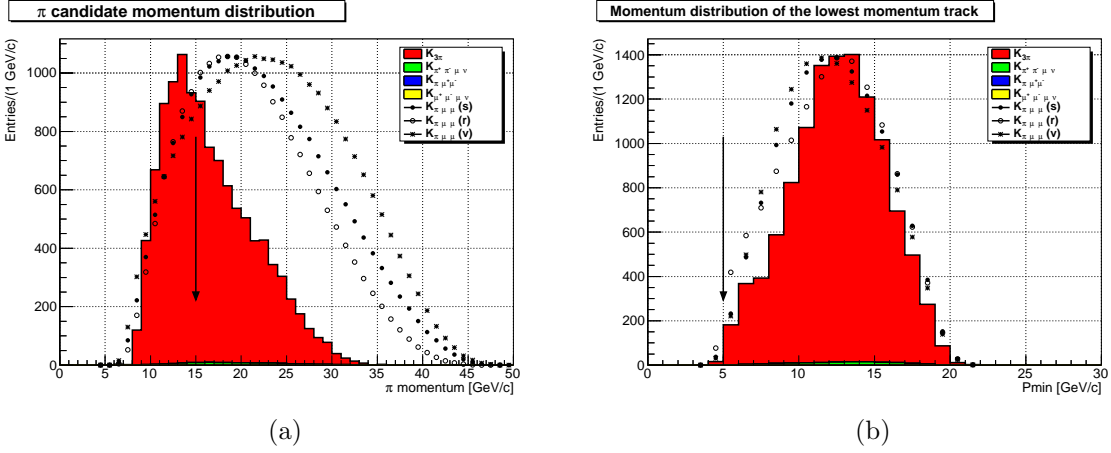
Figure 3.25: Distributions of (a) the π-candidate momentum and (b) the lowest track momentum for signal and backgrounds, obtained from the produced MC samples. The values of the applied cuts are indicated by the arrows. No requirement on the $m_{\pi\mu\mu}$ variable is applied, in order to increase the background statistics.

(a)

(b)
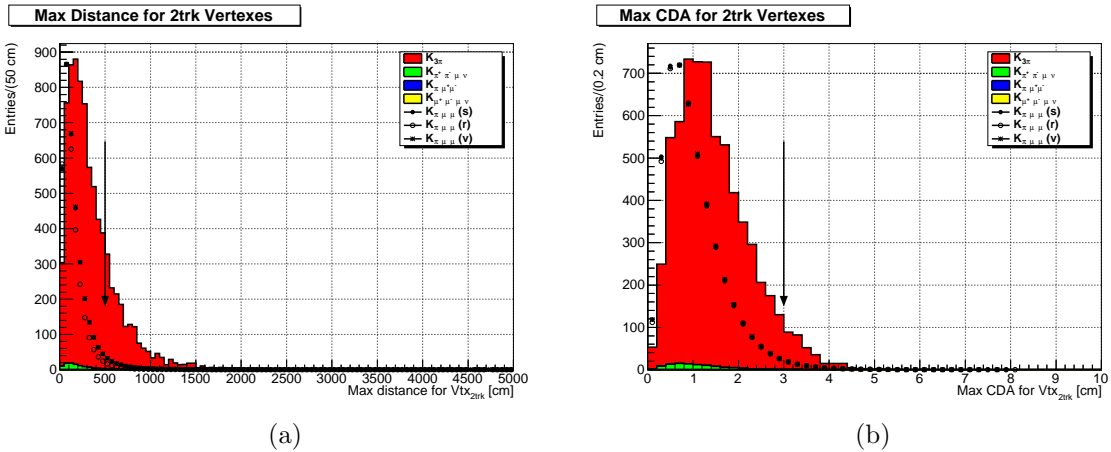
Figure 3.26: Distributions of (a) the maximum distance d_{max}^{2trk} between two reconstructed two-track vertices and (b) the maximum CDA of the three two-track vertices for signal and backgrounds, obtained from the produced MC samples. The values of the applied cuts are indicated by the arrows. No requirement on the $m_{\pi\mu\mu}$ variable is applied, in order to increase the background statistics.
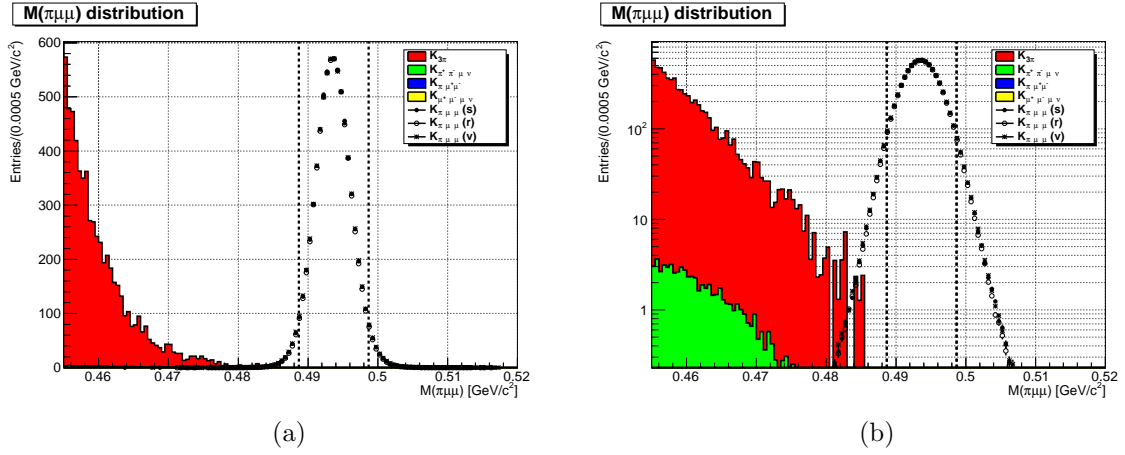
Figure 3.27: Reconstructed invariant mass $m_{\pi\mu\mu}$ distribution for signal and backgrounds, obtained from the produced MC samples: (a) linear scale, (b) logarithmic scale. The boundaries of the signal region, as defined in eq. 3.5, are shown by the dashed lines.

3.8 Results

In this section, the chosen method for the statistical interpretation of the data is described. Finally, the obtained UL for the branching fraction $\mathcal{B}(K^\pm \to \pi^\mp \mu^\pm \mu^\pm)$ is presented.

3.8.1 Statistical framework

The UL for the branching fraction $\mathcal{B}(K^\pm \to \pi^\mp \mu^\pm \mu^\pm)$ has been evaluated using an extension of the Rolke-Lopez method [56, 57] to treat the case of a Poisson process in the presence of unknown backgrounds. The Feldman-Cousins treatment [58] of a Poisson process in the presence of known background was initially adopted, but it was abandoned because the uncertainty on the background evaluation is non-negligible for the performed analysis, due to the limited size of the produced $K^\pm \to \pi^\pm \pi^+ \pi^-$ MC sample. In the following, the statistical formalism is discussed briefly, focussing in particular on the treatment of a Poisson process in the presence of background.

3.8.1.1 Neyman (1937)

The framework introduced by Neyman [59] is the base of the frequentistic school of confidence intervals. Given a parameter μ and its unknown (fixed) true value μ_t, the confidence interval $[\mu_1, \mu_2]$ is defined as the set of values such that the probability

$$P(\mu_t \in [\mu_1, \mu_2]) = \alpha, \tag{3.25}$$

where α is CL, $0 < \alpha < 1$. Such confidence interval can be estimated from a measured quantity x, related to the unknown parameter μ. For every allowed value of μ, an interval $[x_1, x_2]$ such that the probability

$$P(x \in [x_1, x_2]|\mu) = \alpha \tag{3.26}$$

is considered. The set of chosen intervals for all the allowed values of μ defines an acceptance region in the (x, μ) plane, which is called "confidence belt". The confidence interval $[\mu_1, \mu_2]$ resulting from a measurement of the quantity x with outcome x_0 is obtained by selecting the values of μ being in the acceptance region for $x = x_0$.

Particular care must be taken in the choice of the intervals $[x_1, x_2]$. For each value of μ, the eq. 3.26 is satisfied by a set of different intervals. In order to determine the acceptance region uniquely, auxiliary criteria must be specified. In Neyman's approach, the two most common choices are

$$P(x < x_1|\mu) = 1 - \alpha, \tag{3.27}$$

leading to "upper confidence limits", and

$$P(x < x_1|\mu) = P(x > x_2|\mu) = \frac{1 - \alpha}{2}, \tag{3.28}$$

leading to "central confidence intervals". If x is a discrete variable, the interval $[x_1, x_2]$ is determined as the smallest range with a CL exceeding α.

This arbitrariness may induce troublesome cases. For instance, the result may be a non-physical interval or an empty set[7]; in this case, eq. 3.25 is still satisfied and the formalism is not violated, allowing a probability equal to $1 - \alpha$ of having a confidence interval which does not contain the true value μ_t. However, such interpretation is unsatisfactory. Moreover, if the choice of using the upper confidence limit rather than the central confidence interval is based on data, the resulting intervals may be affected by undercoverage, i.e. the CL of the quoted intervals may be mistakenly smaller than α. The Feldman-Cousins approach solves both problems.

---

[7]As an example of this case, Feldman and Cousins [58] treat the case of a Poisson distribution with mean $\mu = 0.5$ in the presence of known mean background $b = 3$. For $\alpha = 90\%$, the confidence interval corresponding to the observation of 0 events is the empty set.

3.8.1.2 Feldman-Cousins (1998)

The Feldman-Cousins method [58] introduces a new ordering principle in the classical Neyman treatment [59], based on the likelihood ratio R, defined as

$$R \stackrel{def}{=} \frac{P(x|\mu)}{P(x|\hat{\mu})}, \tag{3.29}$$

where $P(x|\mu)$ is the likelihood of obtaining x given the true value of μ, and $P(x|\hat{\mu})$ is the likelihood of obtaining x given the physically allowed value $\hat{\mu}$ maximising $P(x|\mu)$. For each value of μ, the interval $[x_1, x_2]$ is built starting from values of x corresponding to the highest R, and new values are added in decreasing order of R, until the sum (or integral) of the $P(x|\mu)$ reaches or exceeds the required CL. Then, as in the Neyman construction, the confidence interval $[\mu_1, \mu_2]$ resulting from the measurement $x = x_0$ is obtained by selecting the values of μ being in the acceptance region for $x = x_0$.

With the addition of the ordering criterion, the physically allowed value $\hat{\mu}$ is always included in the CL by construction. Furthermore, there is no need any longer of choosing between upper/lower confidence limits: the choice is automatically determined by the method.

Feldman and Cousins, as an application of their method, deal with the case of a Poisson process in the presence of known background. In this case, the observable x is the number of observed events, which is the sum of signal events with mean μ and of background events with known mean b. The probability $P(x|\mu)$ is determined by the Poisson statistics:

$$P(x|\mu) = \frac{(\mu + b)^x}{x!} e^{-(\mu+b)}, \tag{3.30}$$

and $\hat{\mu} = \max(0, x-b)$ is obtained maximising $P(x|\mu)$ and requiring it to be physically allowed ($\hat{\mu} \geq 0$). Then, for each considered value of μ, values of x are added to the acceptance region in the order defined by the likelihood ratio R, until the desired CL is reached or exceeded. Finally, as in the Neyman construction, the confidence interval corresponding to the outcome x_0 is defined by the values μ in the acceptance region for $x = x_0$.

99

However, the Feldman-Cousins method cannot be easily generalised to the case where there are many parameters of interest, or adapted to treat problems with several unknown nuisance parameters. These necessities have led to the development of the Rolke-Lopez method.

3.8.1.3 Rolke-Lopez (2001)

Unlike Feldman-Cousins, the Rolke-Lopez method [56,57] is not based on the Neyman construction: it uses an alternative approach based on the so-called "$\log \mathcal{L} + \frac{1}{2}$" method, which consists of extracting confidence intervals by relying on the properties of the χ^2 distribution. Thanks to this choice, the Rolke-Lopez procedure is simpler than the Feldman-Cousins one, and can be generalised to the case of many parameters of interest, or adapted to treat problems with several unknown nuisance parameters. However, it is based on a large-sample theory, so a few prescriptions are needed for the application to small samples.

As an application of their method, Rolke and Lopez provide a treatment for the case of a Poisson process with mean μ in the presence of Poisson-distributed background with an unknown mean b. In this case, due to the additional degree of freedom introduced, the number of observed events x in a defined SR is no longer sufficient to obtain a meaningful result. The missing piece of information is acquired by observing the number of background events y in a control sample where signal is absent, e.g. a MC simulation of the background or a Control Region.

The statistical significance of the control sample with respect to the signal one is determined by the parameter τ, defined as the probability for a background event of being in the control sample divided by the probability of being in the signal sample. For instance, if a MC simulation is used to evaluate the expected number of background events in the SR, τ indicates the size of the MC sample with respect to the data volume (which is the definition of τ adopted in eq. 3.24).

Since the signal and control samples are assumed to be independent, the likelihood

function $P(x, y|\mu, b)$ of μ and b given the observation (x, y) is determined by the product of two Poisson distributions:

$$P(x, y|\mu, b) = \frac{(\mu + b)^x}{x!} e^{-(\mu+b)} \cdot \frac{(\tau b)^y}{y!} e^{-\tau b}. \tag{3.31}$$

The natural generalisation of the likelihood ratio R in eq. 3.29 is the profile likelihood ratio λ, which, in the considered case, is defined as

$$\lambda(\mu|x, y) \stackrel{def}{=} \frac{P(x, y|\mu, \hat{b}(\mu))}{P(x, y|\hat{\mu}, \hat{b})}, \tag{3.32}$$

where $\hat{\mu} = \max(0, x - y/\tau)$ and $\hat{b} = y/\tau$ are the physically allowed values maximising $P(x, y|\mu, b)$ with respect to both μ and b, while $\hat{b}(\mu)$ is a function of μ and is obtained maximising $P(x, y|\mu, b)$ with respect to b only.

The main advantage in using the profile likelihood ratio is that the quantity $-2 \log \lambda$ has an approximate χ^2 distribution with d degrees of freedom, where d is the number of parameters of the models minus the dimension of the subspace over which the numerator of the profile likelihood ratio λ has been maximised [60, 61]. In the considered case, $d = 1$, since the number of parameters is two (μ, b) and the numerator in eq. 3.32 has been maximised over b only. Therefore, the confidence interval $[\mu_1, \mu_2]$ with CL α relative to the outcome (x_0, y_0) can be directly obtained by finding the values corresponding to an increase in the $-2 \log \lambda$ function, with respect to the minimum value, equal to the α percentile of a χ^2 distribution with d degrees of freedom. As example, for $d = 1$ the required increase to obtain a 90% confidence interval is of 2.706.

3.8.1.4 Rolke-Lopez for several background sources

The Rolke-Lopez treatment (discussed above) of a Poisson process in the presence of a Poisson-distributed background with unknown mean can be generalised to n Poisson-distributed backgrounds, all appearing in the same SR, which is the case of interest for the presented analysis. In such extension, n observations in n control

samples are required, which, in general, have different values of τ. Since the signal and all the control samples are assumed to be independent, the likelihood function $P(x, y_1, \ldots, y_n | \mu, b_1, \ldots, b_n)$ of $\mu, b_1, \ldots, b_n$ given the observation $(x, y_1, \ldots, y_n)$ is determined by the product of $n + 1$ Poisson distributions:

$$P(x, y_1, \ldots, y_n | \mu, b_1, \ldots, b_n) = \frac{(\mu + b)^x}{x!} e^{-(\mu + b)} \cdot \prod_i \frac{(\tau_i b_i)^{y_i}}{y_i!} e^{-\tau_i b_i}, \qquad (3.33)$$

where $b \stackrel{def}{=} \sum_i b_i$. Analogously as for the case with 1 background, the profile likelihood ratio λ can be written as

$$\lambda(\mu | x, y_1, \ldots, y_n) \stackrel{def}{=} \frac{P(x, y_1, \ldots, y_n | \mu, \hat{b}_1(\mu), \ldots, \hat{b}_n(\mu))}{P(x, y_1, \ldots, y_n | \hat{\mu}, \hat{b}_1, \ldots, \hat{b}_n)}, \qquad (3.34)$$

where $\hat{\mu}, \hat{b}_1, \ldots, \hat{b}_n$ are the physically allowed values maximising the likelihood in eq. 3.33 over all the parameters $\mu, b_1, \ldots, b_n$, while $\hat{b}_1(\mu), \ldots, \hat{b}_n(\mu)$ are functions of μ and are obtained maximising the likelihood in eq. 3.33 over $b_1, \ldots, b_n$. Finding the maximum likelihood estimators $\hat{\mu}, \hat{b}_1, \ldots, \hat{b}_n$ requires solving a non-linear system of $n+1$ equations, which, in general, cannot be done analitically. However, for the cases in which the analitical computation is not possible, as for the case $n = 4$ considered in the presented analysis, a numerical computation can be always achieved.

As in the case with 1 background, the quantity $-2 \log \lambda$ has an approximate χ^2 distribution with 1 degree of freedom, since the number of parameters is $n + 1$ $(\mu, b_1, \ldots, b_n)$ and the numerator in eq. 3.34 has been maximised over n parameters $(b_1, \ldots, b_n)$. The confidence interval $[\mu_1, \mu_2]$ relative to the outcome $(x_0, y_0^1, \ldots y_0^n)$ is directly obtained as for the case with 1 background only.

3.8.2 Confidence belt for the number of signal events

For each background reported in Tab. 3.5, the number N_{SR} of events observed[8] for each control sample and the relative τ of the sample have been used for the evaluation

---

[8]Due to the discreteness of the Poisson distribution, the value N_{SR} has been approximated to the nearest integer. The relative truncation error is included in the systematic error.

of the confidence belt for the number $N(K^{\pm} \to \pi^{\mp}\mu^{\pm}\mu^{\pm})$ of signal events with the extended Rolke-Lopez method, described in Sec. 3.8.1. Fig. 3.28 shows the obtained confidence belt as a function of the number N_{obs} of data events observed in the SR.
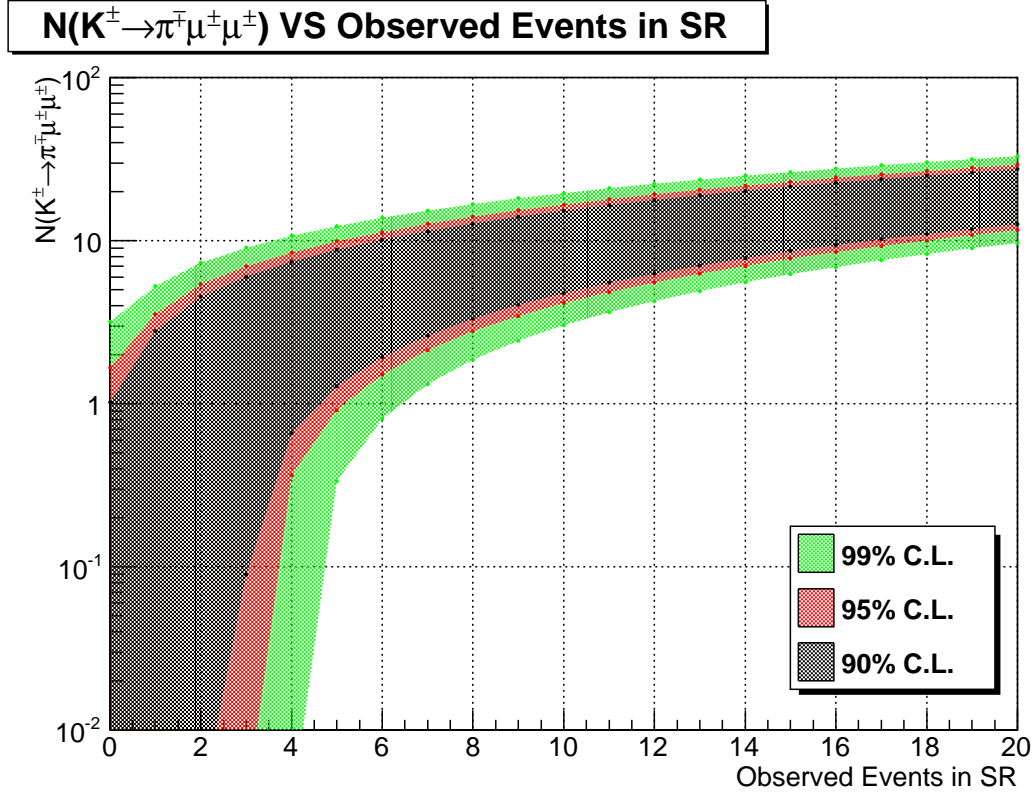
Figure 3.28: Confidence belt for the number $N(K^{\pm} \to \pi^{\mp}\mu^{\pm}\mu^{\pm})$ of signal events, obtained with the extended Rolke-Lopez method, considering all the backgrounds reported in Tab. 3.5.

3.8.3 Upper Limit for $\mathcal{B}(K^{\pm} \to \pi^{\mp}\mu^{\pm}\mu^{\pm})$

After finalising the $K^{\pm} \to \pi^{\mp}\mu^{\pm}\mu^{\pm}$ selection, the number of data events in the SR has been observed. Fig. 3.29 shows the unblinded $m_{\pi\mu\mu}$ plot for data. One event is observed in the SR.

The UL for the number $N(K^{\pm} \to \pi^{\mp}\mu^{\pm}\mu^{\pm})$ of signal events corresponding to such observation is obtained, for different CLs, considering the boundaries of the confidence
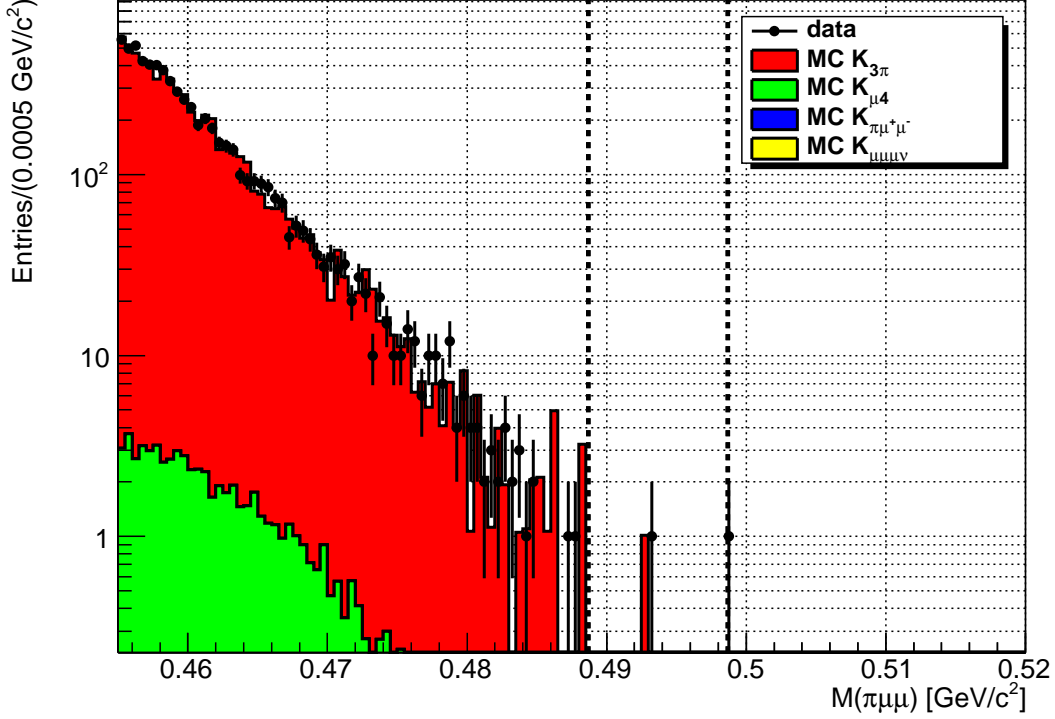
Figure 3.29: Unblinded $m_{\pi\mu\mu}$ distribution obtained for data with the final $K^{\pm} \to \pi^{\mp}\mu^{\pm}\mu^{\pm}$ selection described in Sec. 3.3.2. One event is observed within the Signal Region, indicated by the dashed lines.

belt shown in Fig. 3.28 for $N_{obs} = 1$:

$$N(K^{\pm} \to \pi^{\mp}\mu^{\pm}\mu^{\pm}) \quad < \quad 2.77^{+0.07}_{-0.21} \quad @ \ 90\% \ \text{CL}, \tag{3.35}$$

$$N(K^{\pm} \to \pi^{\mp}\mu^{\pm}\mu^{\pm}) \quad < \quad 3.52^{+0.07}_{-0.21} \quad @ \ 95\% \ \text{CL}, \tag{3.36}$$

$$N(K^{\pm} \to \pi^{\mp}\mu^{\pm}\mu^{\pm}) \quad < \quad 5.25^{+0.06}_{-0.21} \quad @ \ 99\% \ \text{CL}. \tag{3.37}$$

The quoted errors on the ULs are systematic and have been evaluated by adding and subtracting to τ its systematic error and calculating the ULs. The main contribution to the systematic error is due to the uncertainty of the $K^{\pm} \to \pi^{+}\pi^{-}\mu^{\pm}\nu$ branching fraction, which accounts for 60% of the quoted errors.

Using the values of the signal acceptance $\varepsilon_{\pi\mu\mu}$ estimated with the MC simulation (eqs. 3.10–3.12) and the number N_K of kaon decays in the fiducial volume (Sec. 3.4)

these ULs result into constraints on the signal branching fraction $\mathcal{B}(K^{\pm} \to \pi^{\mp} \mu^{\pm} \mu^{\pm})$:

$$\mathcal{B}(K^{\pm} \to \pi^{\mp} \mu^{\pm} \mu^{\pm}) = \frac{N(K^{\pm} \to \pi^{\mp} \mu^{\pm} \mu^{\pm})}{N_K \varepsilon_{\pi\mu\mu}}. \tag{3.38}$$

The 90%, 95% and 99% CL ULs for the branching fraction $\mathcal{B}(K^{\pm} \to \pi^{\mp} \mu^{\pm} \mu^{\pm})$ have been evaluated for each of the three theoretical models considered for the description of the signal. The results are reported in Tab. 3.6.

Table 3.6: Upper limits for the branching fraction $\mathcal{B}(K^{\pm} \to \pi^{\mp} \mu^{\pm} \mu^{\pm})$, obtained for the three theoretical models considered, for different confidence levels.

CL	UL (resonance)	UL (scalar)	UL (vector)
90%	$7.8^{+0.2}_{-0.6} \times 10^{-11}$	$7.3^{+0.2}_{-0.6} \times 10^{-11}$	$6.6^{+0.2}_{-0.6} \times 10^{-11}$
95%	$9.9^{+0.2}_{-0.6} \times 10^{-11}$	$9.3^{+0.2}_{-0.6} \times 10^{-11}$	$8.4^{+0.2}_{-0.6} \times 10^{-11}$
99%	$14.7^{+0.2}_{-0.6} \times 10^{-11}$	$13.9^{+0.2}_{-0.6} \times 10^{-11}$	$12.6^{+0.2}_{-0.5} \times 10^{-11}$

The current best limit on $\mathcal{B}(K^{\pm} \to \pi^{\mp} \mu^{\pm} \mu^{\pm}) = 1.1 \times 10^{-9}$ [1,16] should be compared with the obtained UL at 90% CL for the $\pi\mu^{+}\mu^{-}$-like model (vector). The present analysis improves the limit by a factor 16.

Chapter 4

The NA62 experiment

The NA62 Experiment at CERN SPS [62] aims to measure the branching fraction of the ultra-rare kaon decay $K^+ \to \pi^+ \nu \bar{\nu}$ with 10% precision, collecting ~ 100 events with the SM branching fraction in 3 years of data taking, starting in 2015 and with a test run in 2014. The NA62 detector [63] will be discussed in this chapter, except for the CEDAR/KTAG detector, which will be extensively described in Chapter 5.

4.1 The experimental strategy

A $K^+ \to \pi^+ \nu \bar{\nu}$ event is characterised by a positively-charged track identified as a kaon, a positively-charged track identified as a pion and the absence of any other detected particles. All the other events leading to the same experimental response, such as a $K^+ \to \pi^+ \pi^0$ decay where the π^0 is undetected, can contribute to the background.

In the NA62 experiment, the main expected source of background to $K^+ \to \pi^+ \nu \bar{\nu}$ events is due to the other decay channels of the K^+. In particular, the most frequent K^+ decay channels, reported in Tab. 4.1 [1, 62], have branching fractions up to 10^{10} times greater than the one expected for the signal. Therefore, to achieve a signal-background ratio $S/B \simeq 10$, they must be kept under control at the challenging

level of 10^{11}. Besides, due to the two neutrinos in the final state, it is not possible

Table 4.1: Most frequent K^+ decay channels and relative suppression strategy in the NA62 experiment.

Decay channel	Branching fraction (%)	Suppression strategy
$K^+ \to \mu^+ \nu$	63.55 ± 0.11	μ veto + two-body kinematics
$K^+ \to \pi^+ \pi^0$	20.66 ± 0.08	Photon veto + two-body kinematics
$K^+ \to \pi^+ \pi^+ \pi^-$	5.59 ± 0.04	Charged particle veto + kinematics
$K^+ \to \pi^0 e^+ \nu$	5.07 ± 0.04	E/p + photon veto
$K^+ \to \pi^0 \mu^+ \nu$	3.353 ± 0.034	μ veto + photon veto
$K^+ \to \pi^+ \pi^0 \pi^0$	1.761 ± 0.022	Photon veto + kinematics

to fully reconstruct a $K^+ \to \pi^+ \nu \bar{\nu}$ decay. Thus, hermetic photon vetoes, excellent particle identification systems and a precise measurement of the event kinematics are crucial aspects for the success of the experiment.

Unlike the experiments E787 and E949 [42] (Sec. 1.2.4) which used kaons at rest, the NA62 experiment will be using high-momentum ($75\,\mathrm{GeV}/c$) K^+ decaying in flight [62]. An advantage of this choice is the higher energy of the decay products, which increases the π^0 detection efficiency of the $K^+ \to \pi^+ \pi^0$, the $K^+ \to \pi^+ \pi^0 \pi^0$ and $K^+ \to \pi^0 \ell^+ \nu$ decays ($\ell = e, \mu$). A disadvantage of a high-momentum beam is that pions and protons, which dominate the secondary beam, cannot be efficiently separated from kaons. As a consequence, the tracking detectors upstream of the decay region are exposed to a particle flux ~ 17 times greater than the kaon one. It is worth noting that all the other detectors are not affected by this issue: the detectors downstream of the decay region are not illuminated by the undecayed particles of the beam, which keep travelling in the beam pipe, nor by the muons from pion decays, which are mostly located in the non-instrumented region in and around the beam pipe, thanks to the small transverse momentum released in the decay; the CEDAR/KTAG (Chapter 5), although located upstream of the decay region, is purposely sensitive to the kaon component only.

The kinematics of the $K^+ \to \pi^+ \nu \bar{\nu}$ decay is sketched in Fig. 4.1: since the two neutrinos are undetectable, only the K^+ 3-momentum $\vec{p}_K$ and the π^+ 3-momentum $\vec{p}_\pi$

can be measured. Therefore, the kinematics can be described by the variable $m_{miss}^{2\,(\pi)}$,
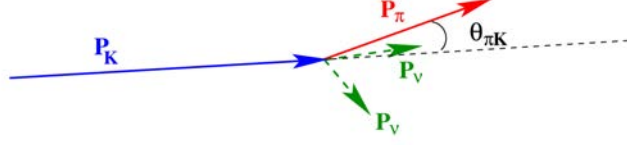
Figure 4.1: Kinematics of the $K^+ \rightarrow \pi^+ \nu \bar{\nu}$ decay.

defined as the square of the difference between the kaon candidate 4-momentum P_K and the pion candidate 4-momentum P_π, assuming the detected particles are actually a K^+ and a π^+:

$$m_{miss}^{2\,(\pi)} \stackrel{def}{=} (P_K - P_\pi)^2 \tag{4.1}$$

$$= m_K^2 + m_\pi^2 - 2E_K E_\pi + 2|\vec{p}_K||\vec{p}_\pi| \cos\theta_{\pi K}, \tag{4.2}$$

where $E_K = \sqrt{|\vec{p}_K|^2 + m_K^2}$, $E_\pi = \sqrt{|\vec{p}_\pi|^2 + m_\pi^2}$ and $\theta_{\pi K}$ is the angle between $\vec{p}_K$ and $\vec{p}_\pi$. If the assumed mass hypotheses are correct, the $m_{miss}^{2\,(\pi)}$ variable is a Lorentz invariant and can be evaluated in an arbitrary reference frame. The $m_{miss}^{2\,(\pi)}$ distribution for the signal and the main K^+ decay channels is examined:

- The three-body decay $K^+ \rightarrow \pi^+ \nu \bar{\nu}$ has a continuous distribution in $m_{miss}^{2\,(\pi)}$, with a lower and an upper limit. Since $P_K = P_\pi + P_\nu + P_{\bar{\nu}}$, $m_{miss}^{2\,(\pi)} = (P_K - P_\pi)^2 = (P_\nu + P_{\bar{\nu}})^2$. The minimum value is reached when the two neutrinos have the same 3-momentum: they behave like a single particle with mass $m_\nu + m_{\bar{\nu}}$, therefore $m_{miss}^{2\,(\pi)} = (m_\nu + m_{\bar{\nu}})^2 \approx 0$. The maximum value is obtained for the configuration with the π^+ at rest in the kaon rest frame: in such reference frame $P_K = (m_K, \vec{0})$ and $P_\pi = (m_\pi, \vec{0})$, leading to $m_{miss}^{2\,(\pi)} = (m_K - m_\pi)^2$.

- The two-body decay $K^+ \rightarrow \pi^+ \pi^0$ results in a peak at $m_{miss}^{2\,(\pi)} = m_{\pi^0}^2$. This follows from the relation $P_K = P_\pi + P_{\pi^0}$.

- The decay $K^+ \rightarrow \mu^+ \nu$, although it is a two-body decay as well, does not result in a peak because the assumption of the pion candidate being a π^+ is wrong:

the muon energy E_μ is wrongly estimated as E_π by associating the pion mass to the muon 3-momentum. The Lorentz invariance is broken by the additional term $\delta P = (E_\pi - E_\mu, \vec{0})$, which does not transform as a 4-vector. Hence, the $m^{2\,(\pi)}_{miss}$ depends on the reference frame and must be evaluated in the laboratory frame. Since

$$m^{2\,(\pi)}_{miss} = (P_\nu - \delta P)^2 = m_\nu^2 - 2(E_\pi - E_\mu)\left(E_K - \frac{E_\pi + E_\mu}{2}\right),$$

and in the laboratory frame $\frac{m_\mu^2}{m_K^2}|\vec{p}_K| \lesssim |\vec{p}_\pi| \lesssim |\vec{p}_K|$, the $m^{2\,(\pi)}_{miss}$ is always negative and approaches 0 for $|\vec{p}_\pi| \to |\vec{p}_K|$.

- The three-body decay $K^+ \to \pi^+\pi\pi$ has a continuous distribution in $m^{2\,(\pi)}_{miss}$, with a lower and an upper limit. Since $P_K = P_\pi + P_{\pi_2} + P_{\pi_3}$, $m^{2\,(\pi)}_{miss} = (P_K - P_\pi)^2 = (P_{\pi_2} + P_{\pi_3})^2$. Analogously as for the $K^+ \to \pi^+\nu\bar{\nu}$ decay, the minimum value is reached when the two undetected pions have the same 3-momentum, leading to $m^{2\,(\pi)}_{miss} = 4m_\pi^2$, while the maximum value is $m^{2\,(\pi)}_{miss} = (m_K - m_\pi)^2$, which is the same as for the signal, and is obtained for the configuration with the π^+ at rest in the kaon rest frame.

Fig. 4.2 shows the $m^{2\,(\pi)}_{miss}$ distribution for signal and backgrounds from the main K^+ decay channels: the backgrounds are normalized according to their branching fraction; the signal is multiplied by a factor 10^{10} [64].

The variable $m^{2\,(\pi)}_{miss}$ can be used to reject the backgrounds from the most frequent K^+ decay channels, which account for 92% of the K^+ decays, by defining two signal mass regions in which a significant increase in the signal-background ratio S/B is expected:

Region I: between 0 and the $K^+ \to \pi^+\pi^0$ peak;

Region II: between the $K^+ \to \pi^+\pi^0$ peak and the $K^+ \to \pi^+\pi^+\pi^-$ threshold $\approx 4m_\pi^2$.
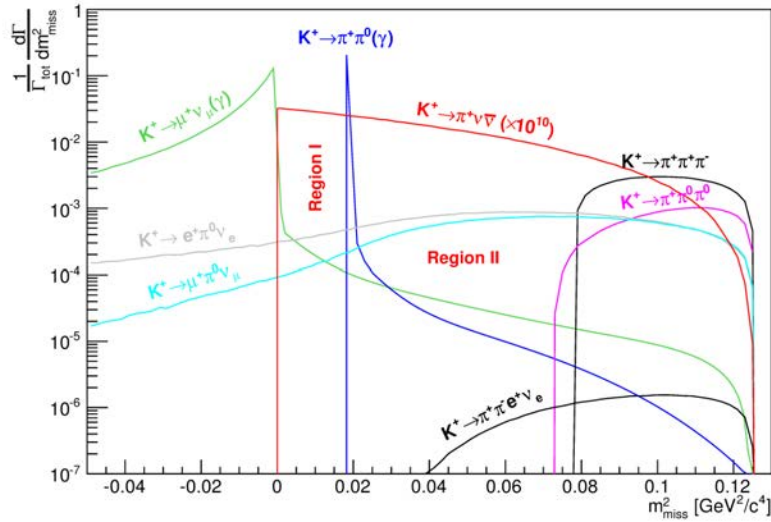
Figure 4.2: $m_{miss}^{2\,(\pi)}$ distribution for signal and backgrounds from the main K^+ decay channels: the backgrounds are normalized according to their branching fraction; the signal is multiplied by a factor 10^{10}.

Moreover, with the introduction of the constraint on the π^+ momentum in the laboratory frame

$$15 \text{ GeV}/c < |\vec{p}_\pi| < 35 \text{ GeV}/c, \tag{4.3}$$

to achieve the required π-μ separation (Sec. 4.3.3), the background rejection power of the $m_{miss}^{2\,(\pi)}$ requirement is further improved, since the $K^+ \to \mu^+\nu$ and $K^+ \to \pi^+\pi\pi$ decays approach the signal regions for higher and lower pion momenta respectively.

4.2   The NA62 beam

The NA62 experiment is located at the ECN3 zone in the CERN North Area and will be using K^+ mesons decaying in flight from an unseparated $75 \text{ GeV}/c$ hadron beam. The unseparated beam is produced by steering to the T10 Beryllium target (Sec. 2.1) the $400 \text{ GeV}/c$ primary proton beam, delivered by the SPS in spills (also called "bursts") with a 10 s flat top and ~ 30 s duty cycle. The secondary beam is shaped by a collimator, which selects only the outgoing particles within an angle of 6 mrad; it is focussed by three quadrupole magnets and bent vertically by the first of two front-end

achromats, each formed of four dipole magnets. The first pair, of different polarities, bends the beam downwards and then upwards, allowing only the particles in a narrow momentum band, centred in $75\,\mathrm{GeV}/c$, to keep travelling along the beam line. All the others particles are deflected by a different angle and are dumped by a set of collimators. At this point, the selected beam passes through a tungsten radiator, $1.3X_0$ thick: this makes positrons lose enough energy via bremsstrahlung radiation to be rejected after the second pair of dipole magnets, which work analogously to the first pair and restore the initial beam trajectory. After the first achromat, another three quadrupole magnets refocus the beam, which at this stage has an average momentum of $75\,\mathrm{GeV}/c$ and a spread of $0.8\,\mathrm{GeV}/c$ (RMS), it is composed of positively-charged particles only and is cleaned from more than 99.6% of the initial positrons [63].

To optimise the kaon identification in the CEDAR/KTAG, a pair of quadrupole magnets makes the beam wider and more parallel: the beam profile and the beam divergence have been measured to be $56 \times 30\,\mathrm{mm}^2$ (± 2 RMS) and $\leq 80\,\mu\mathrm{rad}$ respectively [65]. Another pair, downstream of the CEDAR/KTAG, refocus the beam to make it convergent towards a waist at the end of the experimental area.

Finally, before entering the decay region, the beam passes through the second achromat, which houses the three stations of the GigaTracker (GTK) spectrometer (Sec. 4.3.2.1), respectively placed before, between and after two dipole magnet pairs, in order to measure the beam momentum. After the second achromat, the beam is bent by an angle of $1.2\,\mathrm{mrad}$, in order to compensate for the deflection induced by the magnet MNP33 (Sec. 4.3.2.2), and to match the LKr calorimeter beam pipe hole. The beam profile and the beam divergence at the entrance of the decay region are $55.0 \times 22.8\,\mathrm{mm}^2$ (± 2 RMS) and $90\,\mu\mathrm{rad}$ respectively [63]. At the end of the experimental hall, the residual beam is deflected by $+21.6$ mrad by a last dipole magnet and sent to a beam-dump, in order to avoid the SAC calorimeter (Sec. 4.3.4.3). Fig. 4.3 shows the NA62 beam trajectory downstream of the GigaTracker spectrometer [63].
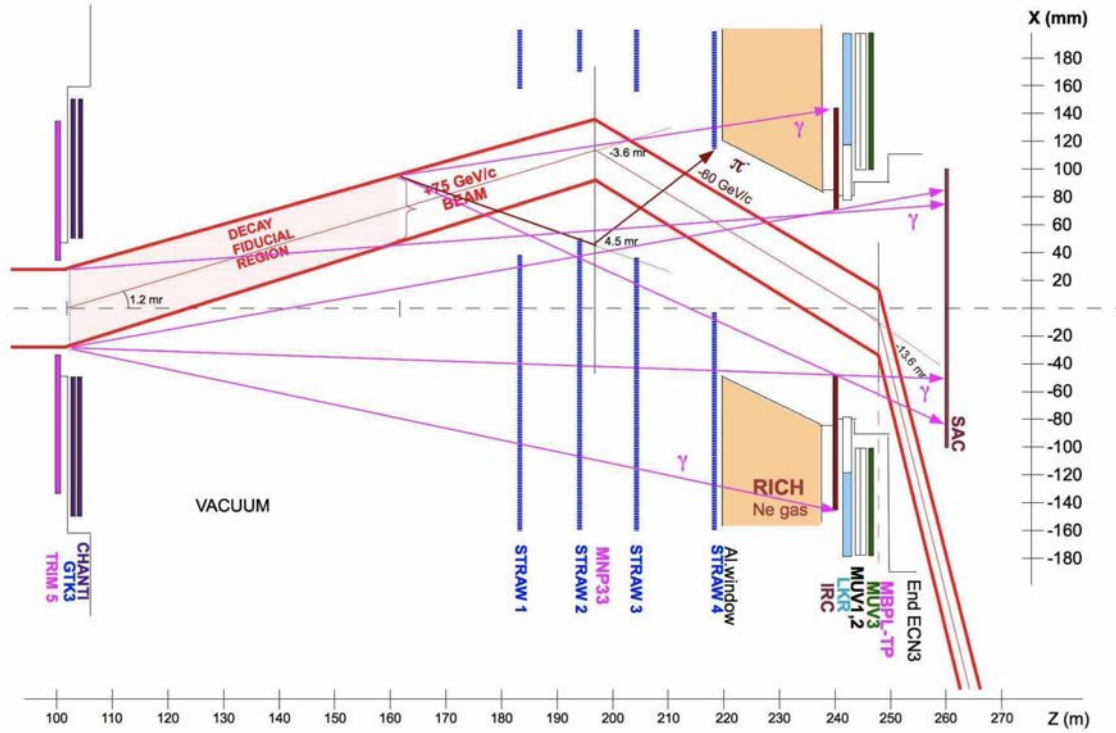
Figure 4.3: Schematic layout of the beam downstream of the GigaTracker spectrometer.

The composition, the rate and the other main beam parameters are shown in Tab. 4.2, together with a comparison with the NA48/2 beam (Sec. 2.1) [63].

4.3 The detector overview

The NA62 detector layout is shown in Fig. 4.4 and will be described in this section. The CEDAR/KTAG detector, whose upgrade, test and commissioning are presented in this thesis, is extensively described in Chapter 5. A detailed description of each individual component of the NA62 detector can be found in Ref. [63]. The Cartesian coordinate system chosen in the laboratory reference frame is the following: the origin is at the centre of the T10 Beryllium target, the z-axis is collinear with the detector axis and points downstream, the y-axis points up and the x-axis is defined to form a right-handed system.

Table 4.2: Comparison between the NA48/2 and the NA62 beams.

Experiment	NA62	NA48/2
Mean Momentum (GeV/c)	75	60
Rate (MHz): p	173	2.9
K^+	45	1.0
π^+	525	11.1
e^+, μ^+	$\sim 0.3, \sim 6$	$\sim 3, \sim 0.13$
Total	750	~ 18
K^+ decays/year in fiducial volume	4.5×10^{12}	1.0×10^{11}
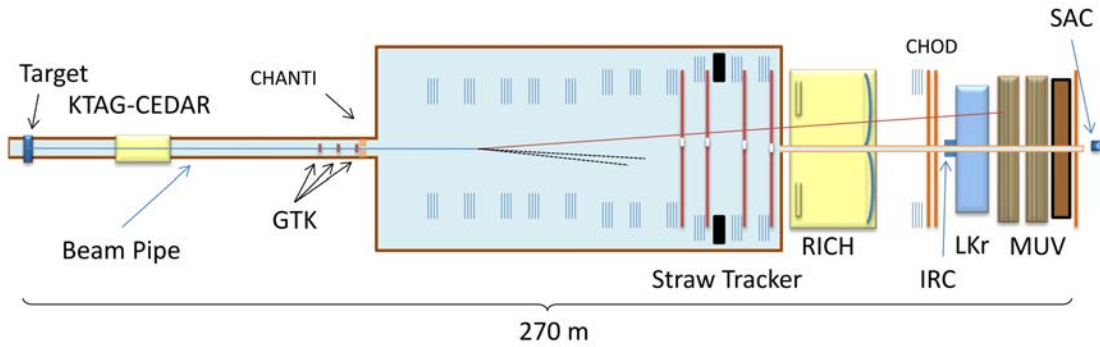
Figure 4.4: The NA62 detector layout.

4.3.1   The decay region

The decay region [63] starts 105 m downstream of the centre of the Beryllium target and is contained in a vacuum (at $< 10^{-6}$ mbar) cylindrical tank, to keep the background due to the beam scattering below about 1 event/year.

The cylindrical tank is 114 m long and its diameter goes from 1.92 m in the first 53 m to 2.4 m in the following 24 m and finally to 2.8 m in its last 37 m, which host the Straw Tracker spectrometer (Sec. 4.3.2.2). Due to the geometric acceptance of the first Straw chamber, the decay region is limited to be 65 m long.

Downstream of the vacuum tank, the undecayed beam particles remain in the vacuum, contained by a thin aluminium pipe with inner and outer diameters of 168 mm and 172 mm, respectively.

4.3.2 Tracking systems

A precise measurement of the kaon and the pion 3-momenta is essential for the selection of the $K^+ \to \pi^+ \nu \bar{\nu}$ decay and to reduce the background using the $m_{miss}^{2\,(\pi)}$ variable, as described in Sec. 4.1. In the NA62 experiment, the two detectors involved in momentum measurement are:

- the GigaTracker spectrometer, to measure the kaon momentum;

- the Straw Tracker, to measure the momenta of the charged decay products.

4.3.2.1 The GigaTracker (GTK) spectrometer

The GigaTracKer (GTK) is a beam spectrometer, situated immediately upstream of the decay region, which provides precise measurements of momentum, time and angle of the incoming hadron beam. The spectrometer is formed of three stations (GTK1, GTK2 and GTK3) mounted around the four dipole magnets of an achromat as shown in Fig. 4.5 [63]. Each station is made of one hybrid silicon pixel detector
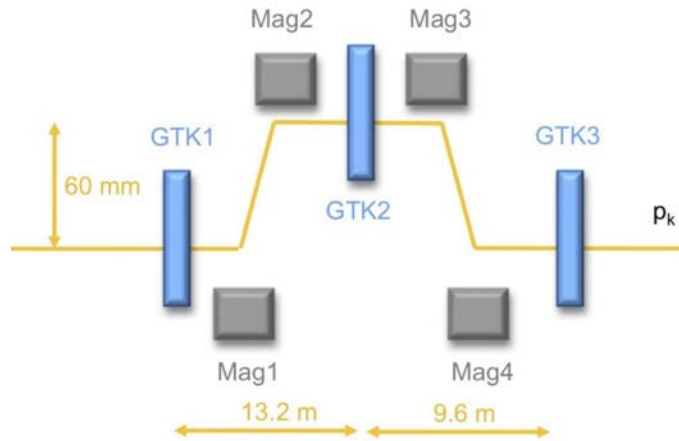
Figure 4.5: Schematic layout of the GTK spectrometer.

with a size of $63.1 \times 29.3 \, \mathrm{mm}^2$ containing 18000 $300 \times 300 \, \mu\mathrm{m}^2$ pixels arranged in a matrix of 90×200 elements [63]. The pixel size of $300 \times 300 \, \mu\mathrm{m}^2$ is small enough to

achieve a measurement of the kaon momentum with a resolution of

$$\frac{\sigma(p)}{p} \sim 0.2\%, \tag{4.4}$$

and of the kaon direction with a resolution of $\sigma_\theta = 16\,\mu$rad (the beam divergence is about $90\,\mu$rad). The required resolutions have put constraints on the choice of a sensor thickness of 200 μm, corresponding to $0.22\% X_0$, since the amount of material crossed by the beam at each station influences the angle measurement.

A challenging aspect of the GTK spectrometer is the high rate environment: due to the use of an unseparated beam, the spectrometer has to sustain a high and non-uniform beam rate of 0.75 GHz in total, with a peak of 1.3 MHz/mm^2 around the centre. Fig. 4.6 shows the expected beam intensity distribution at the GTK3 station [63]. In order to reduce the kaon-pion mismatching to a negligible level, the
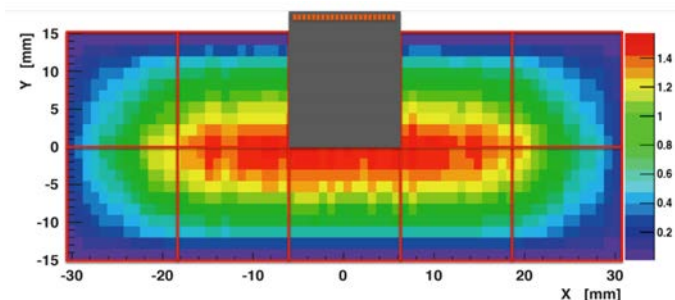
Figure 4.6: Beam intensity distribution over GTK3 station (expressed in MHz/mm^2). One of the 2 x 5 read-out chip is drawn.

required track time resolution using all three stations is 150 ps (RMS). To meet this requirement each silicon sensor is bump-bonded to 2×5 read-out chips (Fig. 4.6), each of which delivers a time resolution of better than 200 ps for a pixel hit.

4.3.2.2 The Straw Tracker

The Straw Tracker [63] is a spectrometer which provides precise measurements of the momentum, position and direction of the charged particles originating from the decay region. It is made of 4 straw chambers and a dipole magnet with momentum

kick $p_t = 270$ MeV/c (corresponding to an integrated magnetic field of ~ 0.86 Tm), placed after the first pair of chambers.

Every chamber is formed of 1792 light straw tubes, arranged on 4 different orientations (called views), orthogonally to the beam axis: X(0°), Y(90°), U(-45°) and V($+45$°). Fig. 4.7a shows a sketch illustrating the view orientations on a single straw chamber [63]. Each view is made of four planes of straw tubes staggered as shown in Fig. 4.7b. Such layout is required for resolving reconstruction ambiguities.

<table>
<tr><td>(a)</td><td>(b)</td></tr>
</table>
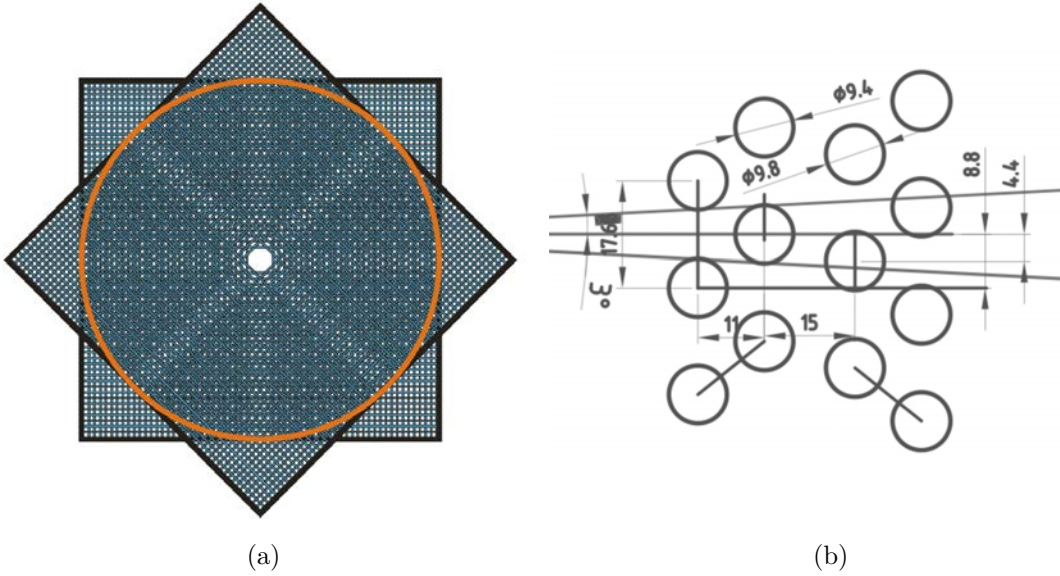
Figure 4.7: Schematic layout (a) of a single straw chamber and (b) of the straws in a view.

The active volume of the detector is octagonal, with radius of 2.1 m, and and each view has a 12 cm wide region for the beam in the middle of the frame without straws. Each straw tube is 2.1 m long and 9.8 mm in diameter and is filled with a gas mixture of Argon (70%) + CO_2 (30%) [63]. With such gas mixture, the point resolution on a single view is $\sigma_x = \sigma_y \leq 130$ μm, while the expected track momentum resolution is

$$\frac{\sigma(p)}{p} = (0.32 \oplus 0.008 \cdot p)\%, \tag{4.5}$$

where the momentum p is expressed in GeV/c. The first term is due to the effect of

the multiple scattering, while the second one is a consequence of the spacial resolution on the reconstructed track points.

4.3.3 Particle identification detectors

Kaon identification is required to reduce to a negligible level the background due to the beam interaction with residual gas in the vacuum tank; pion identification is essential to reject $K^+ \rightarrow \mu^+\nu$ decays. The detectors dedicated to particle identification are:

1. The CEDAR/KTAG, to identify and time-stamp kaons in the unseparated beam;

2. The Muon veto system (MUV), to veto the $K^+ \rightarrow \mu^+\nu$ decays at 10^5 level;

3. The RICH, to provide an extra 10^2 rejection factor for the π-μ separation and precise time measurement.

The detectors for pion identification will be discussed in this section, while the CEDAR/KTAG is treated separately in Chapter 5.

4.3.3.1 The muon veto system (MUV)

The muon veto system (MUV) is formed of three detectors (MUV1, MUV2, and MUV3). The first two modules, MUV1 and MUV2, are downstream of the LKr calorimeter and work as hadronic calorimeters for the measurement of deposited energies and shower shapes of incident particles, while the MUV3 is located behind a 80 cm thick iron wall and is employed as a fast muon veto in the lowest trigger level (L0), as well as for offline muon identification. Fig. 4.8 shows the MUV system [65]. The MUV1 module is a newly constructed detector, while the MUV2 detector is the front module of the former NA48 hadron calorimeter (HAC) described in Sec.2.6, mounted backwards to allow a better servicing access to the PMTs. Both modules are classic iron-scintillator sandwich calorimeters with 24 (MUV1) and 22 (MUV2) layers of scintillator strips, alternated with 25 (MUV1) and 23 (MUV2) iron
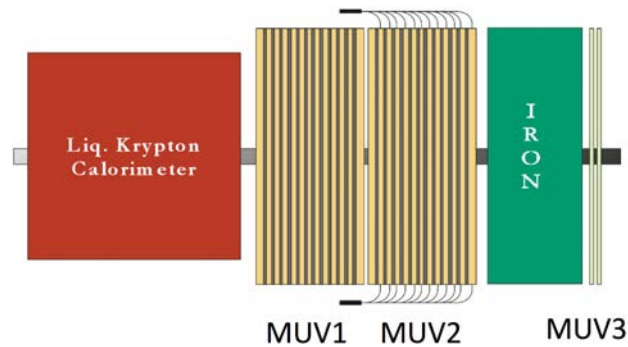
Figure 4.8: Schematics of the MUV system layout.

plates. Each plate has dimensions of $2600 \times 2600 \times 25 \, \text{mm}^3$, and contain a central hole $212 \, \text{mm}$ in diameter[1]. In both modules, the scintillator strips are alternately oriented in the horizontal and vertical directions.

The MUV3 consists of an array of 12×12 scintillator tiles of $220 \times 220 \times 50 \, \text{mm}^3$ size, installed over a surface of $2640 \times 2640 \, \text{mm}^2$. Eight smaller tiles are mounted around the beam pipe. Fig. 4.9 shows the MUV3 layout. The PMTs used for the MUV3

(a)   (b)
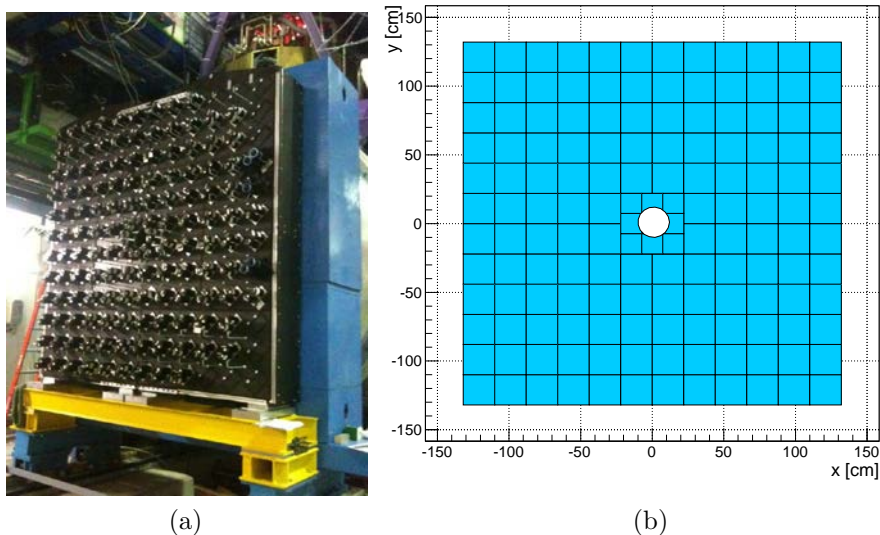
Figure 4.9: (a) The MUV3 detector and (b) the MUV3 layout.

---

[1]The first and the last plate of the MUV1 have a dimension of $3200 \times 3200 \times 25 \, \text{mm}^3$ in order to hold the MUV1 structure.

readout are positioned about 20 cm downstream, in a light-tight box. This geometry reduces to below 250 ps the time jitter caused by different paths of photons from particles hitting different parts of the scintillator tile. Each tile is read out by two PMTs and the coincidence of the two PMT signals is used for timing purposes. This avoids triggering on the early ($\sim$ 2 ns) signals due to Cherenkov photons radiated in the PMT window. The MUV3 time resolution σ_t, as measured in the NA62 Technical Run 2012, is $\sigma_t \approx 500$ ps [65].

4.3.3.2 The RICH detector

A Ring-Imaging CHerenkov counter (RICH) is employed to improve the π-μ separation and to achieve a precise timing of the pion candidate. The RICH consists of a 17 m long vessel, with diameter of 3.8 m, filled with Neon gas at atmospheric pressure and crossed by the beam pipe. Fig. 4.10 shows the RICH vessel installed in the NA62 cavern. The internal optics are made of a mosaic of 20 hexagonal shape spherical

Figure 4.10: The RICH vessel installed in the NA62 cavern.

mirrors ($\sim$ 6 m^2 in total) and are used to image the Cherenkov cone into a ring on its focal plane. To avoid the reflected light intercepting the beam pipe, the mirrors are divided into two spherical surfaces, with centre of curvature respectively on the left and on the right of the beam pipe, which direct the light towards two flanges,

located at the upstream end of the vessel. Each flange has a diameter of about 0.7 m and hosts 1000 PMTs in honeycomb configuration with a centre-to-centre distance of 18 mm. Such granularity is an essential parameter to optimize the angular resolution of the detector. By design, the radius r of a Cherenkov ring obtained at the PMT flanges is

$$r = f \tan \vartheta_c, \tag{4.6}$$

where $f = 17$ m is the focal length of the spherical mirror and ϑ_c is the angle of the Cherenkov emission. The angle ϑ_c for a particle of mass m and momentum p travelling in a radiator with refractive index n is determined by the relation

$$\cos \vartheta_c = \frac{1}{n\beta} = \frac{1}{n}\sqrt{1 + \frac{m^2}{p^2}}, \tag{4.7}$$

where β indicates the particle velocity in units of the speed of light c. The minimum momentum p_{th} required to emit Cherenkov radiation is defined by the condition $\cos \vartheta_c = 1$:

$$p_{th} = \frac{m}{\sqrt{n^2 - 1}}. \tag{4.8}$$

Since the Neon refractive index n at atmospheric pressure is $(n - 1) \approx 66 \times 10^{-6}$, the threshold for Cherenkov emission for pions is $p_{th}^\pi = 12$ GeV/c. This limits the pion momentum to be $p \geq 15$ GeV/c in order to have enough photons to fit a ring. Considering that $n - 1 \ll 1$ and $m/p_{th} \ll 1$, the radius r in eq. 4.6 can be approximated as

$$r = f \tan \vartheta_c \approx f\vartheta_c \approx f\sqrt{\frac{2(n-1)}{n} - \frac{m^2}{np^2}}. \tag{4.9}$$

Hence, by measuring the radius r and using the value of the momentum p measured by the Straw tracker, it is possible to have a measurement of the particle mass m, distinguishing between pions and muons. However, the π-μ separation depends on the track momentum p: for a given radius resolution $\delta r/r$, the corresponding

resolution $\delta m/m$ on the particle mass is

$$\frac{\delta m}{m} \approx - \left[\frac{(n-1)\,p^2}{m^2} - \frac{1}{2} \right] \frac{\delta r}{r}, \qquad (4.10)$$

which deteriorates as the momentum p increases. For momenta $p \geq 35$ GeV$/c$ the probability of a μ being mis-identified as a π is higher than the maximum affordable value (10^{-2}). The required time resolution of the RICH is below 100 ps.

4.3.4 Photon Vetoes

The photon veto system is essential to reduce the background due to many K^+ decay channels, the most challenging of which is the $K^+ \to \pi^+\pi^0$ decay. The requirement on the π^+ momentum $p < 35$ GeV$/c$ guarantees that the two photons from the π^0 have at least a total energy of 40 GeV. Considering a rejection power of 10^4 for the $m_{miss}^{2\,(\pi)}$ condition, the probability to miss both photons must be less than 10^{-8}. A suitable way to satisfy such a requirement is to install hermetic photon vetoes for photons from the decay volume travelling with an angle ϑ up to 50 mrad. With this configuration, only 0.2% of the $K^+ \to \pi^+\pi^0$ events with π^+ momentum between 15 and 35 GeV$/c$ have a low-energy ($E \lesssim 1\,\text{GeV}$) photon escaping at larger angles, while the other one is within the detector acceptance. The detectors providing an angular coverage up to 50 mrad can be divided into three groups:

- The Large Angle Vetoes (LAV): 12 stations (ANTI 1-12) covering the region 8.5 mrad $< \vartheta < 50$ mrad;

- The LKr calorimeter, providing the coverage of the forward region (1.5 mrad $< \vartheta < 8.5$ mrad);

- The Small Angle Vetoes (SAV): the Intermediate Ring Calorimeter (IRC) and the Small Angle Calorimeter (SAC), to cover the region around the beam pipe ($\vartheta \leq 1.5$ mrad).

More than 80% of $K^+ \to \pi^+\pi^0$ events have both photons from the π^0 in the LKr calorimeter acceptance, while most of the remaining events have one photon in the LKr calorimeter and one in the LAVs. Requiring photon vetoes inefficiencies lower than 10^{-4} for photons with $E \gtrsim 1\,\mathrm{GeV}$, the dominant contribution to the $K^+ \to \pi^+\pi^0$ background is due to events with a low-energy photon outside acceptance. For those events, since the photon energies in the π^0 decay are anti-correlated, there is a high-energy photon either in the LKr ($E \gtrsim 20$ GeV) or in the SAV ($E \gtrsim 50$ GeV) acceptance. Therefore, to keep this background under control and reach the required π^0 rejection, the LKr and SAV inefficiencies for photons of such energies must be below 10^{-5}.

4.3.4.1 Large Angle Vetoes (LAV)

The Large Angle Vetoes (LAV) are 12 stations (ANTI 1-12) made of rings of lead-glass blocks recovered from the OPAL electromagnetic calorimeter barrel [66], and provide the coverage of the region 8.5 mrad $< \vartheta <$ 50 mrad. Eleven of them are installed in the NA62 vacuum tank, while the most downstream one (ANTI 12) is located between the RICH and the NA48 hodoscope (Sec. 2.4).

Each block is a trapezoidal Cherenkov counter exploiting lead-glass ($\simeq 74\%$ PbO) as active material and with a PMT glued to one of the block's faces. The typical block dimensions are $\sim 11 \times 11$ cm^2 for the PMT face, $\sim 9 \times 9$ cm^2 for the opposite face and 37 cm for the height. The block equivalent thickness is $\approx 0.66 X_0/$cm. Fig. 4.11 shows the lead-glass block layout in a LAV station: the counters are placed radially to form several rings and each ring is staggered with respect to the adjacent ones by a fifth of the block size, in order to avoid cracks and have always at least 3 overlapping blocks ($\approx 20 X_0$) in the projection along the beam axis. The number of rings belonging to each station and the number of blocks used for each ring vary from station to station, as specified in Tab. 4.3.

The LAV photon inefficiency was measured in 2007 with 200 MeV and 500 MeV

Figure 4.11: Internal view of the ANTI-1.

Table 4.3: Geometrical parameters of the LAV stations.

ID ANTI	Rings	Blocks/ring	Inner radius
1-5	5	32	532 mm
6-8	5	48	772 mm
9-11	4	60	972 mm
12	4	64	1072 mm

electrons at the Frascati Beam Test Facility. The results obtained are [67]:

$$\eta_{\text{LAV}}(200\,\text{MeV}) \;=\; (12.0^{+9.2}_{-5.2}) \times 10^{-5}, \tag{4.11}$$

$$\eta_{\text{LAV}}(500\,\text{MeV}) \;=\; (1.1^{+1.8}_{-0.7}) \times 10^{-5}. \tag{4.12}$$

4.3.4.2 The LKr calorimeter

The NA48 LKr calorimeter is used as a photon veto in the forward angle region $1.5\,\text{mrad} \le \vartheta \le 8.5\,\text{mrad}$. The calorimeter layout and performances are described in Sec. 2.5. The LKr calorimeter photon detection inefficiency $\eta^{\gamma}_{\text{LKr}}$ was evaluated analysing the NA48/2 $K^+ \to \pi^+\pi^0$ data sample obtained from a minimum bias run in 2004. The final result for the inefficiency $\eta^{\gamma}_{\text{LKr}}$ is [67]:

$$\eta^{\gamma}_{\text{LKr}} < 0.9 \times 10^{-5} \quad @\,90\%\ C.L.\ (E_{\gamma} > 10\ \text{GeV}), \tag{4.13}$$

123

which is within the NA62 requirements.

4.3.4.3   Small Angle Vetoes (SAV)

The Intermediate Ring calorimeter (IRC) and the Small Angle Calorimeter (SAC) cover the angles $\vartheta < 1.5$ mrad.

The IRC is a ring-shaped shashlyk calorimeter with an inner radius of 60 mm, an outer radius of 145 mm and 21 cm thick, located immediately in front of the LKr calorimeter, surrounding the beam pipe.

The SAC is a shashlyk calorimeter with a square cross-section of $20.5 \times 20.5\,\text{cm}^2$ and thickness of 21 cm. It is placed at the end of the experimental hall, behind the last magnetic dipole which further deflects the beam by 13.6 mrad towards the beam dump and intercepts the undeflected beam trajectory. In this way it provides coverage also for the region corresponding to the beam pipe.

Both the calorimeters are made of 70 iron-scintillator planes of thickness 1.5 mm+1.5 mm. The chosen thickness corresponds to $\sim 16 X_0$, leading to a photon survival probability of $\lesssim 10^{-7}$. Fig. 4.12 shows respectively the IRC and the SAC calorimeters [63]. The inefficiency η_{SAC} of the SAC calorimeter was evaluated during a test run in 2006,

(a)   (b)
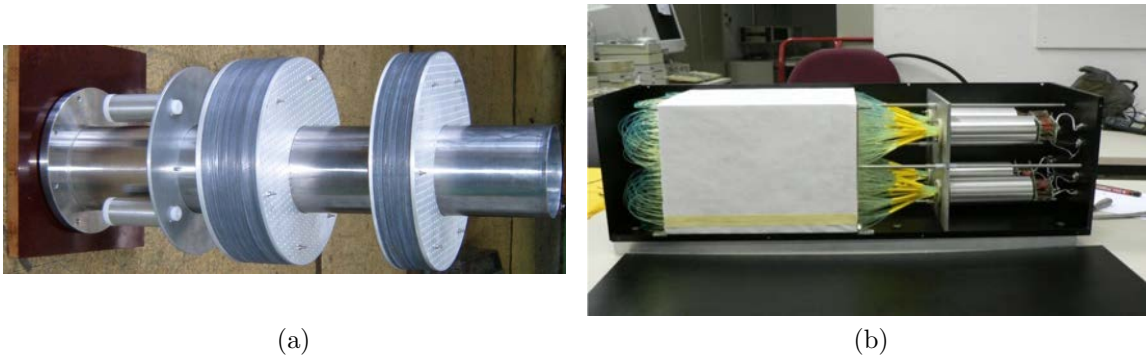
Figure 4.12: (a) The IRC and (b) the SAC calorimeters.

steering a 25 GeV electron beam to the SAC active surface. The result obtained

is [63]:

$$\eta_{\text{SAC}} = (2.9 \pm 0.3) \times 10^{-5}. \tag{4.14}$$

4.3.5 Trigger and Data Acquisition System

The particle rate to which the downstream detectors will be exposed is expected to be $\sim 10\,\text{MHz}$ [68,69]. Due to such a high rate and to the channel count ($\sim 10^5$), a "triggerless" acquisition system in which all the data are unconditionally transferred to PCs is unfeasible for the NA62 experiment. Therefore, a variety of hardware lowest-level (L0) triggers will be used to reduce the overall rate to below ~ 1 MHz preserving most of the decays of interest. The maximum allowed latency of the L0 trigger decision-taking algorithms is $1\,\text{ms}$, limited by the GigaTracker Spectrometer readout. Following a L0 trigger, most sub-detectors will transfer data to dedicated PCs, where two trigger levels (L1 and L2) will be applied via software, to reach a final rate of ~ 10 kHz. For each of the two L1 and L2 trigger levels the maximum allowed latency is $\sim \mathcal{O}(1\,\text{s})$. Fig. 4.13 shows the schematics of the NA62 trigger and data acquisition system.

At the time of the present thesis, different trigger systems and conditions are being considered and tested. In particular, two different technologies are being investigated for the implementation of the L0 Trigger Processor:

FPGA-based: an electronic board hosting field-programmable gate arrays (FPGAs) devices, in which filter algorithms are implemented at the firmware level;

PC-based: a commodity PC which stores data into the memory, performs filter algorithms and interfaces with the sub-detectors acquisition boards via a PCI-Express board [69].

These technologies will be tested and validated during the 2014 data taking, in which the foreseen beam intensity is $\sim 20\%$ of the nominal one.
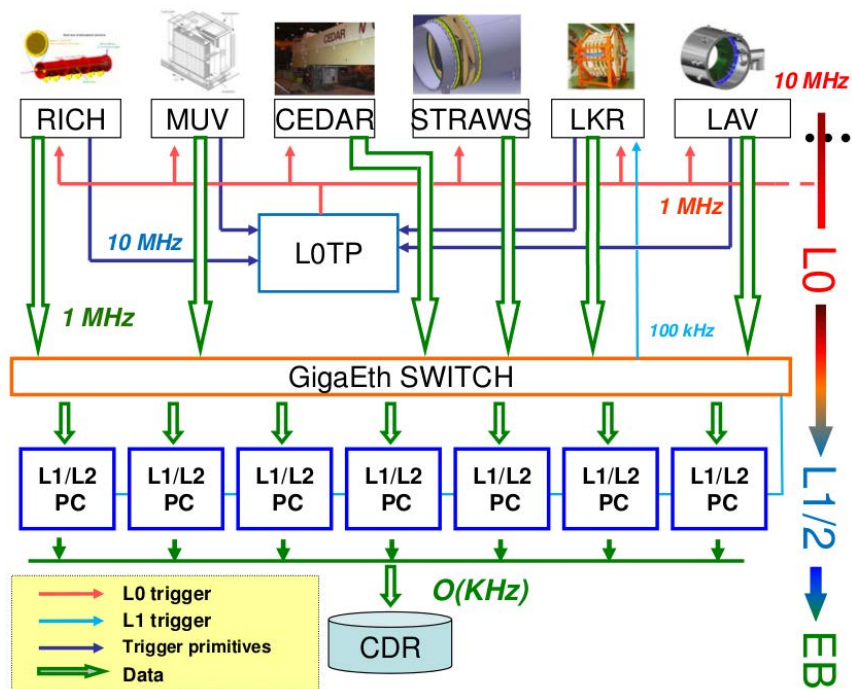
Figure 4.13: Schematics of the NA62 trigger and data acquisition system. The detectors involved into the L0 trigger sends primitive signals to the L0TP, which filters the data and sends trigger signals to the sub-detectors via the trigger distribution system. Data are then readout and transferred to PCs of the NA62 farm, which further reduce the data volume by applying the L1 and L2 software trigger algorithms. Data selected by the L2 trigger level are recorded to the Central Data Repository (CDR).

Chapter 5

The CEDAR/KTAG detector

5.1   Introduction

As discussed in Chapter 4, kaons are a minor component (6%) of the NA62 beam, since their separation in flight from the major beam components (pions and protons) is unfeasible at the beam momentum of $75\,\mathrm{GeV}/c$. As a consequence, a particle flux ~ 17 times greater than the kaon one passes through the NA62 detector, possibly interfering with the experimental measurements. In particular, beam pions interacting with the material upstream the decay volume (e.g. the GTK3) or with the residual gas in the vacuum tank may be scattered and interpreted as originating from $K^+ \to \pi^+ \nu \bar{\nu}$ decays. It has been estimated that the required vacuum pressure in order to keep such background below one event/year should be less than $6 \times 10^{-8}\,\mathrm{mbar}$ [62], a constraint unfeasible for such a large volume. Positive identification of kaons can reduce pion contribution to the $K^+ \to \pi^+ \nu \bar{\nu}$ background below the required level, and is therefore essential to meet the experimental goal.

The kaon identification is achieved by means of a ChErenkov Differential counter with Achromatic Ring focus (CEDAR) placed in the incoming beam. CEDAR counters [70, 71] have been constructed and used at CERN since the early '80s for SPS secondary beam diagnostics. The CEDAR will be filled with nitrogen gas

$(0.03X_0)$, whose refractive index n will be optimised, as a function of the pressure, for the kaon mass m_K and the beam momentum ($P_K = 75\,\mathrm{GeV}/c$). The NA62 experimental strategy requires the following conditions to be satisfied by the CEDAR detector:

- kaon tagging efficiency of at least 95%;

- kaon crossing time measurement with a resolution better than $100\,\mathrm{ps}$;

- pion rejection below 10^{-4};

- capability to perform at a nominal instantaneous rate of $45\,\mathrm{MHz}$ (kaons);

- capability to stand a radiation level of $1\ \mathrm{Gy/year}$.

To cope with the challenging $45\,\mathrm{MHz}$ kaon rate and to achieve the required time resolution, a new photon detector, called Kaon TAGger (KTAG), has been built and assembled for the CEDAR.

An overview of the principles of operation and the description of the upgraded detector, called CEDAR/KTAG, is reported in this chapter, to support the overall comprehension of the NA62 detector and to introduce the tests and data analysis performed during the 2012 Technical Run. A more detailed description of the CEDAR detector can be found in Ref. [71], while further information on its usage within the NA62 experiment can be found in Ref. [63].

5.2   CEDAR principles of operation

Cherenkov light emitted by charged particles traversing a gas radiator is focussed by the optical system (described in Sec. 5.3), to form a ring image of radius $r = f \tan \vartheta_c$, where $f = 3.24\,\mathrm{m}$ is the effective focal length of the optical system and ϑ_c is the angle of Cherenkov light emission. Unlike other Cherenkov detectors as the NA62 RICH (Sec. 4.3.3), CEDAR counters are sensitive to a fixed range of the angle ϑ_c: only the light rings passing through a mechanical diaphragm with radius $R_{\mathrm{DIA}} = 100\,\mathrm{mm}$

and a variable annular aperture $w_{\text{DIA}} = (0 \div 20)$ mm can be detected. Given a diaphragm aperture w_{DIA}, the selected angular range corresponds approximately to $(\vartheta_c^0 - 0.5 w_{\text{DIA}}/f, \vartheta_c^0 + 0.5 w_{\text{DIA}}/f)$, with $\vartheta_c^0 \overset{def}{=} R_{\text{DIA}}/f = 30.9$ mrad. The fixed angular range does not limit the CEDAR functionality: the detector can be set to be sensitive to a specific particle type with mass m_1, in a monochromatic beam with momentum p, by tuning the pressure of the gas (thus the refractive index n), according to the equation

$$\cos \vartheta_c = \frac{1}{n\beta} = \frac{1}{n}\sqrt{1 + \frac{m_1^2}{p^2}}, \tag{5.1}$$

where β indicates the particle velocity in units of the speed of light c. In addition, the CEDAR diaphragm aperture $(R_{\text{DIA}} - 0.5 w_{\text{DIA}}, R_{\text{DIA}} + 0.5 w_{\text{DIA}})$ can be set in order to stop the light from unwanted particles. Such feature makes the CEDAR detector suited for tagging minority particles in a high rate beam. The difference ΔR_c between the Cherenkov ring radius of the considered particle and the one of an unwanted particle with mass m_2 and same 3-momentum $\vec{p}$ is determined by

$$\Delta R_c = f \Delta \vartheta_c = \frac{f}{\tan \vartheta_c} \frac{\Delta \beta}{\beta} \approx \frac{f^2}{R_{\text{DIA}}} \frac{|m_2^2 - m_1^2|}{2p^2}. \tag{5.2}$$

In NA62, $m_1 = m_K$, $m_2 = m_\pi$ and $p = 75$ GeV/c, leading to $\Delta R_c \approx 2$ mm. However, several effects contribute to broadening the light ring distribution and must be taken into account while choosing the CEDAR diaphragm aperture $(R_{\text{DIA}} - 0.5 w_{\text{DIA}}, R_{\text{DIA}} + 0.5 w_{\text{DIA}})$, by adjusting the width w_{DIA}.

5.2.1 Choice of the diaphragm aperture

The most severe effects contributing to broadening the light ring distribution are listed below, sorted by relevance.

Beam divergence: particles with different directions emit non-concentric light rings. A beam divergence of $\Delta \theta_{x,y} = 80\,\mu$rad (RMS) (cf. Sec. 4.2) increases the ring RMS of $\Delta R_{div} = f \Delta \theta_{x,y} \approx 0.26$ mm. It is worth noting that this is a coherent effect: the light ring distribution is broadened because of the

averaging over many particles.

Chromatic dispersion: this effect is due to the dependence of the refractive index n, of a given material, on the light wavelength λ. The corresponding contribution ΔR_{ch} to the ring RMS can be expressed as

$$\Delta R_{ch} \approx \frac{R_{\text{DIA}}}{2\nu}, \tag{5.3}$$

where $\nu = (n_D - 1)/(n_F - n_C)$ is the Abbe number, which characterises the reciprocal dispersion of materials: n_i $(i = D, F, C)$ corresponds to the refractive index of the material at the wavelength λ_i, and $\lambda_D = 589.3\,\text{nm}$, $\lambda_F = 486.1\,\text{nm}$, $\lambda_C = 656.3\,\text{nm}$. Nitrogen at an absolute pressure of $1.7\,\text{bar}$ has an Abbe number $\nu \simeq 35$, resulting to a ring RMS increase of $\Delta R_{ch} \simeq 1.4\,\text{mm}$. However, to improve the detector performances, a chromatic corrector lens was installed within the CEDAR optical system (Sec. 5.3), reducing ΔR_{ch} by a factor of 11 ($\Delta R_{ch} \simeq 0.13\,\text{mm}$) [71].

Multiple scattering: a particle changing direction within the gas radiator emits non-concentric light rings at different positions, resulting in a broader cumulative light ring. The angular deflection (RMS) of a particle, travelling in x/X_0 radiation lengths of matter is described by the formula [1]

$$\vartheta_{sc}(p) = \frac{1}{\sqrt{3}} \frac{13.6\,\text{MeV}}{\beta c p} \sqrt{\frac{x}{X_0}} \left[1 + 0.038 \ln\left(\frac{x}{X_0}\right) \right]. \tag{5.4}$$

The contribution ΔR_{sc} to the ring RMS due to the multiple scattering of $75\,\text{GeV}/c$ beam particles traversing the N_2 gas radiator, which corresponds to $\sim 0.03 X_0$ of material, is $\Delta R_{sc} = f\vartheta_{sc} \approx 0.05\,\text{mm}$.

The quadratic sum of all the above contributions corresponds to a total ring RMS of $\Delta R_{tot} = 0.3\,\text{mm}$ (RMS). Therefore, for applications in NA62, a diaphragm full width with the range $w_{\text{DIA}} = (1.5 \div 2)\,\text{mm}$ is sufficient to accommodate at least 99% of the Cherenkov light produced by kaons (neglecting non-gaussian tails), and is more than 3 standard deviations away from the pion peak. Fig. 5.1 shows the distributions of

Cherenkov light ring radius from kaons and pions at the diaphragm plane, obtained from a simulation with the CEDAR detector filled with N_2 a pressure of 1.7 bar [72].
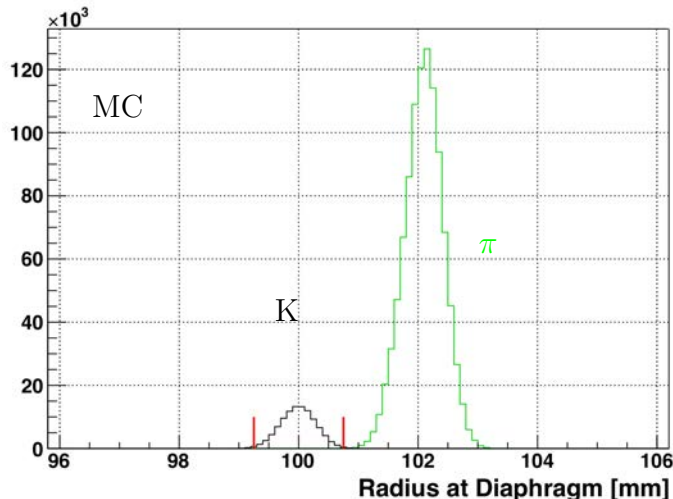
Figure 5.1: Expected distributions of the Cherenkov light ring radius at the diaphragm plane for kaons (black) and pions (green). The operating gas of the CEDAR detector is N_2 at a pressure of 1.7 bar. A diaphragm width of 1.5 mm is showed by red lines.

5.2.2 CEDAR alignment

For a correct operation of the CEDAR detector, the misalignment of the optical axis with respect to the beam axis must be as small as possible. The fine alignment of the optical axis with the beam axis is made by moving the CEDAR downstream end in the x and y directions. For this task, the vessel is supported on three points: one is located at its upstream end and two more are positioned downstream in a V-shape, at a distance $l = 4.35$ m from the first one. The alignment mechanism is based on chariots moved by right-left screw drives, connected to two motors, and it allows to produce displacements of the downstream end of the CEDAR vessel in both horizontal and vertical directions. A misalignment of Δx and Δy respectively along the x and the y axes corresponds to an average ring displacement $\Delta R_{al} = f\sqrt{\Delta x^2 + \Delta y^2}/l$. Therefore, in order to be negligible with respect to the other effects discussed in Sec. 5.2.1, quantified by the total ring RMS $\Delta R_{tot} = 0.3$ mm, the misalignment

must be much smaller than 0.3 mm on both directions. The step resolution of fine displacements in both directions is 0.01 mm and provides an angular positioning within 2 μrad.

5.3   CEDAR optical system

The CEDAR detector is a steel vessel of 55.8 cm external (53.4 cm internal) diameter and 4.5 m length. At the upstream end it is closed by a 1 m-long nose, while the downstream end of the vessel has a spherical head. Two aluminium windows of 150 μm and 200 μm (corresponding to $\sim 0.004 X_0$) seal the upstream and downstream end of the vessel respectively, in conjunction with the beam pipe. As shown in Fig. 5.2a, eight quartz spherical windows are attached at one end of the vessel and
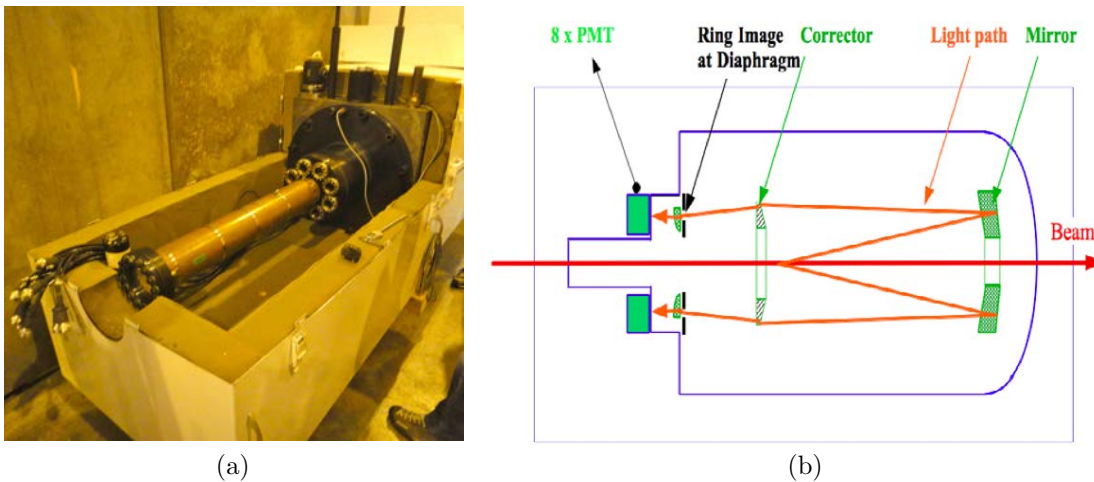
Figure 5.2: (a) picture of the upstream end of the CEDAR vessel with the nose and the quartz windows; (b) sketch of the optical system located inside the vessel.

surround the nose. The vessel is filled with N_2 gas and contains an optical system, sketched in Fig. 5.2b and formed from:

- a Mangin mirror at the downstream end of the vessel;

- a chromatic corrector lens;

- a diaphragm;

132

- eight condenser lenses.

As shown in more detail in Fig. 5.3, the Cherenkov light emitted by beam particles traversing the vessel is reflected back by the mirror, passes through the chromatic corrector and diaphragm. The mirror and the chromatic corrector share the same
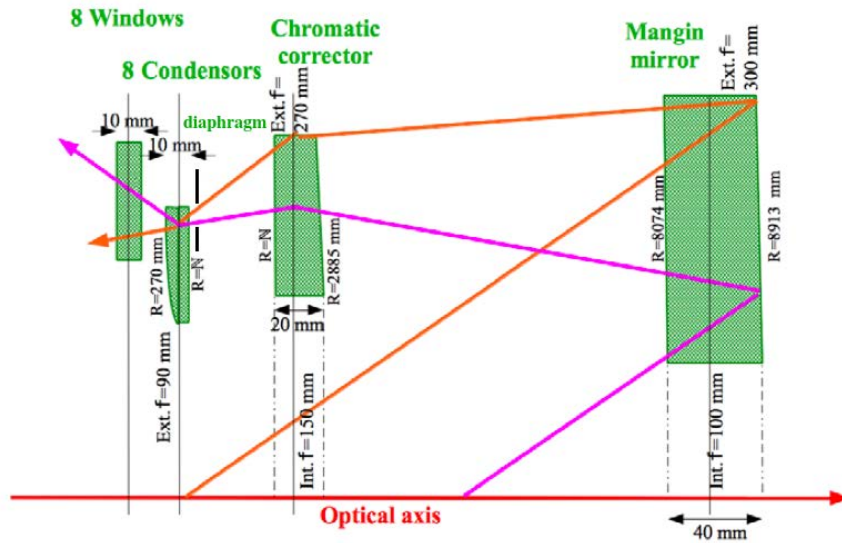
Figure 5.3: The CEDAR internal optical system with a sketch of the light path from two beam particles.

optical axis and have a hole in the centre of $100\,\mathrm{mm}$ and $150\,\mathrm{mm}$ diameter respectively. While a $100\,\mathrm{mm}$ diameter hole is required to avoid interactions with the beam particles, the chromatic corrector one is larger, to allow the propagation of Cherenkov light emitted upstream. As mentioned in Sec. 5.3, the function of the chromatic corrector is to reduce the chromatic dispersion effect, which would otherwise dominate the width of the Cherenkov light rings. Once the light path is corrected, the Cherenkov photons reach the diaphragm, which selects only light rings of radius in the range $(R_{\mathrm{DIA}} - 0.5w_{\mathrm{DIA}}, R_{\mathrm{DIA}} + 0.5w_{\mathrm{DIA}})$. As discussed in Sec. 5.3, the optimal diaphragm width for applications in NA62 is $w_{\mathrm{DIA}} = (1.5 \div 2)\,\mathrm{mm}$. Cherenkov light passing through the diaphragm aperture is focussed by eight condenser lenses in the azimuthal coordinate, as illustrated in Fig. 5.4, to form eight light spots at the quartz window plane. The condenser lenses are mounted off-axis and are radially positioned

in correspondence of the quartz windows. Finally, Cherenkov photons travel through
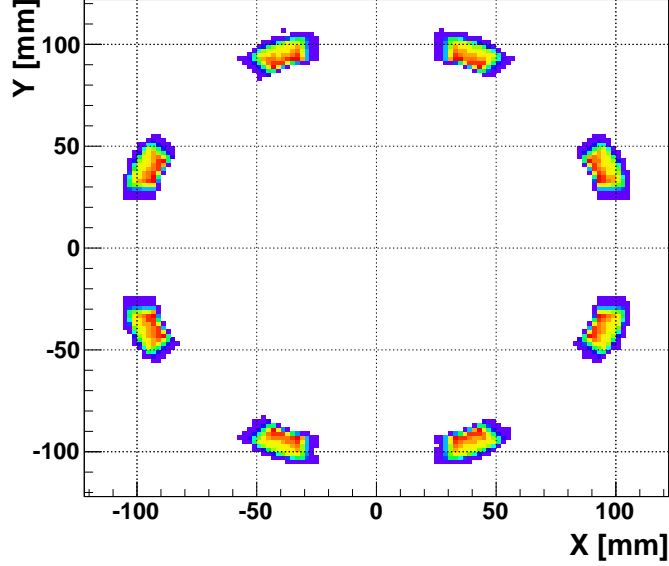
Figure 5.4: Simulated Cherenkov light ring projection at the quartz window plane. The condenser lenses create eight light spots, which are transmitted through the quartz windows.

the quartz windows and reach the eight CEDAR PMTs (EMI 9820qb), mounted at the upstream end of the quartz windows.

5.4 KTAG: the new photon detector

The mean number N_γ of Cherenkov photons emitted at an angle ϑ_c by a particle travelling into a radiator of length L is given by the Frank-Tamm formula [73]

$$N_\gamma = 2\pi\alpha L \sin^2\vartheta_c \int \frac{d\lambda}{\lambda^2}, \tag{5.5}$$

where α is the fine structure constant and λ is the photon wavelength. Using the CEDAR parameters ($L = 4.5\,\mathrm{m}$, $\vartheta_c = 30.9\,\mathrm{mrad}$) and considering the spectral range accepted of $\lambda = (200 \div 600)\,\mathrm{nm}$ [70], one finds $N_\gamma \approx 660$. However, the CEDAR optics selects only a fraction of these photons: the number N_γ^{qw} of photons exiting from the quartz windows, obtained from a MC simulation of the CEDAR detector, is $N_\gamma^{qw} \approx 230$ [74].

Such a mean photon number results into an average of about 4 photoelectrons per particle (N_{pe}) for each one of the original CEDAR PMTs. Since the PMT gain is $G \sim 2 \times 10^7$ and the average current drawn from each PMT must be below $i_{max} \simeq 0.1\,\mathrm{mA}$ [70], it follows that the maximum affordable positively-identified beam particle rate f_{max} for such technology is[1]

$$f_{max} = \frac{i_{max}}{eGN_{pe}} \approx 8\,\mathrm{MHz}. \tag{5.6}$$

It is evident that the original CEDAR PMTs cannot stand the nominal NA62 kaon rate $f_K = 45\,\mathrm{MHz}$. In addition, their time resolution is $\sigma_t \simeq 2\,\mathrm{ns}$; even assuming a 100% PMT efficiency, the resulting resolution σ_K of the kaon crossing time would be $\sigma_K = \sigma_t/\sqrt{8} \simeq 700\,\mathrm{ps}$, which is much higher than the one (100 ps) required from the NA62 experimental programme (Sec. 5.1).

To achieve the NA62 rate and timing requirements, each original CEDAR PMT has been replaced with a high-granularity configuration of single-photon counting photomultipliers. With such choice, the expected photon rate would be distributed on a number of photon detectors higher than 8, relaxing both the constraint on the maximum affordable output rate and the one on the PMT time resolution. For example, the minimum number of PMTs N_{PMT} required for the CEDAR photo-detection in order to have a maximum rate f_{PMT}^{max} on a single channel can be evaluated as

$$N_{\mathrm{PMT}} = N_\gamma^{qw}\epsilon_{\mathrm{QE}}\varepsilon\frac{f_K}{f_{\mathrm{PMT}}^{max}}, \tag{5.7}$$

where ϵ_{QE} is the Quantum Efficiency (QE) of the photo-detector technology and ε is the overall efficiency of the light collection system. Considering the realistic values $\epsilon_{\mathrm{QE}} = 0.25$ and $\varepsilon = 0.7$, it follows that a mean PMT output rate below $f_{\mathrm{PMT}}^{max} = 5\,\mathrm{MHz}$ (see Sec. 5.6) can be achieved by distributing the Cherenkov photons over $N_{\mathrm{PMT}} \simeq 360$ PMTs, which corresponds to 45 PMTs in place of each original CEDAR PMT.

A simulation of the new light path outside the CEDAR vessel is shown in Fig. 5.5a;

---

[1]The symbol e represents the electron charge.

the Cherenkov light (blue) emerging from the quartz windows is reflected radially off eight spherical mirrors (red) and is collected onto eight PMT matrices (green). The mechanical design of the new KTAG photon detector is shown in Fig. 5.5b; an

(a)   (b)
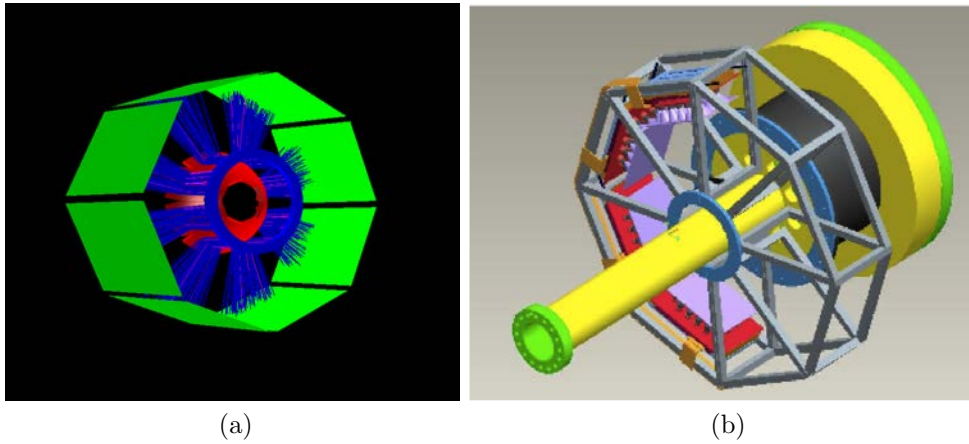
Figure 5.5: (a) new trajectories (blue) of Cherenkov photons exiting the CEDAR quartz windows, reflecting off new mirrors (red) and hitting new PMT matrices (green); (b) mechanical design of the new KTAG detector positioned upstream the quartz windows, surrounding the nose and housing mirrors, light collection cones and PMTs.

additional structure, spider-shaped with eight arms[2], is mounted at the upstream end of the vessel, surrounding the nose and the eight quartz windows. The structure, contained in an additional part referred to as enclosure, is divided into two mirror-symmetric halves and supports the new PMT matrices. The enclosure hosts several components (some of them are shown in Fig. 5.6, obtained from a Geant4 [75] simulation of the KTAG):

- eight focussing lenses mounted at the exit windows of the vessel and called "optical cap" lenses;

- eight spherical mirrors;

- light collection cones machined in eight solid aluminium plates ("light guides");

---

[2]In the following, the space between two arms and the corresponding attached equipment will be referred to as a sector.

- eight solid metallic containers, also called "light boxes", hosting the light guides and the front-end electronics;

- gas and cooling systems.
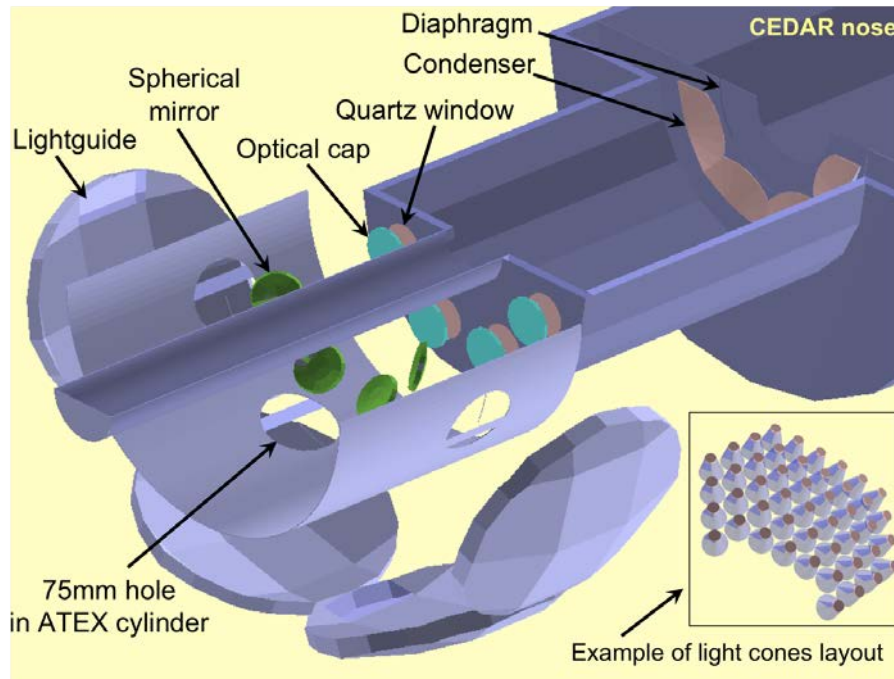
Figure 5.6: Screenshot taken from a Geant4 simulation of the KTAG within the CEDAR upgrade. The components of the optical system outside the CEDAR vessel are sketched.

The function of the optical cap lenses is to correct the divergence of the Cherenkov light exiting the quartz windows, before its reflection off the spherical mirrors. The light collection cones have been designed in order to maximise the light collection efficiency and reduce the dead areas. The new PMT matrices are equipped with 48 single-anode PMTs: this configuration allows a reduction of the photon rate and average anode current per PMT down to a sustainable level at the nominal NA62 beam intensity. Optimisation studies performed with a Geant4-based simulation of the CEDAR/KTAG detector [74, 76], including all the modifications foreseen for application in NA62, determined the working configuration for the Cherenkov light transport and collection system, as well as the number of PMTs employed to collect the light from each quartz window. The simulation aims to keep the kaon

detection efficiency above 95% and the time resolution on kaon crossing time below 100 ps, while varying several parameters, including the number of PMTs, the radius of curvature of mirrors, the mirror positions and the focal length of the optical cap lenses.

The new distribution of Cherenkov light, as expected on the light guides, is presented in Fig. 5.7: each blue dot represents the impact point on the light guide of a Cherenkov photon; the white circles correspond to the active areas of PMTs; the shadowing around the white circles is due to light hitting mainly one side of the cones before being deflected to the PMTs active areas.
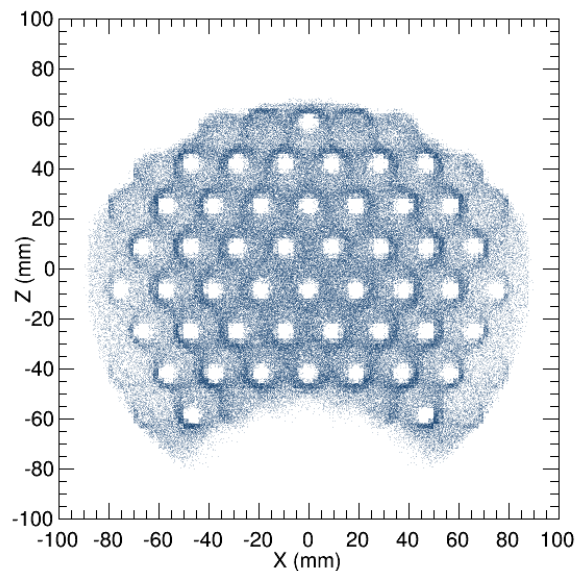
Figure 5.7: Expected distribution of Cherenkov photons on the light guides. Each blue dot represents the impact point on the light guide of a Cherenkov photon; the z-axis running along the rows of PMTs is parallel to the NA62 beam line, the x-axis corresponds to the azimuthal direction.

5.5 Photo-detector technology

The photo-detector technology required for the KTAG must be able to perform single photon counting, which takes place when the individual photo-electrons produced at the photocathode are well separated in time. The PMTs chosen for the KTAG

design are based on metal package photomultipliers of the Hamamatsu R7400U [77] and R9880U [78] series, 03 and 210 types respectively, optimised for single photon counting applications. Both single-anode Hamamatsu PMTs were selected for their size (8 mm diameter active area) and compactness (16 mm x 12 mm cylindrical shape), time performances on single photon detection (~ 300 ps time resolution on single photon detection), resistance to radiation, low dark count rate ($\sim$ few Hz), sensitivity to visible and near-UV wavelengths.

Each KTAG PMT matrix is equipped with 16 R7400U-03 and 32 R9880U-210 Hamamatsu PMTs. However, to allow the possibility of future upgrades, the light guide layout has been designed to contain 64 PMTs. Fig. 5.8a shows the arrangement of the 48 PMTs within a light guide. The reason behind the two types of PMTs involved is historical: those of the first type (R7400U-03) are inherited from the detector prototype tested in the 2012 Technical Run (Chapter 6), while those of the latter are the alternative solution closest in terms of price and performances to the former PMTs being out of production.

The main difference between the two PMT types is the QE: Hamamatsu R7400U-03 PMTs have a typical QE of $\sim 20\%$, while Hamamatsu R9880-210 have a QE of $\sim 40\%$ (peak values). Considering the expected Cherenkov light distribution on the PMT matrices (Fig. 5.7), the hit rate on single PMT is found to be ~ 3.5 MHz (average value) and ~ 5.5 MHz (max value). This can be seen from Fig. 5.8b, which shows the rate distribution and the effect of the configuration with two PMT types: as a direct consequence of their lower quantum efficiency, the R7400U-03 PMTs correspond to the lower rates, while the others exhibit higher rates.

Another difference between the two PMT types is the gain: Hamamatsu R7400U-03 PMTs have a 8-dynode electron multiplier system with a typical gain of 1×10^6 at $V = 900$ V; Hamamatsu R9880-210 PMTs are equipped with a 10-dynode electron multiplier system, thus have a higher typical gain of 2×10^6 at $V = 900$ V.
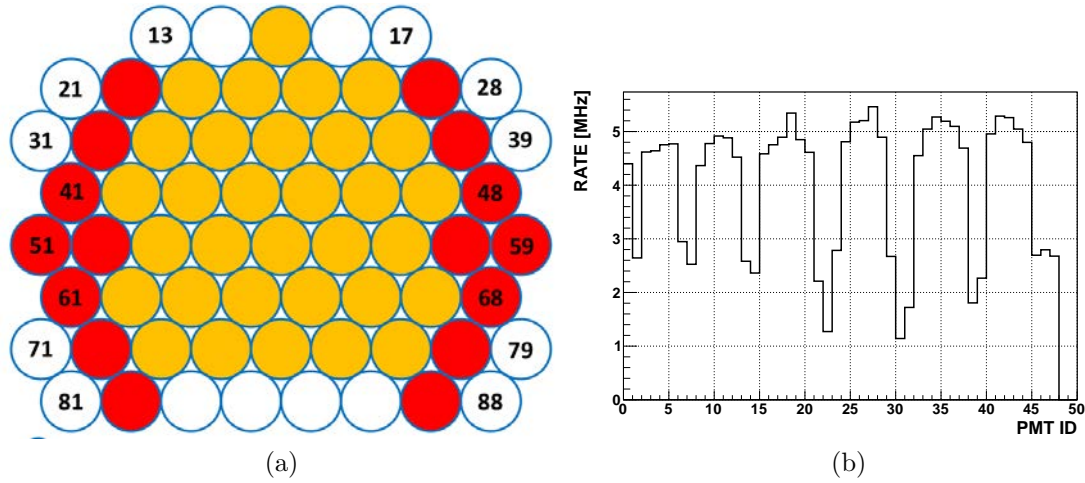
Figure 5.8: (a) Arrangement of the 48 PMTs within a light guide. The 16 PMTs of type R7400U are shown in red. (b) Expected single PMT rate for a CEDAR filled with N_2 at absolute pressure of 1.7 bar and a KTAG configuration with 48 PMTs, radius of curvature of spherical mirrors of 51.68 mm and focal length of the optical cap lenses of 114 mm, at nominal beam intensity.

5.6 Front-end and read-out system

The front-end used to interface the PMTs with the readout system relies on NINO ASIC [79] (8 channels) mezzanine chips. This solution is feasible because the standard Hamamatsu High Voltage (HV) divider is replaced with a customised printed circuit board with differential anode output in order to accommodate the differential input of NINO mezzanines.

In each light box (Fig. 5.9a) a board housing 8 NINO mezzanines[3] is used to shape and discriminate the output signal from PMTs. One of the front-end NINO boards with eight NINO mezzanine chips is shown in Fig. 5.9b: two Control Area Network (CAN) bus connectors at the right hand side of the board are used for communications with the Detector Control System through the Embedded Local Monitoring Board (ELMB); the central connector at the same side is for the low voltage supply and two connectors at the left side of the board connect the front-end with the readout system. The NINO board is screwed to the metallic lid of the light box.

---

[3]The total number of NINO channels per sector is 64 in order to potentially accommodate an upgrade of the KTAG with more PMTs.
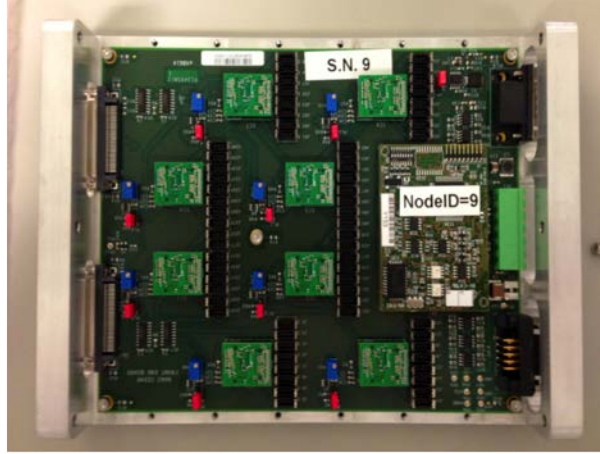
<div align="center">(a)   (b)</div>

Figure 5.9: (a) light box without PMTs, with the metallic lid lifted open and PMT holders attached at the basement. (b) NINO board with two CAN bus connectors and a central voltage connector mounted at the right side of the board and two LVDS connectors at the left side of the board; the NINO board is screwed to the metallic lid of the light box.

The NINO chip operates in Time-Over-Threshold (TOT) mode and its threshold can be set remotely and independently for the 8 NINO mezzanine boards. The NINO Low Voltage Differential Signaling (LVDS) output is sent to 128-channel Time to Digital Converter (TDC) modules, working in a trigger matching mode.

Before reaching the TDC boards, the signals from the KTAG front-end is distributed by passive splitter boards (Fig. 5.10a) over non-consecutive readout channels. This stage is necessary to minimise the read-out inefficiency at the expected rate due to groups of eight (consecutive) readout channels sharing a first latency buffer. The limited buffer size implies a $\gtrsim 10\%$ readout inefficiency for rates above $5\,\mathrm{MHz}$ per channel, if more than one channel shares the same buffer [80]. With the adopted configuration, one single channel is sent to each latency buffer, allowing to reach an inefficiency below 4% for the maximum expected rate of $5.5\,\mathrm{MHz}$ (Sec. 5.5).

Each TDC module contains four High Performance Time to Digital Converter

(HPTDC) chips [80] for precise time tagging of electronics signals. Both the leading and trailing edges of the LVDS output are recorded providing information on the width of the NINO output signal. This is necessary in order to compensate the rising time differences for signals with different amplitudes (slewing corrections). The TDC boards are hosted by TEL62 motherboards (Fig. 5.10b), which are integrated trigger and data acquisition boards developed by the NA62 collaboration.

The TEL62 board [68, 81] is a major upgrade of a FPGA-based readout board inherited from LHCb readout system [82]. It can host up to four TDC boards and is formed from the following components:

- 4 Altera Stratix III FPGAs with a 2 GByte DDR2 memory buffer each, to handle data from the TDC bords;

- 1 central Altera Stratix III FPGA, for triggers handling and data synchronisation;

- a Quad GbE card with four 1 Gbit Ethernet channels, for data and trigger primitives flow (Sec. 4.3.5);

- a commercial Credit-Card PC (CCPC) and a custom card (Glue card) for the board slow control.

To minimise the readout inefficiency discussed above, 8 readout channels are required for each KTAG PMT (7 of them left empty). Therefore, in order to reach the required number of channels, six TEL62 equipped with four TDC boards each are used for the KTAG readout (6 TEL62 × 4 TDC boards × 128 channels = 8 × 8 sectors × 48 PMTs).
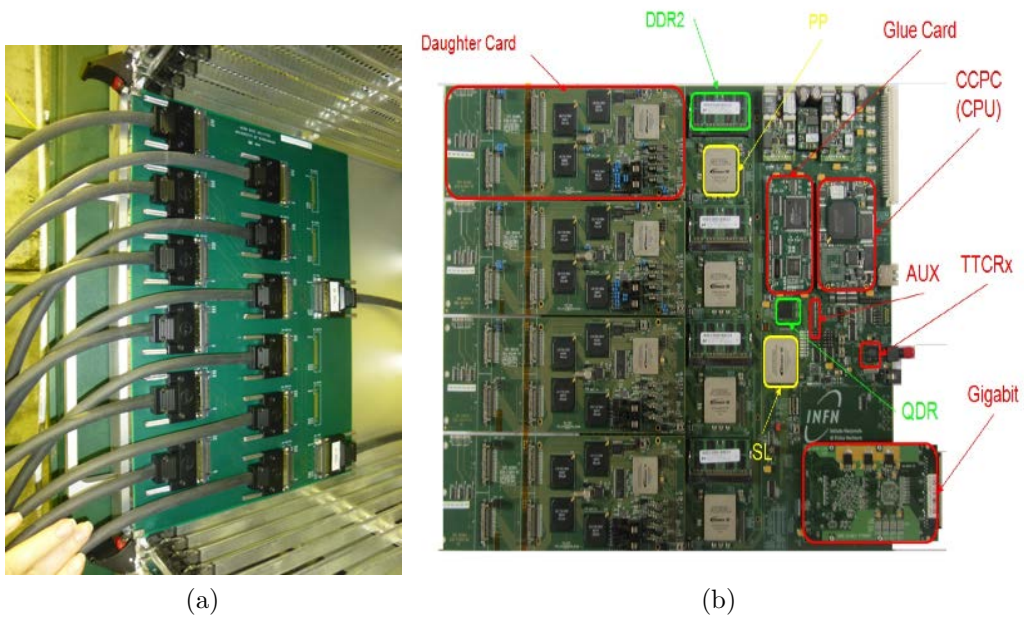
Figure 5.10: KTAG signal readout for the 2014 data taking: (a) picture of a splitter board distributing the 48 PMT signals from a KTAG sector, arranged into 2 LVDS cables (IN-1,IN-2), over 12 LVDS cables (OUT-1,2,..,12); (b) picture of a TEL62, an FPGA-based mother board with built-in PC, 4 daughter cards, memory buffers and data transfer card mounted on it.

Chapter 6

The NA62 Technical Run

The procedures and findings of the NA62 Technical Run which occurred in 2012 are presented in this chapter. The outcome of the commissioning of the new photon detector (KTAG), proposed within the upgrade of the CEDAR Cherenkov counter for usage in the main run of the NA62 experiment at CERN SPS, is reported. With approximately 30% of the upgraded CEDAR/KTAG detector equipped, the ability to distinguish between kaons and pions has been demonstrated by the pressure scan results, while the kaon identification efficiency and the time resolution have been measured relying on a specially-selected kaon sample.

6.1   Introduction

A Technical Run with the partially-installed NA62 detector was held in the ECN3 zone at CERN SPS for the whole duration of November 2012. The final NA62 beam line was set up to steer a hadron beam with the nominal characteristics (Sec. 4.2), except for the intensity, which varied from about 0.2% to 10% of the nominal one. The beam was structured in spills (also called "bursts") with a 10 s flat top and $\sim 30\,\mathrm{s}$ duty cycle and was used to test the sub-detectors in place and to synchronise the Trigger and Data AcQuisition (TDAQ) system. The components of the NA62 detector included in the setup of the Technical Run are sketched in Fig. 6.1 [65] and
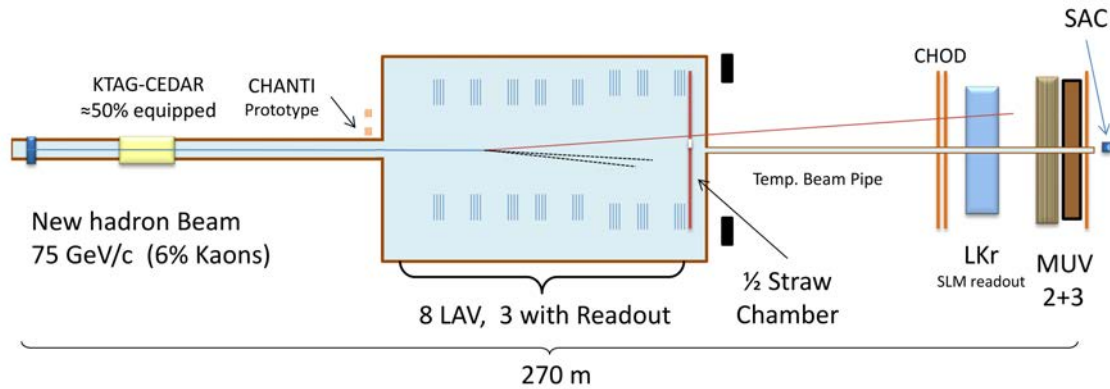
Figure 6.1: The NA62 detector layout during the 2012 Technical Run (cf. Fig. 4.4).

are listed below.

- The CEDAR/KTAG, detailed in Chapter 5, was equipped with only 4 light boxes out of 8, each with 32 PMTs instead of 48. Therefore, the total number of photo-detectors was 128, i.e. one third of the one foreseen for 2014.

- The vacuum tank housing the fiducial decay region (Sec. 4.3.1) was only installed up to the first Straw chamber. It was temporarily sealed downstream with a 4 mm thick aluminium window and connected to a ~ 70 m long beam pipe, to keep the beam in vacuum up to the end of the experimental area.

- The first eight (out of twelve) stations of the LAV system (Sec. 4.3.4.1) were installed in the NA62 beam line and three of them were read-out.

- Two views (out of four) of the first straw chamber (Sec. 4.3.2.2) were installed in the NA62 beam line and read-out with a standalone data acquisition system.

- The hodoscope was fully equipped as illustrated in Sec. 2.4.

- The LKr calorimeter was in its original and final version (Sec. 2.5), and its innermost 64×64 cells were read-out with a partially-upgraded read-out system.

- The MUV2 and MUV3 stations (Sec. 4.3.3.1) were installed in the NA62 beam line and read-out.

- The SAC (Sec. 4.3.4.3) was installed at the end of the experimental area and read-out with a standalone data acquisition system.

All the sub-detectors, except for straw chamber and SAC, were read-out and connected to a common TDAQ interface, synchronised by a 40.08 MHz clock transmitted via an optical fibres distribution system. Sub-detectors control and monitoring were assigned to a Detector Control System (DCS) and Detector Safety System (DSS) platforms, developed for the NA62 collaboration by the CERN Engineering group.

Data acquisition was based on simple hardware trigger conditions, as the logical AND of analogue signals from different sub-detectors, in which the hodoscope Q_1 condition (Sec. 2.4) was always required. The typical trigger frequency was $\sim 10\,\text{kHz}$, limited by the original components of the LKr read-out system and obtained by choosing adequately the trigger downscaling factors. A temporary L0 Trigger Processor (L0TP) was set up, which received the trigger primitives from the sub-detectors involved in the trigger logic, and distributed to all the sub-detectors the timestamps (in units of 25 ns) of the clock cycles in which the trigger signals were produced. The acquisition time windows of all the sub-detectors were 75 ns wide, consisting of three 25 ns frames (clock cycles), the central one of which corresponded to the trigger timestamp.

The work conducted during the Technical Run for the CEDAR/KTAG commissioning and for the study of the detector performances is presented in the rest of the chapter.

6.2 CEDAR/KTAG installation

At the end of September 2012, in preparation for the Technical Run, the CEDAR and the new photon detector (KTAG) were installed in their final position on the NA62 beam line. Fig. 6.2 shows the CEDAR/KTAG detector during the installation.

Four light boxes were mounted in the KTAG enclosure. Each light box contained a

(a)   (b)
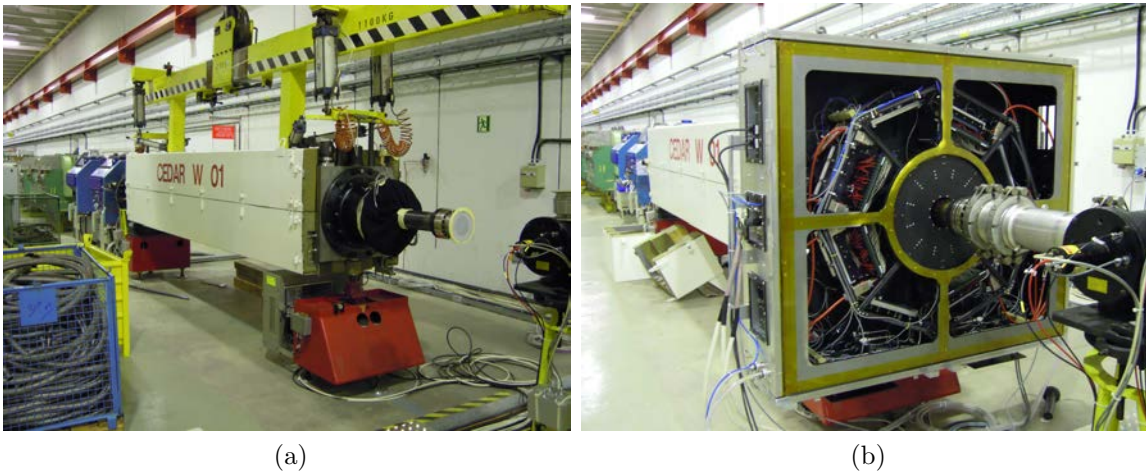
Figure 6.2: (a) The CEDAR detector during the installation into the NA62 beamline. (b) The new photon detector (KTAG) mounted onto the CEDAR.

64-cones aluminium light guide, on which 32 Hamamatsu R7400U-03 PMTs (Sec. 5.5) were mounted, and a front-end NINO board, housing four (out of eight) NINO mezzanine chips (Sec. 5.6). The position of the four equipped sectors and the arrangement of the 32 PMTs within one light guide are shown Fig. 6.3.

Each equipped sector was reached by two cables for the HV supply of PMTs, one

(a)   (b)
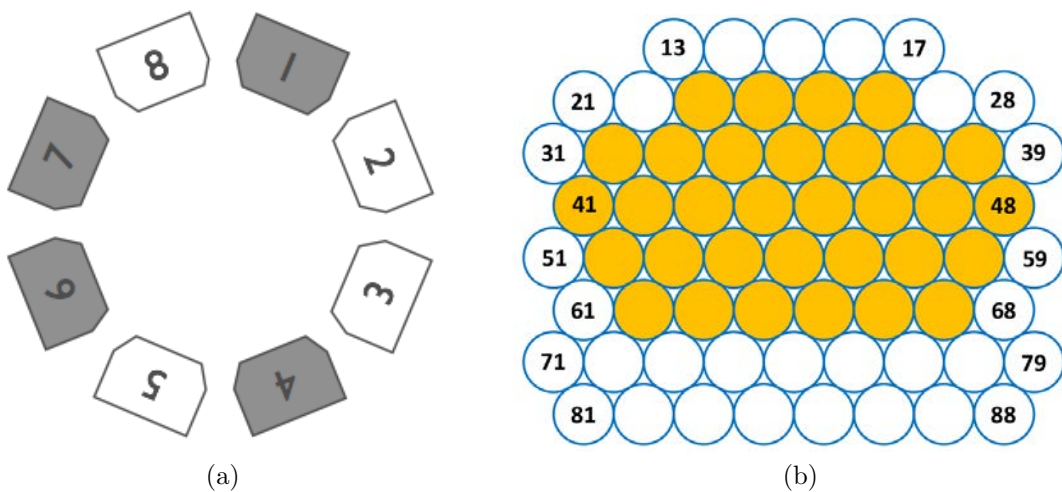
Figure 6.3: (a) Sketch of the CEDAR/KTAG sectors during the Technical Run: only the ones in gray were equipped with light boxes (front view). (b) Arrangement of the 32 PMTs within the 64-cones light guide, during the Technical Run (cf. Fig.5.8a).

147

cable for the Low Voltage (LV) supply of the NINO board, two LVDS cables for the front-end read-out and one CAN bus cable for the communication with the DCS. During the Technical Run the DCS interface was not completed yet and the communications were limited only to the remote setting/reading of PMT HV values and monitoring of temperature sensors placed in the heat-sink to which the NINO board was mounted. The signals from the four NINO boards were sent to the readout system, made of one TEL62 board equipped with one TDC daughter-card with four 32-channels HPTDC chips (Sec. 5.6).

Two electronics racks in the ECN3 zone were dedicated to the CEDAR/KTAG remote control, read-out, cooling and power supply systems. The two panels in Fig. 6.4 show the racks and related sketch with their components as used during the Technical Run. The one on the left-hand side of both panels in Fig. 6.4, called CEDAR-01, contained the 9U Wiener crate hosting the TEL62 readout board, the CAEN HV mainframe and the DSS/DCS boxes, together with other network/optical devices; the one on the right-hand side of both panels in Fig. 6.4, called Rack 171, contained the chiller for the KTAG water-cooling system and the CEDAR motor control panel.

Before the beginning of the Technical Run, during the CEDAR/KTAG installation phase, several hardware tests were performed, thanks to which different problems were detected and fixed. In particular, the two most severe are discussed below.

- Multiple signal reflections were observed, which were recognised to be due to a mismatch between the actual impedance of the NINO mezzanines ($\sim 60\,\Omega$) and the one assumed in the KTAG electronics design ($100\,\Omega$). The NINO impedances were adjusted to $100\,\Omega$ by replacing a resistor on each mezzanine and the reflections disappeared.

- A noise with instantaneous frequency $\sim 240\,\mathrm{MHz}$ and a $600\,\mathrm{kHz}$ burst structure was detected in the signal lines, the source of which was identified to be the Wiener crate power supply. The noise propagated to the near CAEN HV

Position	CEDAR-01	Rack 171
45	EMPTY	EMPTY
44	Optical PP	EMPTY
43	EMPTY	EMPTY
42	Optical splitter	EMPTY
41	Network router	EMPTY
40	Choke/Error PP	
39		
38	DSS	
37		
36	EMPTY	Motor Control Panel
35	LVDS Cable holder	
34		
33		
32		
31		
30		
29	Tel62 crate	
28		
27		
26		
25		
24		
23	EMPTY	
22	EMPTY	
21	EMPTY	
20	EMPTY	
19	EMPTY	
18		
17		
16		CHILLER
15		
14	HV mainframe	
13		
12		
11		
10		
9	DCS BOX	
8		
7	EMPTY	
6	EMPTY	
5	EMPTY	
4	EMPTY	
3	EMPTY	
2	EMPTY	
1	EMPTY	

| (a) | (b) |

Figure 6.4: (a) Picture and (b) sketch of the CEDAR/KTAG racks.

mainframe, entering the signal lines via the HV channels. It was stopped before reaching the PMTs by soldering on the HV patch panel of each light box 32 low-pass filters (one a HV channel) composed by a resistor of $R = 100\,\mathrm{k\Omega}$ and a capacitor of $C = 10\,\mathrm{nF}$ ($RC = 1\,\mathrm{ms}$).

6.3 CEDAR/KTAG software

Reconstruction software and several graphical interfaces were developed in order to analyse and monitor the CEDAR/KTAG performances.

The raw data consist of 32-bit words encoding the read-out channel IDentifiers (IDs) of the fired PMTs, the type of the signal edges (leading or trailing edges) detected by the HPTDC chips and the corresponding timestamps in units of 97.46 ps ($\simeq 25\,\mathrm{ns}/256$). At the reconstruction stage, KTAG hits are defined as the PMT signals associated to the measurements of both leading and trailing edge times t_l and t_t. The presence of both edges is required to evaluate the signal width $t_w \stackrel{def}{=} t_t - t_l$, which, as will be discussed in Sec. 6.5.3, can be used to compensate the different

detection latencies of signals with different amplitudes. About 90% of the signals acquired during the Technical Run had both leading and trailing edges. Based on the reconstructed hits, the kaon candidate time and the numbers of hits and sectors firing for each candidate were evaluated. A kaon candidate was reconstructed if at least one hit was detected. Moreover, a fast time-clustering algorithm was developed to distinguish hits from different candidates close in time.

A ROOT-based Online Data Quality Monitor was developed and integrated in the NA62 data reconstruction framework. The KTAG Online Monitor was extensively used during the Technical Run. In particular, it was an essential component of the CEDAR alignment procedure that will be described in Sec. 6.4.3 and of the CEDAR pressure scan (Sec. 6.4.4). Fig. 6.5 shows three of the KTAG dedicated panels:

a) the signal quality monitor, where the channel synchronisation and the time over threshold distribution are shown;

b) the alignment monitor, where the integrated number of hits per sector for each burst and the up-down/left-right asymmetry indices are shown;

c) the high-level information summary, where the number of hits and of sectors firing per candidate are shown, together with the hit time distribution.

6.4 CEDAR/KTAG commissioning

The first phase of the Technical Run, in which the beam intensity was set to 0.2% of the nominal one foreseen in 2015 (the kaon rate was $\sim 100\,\text{kHz}$), was dedicated to detector commissioning, which included the synchronisation of the KTAG channels and the setting of the CEDAR working conditions (alignment and pressure).

6.4.1 KTAG signal overview

Before performing any alignment or pressure fine-tuning, the CEDAR pressure was set to $P = 1.73\,\text{bar}$, which is the nominal value for kaon detection determined by a
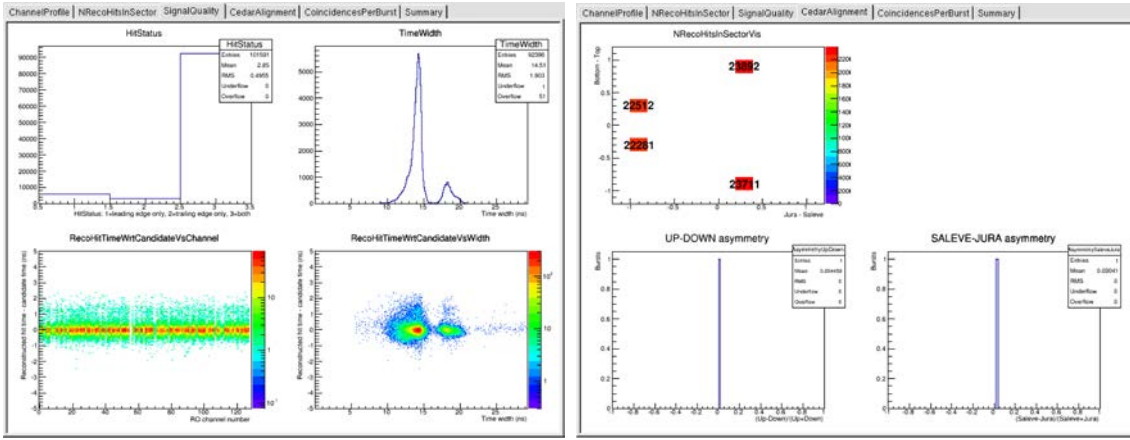
(a)

(b)
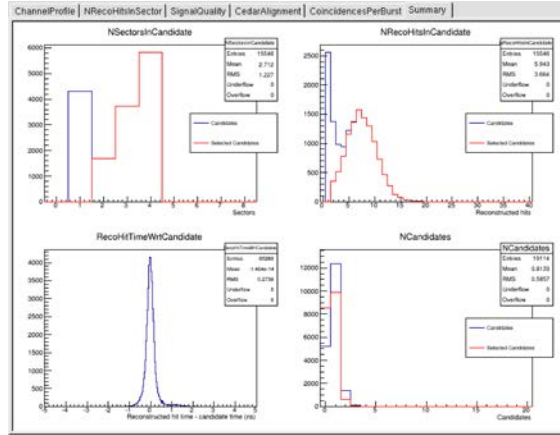
(c)

Figure 6.5: Three of the KTAG Online Monitor panels (plots are described clockwise, from top left). (a) Signal quality monitor: signal detected edges status (1=leading only, 2=trailing only, 3=leading+trailing); Time over Threshold; Time over Threshold vs Signal Time; Channel Time alignment. (b) Alignment asymmetry monitor: number of recorded hits ber burst for each sector; Left-Right asymmetry index; Up-down asymmetry index. (c) High-level information summary: number of firing sectors per candidate; number of firing PMTs per candidate; number of candidates per trigger; PMT hit time with respect to the candidate time.

previous test beam [83], and the diaphragm aperture was set to its maximum value $w_{\mathrm{DIA}} = 20\,\mathrm{mm}$, in order to minimise the effects of a possible CEDAR mis-alignment or of a non-optimal pressure. With these conditions, an average of 7 hits per trigger where observed. A more detailed study of the CEDAR/KTAG response, performed after determining the CEDAR working conditions, will be presented in Sec. 6.5.

The distribution of the KTAG hit times in the 75 ns acquisition time window is shown in Fig. 6.6a. The time $t = 0$ refers to the trigger timestamp and the three 25 ns frames composing the acquisition time window are delimited by dashed lines. The distribution of the signal width t_w is shown in Fig. 6.6b. The presence of a second peak at $t_w \simeq 18$ ns is due to the detection of after-pulses caused by large signals. However, as it will be shown in Sec. 6.5.3, such feature does not affect the PMT time resolution, since the detection latencies are negligible for large signals and no correction is needed.

(a)   (b)
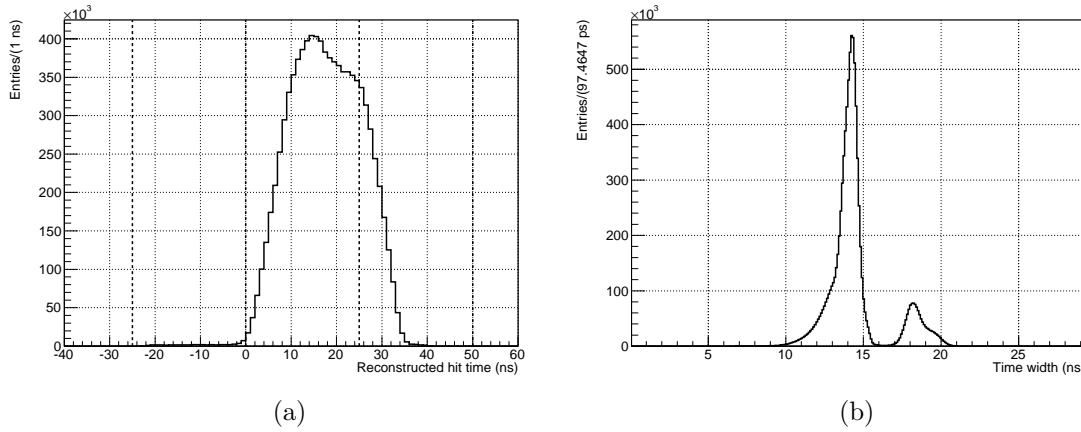
Figure 6.6: (a) Distribution of the KTAG hit times with respect to the trigger timestamp ($t = 0$); the three 25 ns frames composing the acquisition time window are delimited by dashed lines. (b) Distribution of the signal width t_w; the presence of a second peak at $t_w \simeq 18$ ns is a feature due to the signal shape (see text).

6.4.2   KTAG channel synchronisation

Channel synchronisation has been performed using as a reference the kaon candidate time, calculated as the average of all the hit times associated to the same candidate. To reduce the dependence of the candidate time on the individual PMT times, only candidates with a minimum of 6 hits have been considered in the synchronisation procedure. For each channel, the average time offset T_0 from the kaon candidate time has been measured and subtracted. Then, a second iteration has been applied to improve the T_0 values, previously smeared by the temporal mis-alignment of the KTAG channels. Fig. 6.7 shows the channels temporal alignment (a) before and (b)

after applying the T_0-corrections. The typical value of the corrections is $\sim 1\,\mathrm{ns}$.
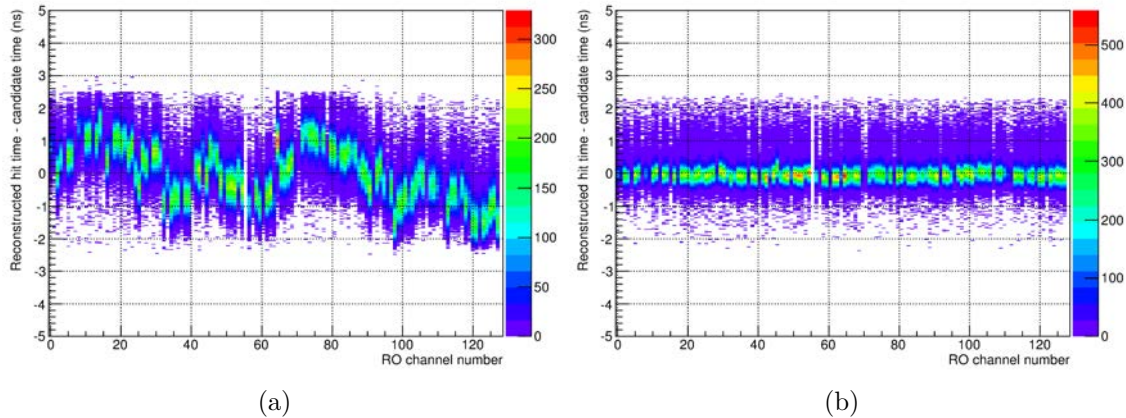
Figure 6.7: KTAG channels temporal alignment (a) before and (b) after applying the T_0 corrections.

6.4.3 CEDAR alignment

As discussed in Sec. 5.2.2, the CEDAR (x, y) alignment is a crucial requirement to maximise the particle identification performances. The CEDAR alignment was fine-tuned by using the standard iterative procedure described in Ref. [71]. Starting from the maximum diaphragm aperture $w_{\mathrm{DIA}} = 20\,\mathrm{mm}$, the CEDAR downstream end was moved in the (x, y) directions in order to obtain a more uniform hit distribution over the four sectors, until all the sectors had a number of hits, integrated over one burst, consistent with each other within 2 standard deviations. The typical integrated number of hits in each sector was ~ 20000. Then, the diaphragm aperture was reduced in steps and the equalisation procedure was repeated for each step, until a diaphragm aperture of $w_{\mathrm{DIA}} = 0.3\,\mathrm{mm}$ was reached. The optimal alignment for the lowest diaphragm aperture was used as working alignment. After determining the working alignment, the diaphragm aperture was set to the nominal value $w_{\mathrm{DIA}} = 2\,\mathrm{mm}$.

6.4.4 Pressure scan

After the CEDAR alignment, a pressure scan was performed in order to tune the CEDAR pressure to the value maximising the kaon identification efficiency. The trigger requirement used for the data acquisition was given by the Q_1 condition and a simultaneous signal from any MUV3 channel ($Q_1 \times$ MUV3). Such a trigger, which is sensitive to both $K^+ \to \mu^+ \nu$ and $\pi^+ \to \mu^+ \nu$ decays, was purposely chosen to check the pion and kaon peaks separation with the current alignment and diaphragm aperture. The CEDAR pressure was initially set above 1.93 bar, which corresponds to the nominal value for proton detection determined by a previous test beam [83]. After collecting one burst with a given pressure, the CEDAR pressure was decreased by ~ 5 mbar, until the pion peak was passed. For each value of the pressure, the number of candidates with at least 2, 3 and 4 firing sectors[1] normalised to the number of triggers have been studied. Fig. 6.8 shows the pressure scan results. Three peaks are resolved. Each of them corresponds to a different beam component: the peak at lower pressure to pions, the intermediate one to kaons and the one at higher pressure to protons. This can be deduced from the relation between the refractive index n and the mass-momentum ratio m/p of a particle emitting Cherenkov radiation with the angle ϑ_c

$$\cos \vartheta_c = \frac{1}{n\beta} \quad \Rightarrow \quad \frac{1}{\beta^2} \equiv 1 + \frac{m^2}{p^2} = n^2 \cos^2 \vartheta_c \tag{6.1}$$

and from the dependence of the refractive index n on the pressure P, which is described by the Lorentz-Lorenz equation [84, 85] in the perfect gas approximation

$$n^2 \approx 1 + 4\pi\alpha \frac{P}{RT} \overset{def}{=} 1 + aP, \tag{6.2}$$

where α is the gas polarisability, R is the universal gas constant and T is the gas absolute temperature. From eqs. 6.1–6.2 follows that

$$P \approx \frac{1}{a \cos^2 \vartheta_c} \left(\sin^2 \vartheta_c + \frac{m^2}{p^2} \right). \tag{6.3}$$

---

[1]In the following, a candidate with n firing sectors will be called "n-fold coincidence".
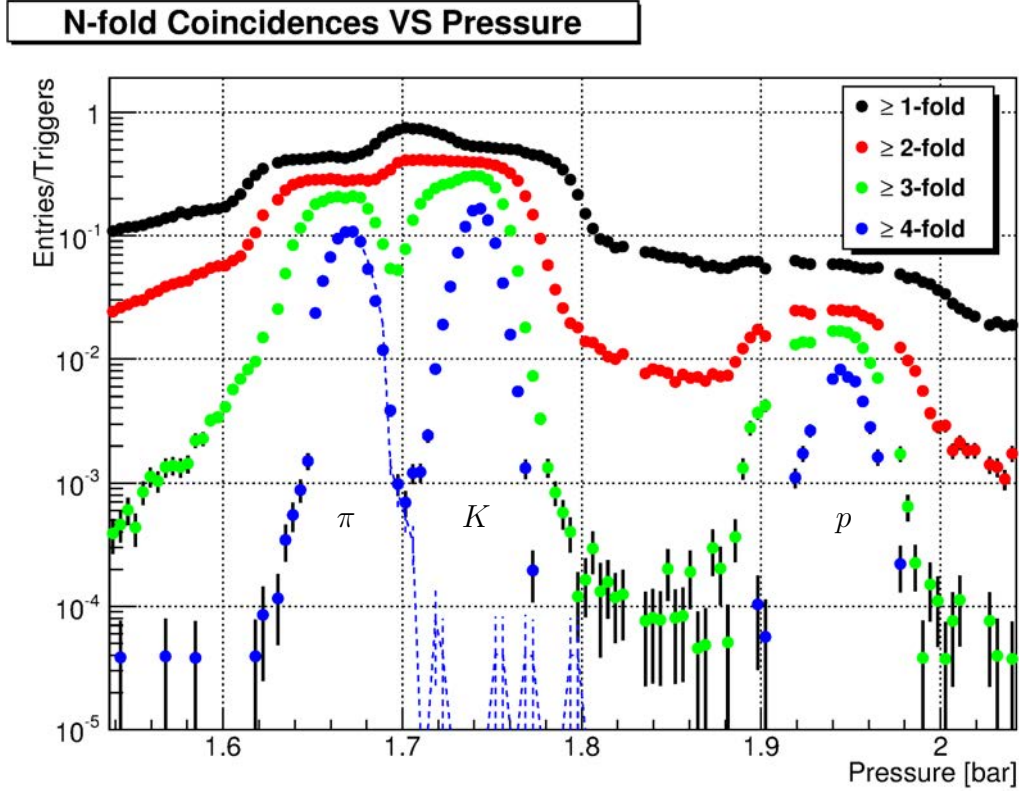
Figure 6.8: CEDAR pressure scan performed during the Technical Run. The dashed line indicates the extrapolated pion peak tail for 4-fold coincidences (see text).

Since the accepted ϑ_c range is fixed by the CEDAR design, the distribution of the momentum p is the same for all the particle types and a depends on the radiator properties only, the only dependence of P on the particle type is determined by the particle mass m. Therefore, from eq. 6.3 follows that particles with higher mass m are detected for higher values of the CEDAR pressure P. It is worth noticing that the height of each peak in Fig. 6.8 is not proportional to the beam composition, due to the bias introduced by the $Q_1 \times$ MUV3 trigger, which selects only the events in which at least a muon is detected.

The value $\bar{P}$ of the CEDAR pressure corresponding to the maximum of the kaon peak was determined by fitting the 4-fold coincidence peak with a gaussian and was found to be $\bar{P} = 1.742 \pm 0.001$ bar, which is consistent with the value found during a previous test beam if an increase of $2\,^{\circ}$C in the room temperature is assumed[2].

---

[2]The previous test beam [83] was held in October 2011 at the EHN1 zone in the CERN NA.

The pion mis-identification probability $P_{mis}^{\pi\,(n)}$ for the n-fold coincidence condition is defined as the probability that an observed n-fold coincidence at the kaon working pressure $\bar{P}$ is due to a pion. Experimentally, it can be estimated as the ratio

$$P_{mis}^{\pi\,(n)} = \frac{\varepsilon_\pi^{(n)}(\bar{P})}{\varepsilon_\pi^{(n)}(\bar{P}_\pi)}, \tag{6.4}$$

where $\varepsilon_\pi^{(n)}(P)$ is the number of n-fold coincidences at the pressure P due to pions normalised to the number of triggers, while $\bar{P}_\pi$ is the pion working pressure. Due to the impossibility of selecting a pure pion sample without a spectrometer and without relying on the CEDAR response, an estimation of the pion mis-identification probability at the kaon working pressure $\bar{P}$ has been provided by extrapolating the higher-pressure tail of the pion peak using the lower-pressure tail and assuming a perfectly symmetric pion peak distribution. Such assumption, due to the asymmetric KTAG layout during the Technical Run (Fig. 6.3a), can be used for the 4-fold coincidence condition only. The extrapolated 4-fold coincidence tail is shown in Fig. 6.8 with a dashed line. With the described method and assumption, a 90% CL UL on the pion mis-identification probability $P_{mis}^{\pi\,(4)}$ has been obtained:

$$P_{mis}^{\pi\,(4)} < 8.5 \times 10^{-4} \quad @\ 90\%\ \text{CL}, \tag{6.5}$$

which is of the same order of the maximum pion mis-identification probability allowed to meet the NA62 requirement (10^{-4}), despite only $\approx 30\%$ of the detector being equipped. In particular, to further reduce the pion mis-identification probability, n-fold coincidence requirements with $n > 4$ could be used in 2014.

6.5   Technical Run results

After the detector commissioning, the beam intensity was increased until reaching the 2% of the nominal 2015 value, leading to a kaon rate of $\sim 1\,\text{MHz}$. The CEDAR/KTAG detector was set to the working conditions found during the commissioning phase (diaphragm aperture $w_{\text{DIA}} = 2\,\text{mm}$, pressure $\bar{P} = 1.742\,\text{bar}$ and fine-tuned alignment).

The analysed data were collected with a trigger consisting of the logical AND between the Q_1 condition and a simultaneous signal from any NHOD channel ($Q_1 \times$ NHOD), which selects events with at least one charged track and at least one shower in the LKr calorimeter. Although this trigger is not sensitive to most of the pion decays, there is a significant ($\gtrsim 30\%$) non-kaon component in the acquired events due to the strong interactions of protons and pions from the beam with the material upstream the LKr calorimeter, especially with the first $40\,\text{m}$ of the beam pipe temporarily installed to replace the missing part of the vacuum tank. In order to evaluate the CEDAR/KTAG kaon identification efficiency and to study in detail the detector response, a kaon sample has been selected by reconstructing π^0 decays in the fiducial volume with a simultaneous charged track. Such event selection is sensitive to kaon decays such as the $K^+ \to \pi^+\pi^0$, the $K^+ \to \pi^0\ell^+\nu$ ($\ell = e, \mu$) and the $K^+ \to \pi^+\pi^0\pi^0$, which correspond to a total branching fraction of $\sim 31\%$, while rejecting most of the beam interactions.

6.5.1 Kaon candidate selection

The standard $K^+ \to \pi^+\pi^0$ event selection [65], finalised by the NA62 collaboration for the Technical Run data analysis, has been implemented without applying any CEDAR/KTAG requirement or specific cuts to reject the other kaon decays with a reconstructed π^0. The resulting selection is described below.

The kaon 3-momentum $\vec{p}_K$ is assumed to be the same for all the events and equal to the average nominal beam 3-momentum. Analogously, the beam transverse size is neglected and the nominal beam trajectory is assumed for all the events. LKr energy clusters fulfilling the following requirements are defined as photon-candidate clusters:

- fully contained in the LKr acceptance and at least $2\,\text{cm}$ away from the closest dead cell;

- distribution of the reconstructed energy deposition consistent with being an electromagnetic cluster;

- energy in the range $(3,65)$ GeV;

- at least 20 cm away from any other cluster, in order to avoid cluster merging effects.

Events with less than two photon-candidate clusters in the LKr have been rejected. For each pair (i,j) of photon-candidate clusters within 1 ns from each other, the π^0 decay vertex $\vec{X}_{vtx}^{(i,j)}$ has been reconstructed assuming the two clusters were produced by a $\pi^0 \rightarrow \gamma\gamma$ decay and requiring $\vec{X}_{vtx}^{(i,j)}$ to be along the kaon trajectory. Starting from the relation

$$m_{\pi^0}^2 = (P_i + P_j)^2 = 2E_iE_j(1 - \cos\vartheta_{ij}) \approx E_iE_j\vartheta_{ij}^2, \qquad (6.6)$$

where $P_{i,j}$ and $E_{i,j}$ are the 4-momentum and the energy of the photon i,j respectively and ϑ_{ij} the angle between the two photon directions, the neutral vertex coordinate $z_{vtx}^{(i,j)}$ can be reconstructed as

$$z_{vtx}^{(i,j)} \approx z_{\text{LKr}} - \frac{1}{m_{\pi^0}}\sqrt{E_iE_j[(\vec{X}_i - \vec{X}_j)^2]}, \qquad (6.7)$$

where z_{LKr} is the LKr front plane z-coordinate, while $E_{i,j}$ and $\vec{X}_{i,j}$ are the reconstructed energy and position[3] of the clusters i,j respectively. If the reconstructed decay vertex $\vec{X}_{vtx}^{i,j}$ is within the nominal decay region $(105\,\text{m} \leq z \leq 180\,\text{m})$ a π^0-candidate is reconstructed. The π^0-candidate 4-momentum P_{π^0} is obtained by summing the two 4-momenta $P_{i,j}$ of the photon-candidate clusters i,j and the π^0 time is estimated as the average of the two clusters times.

A charged track is reconstructed if two hits (one for each plane) within 5 ns from each other are detected in the same HOD quadrant (Q_1 condition).

All the events with exactly one reconstructed π^0 and at least one reconstructed track within 3 ns from the reconstructed π^0 have been considered. With the described requirements, ~ 140000 events have been selected from the analysed data sample,

---

[3]The LKr front plane z-coordinate z_{LKr} is taken as z-coordinate of the clusters.

corresponding to ~ 500 bursts. The kinematics of such events has been studied by reconstructing the squared missing mass variable $m_{miss}^2(\pi^0)$, defined as

$$m_{miss}^2(\pi^0) = (P_K - P_{\pi^0})^2 = m_K^2 + m_{\pi^0}^2 - 2E_K E_{\pi^0} + 2\vec{p_K} \cdot \vec{p_{\pi^0}}. \qquad (6.8)$$

Fig. 6.9 shows the distribution of the squared missing mass $m_{miss}^2(\pi^0)$, compared with the ones obtained from MC samples simulating the Technical Run conditions for the most common K^+ decays involving at least a π^0, produced by the NA62 collaboration. As expected, the selected kaon sample is mostly composed of $K^+ \rightarrow$
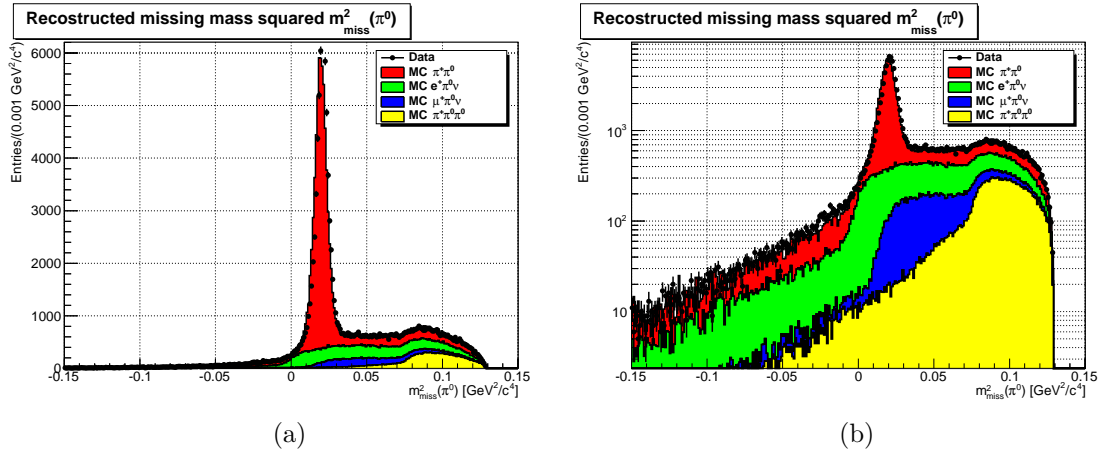
Figure 6.9: Squared missing mass $m_{miss}^2(\pi^0)$ obtained from the Technical Run, compared with the MC simulation of the most common K^+ decays involving at least a π^0: (a) linear scale, (b) logarithmic scale. The MC samples are normalized according to their branching fractions.

$\pi^+\pi^0$, $K^+ \rightarrow \pi^0 \ell^+ \nu$ $(\ell = e, \mu)$ and $K^+ \rightarrow \pi^+\pi^0\pi^0$ decays. The resolution of the $K^+ \rightarrow \pi^+\pi^0$ peak at $m_{miss}^2(\pi^0) = m_\pi^2$ is about $3.8 \times 10^{-3}\,\mathrm{GeV}^2/c^4$ [65].

6.5.2 KTAG efficiency

The KTAG response has been studied for the kaon sample selected as described in Sec. 6.5.1. The n-fold coincidence conditions with $n = 1, 2, 3, 4$ have been considered as possible kaon identification criteria. For each value of n, the KTAG efficiency has been measured as the fraction of selected events in which the reconstructed

kaon decay is associated to a KTAG candidate satisfying the n-fold coincidence requirement. KTAG candidates are associated to the reconstructed kaon decays if they are within 3 ns from the expected kaon time t_K, determined as the average of the time of the reconstructed π^0 and the time of the reconstructed track. Both π^0 and track time resolutions are about 700 ps (RMS), therefore the resolution of the expected kaon time is $\sigma_K(t) \approx 500$ ps (RMS). The clustering algorithm used during the Technical Run to organise KTAG hits in candidates grouped all the hits within 2.5 ns from the candidate time in the same candidate. Therefore, the minimum possible time difference Δt between two reconstructed candidates is 2.5 ns. In particular, if $\Delta t < 6$ ns, it is possible to have more than one candidate associated to the same reconstructed kaon decay. In that case, the one with bigger number of hits is chosen. This choice prevents from considering as inefficient those events in which the kaon decay would be associated to the wrong KTAG candidate, mainly due to a close pion or proton[4] accidentally firing a small number of PMTs (≤ 2). Fig. 6.10 shows the obtained distributions of the number of PMTs and sectors firing for each KTAG kaon candidate, compared with the MC simulation. An excess of
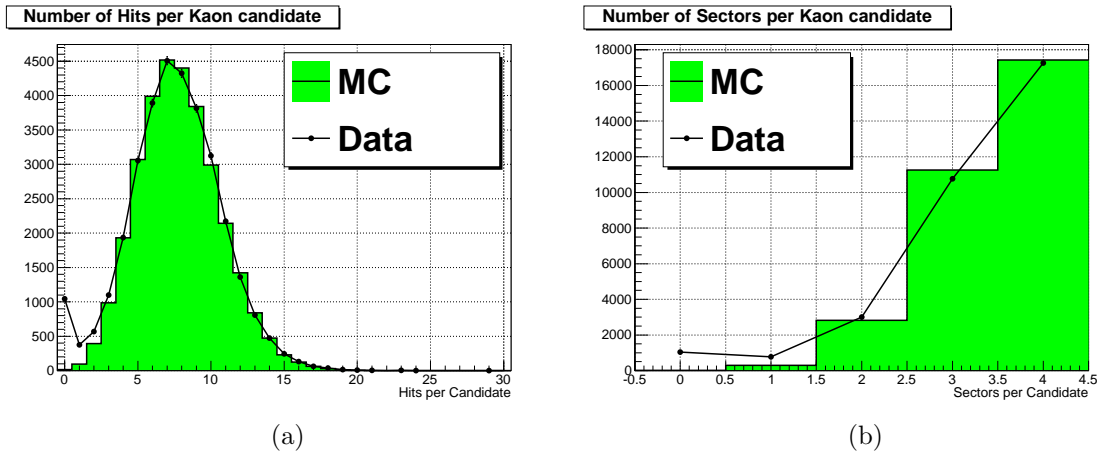
Figure 6.10: Distribution of the number of (a) KTAG hits and (b) KTAG sectors firing for the selected kaon sample, compared with the expected MC distributions.

data events with 0 hits (and therefore 0 sectors) is observed, corresponding to 3.1% of the selected sample.

---

[4]At 2% of the nominal beam intensity, $\sim 10\%$ of kaons are within 3 ns from a pion or a proton.

In order to disentangle possible dependencies on the data acquisition from the intrinsic KTAG inefficiency, the KTAG efficiency has been measured as a function of several TDAQ-related quantities as the burst number, the event time with respect to the beginning of the burst and the the kaon decay time with respect to the trigger timestamp. The results are shown in Fig. 6.11. While the efficiency does

(a)

(b)

(c)
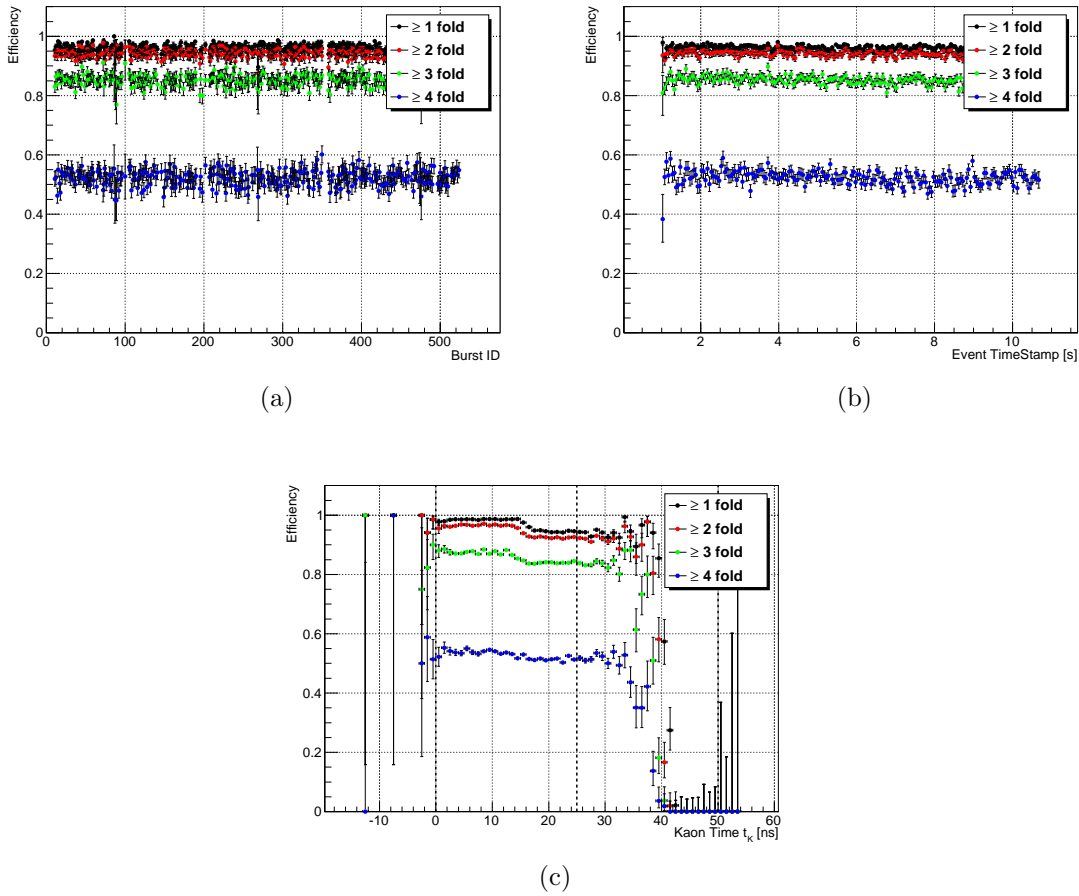
Figure 6.11: KTAG efficiency measured for the selected kaon sample as a function of (a) the burst number, (b) the event time with respect to the beginning of the burst and (c) the kaon decay time with respect to the trigger timestamp.

not show any significant dependence on the burst number or on the event time with respect to the beginning of the burst, it does show a dependence on the kaon decay time with respect to the trigger timestamp, clearly indicating a problem related to the data acquisition. The three 25 ns frames composing the acquisition time window are delimited by dashed lines in Fig. 6.11c. The inefficiency in the last frame

161

$(25\,\mathrm{ns} < t < 50\,\mathrm{ns})$ is due to the loss of trailing edges occurred outside the acquisition time window, because, as discussed in Sec. 6.3, all the hits were required to have both leading and trailing edges, in order to preserve the signal width information[5]. However, such inefficiency is well understood and is negligible, due to the small number ($\lesssim 0.8\%$) of events populating the region $35\,\mathrm{ns} < t < 50\,\mathrm{ns}$. On the contrary, the $\sim 5\%$ efficiency drop in the second frame ($0\,\mathrm{ns} < t < 25\,\mathrm{ns}$), which contains by construction most of the triggered events, is not explained and, as will be shown below, accounts for a significant fraction of the events with 0 hits.

A simple explanation of this behaviour is that for a certain percentage of triggers ($\sim 5\%$), corresponding to the increase in inefficient events for the last half of the second frame ($t \gtrsim 15\,\mathrm{ns}$), the KTAG acquisition time window was anticipated by one clock cycle ($25\,\mathrm{ns}$) with respect to the acquisition windows of the other detectors considered (HOD and LKr). In fact, in this hypothesis, the edge of the KTAG acquisition time window would be at the end of the second frame ($t = 25\,\mathrm{ns}$) instead of the end of the third ($t = 50\,\mathrm{ns}$), for about 5% of the triggers. Given the KTAG signal width distribution (see Fig. 6.6b), almost all ($> 99\%$) the KTAG candidates in the last $\sim 10\,\mathrm{ns}$ of the second frame would lose all the trailing edges of their signals. Consequently, no hits would be reconstructed for $t \gtrsim 15\,\mathrm{ns}$ and those events would be considered as inefficient. Fig. 6.12 shows the sketch of the described mechanism.

If the $\sim 5\%$ drop in the KTAG inefficiency for $t \gtrsim 15\,\mathrm{ns}$ is caused by the described mechanism, it should disappear when reconstructing also hits with no trailing edge. This prediction has been tested, and the results are shown in Fig. 6.13, compared with the previously-determined efficiencies. Requiring at least a leading edge (and therefore enabling the hit reconstruction in case of missing trailing edges) eliminates the efficiency drop in the second part of the acquisition window. This confirms the shift of the acquisition time window occurs through the described mechanism.

However, regarding the actual cause of the shift of the acquisition time window, no conclusive evidence has been found yet, at the time of the present thesis. A

---

[5]As will be discussed in Sec. 6.5.3, the signal width information can be used to improve substantially the KTAG time resolution.
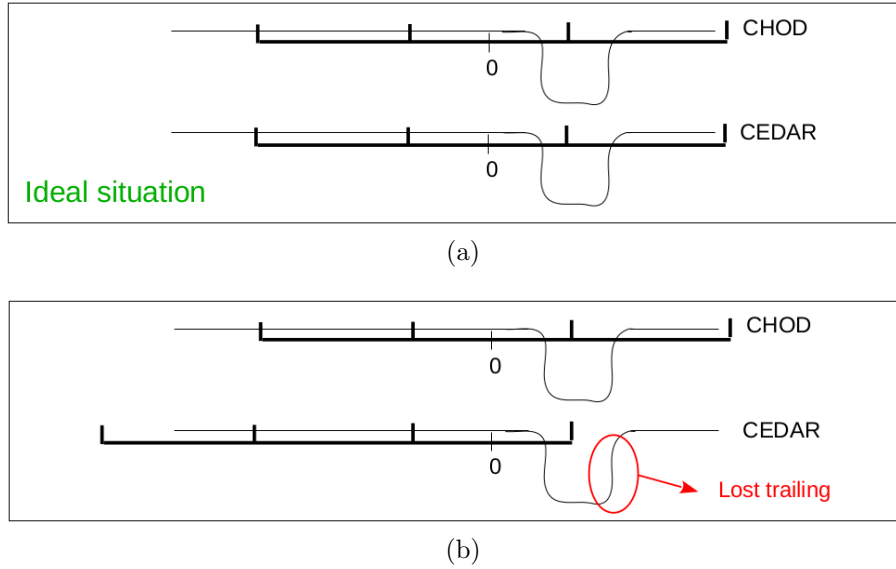
Figure 6.12: Sketch of a simple mechanism explaining the inefficiency trend in Fig. 6.11c: (a) in the ideal situation, the KTAG acquisition window is synchronised to the HOD one and all the KTAG hits are acquired. (b) When the KTAG acquisition window is anticipated by a clock cycle (25 ns), the trailing edges of the KTAG hits may be lost, depending on the time of the event with respect to the trigger, and the event may be considered as inefficient.

possible cause has been identified: the analogue signal from the HOD channels has a jitter of $\sim 5\,\mathrm{ns}$, which is corrected offline, due to the different track impact points along the same strip. This causes the trigger signal to be anticipated or delayed depending on the impact point; in case of an event close to the beginning or the end of one 25 ns frame, the corresponding trigger could migrate in another frame, determining the observed shift of the acquisition time window with respect to the other detectors. The observed inefficiency drop would therefore be caused by the HOD time window delayed by a clock cycle (which is equivalent to having the KTAG window anticipated). In particular, considering the given jitter and the possibility of moving on both directions, the described mechanism should affect about 10% of the triggers, which is consistent with the observed effect.

The effect of the inefficiency due to the data acquisition on the distributions of the number of KTAG hits and sectors has been evaluated by comparing the previous results (Fig. 6.10) with the ones obtained from the sub-sample of events with $t < 10\,\mathrm{ns}$,
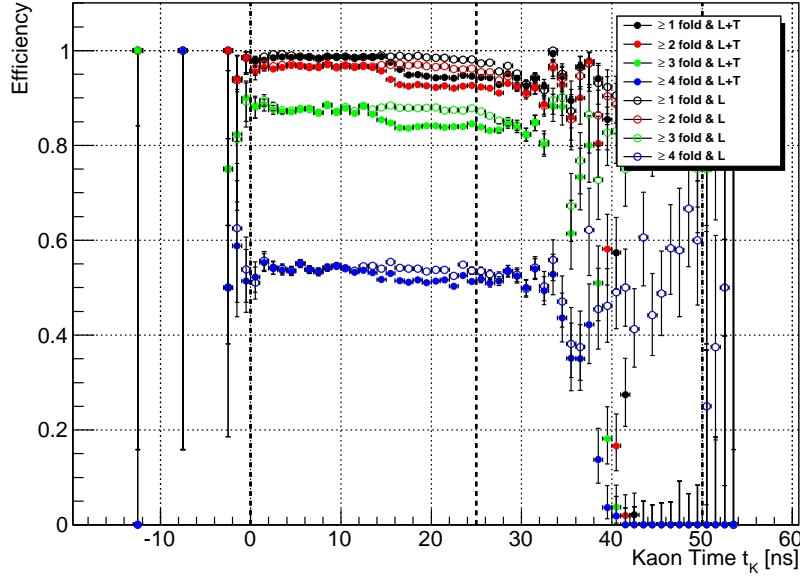
Figure 6.13: KTAG efficiency measured for the selected kaon sample as a function of the kaon decay time with respect to the trigger timestamp. Two different edge requirements are considered: leading and trailing edge (L+T); at least one leading (L).

not affected by the trailing edge loss. Such comparison is shown in Fig. 6.14 from which it is possible to notice that most of the events with 0 hits observed in Fig. 6.10 ($\sim 55\%$) were due to the detected inefficiency. Furthermore, the distribution obtained for the sub-sample of events with $t < 10$ ns, requiring both leading and trailing edges, is not different from the ones obtained relaxing the edge requirement and including also events with no trailing edges. Therefore, the mechanism involved in the trailing edge loss is relevant at the edge of the acquisition window only.

The KTAG efficiencies measured with the initial kaon sample and with the sub-sample not affected by the TDAQ-related inefficiency ($t < 10$ ns) are reported in Tab. 6.1, for 1, 2, 3 and 4-fold coincidence conditions and compared with the MC expectation.

The obtained results can be used to extrapolate qualitatively the KTAG efficiency to the full detector configuration. Given the mean number N_{PMT} of hits observed during the Technical Run, the mean number N_{PMT}^{2014} expected with the full detector varies
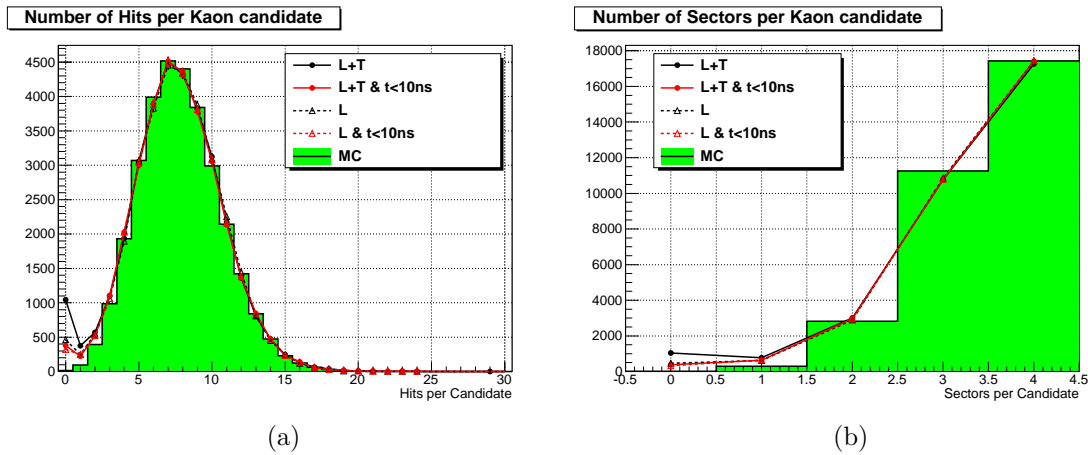
Figure 6.14: Distribution of the number of (a) KTAG hits and (b) KTAG sectors for the selected kaon sample, compared with the ones obtained from the sub-sample with $t < 10$ ns, not affected by the trailing edge loss. Two different edge requirements are considered: leading and trailing edge (L+T); at least one leading (L).

Table 6.1: KTAG efficiency measured with the selected kaon sample and the sub-sample not affected by the TDAQ-related inefficiency ($t < 10$ ns) for 1, 2, 3 and 4-fold coincidence conditions. The last column shows the MC expectation values.

N-fold	Efficiency (%) [total]	Efficiency (%) [$t < 10$ ns]	Efficiency (%) [MC]
≥ 1	96.84 ± 0.10	98.82 ± 0.06	99.96 ± 0.01
≥ 2	94.47 ± 0.13	96.85 ± 0.10	99.03 ± 0.05
≥ 3	85.33 ± 0.20	87.67 ± 0.18	90.15 ± 0.17
4	52.55 ± 0.28	54.13 ± 0.28	54.76 ± 0.28

between $2N_{\text{PMT}} \lesssim N_{\text{PMT}}^{2014} \lesssim 3N_{\text{PMT}}$ depending on the assumptions. The most optimistic is to assume a uniform light distribution over a light guide, which gives $3N_{\text{PMT}}$ due to a factor 3 in the number of PMTs in 2014 with respect to those used in the Technical Run. The most conservative assumption gives $2N_{\text{PMT}}$, by considering only the increase in the number of hits due to the four additional sectors to be installed along the four used during the Technical Run. Furthermore, the residual 2% of events with ≤ 1 hits observed in the data and not reproduced by the MC simulation has been conservatively added to the extrapolation. The results are reported in Tab. 6.2. With both the assumptions considered, the n-fold coincidence condition with $n = 5$ meets the NA62 requirement for kaon identification efficiency ($> 95\%$).

Table 6.2: KTAG efficiency extrapolated for the full detector, using different assumptions, for 1, 2, 3 and 4-fold coincidence conditions.

N-fold	2014 Efficiency (%) $[2N_{\text{PMT}}]$	2014 Efficiency (%) $[3N_{\text{PMT}}]$
≥ 5	96.32 ± 0.06	97.93 ± 0.05
≥ 6	89.12 ± 0.10	97.29 ± 0.05
≥ 7	67.08 ± 0.15	91.68 ± 0.09
≥ 8	29.03 ± 0.14	63.40 ± 0.15

6.5.3 KTAG time resolution

The KTAG time resolution $\sigma_{\text{KTAG}}(t)$ for kaon tagging is a function of the average PMT time resolution $\sigma_{\text{PMT}}(t)$ and the mean number of hits per kaon candidate N_{PMT}:

$$\sigma_{\text{KTAG}}(t) = \frac{\sigma_{\text{PMT}}(t)}{\sqrt{N_{\text{PMT}}}}. \tag{6.9}$$

During the Technical Run, a value of $N_{\text{PMT}} = 7.86 \pm 0.02$ was measured (Fig. 6.14a). After the channel synchronisation (T_0 corrections, Sec. 6.4.1), the measured mean PMT time resolution is $\sigma_{\text{PMT}}(t) = (317.1 \pm 1.0)\,\text{ps}$ (RMS), which corresponds to a KTAG time resolution of $(113.1 \pm 0.4)\,\text{ps}$ (RMS). The obtained value can be further improved by evaluating channel-by-channel corrections to compensate the different detection latencies of signals with different amplitudes (called "slewing corrections"). For each channel, the difference $\Delta t_{\text{PMT}} \overset{def}{=} t_K - t_{\text{PMT}}$ between the kaon candidate time t_K and the mean hit time t_{PMT} has been studied as a function of the signal width t_w. The function

$$\Delta t_{\text{PMT}} = \begin{cases} \Delta t'_{\text{PMT}} & \text{if } t_w < t'_w, \\ \Delta t'_{\text{PMT}} + \frac{\Delta t''_{\text{PMT}} - \Delta t'_{\text{PMT}}}{t''_w - t'_w}(t_w - t'_w) & \text{if } t'_w \leq t_w \leq t''_w, \\ \Delta t''_{\text{PMT}} & \text{if } t_w > t''_w, \end{cases} \tag{6.10}$$

with $t'_w = 10\,\text{ns}$ and $t''_w = 15\,\text{ns}$ (see Fig. 6.6b), has been used to fit the data, extracting the values of $\Delta t'_{\text{PMT}}$ and $\Delta t''_{\text{PMT}}$. The typical obtained values are $\Delta t'_{\text{PMT}} \sim 800\,\text{ps}$ and $\Delta t''_{\text{PMT}} \sim -100\,\text{ps}$. Then, for each hit, the latency Δt_{PMT} has been evaluated and subtracted. Fig. 6.15 shows the distribution of the time difference Δt_{PMT} as a function of the corresponding signal width t_w, integrated for all the KTAG channels, before
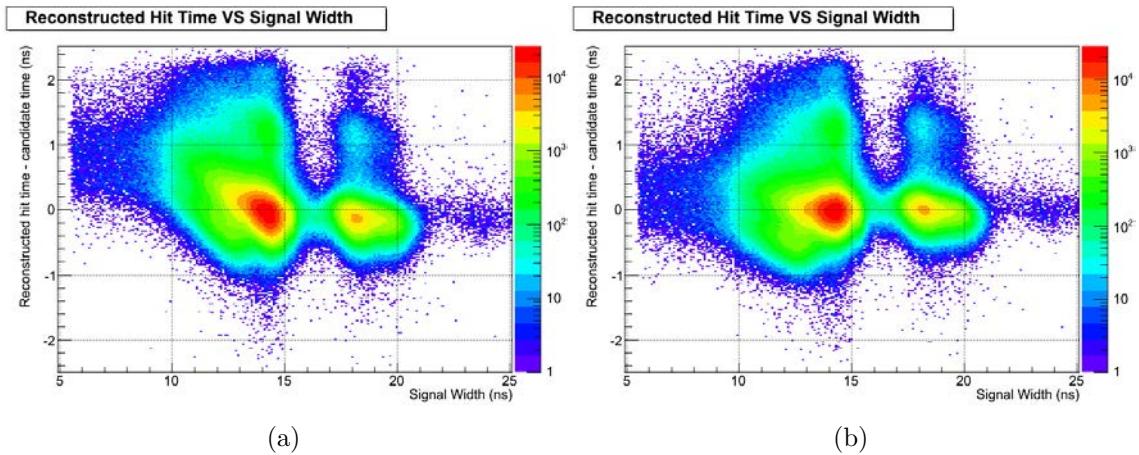
Figure 6.15: Relation between the signal width t_w and the PMT time deviation Δt_{PMT} from the candidate time (a) before and (b) after applying the slewing corrections. Before applying the slewing corrections, different latencies affect hits with different widths $t_w \lesssim 15\,\text{ns}$, resulting into a broader projection along the ordinate axis. After applying the slewing corrections, hits with different widths are synchronised. The sub-structure present for $\Delta t_{\text{PMT}} \gtrsim 1\,\text{ns}$ is due to delayed PMT responses due to electrons scattering off the first dynode.

and after applying the slewing corrections. The distributions of the PMT time with respect to the kaon candidate time, obtained at the different correction stages, are compared and shown in Fig. 6.16.

With both the T_0 and the slewing corrections, the evaluated PMT time resolution is $\sigma_{\text{PMT}}(t) = (287.1 \pm 0.8)\,\text{ps}$ (RMS), corresponding to a KTAG time resolution of

$$\sigma_{\text{KTAG}}(t) = \frac{\sigma_{\text{PMT}}(t)}{\sqrt{N_{\text{PMT}}}} = (102.4 \pm 0.3)\,\text{ps} \quad (\text{RMS}). \tag{6.11}$$

The introduction of the slewing corrections reduces the KTAG time resolution by about 10%, allowing us to reach the level of the NA62 time requirement (100 ps) with less than half the detector equipped. This result can be used to estimate qualitatively the expected time resolution $\sigma_{\text{KTAG}}^{2014}(t)$ for the full detector. An optimistic extrapolation is obtained assuming a uniform light distribution over a light guide: considering that the number of PMTs in 2014 will be three times the one of the Technical Run one

167
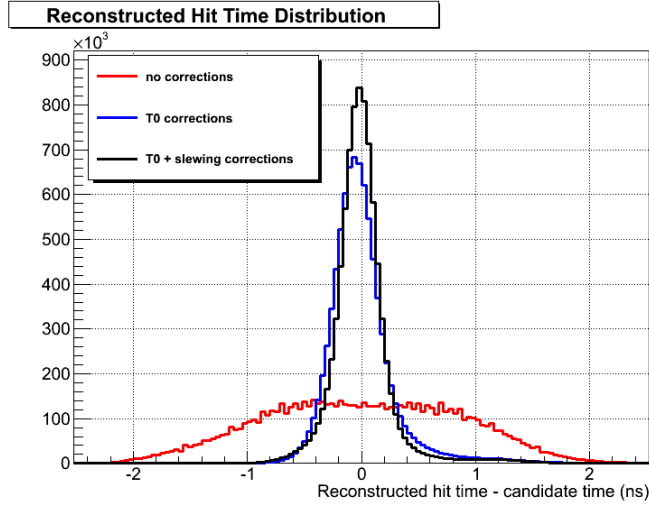
Figure 6.16: PMT time distribution with respect to the kaon candidate time, at different correction stages.

finds

$$\sigma_{\text{KTAG}}^{2014}(t) = \frac{\sigma_{\text{KTAG}}(t)}{\sqrt{3}} \simeq 60 \, \text{ps}. \tag{6.12}$$

On the other hand, the most conservative extrapolation is obtained by considering only the increase in the number of hits due to the presence of eight sectors (with 32 PMTs each) instead of four:

$$\sigma_{\text{KTAG}}^{2014}(t) = \frac{\sigma_{\text{KTAG}}(t)}{\sqrt{2}} \simeq 70 \, \text{ps}. \tag{6.13}$$

Therefore, the expected KTAG time resolution for 2014 is $60 \, \text{ps} \lesssim \sigma_{\text{KTAG}}^{2014}(t) \lesssim 70 \, \text{ps}$, which is at least 30% better than the NA62 time requirement.

Conclusions

Our understanding of the fundamental interactions of nature has been deeply enhanced by kaon physics. Nowadays, after more than 60 years since their discovery, kaons still play a unique role in the experimental challenge of probing the SM flavour sector with ever-increasing precision. Both the NA48/2 and NA62 experiments, the two most recent in a long tradition of fixed-target kaon experiments at CERN, exploit the clean environment of kaon decays to search for BSM physics. This thesis aims at contributing to this effort in a dual way: by searching for the LNV $K^{\pm} \to \pi^{\mp}\mu^{\pm}\mu^{\pm}$ decay with data collected by the NA48/2 experiment, and by validating the performances of the kaon identification detector in preparation for the NA62 experiment.

The presented search for the $K^{\pm} \to \pi^{\mp}\mu^{\pm}\mu^{\pm}$ decay has been performed on the full NA48/2 data sample collected in 2003 and 2004, corresponding to 1.8×10^{11} kaon decays in the fiducial volume. A blind analysis has been carried out in order to avoid any bias during the finalisation of the event selection criteria. Three theoretical models have been considered for the MC simulation of the $K^{\pm} \to \pi^{\mp}\mu^{\pm}\mu^{\pm}$ decay, one of which, of particular interest, describes the $K^{\pm} \to \pi^{\mp}\mu^{\pm}\mu^{\pm}$ decay occurring via a resonant Majorana neutrino. For this model, only the signal acceptance due to short-living ($\Gamma_{N_4} = 1\,\mathrm{MeV}$) Majorana neutrinos with mass $m_{N_4} = 300\,\mathrm{MeV}/c$ has been evaluated. The acceptance study for different Majorana neutrino masses and lifetimes is foreseen as further development of the presented analysis. The event selection has been tuned, using a dedicated MC simulation, to reject the main background, due to $K^{\pm} \to \pi^{\pm}\pi^{+}\pi^{-}$ decays with two subsequent same-sign pion decays. A dedicated

optimisation of the muon reconstruction for a di-muon search has led to a $\sim 70\%$ (relative) increase in the signal acceptance. The muon identification efficiency has been monitored during the whole 2003 and 2004 by reconstructing $K^{\pm} \rightarrow \mu^{\pm}\nu$ decays, and the number of kaon decays has been determined by selecting $K^{\pm} \rightarrow \pi^{\pm}\pi^{+}\pi^{-}$ decays. The observation of 1 data event in the signal region, for $1.36 \pm 0.97_{stat} \pm 0.06_{syst}$ expected background events, is interpreted as an upper limit on the number of $K^{\pm} \rightarrow \pi^{\mp}\mu^{\pm}\mu^{\pm}$ decays in the analysed data sample, by using the Rolke-Lopez statistical method. Given the evaluated signal acceptances and the measured number of kaon decays, such a limit implies ULs for the branching fraction $\mathcal{B}(K^{\pm} \rightarrow \pi^{\mp}\mu^{\pm}\mu^{\pm})$ within the theoretical models considered for the description of the signal. At 90% CL, the least stringent UL determined is

$$\mathcal{B}(K^{\pm} \rightarrow \pi^{\mp}\mu^{\pm}\mu^{\pm}) < 7.8^{+0.2}_{-0.6} \times 10^{-11} \quad @ \; 90\% \; \text{CL}$$

which improves the previous best limit by one order of magnitude. The systematic uncertainty of the ULs has been evaluated to be about 8% and is dominated by the error on the $K^{\pm} \rightarrow \pi^{+}\pi^{-}\mu^{\pm}\nu$ branching fraction, which is taken as an external parameter.

The work conducted for the commissioning of the partially-equipped CEDAR/KTAG detector during the NA62 Technical Run has been reported, together with the study of the detector performances, accomplished with a dedicated analysis of the Technical Run data. The commissioning phase included the CEDAR alignment and a pressure scan, which, showing a clear separation between the pion and the kaon peaks for the 4-fold coincidence condition, validated the CEDAR alignment and the chosen diaphragm aperture. From the pressure scan, an UL at 90% CL on the pion mis-identification probability $P_{mis}^{(4)}$ at the nominal kaon pressure has been evaluated by extrapolating the higher-pressure tail of the pion peak from the lower-pressure tail and assuming a symmetric pion peak distribution:

$$P_{mis}^{(4)} < 8.4 \times 10^{-4} \quad @ \; 90\% \; \text{CL},$$

which is of the same order of the mis-identification probability required by the NA62 experiment (10^{-4}). After the detector commissioning, the kaon identification efficiency and the time resolution of the CEDAR/KTAG detector have been measured, using a purposely-selected kaon sample, obtained reconstructing π^0 decays in the fiducial volume with a simultaneous charged track. The efficiencies of the n-fold coincidence conditions ($n = 1, 2, 3, 4$) have been evaluated and the extrapolation to the full-sized detector indicates that efficiencies above the NA62 requirement (95%) can be reached for the n-fold coincidence condition with $n = 5$. The time resolution for kaon candidates has been measured to be

$$\sigma_{\text{KTAG}}(t) = (102.4 \pm 0.3)\,\text{ps} \quad (\text{RMS}),$$

which is already at the level of the resolution required by the NA62 experiment ($100\,\text{ps}$) and corresponds to an extrapolated time resolution $60\,\text{ps} \lesssim \sigma_{\text{KTAG}}^{2014}(t) \lesssim 70\,\text{ps}$ for the fully equipped detector.

Bibliography

[1] Particle Data Group, J. Beringer *et al.*, Phys.Rev. **D86**, 010001 (2012).

[2] S. Petcov, Sov.J.Nucl.Phys. **25**, 340 (1977).

[3] S. Petcov, Adv.High Energy Phys. **2013**, 852987 (2013), 1303.5819.

[4] A. Atre, T. Han, S. Pascoli, and B. Zhang, JHEP **0905**, 030 (2009), 0901.3589.

[5] R. Mohapatra and A. Smirnov, Ann.Rev.Nucl.Part.Sci. **56**, 569 (2006), hep-ph/0603118.

[6] P. Minkowski, Phys.Lett. **B67**, 421 (1977).

[7] M. Gell-Mann, P. Ramond, and R. Slansky, Conf.Proc. **C790927**, 315 (1979), 1306.4669.

[8] B. Bajc, M. Nemevsek, and G. Senjanovic, Phys.Rev. **D76**, 055011 (2007), hep-ph/0703080.

[9] A. de Gouvea, J. Jenkins, and N. Vasudevan, Phys.Rev. **D75**, 013003 (2007), hep-ph/0608147.

[10] L. S. Littenberg and R. Shrock, Phys.Lett. **B491**, 285 (2000), hep-ph/0005285.

[11] A. Ali, A. Borisov, and N. Zamorin, Eur.Phys.J. **C21**, 123 (2001), hep-ph/0104123.

[12] G. Cvetic, C. Dib, S. K. Kang, and C. Kim, Phys.Rev. **D82**, 053010 (2010), 1005.4282.

[13] C. Boehm, Y. Farzan, T. Hambye, S. Palomares-Ruiz, and S. Pascoli, Phys.Rev. **D77**, 043516 (2008), hep-ph/0612228.

[14] Z. Chacko, L. J. Hall, S. J. Oliver, and M. Perelstein, Phys.Rev.Lett. **94**, 111801 (2005), hep-ph/0405067.

[15] J. Batley *et al.*, CERN-SPSC-2000-003 (2000).

[16] NA48/2 Collaboration, J. Batley *et al.*, Phys.Lett. **B697**, 107 (2011), 1011.4817.

[17] LHCb Collaboration, R. Aaij *et al.*, Phys.Rev.Lett. **112**, 131802 (2014), 1401.5361.

[18] LHCb Collaboration, R. Aaij *et al.*, Phys.Rev.Lett. **108**, 101601 (2012), 1110.0730.

[19] LHCb Collaboration, R. Aaij *et al.*, Phys.Rev. **D85**, 112004 (2012), 1201.5600.

[20] LHCb Collaboration, R. Aaij *et al.*, Phys.Lett. **B724**, 203 (2013), 1304.6365.

[21] S. Glashow, J. Iliopoulos, and L. Maiani, Phys.Rev. **D2**, 1285 (1970).

[22] N. Cabibbo, Phys.Rev.Lett. **10**, 531 (1963).

[23] M. Kobayashi and T. Maskawa, Prog.Theor.Phys. **49**, 652 (1973).

[24] L. Wolfenstein, Phys.Rev.Lett. **51**, 1945 (1983).

[25] D. Rein and L. Sehgal, Phys.Rev. **D39**, 3325 (1989).

[26] J. S. Hagelin and L. S. Littenberg, Prog.Part.Nucl.Phys. **23**, 1 (1989).

[27] M. Lu and M. B. Wise, Phys.Lett. **B324**, 461 (1994), hep-ph/9401204.

[28] G. Buchalla and A. J. Buras, Nucl.Phys. **B412**, 106 (1994), hep-ph/9308272.

[29] G. Buchalla and A. J. Buras, Nucl.Phys. **B548**, 309 (1999), hep-ph/9901288.

[30] W. Marciano and Z. Parsa, Phys.Rev. **D53**, 1 (1996).

[31] J. Bijnens and K. Ghorbani, (2007), 0711.0148.

[32] G. Isidori, F. Mescia, and C. Smith, Nucl.Phys. **B718**, 319 (2005), hep-ph/0503107.

[33] F. Mescia and C. Smith, Phys.Rev. **D76**, 034017 (2007), 0705.2025.

[34] J. Brod, M. Gorbahn, and E. Stamou, Phys.Rev. **D83**, 034030 (2011), 1009.0947.

[35] M. Gorbahn and U. Haisch, Nucl.Phys. **B713**, 291 (2005), hep-ph/0411071.

[36] A. Buras, M. Gorbahn, U. Haisch, and U. Nierste, Phys.Rev.Lett. **95**, 261805 (2005), hep-ph/0508165.

[37] A. J. Buras, M. Gorbahn, U. Haisch, and U. Nierste, JHEP **0611**, 002 (2006), hep-ph/0603079.

[38] J. Brod and M. Gorbahn, Phys.Rev. **D78**, 034006 (2008), 0805.4119.

[39] M. Atiya *et al.*, Nucl.Instrum.Meth. **A321**, 129 (1992).

[40] B. Bassalleck *et al.*, BNL-67247 (1999).

[41] E949 Collaboration, E787 Collaboration, S. Adler *et al.*, Phys.Rev. **D77**, 052003 (2008), 0709.1000.

[42] E949 Collaboration, A. Artamonov *et al.*, Phys.Rev.Lett. **101**, 191802 (2008), 0808.2459.

[43] G. Isidori, L. Maiani, and A. Pugliese, Nucl.Phys. **B381**, 522 (1992).

[44] NA48/2 Collaboration, J. Batley *et al.*, Eur.Phys.J. **C52**, 875 (2007), 0707.0697.

[45] NA48 Collaboration, V. Fanti *et al.*, Nucl.Instrum.Meth. **A574**, 433 (2007).

[46] R. De Wolf, R. Moore and T. White, NA48-94-01 (1994).

[47] NA48/2 Trigger Group, NA48-03-05 (2003).

[48] S. Anvar *et al.*, IEEE Trans.Nucl.Sci. **45**, 1776 (1998).

[49] E. Goudzovski, NA48/2 Collaboration meeting 16/04/2008.

[50] M. D. Beer, NA48-00-23 (2000).

[51] R. Brun, F. Carminati, and S. Giani, (1994).

[52] C. Biino *et al.*, COmPACT User's Guide (2007).

[53] R. Frühwirth, Nucl.Instrum.Meth. **A262**, 444 (1987).

[54] T. J. Gershon, NA48-98-25 (1998).

[55] J. Bijnens, G. Ecker, and J. Gasser, Nucl.Phys. **B396**, 81 (1993), hep-ph/9209261.

[56] W. A. Rolke and A. M. Lopez, Nucl.Instrum.Meth. **A458**, 745 (2001), hep-ph/0005187.

[57] W. A. Rolke, A. M. Lopez, and J. Conrad, Nucl.Instrum.Meth. **A551**, 493 (2005), physics/0403059.

[58] G. J. Feldman and R. D. Cousins, Phys.Rev. **D57**, 3873 (1998), physics/9711021.

[59] J. Neyman, Philos. Trans. R. Soc. London **A236**, 333 (1937).

[60] S. Wilks, Annals Math.Statist. **9**, 60 (1938).

[61] G. Casella and R. L. Berger, *Statistical Inference* (Duxbury, 1990).

[62] G. Anelli *et al.*, CERN-SPSC-2005-013 (2005).

[63] NA62 Collaboration, E. Cortina *et al.*, NA62-10-07 (2010).

[64] G. Ruggiero, (2013), PoS (KAON2013) 032.

[65] NA62 Collaboration, A. Ceccucci *et al.*, SPSC-SR-115 (2013).

[66] OPAL Collaboration, K. Ahmet *et al.*, Nucl.Instrum.Meth. **A305**, 275 (1991).

[67] NA62 Collaboration, A. Ceccucci *et al.*, SPSC-M-760 (2007).

[68] B. Angelucci *et al.*, Journal of Instrumentation **9**, C01055 (2014).

[69] M. Pivanti *et al.*, Journal of Physics: Conference Series **513**, 012008 (2014).

[70] C. Bovet, S. Milner, and A. Placci, IEEE Trans.Nucl.Sci. **25**, 572 (1978).

[71] C. Bovet, R. Maleyran, L. Piemontese, A. Placci, and M. Placidi, (1982).

[72] A. Romano, Leptonic decays and Kaon Identification at the NA62 experiment at CERN, PhD thesis, 2012.

[73] I. Tamm, J.Phys.(USSR) **1**, 439 (1939).

[74] E. Goudzovski, CEDAR Working Group Meeting 9/04/2013.

[75] GEANT4, S. Agostinelli *et al.*, Nucl.Instrum.Meth. **A506**, 250 (2003).

[76] http://sergiant.web.cern.ch/sergiant/NA62FW/html/index.html.

[77] Hamamatsu, User's Data Sheet .

[78] Hamamatsu, User's Data Sheet .

[79] F. Anghinolfi *et al.*, Nucl.Instrum.Meth. **A533**, 183 (2004).

[80] J. Christiansen, HPTDC High Performance Time to Digital Converter, Version 2.2 for HPTDC version 1.3, 2004.

[81] E. Pedreschi, M. Sozzi, F. Spinella, NA62-10-06 (2010).

[82] G. Haefeli *et al.*, Nucl.Instrum.Meth. **A560**, 494 (2006).

[83] CEDAR Working Group, NA62-12-05 .

[84] H. A. Lorentz, Ann.Phys. **9**, 641 (1880).

[85] L. Lorenz, Ann.Phys. **11**, 70 (1880).

Appendix A

Determination of the E/p spectra

The $e^\pm$, $\mu^\pm$ and $\pi^\pm$ samples used to determine the E/p spectra shown in Fig. 3.1 have been obtained applying the selections listed below.

$e^\pm$ **sample:** In order to select an electron sample not affected by any E/p requirement, $K^\pm \to \pi^\pm \pi^0$ decays followed by a $\pi^0 \to e^+ e^- \gamma$ decay have been reconstructed. The electron mass has been assumed for the different-sign track and for the one of the two same-sign tracks with highest E/p ratio. The considered $e^\pm$ sample has been based on the different-sign tracks only, to which no E/p requirement is applied. The following conditions have been required:

- exactly three tracks, within the detector acceptance and not associated to any reconstructed muons, and exactly one reconstructed three-track vertex, required to be in the fiducial volume and with $\chi^2 < 20$;

- exactly one energy deposition cluster in the LKr with energy $E > 2\,\text{GeV}$, within 12 ns from the average of the track times and not consistent with being due to any track energy deposition;

- total momentum p_{tot} and total transverse momentum $p_{\perp tot}$ of the three tracks and the reconstructed photon consistent with the kaon nominal 3-momentum: $|p_{tot} - 60\,\text{GeV}/c| < 5\,\text{GeV}/c$ and $p_{\perp tot} < 10\,\text{MeV}/c$;

- reconstructed invariant mass $m_{ee\gamma}$, defined as

$$
\begin{aligned}
m_{ee\gamma}^2 \;\;\overset{def}{=}\;\; & (P_{e^+} + P_{e^-} + P_\gamma)^2 \\
= \;\; & 2m_e^2 + 2E_\gamma(E_{e^+} + E_{e^-}) - 2\vec{p}_\gamma \cdot (\vec{p}_{e^+} + \vec{p}_{e^-}) \\
& + 2(E_{e^+} E_{e^-} - \vec{p}_{e^+} \cdot \vec{p}_{e^-}),
\end{aligned}
\tag{A.1}
$$

satisfying the condition $|m_{ee\gamma} - m_{\pi^0}| < 8\,\text{MeV}/c^2$;

- reconstructed invariant mass $m_{\pi\pi^0}$, defined as

$$
\begin{aligned}
m_{\pi\pi^0} &\overset{def}{=} (P_\pi + P_{\pi^0})^2 \\
&= m_\pi^2 + m_{\pi^0}^2 + 2(E_\pi E_{\pi^0} - \vec{p}_\pi \vec{p}_{\pi^0}),
\end{aligned}
\tag{A.2}
$$

satisfying the condition $|m_{\pi\pi^0} - m_K| < 8\,\mathrm{MeV}/c^2$;

- the highest E/p ratio of the same-sign tracks is required to be greater than 0.95 and the lowest smaller than 0.85.

With the described requirements, 6.8×10^5 $e^\pm$-tracks with a momentum in the range $[5,50]\,\mathrm{GeV}/c$ have been selected from a subset of the FULL data sample[1].

$\boldsymbol{\mu^\pm}$ **sample:** The μ sample consisted of 4.6×10^5 μ-tracks, obtained from a subset of the previously selected $K^\pm \to \mu^\pm \nu$ candidates (from the MB2004 sample) used to study the muon identification efficiency (Sec. 3.5.1). Muon-candidate tracks associated to a reconstructed muon with status 1 or 2 (Sec. 3.5.2) and with a momentum in the range $[5,50]\,\mathrm{GeV}/c$ have been selected.

$\boldsymbol{\pi^\pm}$ **sample:** A total of 1.7×10^6 π-candidate tracks have been obtained from a subset of the $K^\pm \to \pi^\pm \pi^+ \pi^-$ candidates (from the D100 sample) selected to measure the integrated kaon flux (Sec. 3.4). Pion-candidate tracks with no associated muons and with a momentum in the range $[5,50]\,\mathrm{GeV}/c$ have been selected.

---

[1]See Sec. 3.2.1 for a detailed description of the considered data samples.

Appendix B

MUV alignment study

During the muon reconstruction efficiency study (Sec. 3.5), an unexpected MUV misalignment has been observed. Fig. B.1 shows the difference between the x (y) coordinate of the extrapolated track impact point at the MUV2 (MUV1) plane and the reconstructed muon x (y) coordinate, for the selected $K^{\pm} \to \mu^{\pm}\nu$ data and MC samples. An overall shift of ~ 2 cm is evident, on both the x and y directions, between
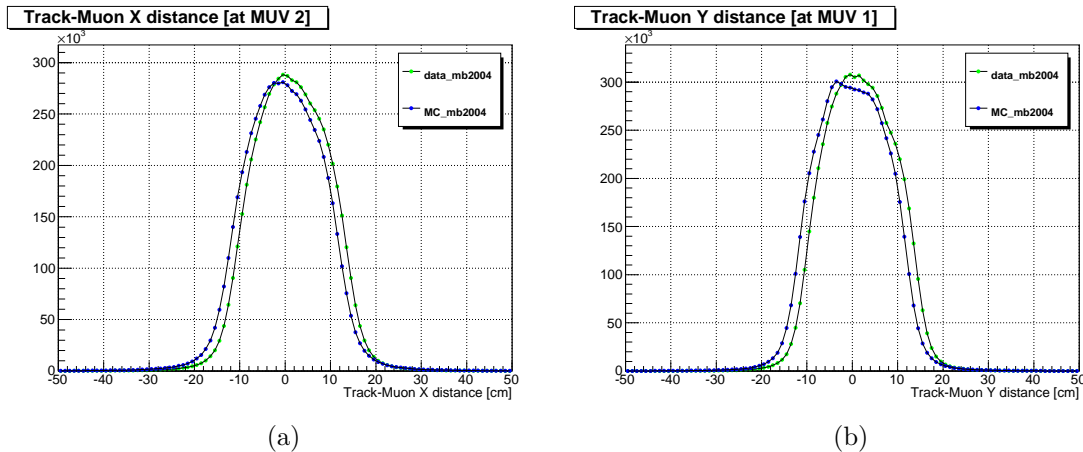
Figure B.1: Distributions of the projections along the (a) x and (b) y axes of the distance between the expected track impact point and the reconstructed muon coordinates, for the selected $K^{\pm} \to \mu^{\pm}\nu$ data and MC samples.

the data and MC samples. In order to investigate the origin of the disagreement, the subset of $K^{\pm} \to \mu^{\pm}\nu$ events with exactly one track has been considered.

The position of each MUV1 (MUV2) strip along the y (x) direction has been checked, for both data and MC, by studying the fraction of the selected events with at least one hit in the strip channels, as a function of the y (x) coordinate of the expected track impact point, determined by extrapolating the track trajectory to the MUV

plane involved.

This method has led to a profile of each MUV strip along the direction orthogonal to the strip length, which has been used to estimate the MUV strip centre position. Fig. B.2 shows two examples of the obtained profiles, for the strip 3 of the MUV1 and the strip 5 of the MUV2. Each MUV1 (MUV2) strip centre has been evaluated

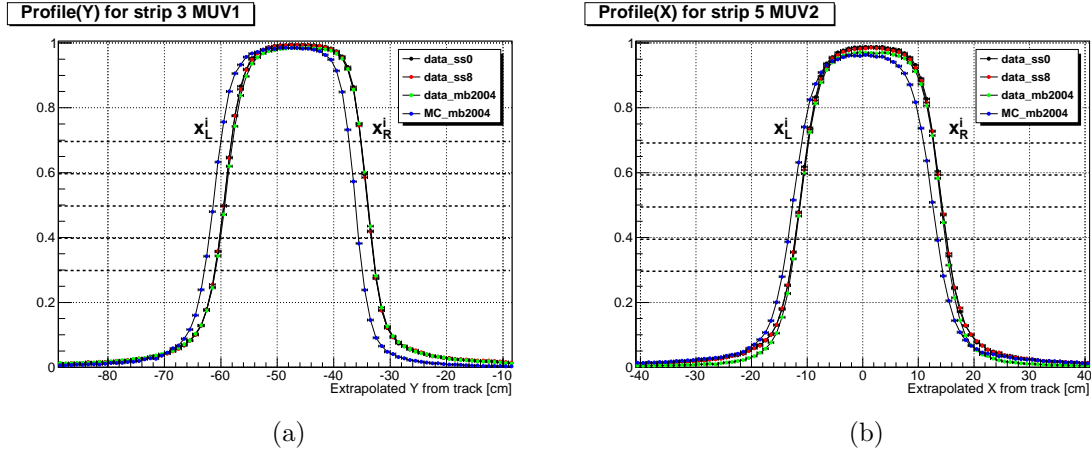(a)   (b)

Figure B.2: Fraction of events with at least a hit in the strip channels as a function of the expected track impact point coordinate orthogonal to the strip length, for the selected $K^{\pm} \to \mu^{\pm}\nu$ data and MC samples, (a) for the strip 3 of the MUV1 and (b) for the strip 5 of the MUV2. The dashed lines indicate some of the heights y_{th}^i of the strip profile used to determine the corresponding values x_L^i and x_R^i.

by finding the values y_L^i and y_R^i (x_L^i and x_R^i) corresponding to 100 given heights ε_{th}^i of the strip profile, between 0.3 and 0.7 times the maximum value of the profile, as illustrated in Fig. B.2. Then, the strip centre coordinate y_c (x_c) has been determined by the average

$$y_c = \sum_{i=1}^{100} \frac{y_L^i + y_R^i}{2}, \quad \left(x_c = \sum_{i=1}^{100} \frac{x_L^i + x_R^i}{2} \right). \tag{B.1}$$

The same method has been applied to the MC sample, in order to validate the strip centre evaluation procedure and to estimate the bias on the y_c (x_c) measurements introduced by the non-uniform momentum distribution along the strip width and the consequent different multiple scattering contributions at the strip edges. Fig. B.3 shows the difference between nominal[1] and estimated strip centres for each strip, for both data and MC samples. The estimated strip centres values for the MC sample are consistent with the nominal ones for all the MUV strips. This indicates that the evaluation procedure performed is valid and is not dominated by biases due to any asymmetries in the profile shapes, and also that the MC simulation is consistent with the COmPACT reconstruction software. On the other hand, data show a non-zero

---

[1]The MUV strip centre coordinates were measured in 1994 and are stored in the COmPACT framework; in the following they will be referred to as "nominal" strip centres coordinates.
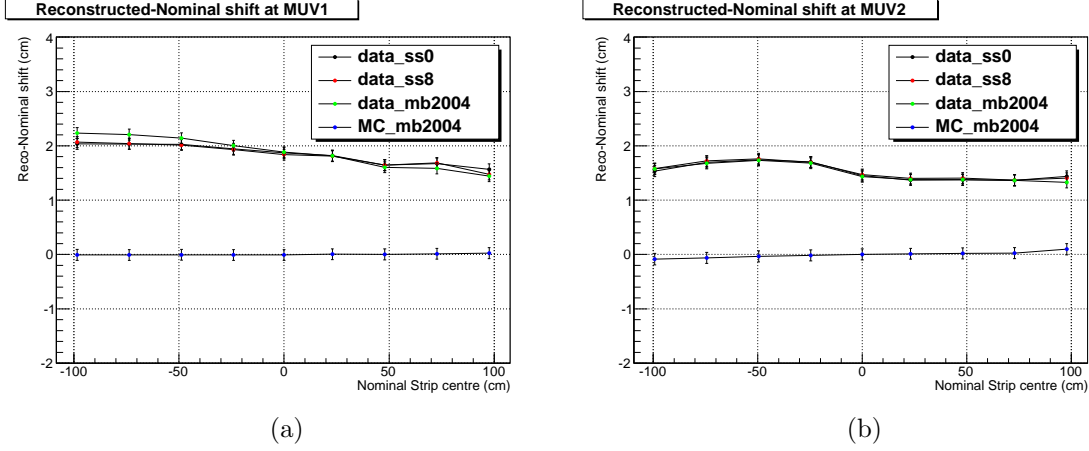
Figure B.3: Difference between the nominal and the estimated strip centres as a function of the nominal strip centre, for (a) MUV1 and (b) MUV2 strips, obtained from the selected $K^{\pm} \to \mu^{\pm}\nu$ data and MC samples.

shift for each strip:

- MUV1 strips (Fig. B.3a) are affected by a global shift and by a position-dependent contribution, as shown by the presence of a slope;

- MUV2 strips (Fig. B.3b) are affected by a global shift and by a smaller additional shift of a subsector.

The presence of the slope for the MUV1 strip centres is consistent with a shift of the MUV1 plane along the z-axis. In that case, the track trajectories would be extrapolated to the wrong plane z'_{MUV1}, leading to a wrong estimate y'_c of the strip centre y_c:

$$y'_c = y_c + \frac{y_c - y_{\text{DCH}}}{z_{\text{MUV1}} - z_{\text{DCH}}}(z'_{\text{MUV1}} - z_{\text{MUV1}}), \qquad \text{(B.2)}$$

where z_{DCH} is the DCH plane z-coordinate and y_{DCH} is the track impact point coordinate at the DCH plane. From eq. B.2 it is straightforward to demonstrate that the relation between the strip centre shift $\delta y_c \overset{def}{=} y'_c - y_c$ depends linearly from the MUV1 strip centre coordinate y_c:

$$\delta y_c = \frac{z'_{\text{MUV}} - z_{\text{MUV}}}{z_{\text{MUV}} - z_{\text{DCH}}}y_c - \frac{z'_{\text{MUV1}} - z_{\text{MUV1}}}{z_{\text{MUV1}} - z_{\text{DCH}}}y_{\text{DCH}} \overset{def}{=} my_c + q. \qquad \text{(B.3)}$$

After checking the MUV1 z-coordinate from the NA48/2 official database, a difference of 38 cm was found with respect to the value used in the official MC and COmPACT software. Fig. B.4 shows the updated versions of the plot in Fig. B.3a after correcting the MUV1 z position in the MC simulation and in the COmPACT software.

The additional shift affecting a MUV2 subsector has been measured to be 3 mm, by
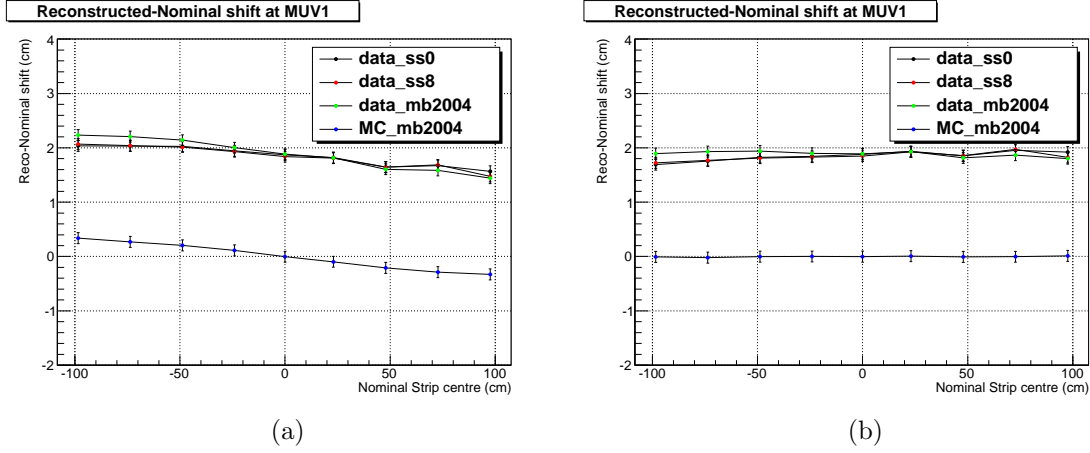
Figure B.4: Difference between the nominal and the estimated strip centres as a function of the nominal strip centre for MUV1 strips, after correcting the MUV1 z position (a) in the MC simulation and (b) in the COmPACT software (cf. Fig. B.3a).

fitting the shift of the strips involved with a constant. Then, the centres of such strips have been translated accordingly in software.

Finally, the δx (MUV2) and δy (MUV1) shifts have been measured from data by averaging the shifts of all the strips over the different super-samples considered:

$$\delta x = (1.40 \pm 0.02)\,\text{cm}, \quad \delta y = (1.86 \pm 0.02)\,\text{cm}. \tag{B.4}$$

Fig. B.5 shows the difference between new nominal strip centres and estimated ones as a function of the new nominal strip centre, for both data and MC samples. The residual strip shift is $\sim \mathcal{O}(1\,\text{mm})$.
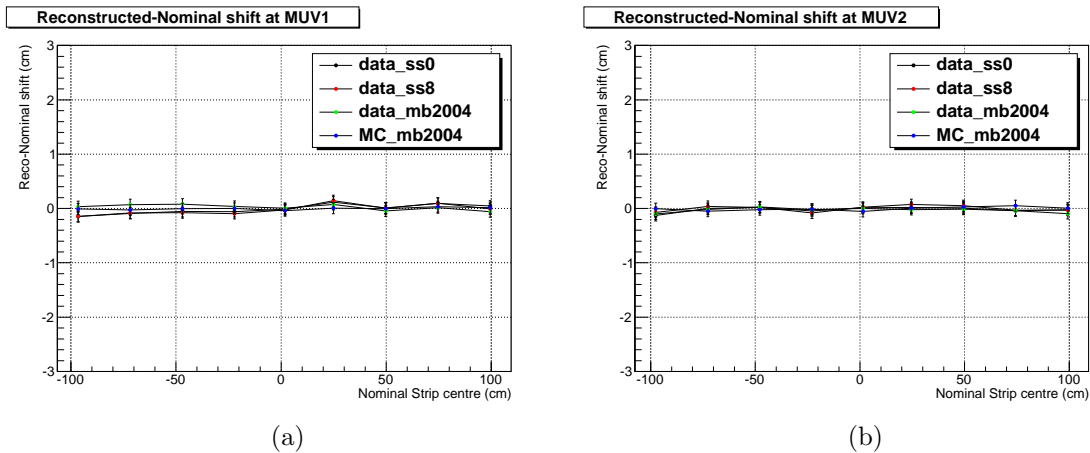

Figure B.5: Difference between new nominal strip centres and estimated ones as a function of the new nominal strip centre, (a) for MUV1 and (b) for MUV2 strips.

Appendix C

$K^{\pm} \rightarrow \pi^{\pm}\pi^{+}\pi^{-}$ MC production

As discussed in Sec. 3.6.1.1, a simulation of $\mathcal{O}(10^{10})$ $K^{\pm} \rightarrow \pi^{\pm}\pi^{+}\pi^{-}$ decays is required to precisely study the $K^{\pm} \rightarrow \pi^{\mp}\mu^{\pm}\mu^{\pm}$ background. However, neither the full simulation nor the standard fast mode are feasible: the first, due to the pion shower development in the LKr, is expected to take more than 6×10^{6} KSI2K hours of CPU time, corresponding to a time of ~ 4 years, assuming a set of 100 continuously running parallel jobs; the second, which exploits LKr shower libraries developed by the NA48 collaboration, does not simulate properly the multiple Coulomb scattering of muons, which plays a crucial role in the muon mis-reconstruction. The latter is a consequence of the shower libraries implementation: particle tracking is stopped at the entrance of the LKr and shower libraries are called. However, it cannot be re-enabled for the particles which keep travelling downstream the LKr (e.g. muons), therefore their trajectories are extrapolated up to the MUV system.

Since the actual number of events of interest, i.e. those events which could contribute to the $K^{\pm} \rightarrow \pi^{\mp}\mu^{\pm}\mu^{\pm}$ background, is much smaller than the required number of events, the problem has been solved by implementing an optimised mode, which simulates all the events up to the LKr entrance; filter the events exploiting the information from the first simulation stage; and complete the simulation only for those events which meet user-defined selection criteria. Such simulation mode has been named Super-TURBO (STURBO), in analogy to the standard fast mode, which is called TURBO. The working principle of the STURBO mode is sketched in Fig. C.1.
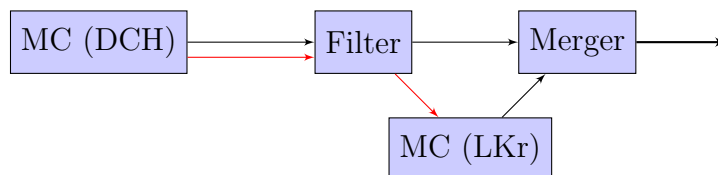

Figure C.1: Sketch of the working principle of the STURBO mode. Black and red arrows indicate respectively the COmPACT and the binary files input/output.

As the standard fast mode, the simulation in the STURBO mode stops the tracking at the entrance of the LKr; then, instead of calling the shower libraries, it stores in a buffer the relevant information (type, position, direction, momentum) of the first 1000 particles (for each event) reaching the LKr aluminium window. At the end of the event, particles in the buffer are sorted in descending order of momentum and the first 100 are stored in an external binary file. Once all the events are processed, the standard output in the COmPACT format and the custom binary file with the information of the stopped particles are written. This first simulation stage reproduces only the particle tracking and the detector responses upstream the LKr aluminium window. Among the upstream detectors there is the magnetic spectrometer, the response of which is fully simulated: for this reason, this MC stage is called "DCH". The DCH simulation outputs, i.e. the external binary file and the standard output in the COmPACT format, are read by a filtering routine which selects the events satisfying user-defined conditions involving variables already defined at the DCH stage (e.g. $m_{\pi\mu\mu}$, $\vec{p}_{\perp 3trk}$, $m_{miss}^{2\,(\pi)}$) and write the filtered COmPACT and binary files. The filtered binary file is then used as input of the second simulation stage, called "LKr", in which the events restart from the point in which they were terminated at the DCH stage and the particle tracking in the downstream detectors is simulated. Once the LKr simulation stage is concluded, a COmPACT file containing the remaining part of the event information is written. At this point, the two COmPACT files from the DCH and LKr stages are merged event-by-event and the final COmPACT file, containing all the information, is produced.

After the implementation, the STURBO mode has been validated producing $K^{\pm} \to \pi^{\pm}\pi^0$ decays. This choice is intended to exploit at the same time information from the DCH stage (e.g. π^+ momentum) and from the LKr stage (e.g. π^0 reconstruction). The first test has been performed by using a "transparent" filter, i.e. reproducing with the STURBO mode all the events, without any rejection at the filter stage. Fig. C.2a shows the distribution of the $K^{\pm} \to \pi^{\pm}\pi^0$ invariant mass variable $m_{\pi\pi^0}$, defined as

$$m_{\pi\pi^0}^2 = (P_\pi + P_{\pi^0})^2 = m_\pi^2 + m_{\pi^0}^2 + 2E_\pi E_{\pi^0} - 2\vec{p_\pi} \cdot \vec{p_{\pi^0}}, \qquad \text{(C.1)}$$

for the STURBO mode with transparent filter, compared to the full MC simulation. Then, a filter on the missing mass variable $m_{miss}^{2\,(\pi)}$ has been applied: $0.018\,\text{GeV}^2/\text{c}^4 < m_{miss}^{2\,(\pi)} < 0.022\,\text{GeV}^2/\text{c}^4$. Fig. C.2b shows the $m_{miss}^{2\,(\pi)}$ distribution obtained with the STURBO mode, compared to the full MC simulation.

After the STURBO mode validation, the $K^{\pm} \to \pi^{\pm}\pi^+\pi^-$ MC simulation has been produced. As filtering conditions, the $K^{\pm} \to \pi^{\pm}\pi^+\pi^-$ events are required to have at least one three-track vertex, the tracks of which satisfy all the following conditions:

- $K^{\pm} \to \pi^{\mp}\mu^{\pm}\mu^{\pm}$ invariant mass variable $m_{\pi\mu\mu} > 0.455\,\text{GeV}/c^2$;

- total momentum $50\,\text{GeV}/c < |\vec{p}_{3trk}| < 70\,\text{GeV}/c$;

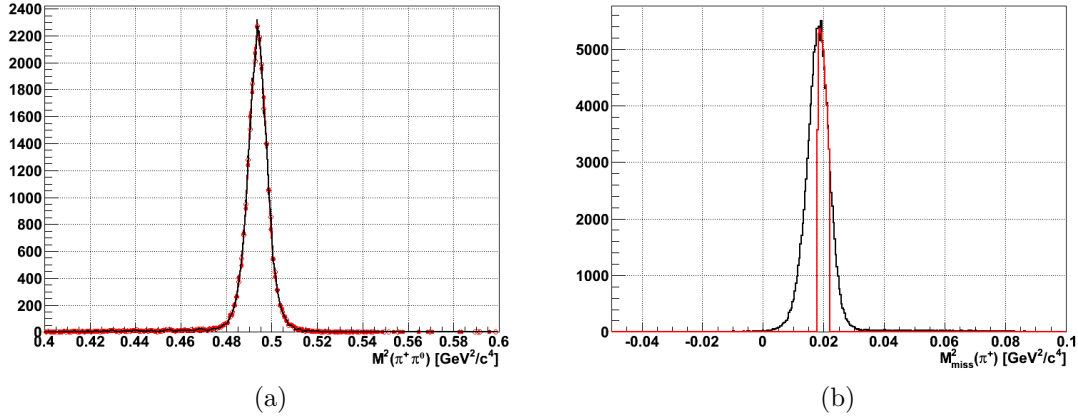- total transverse momentum $|\vec{p}_{\perp 3trk}| < 31.6\,\text{MeV}/c$.

Figure C.2: Distributions obtained simulating $K^+ \to \pi^+\pi^0$ decays with the STURBO mode (red): (a) reconstructed invariant mass $m_{\pi\pi^0}$ for a MC sample obtained applying a "transparent" filter and (b) $m^{2\,(\pi)}_{miss}$ variable for a MC sample on which the filter $0.018\,\mathrm{GeV^2/c^4} < m^{2\,(\pi)}_{miss} < 0.022\,\mathrm{GeV^2/c^4}$ has been applied. The relative distributions obtained with the full MC simulation are shown for comparison (black).

With the above conditions, $\sim 1\%$ of the $K^\pm \to \pi^\pm\pi^+\pi^-$ events is selected for the simulation of the LKr stage. The total CPU times and the mean CPU times per event for the different stages, compared with the full MC, are summarised in Tab. C.1. The total CPU time required for the $K^\pm \to \pi^\pm\pi^+\pi^-$ production with the STURBO

Table C.1: CPU times for the different stages of the STURBO mode, compared with the full MC simulation. The total CPU time has been evaluated considering 10^{10} full event, i.e. 10^{10} DCH events and 10^8 LKr events (1% filtering).

MC mode	CPU time/event (KSI2K s)	Total CPU time (KSI2K s)
DCH	0.081	8.1×10^8
LKr	1.111	1.1×10^8
full	2.317	2.3×10^{10}

mode is 25 times shorter than the one of the full simulation. It is worth noticing that the sum of CPU times per event for the DCH and LKr stages is less than the CPU time per event required for the full simulation: this is due to the fact that the filtering condition $m_{\pi\mu\mu} > 0.455\,\mathrm{GeV}/c^2$ selects mostly events with at least one $\pi^\pm \to \mu^\pm\nu$ decay (see Fig. 3.10), in which the mean number of hadronic showers in the LKr is significantly smaller (and so is the CPU time).